Equilibrium and Phase Stability of Nanoparticles

By
Nadi Braidy, M.Sc., B.Eng.

A Thesis
Submitted to the School of Graduate Studies
in Partial Fulfilment of the Requirements
for the Degree
Doctor of Philosophy

McMaster University

DOCTOR OF PHILOSOPHY (2007) McMaster University
(Department of Materials Science and Engineering) Hamilton, Ontario

TITLE: Equilibrium and Phase Stability of Nanoparticles
AUTHOR: Nadi Braidy, M.Sc., B.Eng.
SUPERVISOR: Gianluigi A. Botton
NUMBER OF PAGES: xvi, 203

Abstract

We explore the effect of size on the phase stability of nanosystems by comparing calculated trends with the annealing behavior of nanoparticles (NPs) initially in a core-shell configuration. The NPs are characterized using a variety of transmission electron microscopy (TEM) techniques.

We first theoretically consider the equilibrium within a Au-Pt NP of a given size. When considering the contribution of surface and interface energies, we note the appearance of a restricted composition range of the phase diagram over which the liquid and solid phases cannot coexist in a core-shell configuration. A critical radius of ~42 nm is identified below which the NP is single-phased for any composition. It is demonstrated that both branches of the miscibility gap of the Au-Pt phase diagram shift towards the Au-rich composition with increasing curvature. The magnitude of the shift is found to be strongly correlated with the coupling of nonlinear terms entering the Gibbs energy. The main contribution to the shift arises from the composition-dependent surface energy, calculated by considering the selective adsorption of Au to the surface, evaluated using the available thermodynamic properties of the Au-Pt system.

An array of TEM-related analytical methods were developed or adapted for the characterization of individual NPs. In particular, chemical maps with quantitative information from a NP with a spatial resolution of ~1.2 nm could be achieved, with their corresponding error analysis. We introduce an algorithm to retrieve the radial elemental composition from the projected chemical map of a NP if a spherical symmetry can be assumed and test it with NPs of known structures. We also present a technique to determine the composition of a NP having one of the elements depleting during analysis, and test it experimentally with 5–20 nm Au-Ag NPs. Typically, for every Ag characteristic X-ray detected, one Ag atom is lost to knock-on damage. We discuss the detection limit of the method as a function of NP size and composition.

We follow the structural evolution of a ~20 nm Au(core) Pt(shell) NP during annealing at various temperatures between 300 and 800 °C. At low temperatures, interdiffusion occurs between the core and the shell, while at temperatures above ~600 °C, the configuration evolves towards one composed of Au- and Pt-rich spherical caps, separated by a relatively flat interface. We could measure a 5–10% shift in the composition of each phase with respect to the bulk phase diagram that we assigned to capillarity effect. The shift agrees qualitatively with the calculated trends. The ratio of the surface to the interface energy is measured directly from a TEM micrograph of a segregated NP and is in close agreement with the calculated ones.

This work contributes to the understanding of the phase stability of binary NPs. The prospect of extending these studies to NPs of other bimetallic systems while probing their properties seems promising, especially in view of their catalytic, magnetic and optical potential.

Acknowledgements

I first and foremost wish to express my most sincere gratitude to Dr Gianluigi Botton, my thesis supervisor and mentor, for his guidance and support. He has passed along to me his passion for electron microscopy and his appreciation of genuine materials science, which I consider the most valuable acquisitions of my PhD.

I am extremely grateful to Dr Zygmunt Jakubek (NRC), a member of my supervisory committee, for his constructive criticism and encouragement. His time and efforts were greatly appreciated not only during my trips to the NRC but also for his active involvement in the data analysis at McMaster. I would like to acknowledge Drs Gary Purdy and Dmitri Malakhov from the department of Materials Science and Engineering (MSE, McMaster), also members of my supervisory committee, for scientific guidance and numerous scientific discussions pertaining to the fields of thermodynamics, physical chemistry and metallurgy.

I thank Dr Alex Adronov, from the Chemistry Department (McMaster) for giving me access to his lab bench. He and his group gave me the chance to discover the interesting field of synthetic chemistry. Dr Sonia Behal (previously from the Chemistry Department, McMaster) is acknowledged for providing me with the CoCoO specimen.

I was extremely lucky to have had many enlightening, fruitful and interesting discussions pertaining to my thesis with Drs Ray Egerton (Alberta University), Drs David Embury (MSE), John Preston (Brockhouse Institute for Materials Research, McMaster), Hatem Zurob (MSE), Olivier Bouaziz (ARCELOR), Mohamed Gouné(ARCELOR) and Dr Yves Bréchet (INPG, Grenoble).

This PhD could not have been possible without the help of dedicated staff of the BIMR, namely Andy Duft, Fred Pearson and Jim Garrett. I shall be indebted to them for not only actively contributing to my experiments but for passing along some of their skills and knowledge which will definitely be useful in my career.

I am thankful to Dr Benoit Simard (SIMS, NRC) for the collaboration with his group and for giving me access to the laser equipment. Séphane Dénommée, Dr Chris Kingston and Dean Ruth are thanked for their support during my visits at the NRC.

Dr Martin Hÿtch (CNRS, Toulouse) is acknowledged for his contribution on the strain maps shown in Fig. 6.9. I wish to thank the hospitality and involvement of Dr Jean-Luc Rouvière (CEA, Grenoble) during my visit at the CEA (Grenoble).

I am thankful for the help and moral support of Micheal FitzPatrick (undergrad student, McMaster) for the specimen preparation during the summer of 2006. I wish to acknowledge Dr Yew Ming Cheng for teaching me the art of preparing TEM thin carbon film deposition. The JEOL hotstage loan of Dr Vuko Perovic (Kinetrix) is greatly appreciated.

I wish to express my appreciation to the present and past staff of the MSE and BIMR administrative office (Elvira Evangelista, Mary Mitchell, Jane Mah, Betty Petro and Anne Reynolds). Their professionalism, kindness and smiles shall be remembered. The scholarly culture which prevails at the MSE and the BIMR and the willingness of staff and faculties to help and assist were instrumental to the success of this project.

On a personal note, Drs Florent Lefebvre-Schlick (now at Algoma), Arnaud Weck (now at University of British Columbia), Boris Martin (now with Engineers Without Borders) and Shane Turcott (now with Liburdi): Thanks for the great times, lunches, outings and parties! You are the only friends with whom I can also have fun discussing science and who were kind enough to listen to me wining about Cu contamination. You were part of the fun times during this PhD and I am still convinced that we will end up starting up an MSE department in a Canadian university one day !

This thesis would not have even started without the continuous support, kindness and love of my parents and family. Their encouragement and patience were most welcomed in times of doubt. An extra chapter in this thesis would probably not suffice to describe my love and gratitude to my sweetheart, Marie-Josée Colbert. Her love and support were essential for my survival during this program: I thank you (and apologize) from the bottom of my heart to have endured part of my burden upon you.

À Léa,
qui a su devenir plus grande qu'elle-même.

Table of Contents

List of Figures

List of Tables

Chapter 1

Introduction

The phenomenon of capillarity can lead to drastic change in the phase stability of materials, and consequently on their properties. Capillarity can arise from a high surface-to-volume ratio which scales with the curvature of internal or external boundaries of crystallites or particles. It has become common practice to observe the appearance of new phases or to stabilize high-temperature phases in single-phase materials that are prepared with a high surface-to-volume ratio. This effect can be used to obtain a new set of materials properties, usually unavailable at room temperature.

A new range of properties becomes available through the design of nanoparticles (NPs) with two or more elements. In this case, the optical, magnetic or catalytic properties, to name a few, not only depend on size but also on composition, presence of segregation within NPs, or a particular phase, etc. Significant attention has been recently devoted to the exploration of unique size-dependent physical and chemical properties of nanometer-sized metal particles and their potential use in advanced applications (Feldheim and Foss 2001). For example, the environmental (Kim et al. 2001) and biological (Elghanian et al. 1997; Storhoff et al. 1998; Storhoff et al. 2000; Taton et al. 2000; Jin et al. 2001; Park et al. 2002) applications make use of metal NPs optical properties, while catalytic (Lyman et al. 1990; Yudasaka et al. 2002; Kingston and Simard 2003; Arepalli 2004) and sensor ones (Sharma and Gupta 2006) take advantage of composition-dependent properties of alloyed NPs.

With recent progress in synthetic chemistry and physical deposition methods, it is possible to fabricate a variety of NPs of various size, shape and composition. In parallel, advances in characterization techniques, especially related to transmission electron microscopy (TEM), opened a new window for the investigation of size-dependent nanostructures. Given the technological importance of NPs, it has become paramount to apply the "process-(nano)structure-properties" paradigm to nanoscience and nanotechnology.

There exists no unified theory that allows one to predict the phase of a NP at a given size, composition and temperature due to the existence of a division developing between theory and experiment. On one hand, when a size-related phenomenon is explained in terms of surface effects, it is done under a given set of assumptions and approximations exclusive to this system. On the other hand, some theoretical studies have appeared but are generally not supported by experimental data.

On the theoretical aspect, the melting behavior of single-phase NPs is well established and readily confirmed by experiments. Indeed melting of NPs is thought to

begin with the appearance of a liquid skin on a NP whose thickness increases over a small range of temperature until the droplet becomes completely liquid (Couchman and Jesser 1977). However, for binary NPs, several extra aspects need to be taken into account. In particular, the surface and interface energies can no longer be taken as constants with temperature and composition. In addition, one can expect a constraint on mass balance to limit the composition range over which nucleation within a NP is possible. We need to realize that the radius of a NP can be considered as an extensive variable (by introducing an overpressure on the system), and therefore, can induce phase transformation. Some of these aspects were considered for simple ideal systems, but how would this translate for a binary alloy described by a set of elaborated Gibbs functions?

When considering the phase stability of solid NPs, the situation can be even more complex. In addition to the composition and temperature dependence, the surface energy exhibits anisotropy and it becomes questionable whether a spherical symmetry, such as those observed for melting NPs, can be stable for solid NPs. A number of questions can further be asked: What would be the nature of an internal interface within a NP and how would it affect its phase stability? Theoretical and experimental approaches to understand the phase stability of solids often are based on the analysis of a precipitate nucleating coherently within a matrix. However, for an isolated, unconstrained NP, how will the solubility of a phase (with respect to its mother phase) vary with size? If a miscibility gap exists in the phase diagram of the alloy, what are the expected topological variations with the NP size?

There exist several challenging aspects to these types of experiments. Firstly, one needs to find a method to synthesize thermodynamically stable NPs with controlled size and composition, a challenge considering the enhanced reactivity of NPs. Secondly, the composition and the crystalline nature of the phase(s) constituting individual NPs of a given nominal composition and size should be determined at various temperatures. Experimentally, this requires one to anneal the NPs for a time long enough to allow the NPs to reach an equilibrium state while avoiding coalescence, contamination or the formation of an oxide shell. Upon annealing, it would also be of interest to study the possible pathways of an evolving structure. This would also allow the experimentalist to verify if the annealing time was sufficient at a given temperature for the NPs to reach equilibrium and determine experimentally the most stable configuration.

TEM is the only characterization method that allows the determination of size, shape and phase of individual NPs and makes it the ideal tool to study their phase stability. When combined with analytical methods such as energy-dispersive X-ray spectrometry (EDXS) or electron energy-loss spectrometry (EELS), precise quantitative information can be mapped within a NP with a high spatial resolution. However, the ability to generate information from a NP will be limited by the extremely low signal emitted by the small interaction volume between the electron beam and the NP. Consequently, it becomes especially important to assess the precision and the

limits of the analytical methods. In this case, what can be expected in terms of spatial resolution and analytical precision? The signal could always be enhanced by increasing the dose, but electron-beam damage then becomes an issue. For fragile nanostructures, it has become apparent that the characteristic signal becomes convolved with concomitant degradation of the detection limits. A corollary question can then be asked: Would there be a method to perform quantitative analysis while accounting for electron-beam damage and if so, how would the traditional definition of detection limits be affected?

In this thesis we propose to study the phase stability of Au-Pt NPs. There are many advantages to investigate the size effect on Au-Pt NPs. Firstly, there exists an easy method to fabricate Au-Pt alloyed NPs of various compositions and sizes *via* wet chemistry. Secondly, the noble character of the metals protects them against the formation of an oxide upon annealing at high temperature. The bulk Au-Pt phase diagram is readily available (Okamoto and Massalski 1985) along with its corresponding thermodynamic functions. Next, Au and Pt are some of the most investigated metals in the literature, where precise value of their physical properties such as density, surface energy, etc. can be easily found. Finally, the EDXS signal of Au and Pt are strong, thus facilitating their analysis (although some signal overlap is expected).

In the first part of this thesis, the liquidus and solidus are recomputed based on the equilibrium of a NP in solid-core liquid-shell configuration. The impact of NP size on the miscibility gap will also be theoretically investigated. These trends are then compared with those obtained by the observation of the annealing behavior of Au-Pt NPs initially in a core-shell configuration. The NPs will be thoroughly analyzed using a variety of TEM-related tools that we have either developed or adapted to the study of NPs.

This work is organized as follows. In Chapter 2, we recall the governing equations for the Gibbs-Thomson effect, underlying the size-dependent behavior of NPs. We also review the present state of knowledge of the dependence of the phase of binary NPs with size. We next combine the features of various existing models to examine the effect of size on the topology of the bulk Au-Pt phase diagram in Chapter 3. Here, we shall be concerned with the equilibrium of a NP having a solid core surrounded by a liquid shell to redraw the solidus and liquidus boundaries as a function of size. We have used a modified version of the Gibbs-Thomson equation to examine the variation of the miscibility gap with size. The case at hand here is quite different from the traditional Gibbs-Thomson effect: indeed, a single Gibbs function describes the Au-Pt solid phase unlike the situation of the increased matrix solubility in the surroundings of a small precipitate which is the outcome of the interplay between two Gibbs energy curves.

In Chapter 4, specific mapping functions were developed and working conditions were optimized to capture the extremely low signal generated by such a small volume. We succeeded in generating quantitative EDXS composition maps and profiles (together with their error analysis) having a spatial resolution better than 1.2 nm

combined to an excellent analytical precision. These mapping techniques are original methods that are not implemented in commercial TEM-related software and were specifically developed and tested for this application. The high level of spatial and chemical accuracy provided the necessary tools to conduct a full description of individual NPs required for the study of the stability of such systems.

In Chapter 5, we study the limits of analytical microscopy when electron beam-induced damage occurs during the analysis of a binary NP. We develop an experimental method to determine the composition of a binary NP while accounting for depletion during the analysis. The method is tested for Au-Ag NPs of various sizes and compositions. We also evaluate the detection limit of analytical microscopy and explore its consequence on the investigation of size-dependent phase diagrams.

The core experimental results are reported in Chapter 6. Chemically prepared NPs, initially in a core-shell configuration, are annealed at various times and temperatures. The NPs morphology, internal structure and chemical distribution are then probed with the analytical tools developed in Chapter 4 and compared to the trends outlined in Chapter 3.

Note that synthesis of stable, binary NPs can become extremely difficult owing to their intrinsically high reactivity. It should be mentioned that the original idea was to study the phase stability of Ni-Ti NPs which could be prepared by laser ablation under a background pressure. The systematic formation of a Ti oxide on the surface of NPs was unavoidable, thus preventing the study of a *binary* system. Although we were unsuccessful in studying the phase stability with these systems, a number of pertinent results were obtained and are summarized in Appendix A. We discuss the various nanostructured morphologies obtained by varying the laser chamber pressure. We also report on the characterization of the different types of nanostructures using an array of TEM-related techniques.

There was also an unsuccessful attempt to prepare stable Au-Pt NPs at high temperature, using a laser-based synthesis method. Appendix B summarizes the outcome of a series of experiments where Au-Pt NPs were prepared by the laser ablation of a powder mixture of graphite, Au and Pt pressed into a pellet. The pellet was inserted at the center of a tube furnace and was ablated under partial vacuum. The ablated species condensed into Au-Pt NPs covered by amorphous carbon. The setup allowed the NPs to anneal while drifting in the tube before being collected on a cold trap. Unfortunately, the NPs were systematically contaminated with an unacceptable amount of Fe for the study of binary NPs. The technique nevertheless holds the potential of easily preparing isolated Au-Pt NPs where some control over the composition, size and the size distribution could be achieved by adjusting the pellet composition, furnace temperature and drift time.

Appendix C includes the required Digital Micrograph™ (DM) routines to generate a quantitative concentration map or profile with their corresponding uncertainty estimates. A DM code to perform a numerical inverse Abel transform on a set of data

TABLE 1.1: List of acronyms used in the body of this work.

ADF	Annular dark-field
BF	Bright field
CM12	Philips™ TEM using a LaB_6 filament operated at 120 kV
DM	Gatan Digital Micrograph™
DTSA	DeskTop Spectrum Analyzer
EDX(S)	Energy-dispersive X-ray (spectrometry or spectroscopy)
EELS	Electron energy-loss spectrometry or spectroscopy
EFTEM	Energy-filtered TEM
(E)DP	(Electron) diffraction pattern
(i)FFT	(inverse) Fast Fourier Transform
HAADF	High-angle ADF
HREM	High resolution TEM
INCA	Oxford™ software to analyze EDXS data
JEMS	Java Electron Microscopy Simulation™ software
JEOL	JEOL™ TEM using a field-emission gun operated at 200 kV (unless otherwise stated)
MMF	Minimal detectability limit
NP(s)	Nanoparticle(s)
PLD	Pulsed Laser Deposition
STEM	Scanning TEM
TEM	Transmission Electron Microscope or Microscopy
UHV	Ultra High Vacuum
ZA	Zone Axis
ZLP	Zero-Loss Peak

following Bracewell's algorithm (Bracewell 1986, p262-6) are listed in Appendix D. In Appendix E, the rate of depletion of a beam-sensitive NP is examined with a surface-limited model and compared to the volume-limited model. Finally, the Matlab™ code to simulate interdiffusion of a core-shell particle with a moving boundary is reproduced in Appendix F.

A note on nomenclature: the prefix "nano-" describes a characteristic length below 100 nm. "Clusters" refer to an ensemble of atoms which size is typically below 5 nm in diameter, "nanoparticles" are considered larger than 5 nm and below 100 nm and particles are referred to as round objects of any size. We make a distinction between aggregates (aggregation) and agglomerates (agglomeration): particles in an aggregate preserve their boundaries while sintered particles are in an agglomerated state. It should also be noted that the symbols chosen to represent variables are consistent only within the scope of a chapter.

Chapter 2

Review on the Phase Stability of Binary Nanosystems

2.1 Introduction

The Gibbs-Thomson equation, which describes the effect of the curvature of a phase on its equilibrium, has been used to model a number of phenomena in the area of material science, including phase nucleation, Ostwald ripening (Porter and Easterling 1992, p131), etc. This relation is also the corner stone of Pawlow's model (1909) to describe the meting point depression with decreasing crystallite size.

Phase diagrams are used extensively to predict the nature of a phase at a given temperature and composition. Tabulated phase diagrams usually assume the intensive variable of pressure to be a constant equal to the atmospheric pressure and are valid only at equilibrium. Relaxing any of these conditions (e.g. pressure, reaction time, etc.) will add an extra axis to the usual temperature-composition(s) plot. Such a plot allows one to quickly visualize any shift of the phase boundaries with the additional variable. This 3D phase diagram can also help identify the repression of a phase or the appearance of new phases, provided that their thermodynamic description is available.

The size of a nanoparticle (NP) can also constitute an extra variable to the phase diagram. As the NP size decreases, the energy associated with the surface and the existing internal boundaries becomes comparable to that of the volume. Therefore, phase diagrams, which are derived from the thermodynamic description of a system, should thus be revisited to factor in nanoscale phenomena. This Chapter presents a review of the literature on the topic of phase stability of nanoparticles with a focus on size-dependent binary systems.

We will mainly be concerned with isolated NPs but briefly mention some of the extensive work done on coherent phase diagrams (see Larché 1990, for a good review), a concept developed for coherent precipitation in alloys. We start with a brief historical note and a review of the basic governing thermodynamic equations. Phase transition and phase transformation of single components will be discussed at this point. In Section 2.3 we review the solubility enhancement observed with decreasing NP size. In Section 2.4 several existing models for the construction of a size-dependent phase diagram are compared. We devote a subsection on atomistic calculations of the sta-

bility of clusters and NPs and on the few experimental observations related to the topic of phase stability of binary NPs.

2.2 Single-Phase Systems

2.2.1 Historical Notes and Fundamental Relationships The effect of size on materials properties and phase transformation takes root in the phenomenon of capillarity, the action by which a liquid rises in a small diameter tube having one of its end immersed. The formalism of the theory of capillarity is based on the concept of surface tension and is credited to Thomas Young (1773–1829) (Young 1805). The mathematical treatment was later provided by Pierre-Simon de Laplace (1749–1827) (Laplace 1829). The generalized Young-Laplace equation expresses the variation of pressure between two fluids ΔP separated by a curved interface. This interface is characterized by a surface tension γ and is described geometrically by the radii of curvature r_1 and r_2:

$$\Delta P = \gamma \left(\frac{1}{r_1} + \frac{1}{r_2} \right) = \gamma \kappa, \tag{2.1}$$

where κ is the mean curvature. For a sphere, $r_1 = r_2 = r$ which reduces to the well-known Kelvin equation for a spherical particle:

$$\Delta P = \frac{2\gamma}{r}. \tag{2.2}$$

This equation could be derived by taking several approaches: *(i)* using Lagrangian mathematics (the demonstration was carried amongst others by Hillert (1998, p390-2)); *(ii)* with variational calculus by minimizing the Helmholtz free energy functional representing the system; and *(iii) via* a mechanistic approach with a simple force balance (the latter method being less rigorous than the two others (Pellicer et al. 1995)).

The Gibbs-Thomson* equation relates the chemical potential, μ, to the curvature:

$$\mu_\beta - \mu_\alpha = \gamma V_\alpha \kappa, \tag{2.3}$$

*The name "Thomson" here doesn't refer to only one scientist but three. The equation was first reported in (1871) by Sir William Thomson (who was later knighted Lord Kelvin) based on the experiments of his brother, Prof James Thomson in 1849 and 1862. The equation was later recast by J. W. Gibbs (1875, 1878) and Sir Joseph Jones Thomson (1888, p162-3) to describe the effect of curvature on the equilibrium between a droplet surrounded by its vapor.

where the subscripts β and α refer respectively to the matrix in equilibrium with a particle having a mean curvature κ and a molar volume V_α.

The theory underlying Eq. 2.3 was used to explain the inverse relationship between the melting point depression with particle radius by Pawlow (1909). This inverse relationship was extended by Hanzen (1960) and refined by Buffat (Buffat and Borel 1976) by adding higher order terms to Eq. 2.3. The size-dependent melting point was reconsidered with the existence of a liquid skin surrounding a solid core upon melting (Couchman and Jesser 1977).

It is also possible to evaluate the melting point depression by expressing the surface energy using a quasi-chemical approach. Wautelet (1991) derived a simple relation based on the energy of formation of intrinsic defects:

$$T_m = T_m^\infty \left(1 - \frac{\alpha}{2R}\right), \tag{2.4}$$

where α is a constant ranging between 0.4 and 3.3 nm. α is found to be related semi-empirically to the melting point, T_m, and to the energy of formation of defects, E_f, in a given material according to $E_f/T_m = (0.24 + 0.30\alpha)\,\mathrm{m\,eV\,K^{-1}}$, where values of E_f for various materials can be found in Wautelet (1990).

2.2.2 Allotropic Nanophase Transformation A parallel can be established between the effect of the size of a particle on phase transformation and an increase of the pressure of a system. This explains the experimental evidence for the temperature depression of allotropic phase transformation point with increasing size. To cite a few studies, Illy et al. (1999) demonstrated that Ni clusters in the 1–4 nm diameter range adopted the HCP phase at room temperature instead of the bulk FCC phase. Similarly, Ram (2001) noticed that Co NPs in the 10–20 nm diameter range adopted an FCC phase at room temperature (normally stable for T >427 °C) while the metastable BCC phase was stabilized in the 2–5 nm diameter range. Both crystalline structures are different from the stable allotrope of Co at room temperature, HCP. The results were explained in terms of the *difference* in the surface energy between both allotropes (60 $\mathrm{mJ/m^2}$), with the phase having the lowest surface energy being more stable for smaller NP sizes.

Pure cubic zirconia is formed near 2560 K while the monoclinic and tetragonal phases are stable below 1480 K and between 1480 and 2560 K, respectively. According to the study of Sugimoto (2001), the monoclinic phase is stable for particles larger than 60 nm in diameter, while the tetragonal phase is stable in NPs having a diameter between 15 and 60 nm in diameter. The cubic phase would be stable for clusters with sizes below 2 nm in diameter (Tsunekawa et al. (2003)), an observation which agreed with computer simulations of cluster stability with respect to the enhanced oxygen deficiency with increasing surface-to-volume ratio.

We can give many examples of solid-state reactions and transformations that are known to be influenced by size or curvature, for example: sintering (Herring 1950), diffusion (Shibata et al. 2002; Kobayashi et al. 2002), precipitation (Purdy 1971) and ordering (Cheng et al. 2005; Hirotsu and Sato 2005).

2.3 Surface and Solubility

2.3.1 Solubility It can be demonstrated (Porter and Easterling 1992, p47) that the solubility of a precipitate in a matrix will increase with curvature according to:

$$X_\alpha = X_\alpha^\infty \exp\left(-\frac{\gamma V_\alpha \kappa}{RT}\right) \tag{2.5}$$

provided that the following conditions are met: *(i)* the solubility must be very low and *(ii)* the variation of the activity over the composition range where the shift occurs must be constant. If these requirements cannot be satisfied, one needs to solve the following set of equations for the composition shift in both the precipitate and the matrix (Trivedi 1975, p152):

$$\ln\left(\frac{\nu_{i,\alpha}}{\nu_{i,\alpha}^\infty}\frac{\nu_{i,\beta}}{\nu_{i,\beta}^\infty}\right) + \ln\left(\frac{X_{i,\alpha}}{X_{i,\alpha}^\infty}\frac{X_{i,\beta}}{X_{i,\beta}^\infty}\right) = -\frac{\gamma V_{i,\alpha}\kappa}{RT} \quad i = A, B, \tag{2.6}$$

where the superscript ∞ denotes the value in the presence of a flat (equilibrium) interface, $\nu_{i,j}$ and $X_{i,j}$ are the activity coefficient and fraction of component i in phase j, respectively. Eq. 2.6 uses implicitly the approximation $\gamma\kappa \ll P_0$, where P_0 is the pressure of the phase α having a flat interface. Indeed, the equation can be derived (Trivedi 1975, p146) using a truncated Taylor expansion of the chemical potential:

$$\mu_\alpha(P_\alpha) = \mu_\alpha(P_0 + \gamma\kappa) \approx \mu_\alpha(P_0) + \left.\frac{\partial\mu}{\partial P}\right|_{P_0}\gamma\kappa, \tag{2.7}$$

where $\left.\partial\mu/\partial P\right|_{P_0}$ is simply the molar volume, V_α, evaluated at P_0. Second order terms can be added to Eq. 2.7 whenever $\gamma\kappa$ becomes comparable to P_0, as it was done, for example, by Buffat and Borel (1976) to refine the model describing the size-dependent melting behavior:

$$\mu(T,\, P) \;=\; \mu(T_0,\, P_0) + \left.\frac{\partial\mu}{\partial P}\right|_{P_0}(P - P_0) + \left.\frac{\partial\mu}{\partial T}\right|_{T_0}(T - T_0)$$

$$+\frac{\partial^2\mu}{\partial P^2}\Big|_{P_0}\frac{(P-P_0)^2}{2}+\frac{\partial^2\mu}{\partial T^2}\Big|_{T_0}\frac{(T-T_0)^2}{2}$$
$$+\frac{\partial^2\mu}{\partial P\partial T}\Big|_{P_0,T_0}(P-P_0)(T-T_0)+\ldots \quad (2.8)$$

where $\partial\mu/\partial P|_{P_0}$ can be interpreted as the molar volume (evaluated at P_0), $\partial\mu/\partial T|_{T_0}$ as the entropy per unit mass (evaluated at T_0). It can be demonstrated that $\partial^2\mu/\partial P^2|_{P_0}$ is related to the isothermal compressibility (evaluated at P_0), $\partial^2\mu/\partial T^2|_{T_0}$ to the specific heat (evaluated at T_0) and $\partial^2\mu/\partial P\partial T|_{P_0,T_0}$ to the linear-expansion coefficient (evaluated at P_0 and T_0). If the variation of some of these properties with temperature or pressure is significant, they need to be included in the analysis for a complete description of the size-induced solubility shift.

Spontaneous alloying was observed on a number of bimetallic systems by Mori and Yasuda (1991, 1992, for example). The first occurrence of such experiment involved exposing pure Au NPs to the Cu atoms supplied by an evaporator set in the chamber of a transmission electron microscope (TEM). Upon exposure, the NPs would almost instantaneously form an homogeneous alloy with the evaporated species at ambient and even sub-ambient (Yasuda et al. 1993) temperatures. According to the authors, such a high rate of alloying at room temperature could only be explained by an enhanced diffusion process occurring for NPs as compared to the bulk. They deduced that the diffusion coefficient for nanosystems must be several orders of magnitude higher than their bulk equivalent.

It can be argued that the evaporated atom have a sufficient kinetic energy to penetrate within the NPs. In this case, diffusion is unlikely to play a role in the alloying process thus explaining the occurrence of the phenomena at temperatures as low as 125 K (Yasuda et al. 1993). Surprisingly, this simple hypothesis is not discussed in the papers related to the topic, although the authors demonstrate that the heat generated by the kinetic energy of incoming particle could not induce alloying (Yasuda et al. 2000).

The same conclusions were reached with respect to a number of different metallic systems explored by Mori and Yasuda (Au-Zn, In-Sb, Au-Sb, Au-Pb, Au-Al, ZnS-CdSe, Ag-I, Au-Sn and In-Sn), where metastable phases could often be observed. We will refer to these studies later in this Chapter, when discussing size-dependent phase diagrams. There have been attempts to simulate the phenomenon of spontaneous alloying using Monte-Carlo simulation (Shibata et al. 2002; Kobayashi et al. 2002) and molecular dynamics simulations (Shimizu et al. 2001). According to these simulations, the vacancies would enhance interdiffusion within a NP much more than it would for a bulk alloy.

2.3.2 Surface and Interface Energy The value of the surface energy, γ, is essential for the analysis of size-related effects. The surface energy, γ, can be defined as the

reversible work required to create a unit area of the interface at constant temperature, volume and chemical potential (Trivedi 1975, p140):

$$\gamma \equiv \left(\frac{\partial W}{\partial A}\right)_{T,V,\mu_\alpha} . \tag{2.9}$$

The values of the surface energy for various metals are tabulated in the early work of Jones (1971) for solids close to their melting point. There exist many attributes to the surface energy and we shall list a number of them:

1. For single components, the surface energy decreases with temperature. The variation is linear with a slope equal to the surface entropy per unit area (to a first-order approximation) (Trivedi 1975, p145).

2. The surface energy of binary alloys is dependent on the composition. For liquid-gas systems, the adsorbent is known to have a large effect on the value of the surface energy. The variation of the surface energy is seldom linear and can be predicted if the thermodynamic interaction parameters are available. There is an extensive literature on the methods of computing the surface energy of a binary mixture of miscible (Cahn and Hilliard 1958, for example) and immiscible (Butler 1932, for example) fluids. The latter approach makes use of the Gibbs adsorption isotherms to compute an equilibrium between the surface and the bulk and estimates the fraction of material adsorbed on the surface. The method was only recently applied in theoretical studies involving solids (Tanaka and Hara 2001a), as we will discuss in the next section.

3. The surface energy is isotropic in liquids and anisotropic in solids. This anisotropy is known to control the equilibrium shape of a crystal which can be deduced using the so-called Wulff plot (Wulff 1901; Herring 1951). The approach has been extended and generalized to one referred to as "Vector Thermodynamics" (Hoffman and Cahn 1972; Cahn and Hoffman 1974).

4. There has been some discussion more than fifty years ago (Tolman 1949; Koenig 1950), recently resuscitated by Lu and Jiang (2004), on the possibility of surface energy dependence on curvature. According to theory and some experiments, the surface energy should decrease with increasing curvature and this change could be significant in the nanometer range.

5. Surface segregation is thought to be significant for small particles. Although surface segregation in bulk alloys is a subject of numerous studies starting with the pioneering work of Williams and Nason (1974), there is very scarce experimental evidence on the subject for nanoparticles (Hajcsar et al. 1987). Nevertheless, theories based on the concepts of Gibbs adsorption and molecular dynamics simulation on the topic can be found (Foiles 1985; Hajcsar et al. 1987). There have been some reports (Dvoryadkina et al. 1980; Ivanov et al.

1983; Ivanov and Borisov 1988) claiming that the surface segregation should occur in NPs due to the increase of the surface stress with curvature. Their treatment is very similar to that pioneered by Cahn (Cahn 1980; Cahn and Larché 1982) although the latter is based on a more generalized approach. In Cahn's treatment (1980) a careful distinction between surface stress (tension) and surface energy is made by describing the area as a standard state of strain (Lagrangian definition). This definition enables the consideration of the equilibrium of small crystals of substitutional and interstitial solid solutions in a rigorous manner.

2.4 Size-Dependent Phase Diagram

2.4.1 Models Based on Gibbsian Thermodynamics So far, we have discussed the effect of size (or curvature) on single component phase transitions and solubility limits. Calculating the effect of size on the stability of binary systems is more challenging but a few complementary approaches have been developed so far to address this topic. In the following discussion we categorize the methods found in the literature and refer to them by their author's name. There have been many treatments on the phase stability for thin films (e.g. Christensen et al. 1997), multi layers (e.g. Sun and Purdy (2006)), pellets and powders (Suresh et al. 2003) and particles in a matrix (Cahn and Larché 1982; Ardell and Maheshwari 1995, for instance) but the following review will focus on isolated NPs.

Tanaka and coworkers (Tanaka and Hara 2001a; Tanaka and Hara 2001b) used the thermodynamic data of a system to redraw the phase diagrams of hypothetical and real binary systems for various particle sizes. To recalculate the size-dependent solidus and liquidus, the authors simply added to the molar Gibbs energy of the solid and the liquid the capillarity functions ($2\gamma V_j/r$, with j = Liquid or Solid), with respect to a reference surface state. The strength of their calculations lies in the effort of including a temperature and composition dependence to various physical properties. For example, the surface energy of the liquid is solved using Butler equations and is temperature-dependent; the molar volume of the liquid is considered to vary linearly with temperature and composition; the molar volume contraction upon solidification is also taken into account. Without referring to it specifically, Tanaka's work included some of the higher order terms of Eq. 2.8. The approach offers a quick and easy method to evaluate the impact of adding the capillarity terms to the Gibbs energy on the phase diagram. Parts of the method, namely the computation of the surface energy using Butler formulae, has been incorporated into a software (Tanaka et al. 2000) that can retrieve the thermodynamic functions from existing databases (the approach referred to as CALPHAD: computer CALculation of PHAse Diagrams

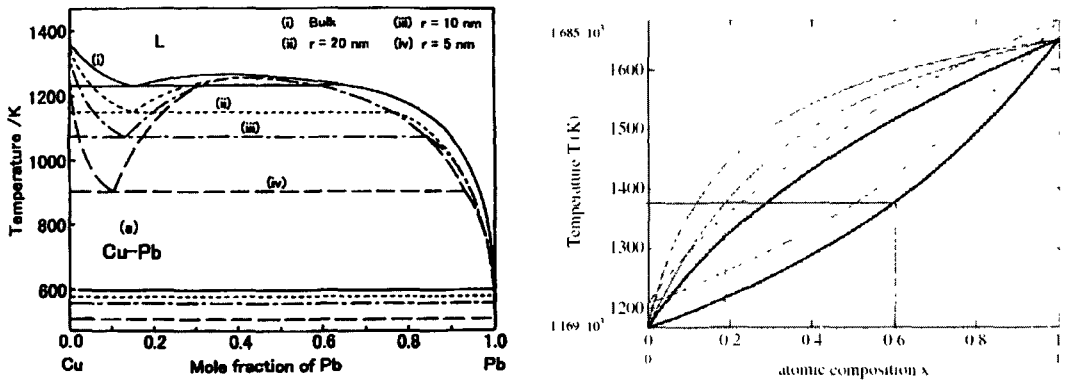

(a) (b)

FIG. 2.1: (a) Cu–Pb size-dependent phase diagram for NPs with various radii (legend annotated on graph). Reproduced from Tanaka and Hara (2001b, Fig. 5a). (b) Solidus and liquidus shift for a Si-Ge regular solution. Dashed and bold lines refer to the bulk and to a NP with 10^6 atoms, respectively. Surface composition of the NP is traced with thin lines. Reproduced from Vallée et al. (2001, Fig. 5).

(Kaufman and Bernstein 1970)). Technically, there is a potential for the technique to be completely handled by software packages such as Thermo-Calc (Sundman et al. 1985).

On the other hand the juxtaposition of phases is not specified in Tanaka's treatment. One can guess that the capillarity-related terms correspond to a situation where a NP can be either a solid or a liquid, but the possibility of the phase coexistence is ignored. In other words, the recalculated phase boundaries delimit only the stability region of a single-phase NPs on a phase diagram. Fig. 2.1(a) shows an example of recalculated Cu-Pb phase diagram for NPs of various radii (Tanaka and Hara 2001b). For example, a 5 nm radius Cu-10% at. Pb NPs will be in a liquid state at a temperature as low as about 900 K, which is ~320 K lower than the bulk monotectic temperature. However, below this temperature, in the two-phase region, Tanaka's calculations cannot be considered valid, since the existence of a two-phase region results in the creation of an interface, whose properties are not included in the calculations. Similarly, just below 900 K, when decreasing the radius of a droplet from the bulk to 5 nm the solubility of Cu in Pb would increase from ~3 to 7% at. Cu, but the model fails as soon as precipitation occurs. There are two assumptions in their treatment that should be noted: *(i)* the surface energy is isotropic, a valid approximation only at a temperature close to the melting point and *(ii)* the surface energies are computed using Butler equations, which are validated for liquids only and are used as a trial for solids.

Wautelet and co-workers wrote a series of papers on size-dependent phase diagrams. By adding a simple capillary term to the Gibbs energy curves of the phases

(Eq. 2.4), the phase boundaries are redrawn for ideal solutions (Wautelet et al. 2000) and regular solutions (Vallée et al. 2001) for the specific case of complete miscibility in the solid. The authors approximate the surface energy as a linear combination of those of the pure constituents and consider it as temperature-independent.

There is, however, an inconsistency in their treatment of the capillarity term: instead of adopting the Laplace equation, they consider a term equal to the ratio of the area to the volume. This is justified by the authors by assuming that the contribution of the surface energy is equal to area occupied by the surface atoms times the surface energy (per unit area). It should have been recognized that the ratio A/V and the Laplace equation differ by a factor $\partial \ln V / \partial \ln A$ and for a sphere, this factor is equal to $2/3$[†]. Nevertheless, the same authors extended their approach to NPs of various shapes (Wautelet et al. 2003a; Wautelet et al. 2003b). The effect of surface segregation is added to their model by considering that the enthalpy of the atoms at the surface is different from that of the atoms in the rest of the particle. The difference is expressed by a simple broken bonds model (Vallée et al. 2001). An example of a recalculated Si-Ge phase diagram for a 10^6 atoms NP ($\sim$17 nm radius NP) is shown in Fig. 2.1(b) (thick line) where the composition of the surface due to surface segregation is shown as the thin solid line. The general conclusions are identical to those of Tanaka, namely, a depression of the temperature liquidus and solidus for the whole composition range.

There is an implicit assumption of an infinite reservoir of atoms in theoretical studies which conclude on an increased solubility with curvature. This assumption is wrong if the number of atoms is finite within a volume, such as for an isolated NP. Shirinyan and coworkers have suggested an approach that considers depletion as a constraint to the nucleation of a phase within a NP (Shirinyan and Gusak 2004a; Shirinyan and Wautelet 2004b). The outcome of their calculations leads to the creation of a nucleation window on the phase diagram where solidification can occur. Furthermore, the authors make a distinction between the composition range where the phase is stable and the compositions of the separating phases, which no longer coincide on the phase diagram (Shirinyan et al. 2005). The authors then adapted their method to investigate theoretically the possibility of precipitation within a Cu-Ni NP. The core-shell configuration was chosen and the effect of various parameters on the phase diagram were explored: *(i)* starting phase (solid or liquid), *(ii)* juxtaposition of the phase (solid or liquid in the core), and *(iii)* the possibility of a nucleation energy barrier associated with nucleation. For example Fig. 2.2 compares the liquidus and solidus of the bulk phase (dashed lines) diagram with those computed for a 30 nm radius NP (solid lines and symbols), assuming no penalty due to the existence of a nucleation barrier. The authors observed the narrowing of the phase field to a point where the solidus and liquidus collapse for $X \lesssim 10$ and $X \gtrsim 75\%$ at. Ni.

[†]This factor would also be valid for any geometrical shape that can be defined by one variable (e.g. cube, regular polyhedron, etc.). The relationship $A = \mathrm{d}V/\mathrm{d}r$ usually holds for simple symmetrical

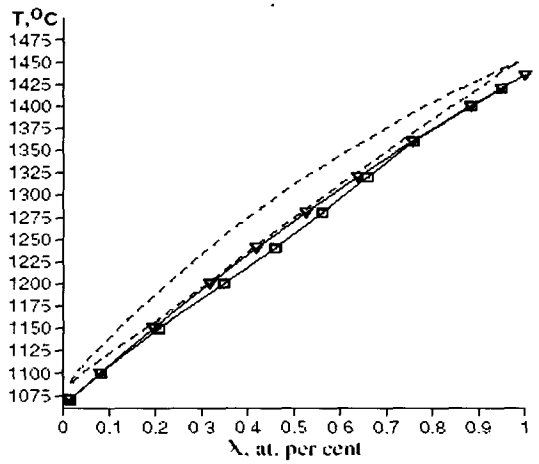

FIG. 2.2: Phase diagram comparing the liquidus and the solidus for bulk (dashed) and for a 30 nm radius Cu-Ni NP (full line with symbols). Reproduced from Shirinyan et al. (2006b, Fig. 4).

So far, all the models reviewed assumed a core-shell configuration. Experimental evidences of the formation of a solid core and liquid shell in a two-components NP were first provided by Gile (1982) and Allen and Jesser (1984). Nevertheless, Weissmüller et al. (2004) developed a size-dependent phase diagram of a spherical NP composed of two contiguous spherical caps. The authors considered an interface which curvature depends on the phase fraction while keeping the shape of the particle spherical. This is done by forcing the interface to meet at right angle the spherical surface for any phase fraction. Here, the authors considered the interface energy to be simply proportional to A/V, which agrees with Wautelet's approach, but is in disagreement with the other models. The magnitude of the interface energy is considered to vary with the phase fraction and is thus tied to the area. The total molar Gibbs energy of a NP would not be found using the common tangent construction but using a construction similar to Fig. 2.3(a). In this case, A and B correspond to the arbitrarily chosen composition of the α and the β phase, respectively. ΔG_c is the interface energy per mole of alloy, which is a function of the phase fraction, as shown by the drawing. For a given temperature, size and nominal composition, all the possible states of the NP (single solid phase, single liquid phase or two phases) are computed and drawn on an energy-composition diagram. The stable state as a function of composition is identified by the lower envelope of the set of functions describing all possible states. An example of the size-dependent hypothetical phase diagram computed according to this model is given in Fig. 2.3(b) for a 5 nm diameter NP. Of note, the phase diagram now includes a region where discontinuous melting is possible due to the unfavorable energy cost of large interface, when the phase fraction approaches 0.5.

shapes but a generalized form of the identity for faceted shapes exists (Fjelstad and Ginchev 2003; Weisstein 2003).

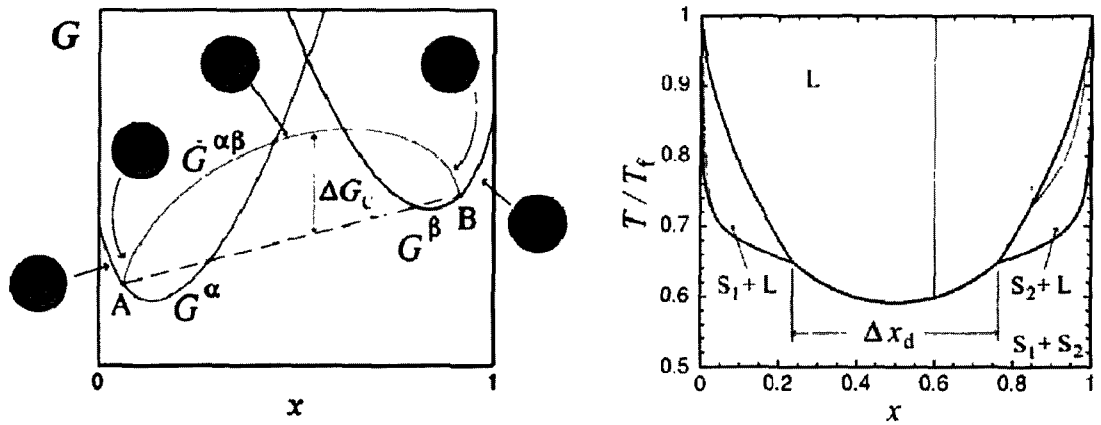

FIG. 2.3: (a) Example of energy diagram representing the phase separation in a NP according to the model of Weissmüller. Phases α and β coexist within the NP as spherical caps making a 90° dihedral angle with the surface of the NP. The interface energy, ΔG_c is considered proportional to the interfacial area (γA), itself a function of the phase fraction having arbitrary compositions A and B, respectively. The total Gibbs energy is the sum of the alloy energy (common tangent, dashed line) and the interfacial energy (segment with negative curvature). (b) Phase diagram of a two-components 5 nm diameter NP overlaid on the bulk phase diagram (phase fields shaded in grey). Thin lines are the "ties lines" in the Solid + Liquid phase fields. Discontinuous melting occurs in the composition interval Δx_d. Reproduced from Weissmüller et al. (2004, Figs. 1a and 2c).

When comparing Weissmüller's and Shirinyan's models, it becomes obvious that the selection of the configuration or juxtaposition is paramount. Indeed, while Weissmüller notes that the composition range of discontinuous melting lies close to the equimolar phase fraction for a geometry composed of a interface separating two spherical caps, Shirinyan's model predicts that the composition range for discontinuous melting should prevail for dilute phase fraction. The two apparently conflicting models can nevertheless be reconciled. In both models, there is an energy penalty associated with the creation of an interface which scales with the ratio of the area over the volume. For a core-shell configuration (Shirinyan's model), the ratio is maximized for dilute phase fraction while for the case of spherical caps (Weissmüller's model), the area is maximized when the phase fraction are equal. For an equimolar phase fraction, it can be easily demonstrated that the area of a core-shell configuration is $2^{4/3}$ larger than that of a flat interface separating two hemispheres. In fact, it can also be shown[‡] that the area of the interface of a core shell configuration is

[‡]In the geometry suggested by Weissmüller, the interface area, A_W can be approximated by the function $A_W = \pi R^2 \left\{ 2^{1/3} [4p(1-p)]^{2/3} + [1 - 2^{1/2} 4p(1-p)] \right\}$ where R is the outer radius and p, the phase fraction. Similarly, the interface area of a core-shell can be written as a function of the phase fraction: $A_S = 4\pi R^2 p^{2/3}$. A_W shows a maximum at $p = 1/2$ while A_S is an increasing

always larger than the area of the interface of the geometry proposed by Weissmüller, independently of the phase fraction.

Jesser et al. (2004) used a very rigorous approach to construct a model that allows the calculation of size-dependent Pb-Bi phase diagram. In particular, the model includes materials properties such as temperature and composition-dependent surface energy and molar volume for both α and ε phases. The composition dependency of the surface energy is computed according to the methodology proposed by Tanaka, as mentioned in this Section. Depletion and surface segregation are both considered under the constraint of mass balance. In the same way as others, the authors noted a region of the phase diagram where discontinuous melting can occur, as exemplified in Fig. 2.4(a). Starting at the bottom of Fig. 2.4(a), a 10 nm radius NP with a nominal composition of 0.2 at. Bi will be stable below ~466 K and at higher temperature, will phase separate into a concentric configuration with a depleted solid core and an enriched liquid shell. As the temperature is increased from ~466 K to ~492 K, solute is exchanged between the solid and the liquid following the melting path on the diagram. Above 492 K, the NP transforms discontinuously to a liquid particle, due to the energy cost of maintaining an inner interface. The size-dependent phase diagrams of a 5 (front panel) and 10 nm (back panel) radius Pb-Bi NPs are shown in Fig. 2.4(b). The regions of the phase diagram where a liquid and a solid (either the α or β) phases coexist within a NP are delimited by solid thick lines. For a two-phase particle, the composition of the liquid and the solid can be read off the thin lines. Again, the recomputed phase diagram is shifted to lower temperature, compared to the bulk phase diagram (dashed lines).

The problem of size-dependent phase diagram of free NPs was also tackled from a different angle. The concept of "coherent phase diagrams" was introduced by Cahn and Larché (1984) with phase diagrams recalculated for a two-phase system separated by a coherent interface by including the elastic contribution to the free energy. The concept was used to extend the theory of nucleation to coherent precipitates (in a matrix). Coherent phase transformations were reviewed some time ago by Larché (1990). The concept was later applied to free particles by Johnson (2001). Johnson examined the stability conditions of an initially homogeneous and isotropic particle against spinodal decomposition. Segregation would theoretically occur with a spherical symmetry, where the phases would be separated by a diffuse interface. Intrinsic and extrinsic radial stresses were taken into account in the free energy to calculate the onset of decomposition and describe the decomposition kinetics.

Based on Johnson's model, Huh et al. (2005) examined the equilibrium between two phases described by a regular solution in a composite sphere configuration. In this model, the interface is considered sharp and coherent and the associated excess thermodynamic quantities are neglected. The surface of the composite sphere, is subjected to a surface tension and a traction applied on the surface. The temperature-

function of p. For $p \to 0$, it can be shown by applying Hospital's rule that the ratio A_W/A_S is maximal and tends towards $2^{-1/3}$, which is smaller than unity. Therefore, it $A_W < A_S$ for all p.

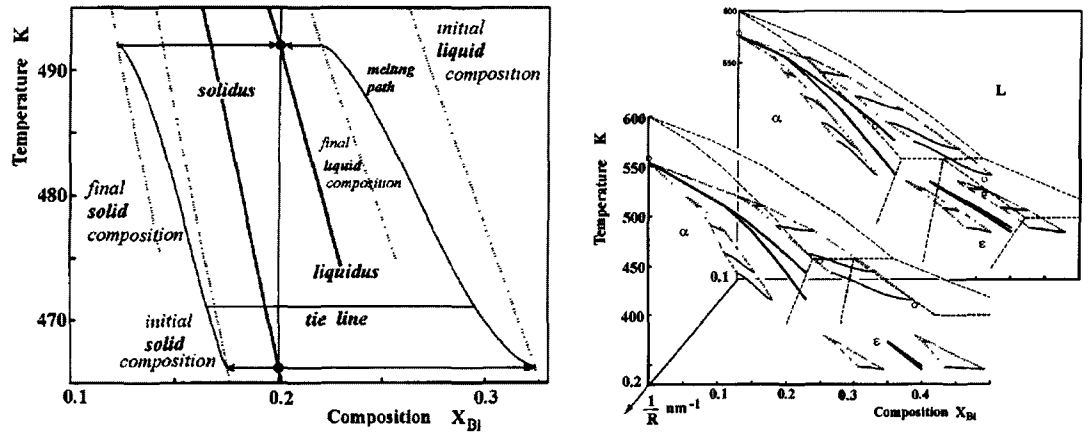

FIG. 2.4: (a) Discontinuous melting path of a 10 nm NP with a nominal composition of 20% at. Bi. (b) Stack of phase diagram for a 5 and 10 nm radius NP. Bulk phase diagram is plotted with dashed lines and experimental points are stars and circles. Thick lines delimit the conditions in which two phases can coexist within the NP. Dotted lines delimit the composition of the coexisting phases. Possible melting paths are drawn in thin continuous lines. Reproduced from Jesser et al. (2004, Figs. 7 and 9).

composition-pressure coherent phase diagram of such a system was plotted for various dimensionless mechanical and chemical properties. The size enters in the dimensionless parameter "effective pressure", where the pressure is taken as the sum of the external traction applied per unit area of the surface and the curvature-induced pressure (Eq. 2.2)[§]. Apparently, the miscibility gap can be either extended or reduced, depending on the sign and magnitude of the deviation from Vegard's law. We can express the dependence of the lattice parameter a on composition, X: $a(X) = \eta_c X + 1/2\eta_{cc}X^2$, where η_c and η_{cc} are coefficients[¶]. For an alloy following Vegard's law, $\eta_{cc} = 0$ and no change in the miscibility gap is observed. Fig. 2.5 shows the 3D phase diagram of the miscibility gap for increasing effective pressure when $\eta_{cc} = 0.04$. In this specific case, the miscibility gap is repressed. However, for negative values of η_{cc}, the opposite occurs. It was concluded that the size affects the miscibility gap only through non-linear terms of the compositional strains. We will show in Chapter 3 how this last statement can be generalized for nonlinear terms of the expression relating the surface energy to the composition.

[§]When referring to the surface tension, Johnson (2001) and Huh et al. (2005) made the distinction between surface tension and surface energy in their model: in the presence of strain, they are numerically different, as discussed by Cahn (1980).

[¶]Experimentally, η_c and η_{cc} can be determined for an alloy by fitting a quadratic equation to the lattice parameter vs composition curve.

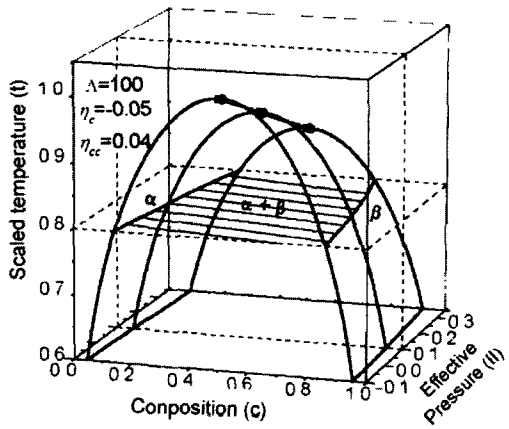

FIG. 2.5: Coherent phase diagram of a miscibility gap as a function of effective pressure. The main parameters governing the shift of the phase diagram with pressure are η_c and η_{cc}, the coefficients of a quadratic polynomial expressing the dependence of the lattice parameter on composition. For a typical metal, an effective pressure of 0.1 corresponds to a 4.6 nm radius NP. Reproduced from (Huh et al. 2005, Fig. 3).

All of the theoretical models found in the literature up to this point fall in either of the categories listed in Table 2.1 or use a combination of the available features. It can be appreciated that the most precise work done so far was performed by Jesser (1999, 2004). Furthermore, the latter study is amongst the very few that reports experimental evidence to support its model.

2.4.2 Molecular Dynamics Simulations Let us realize that the thermodynamic description of a NP can be done by adding surface and size-related terms to the free energy related to strain, shape, interface, etc. We can refer to this method as a "top-down" approach for minimization. The past few decades have witnessed the emergence of molecular dynamics or atomistic simulations to find the state of minimal energy of an ensemble of atoms in a given environment. The challenge is to appropriately describe the interaction energy between neighboring atoms. The technique is computationally intensive and the simulation time increases drastically with the number of atoms in the ensemble but is routinely used to analyze clusters or small NPs.

We can cite a few molecular dynamics or atomistic simulations studies that have contributed to the topic of size-dependent phase stability of binary systems. These are summarized in Table 2.2. The atomistic calculations can be used to determine the phase of an ensemble of atoms or to simulate other features typical to clusters, such as surface segregation (Liu et al. 2006), defects and vacancies (Rodríguez-López

TABLE 2.1: Comparison of various features of the existing approaches for computing a size-dependent phase diagram. *Implementation* refers to the expected complexity of the numerical calculations. *Capillarity function* refers to the mathematical function used to include the capillarity energy into the phases: it is either done using the differential form, ($\mathrm{d}A/\mathrm{d}V$) or an integral form (A/V). *Stress*: indicates whether radial stress is included in the minimization. $\gamma(T)$: surface energy dependence on temperature (linear or constant). $\gamma(X)$: surface energy dependence on composition (linear or computed using Butler equations). $V_m(T)$ and $V_m(X)$: molar volume dependence on temperature and composition, respectively (constant, linear, or quadratic). *Surface segregation* indicates whether this feature was taken into account and if so, the model used to estimate the effect: Quasi-chemical (broken bonds model) or Gibbs adsorption isotherm. *Mass conservation* indicates whether this feature was taken into account or not. *Juxtaposition* refers to the geometry of the phase assumed by the model. *Theoretical system* and *Experimental data* indicates which binary systems were explored and if experimental data confirms the model.

Author	**Tanaka**	**Wautelet**	**Shirinyan**	**Jesser**	**Weissmüller**	**Huh**
Reference	2001a 2001b	Vallée et al. 2001	2006b	2004	2004, Wilde et al. 2007	2005
Implementation	Easy	Very easy	Hard	Very Hard	Hard	Very Hard
Capillarity function	$\mathrm{d}A/\mathrm{d}V$	A/V	$\mathrm{d}A/\mathrm{d}V$, nucleation barrier	$\mathrm{d}A/\mathrm{d}V$	A/V	$\mathrm{d}A/\mathrm{d}V$
Stress	No	No	No	No	No	Yes
$\gamma(\mathbf{T})$	Linear	Constant	Constant	Linear	Constant	Constant
$\gamma(\mathbf{X})$	Butler	Linear	Linear	Butler	Constant	Constant
$\mathbf{V_m(T)}$	Linear	Constant	Constant	Linear	Constant	Linear
$\mathbf{V_m(X)}$	Linear	Constant	Linear	Quadratic	Constant	Quadratic
Surface segregation	No	Quasi-chemical	No	Gibbs adsorption	No	No
Mass conservation	No	No	Yes	Yes	No	Yes
Juxtaposition	Single phase	Single phase	Core-shell	$\mathrm{Liquid_{core}}$-$\mathrm{Solid_{shell}}$	Spherical caps	Core-shell
Theoretical systems	Cu-Pb, Cu-Bi, Au-Si	Si-Ge, Si-Al	Cu-Ni	Pb-Bi	Simple eutectic	Dimensionless regular solution
Experimental data	No	No	No	Yes	No	No

TABLE 2.2: Comparison of various molecular dynamics studies on the stability of binary clusters. Models are referred to by their author. *Interatomic potential* EM: effective medium (Jacobsen et al. 1987), EAM: embedded-atom model, (Daw and Baskes 1984) or S-C: Sutton-Chen, (1990)).

Author	**Interatomic potential**	**Cluster Dimension (nm)**	**System**	**Main Findings**
Christensen et al. 1995	EM	3.8	Regular solution	Spinodal repressed below critical size.
Ramos de Debiaggi 1999	EAM	2.8	Ni-Al	NiAl(B2) and $Ni_3Al(L1_2)$ stable in NP with the occurrence of an $L1_0$ phase. Large deviation from stoichiometry permitted.
Rodríguez-López et al. 2004	S-C	1.5–3	Au-Pd Au-Cu	Nature of stabilizing defects in a bimetallic cluster are composition-dependent.
Liu et al. 2006	EAM	2.6	Au-Pd	Pd-core Au-shell would be the equilibrium configuration.
Mejía-Rosales et al. 2006	S-C	1.5-3	Au-Pd	Melting transition composition-dependent. Au surface segregation during melting.
Xiao et al. 2006	EAM	0-14	Au-Pt	Alloying is promoted for small-sized, dilute NPs as compared to the bulk. A core-shell structure further stabilizes the formation of a solid solution.

et al. 2004), the appearance of different phases and ordering (Ramos de Debiaggi 1999), and melting behavior (Mejía-Rosales et al. 2006).

Using interatomic potentials described by the effective medium theory (Jacobsen et al. 1987), Christensen et al. (1995) found the existence of a critical cluster size below which phase separation is forbidden in clusters of a number of bimetallic systems that can be described by a regular solution model. This behavior could be predicted using a simple continuum approach but the atomistic simulations were necessary to include the possibility of surface segregation. These calculations were confirmed by a molecular dynamics study on the Au-Pt system, which revealed that a negative heat of formation may occur in the situation of small and dilute Au-Pt alloyed NPs. The core of the calculation lies in the assumption that the cohesive energy of the atoms decreases with the NP size according to a relation derived by Qi and Wang (2002):

$$E_p = E_b(1 - d/D) \tag{2.10}$$

where E_b is the bulk cohesive energy and E_p, the cohesive energy of a NP of diameter D and atomic size d. Furthermore, the authors claimed that a core-shell configuration stabilizes the atomic ensemble as a result of surface segregation, which explains "...why the core-shell structure occurs in many nanoalloy systems" (Xiao et al. 2006). It should be noted that this statement is not necessarily confirmed by experiments reporting on the structure of thermodynamically stable NPs, as will be discussed in the next Section.

2.4.3 Experimental Reports for Size-Dependent Phase Diagrams We summarize in this Section studies that report on empirical, size-dependent phase diagrams. These were constructed by identifying the phase and measuring the size and the composition of individual NPs. The information is then plotted at a given temperature to define a stability region on the temperature-composition-size phase diagram. We selected studies that reported on thermodynamically stable NPs in contrast with metastable phases far from equilibrium, such as those obtained by laser ablation or mechanical alloying, for instance.

A list of experiments, where portions of the phase diagrams for binary NPs were redrawn for a given size, is given in the introduction of the paper of Allen and Jesser (1984) and is summarized here. The Al-rich part of the Al-Cu phase diagram was replotted for 25 nm diameter NPs by Palatnik and Boiko (1961) and an increased solubility of Cu in the NP was noted. High-temperature *in-situ* experiments were also performed on In-Sb (Berman 1975) and Pb-Bi NPs (Gile 1982): the depression of the melting point of alloyed NPs was observed to be dependent not only on size but also on the composition. The In-Sn and Bi-Sn system were explored by Allen and Jesser (1984): 40 nm diameter In-Sn NPs exhibited an amorphous phase for NPs having a composition close to the two-phase field, as shown by asterisks symbols at room temperature in Fig. 2.6(a). Discontinuous melting was observed for the first time by *in-situ* hotstage TEM in Bi-Sn NPs. As mentioned, similar findings were reported for the Pb-Bi system (Jesser et al. 2004). A shift of the liquidus and solidus towards lower temperatures was also experimentally demonstrated for 40 nm diameter NPs.

Solid Bi-Sn NPs were examined later by Schamp and Jesser (2006). The authors experimentally show the existence of a critical size below which the NPs are single-phased over all the composition range (Fig. 2.6(b)). Of note, a core-shell configuration was not observed when segregation occurred within larger NPs; instead a flat interface could be observed to separate the phases[‖]. This type of interface could also be observed in a study on segregated Ag-Cu (Howe et al. 2003) and Ag-Au-Cu

[‖]Fig. 2 in Schamp and Jesser (2006) shows a TEM micrograph of an ensemble of Bi-Sn NPs. For two-phase NPs with apparently equal phase fraction, a flat interface appears to be separating the Bi-rich and Sn-rich phases. Although uncommented, closer inspection of Fig. 1 of the same paper shows the occurrence of curved interface, for NPs having a phase fraction differing from ~0.5.

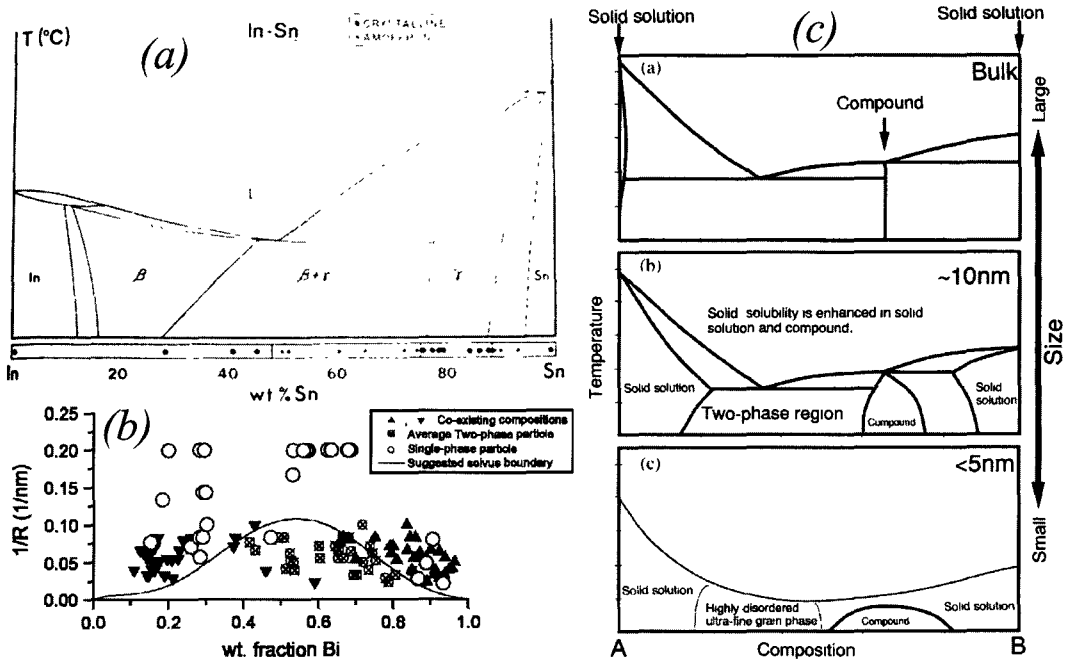

FIG. 2.6: Examples of experimental reports of size-dependent phase diagrams. (a) Room-temperature observations of 40 nm diameter NPs. NPs were found to be crystalline (circles) or amorphous (stars), depending on their composition. Reproduced from Allen and Jesser (1984, Fig. 2). (b) Reciprocal size-composition diagram showing the composition of single-phase Bi-Sn NPs (open circles). The nominal compositions of two-phase NPs are also displayed (crossed squares) together with the composition of the coexisting phases (triangles). Reproduced from Schamp and Jesser (2006, Fig. 3). (c) Bulk Au(A)-Sb(B) phase diagram (top panel) compared schematically to the expected phase diagram of Au-Sb NPs having a ~10 nm diameter (center panel) and for a NP with a diameter below 5 nm (bottom panel). Reproduced from Yasuda and Mori (2002, Fig. 4).

(Chatterjee et al. 2004) NPs. In these specific cases, it was thought that anisotropy could play a role in the equilibrium configuration and the juxtaposition of the phases.

As mentioned earlier, Yasuda and Mori (2002) synthesized and characterized Au-Sb NPs. The authors examined the phase and the chemistry of Au-Sb NPs having a diameter between 4 and 10 nm and a composition ranging from 15 to 77% at. Sb (as determined using a combination of HREM and EDXS). NPs larger than ~10 nm having a nominal composition in the two-phase region were observed to be separated in Au-rich and $AuSb_2$, as shown in Fig. 2.7(a). The composition of each phases constituting the NP was deduced from an EDX spectrum acquired by positioning the probe on either side of the interface. The authors could detect the presence of up to 15% at. Sb in NPs having the crystalline structure of FCC Au, a composition considerably higher than those predicted by the bulk phase diagram (Fig. 2.6(c), top panel). Furthermore, the authors could measure a higher solubility of Au and Sb in the $AuSb_2$ compound, which is stoichiometric according to the bulk phase diagram.

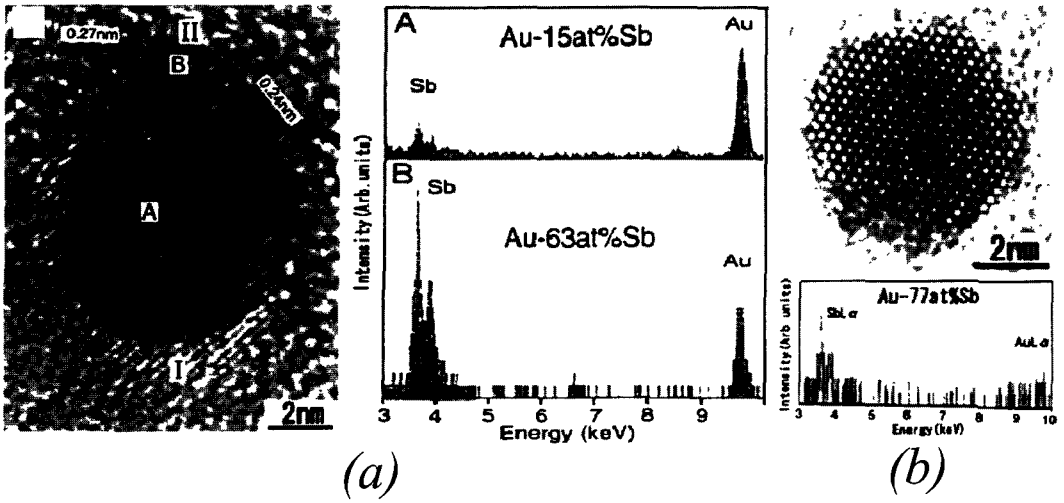

FIG. 2.7: HREM micrographs and EDX spectra taken from Au-Sb NPs. NP in (a) is separated in two phases. The phase at the bottom of the NP is identified as $AuSb_2$ (marked with "I") and the one at the top, as a Au-rich solid solution (marked with "II"). The corresponding EDX spectra were acquired from positions "A" and "B", marked on the phases constituting the NP. (b) NP identified as $AuSb_2$ phase with corresponding EDX spectrum. Adapted from Yasuda and Mori (2002, Figs. 2b and 3c).

For example, the authors have assigned the HREM fringes of the NP in Fig. 2.7(b)** (top panel) to the $AuSb_2$ phase. However, the authors measured 77% at. of Sb within the NP, concluding to an enhancement of the solubility of about 10%, with respect to the stoichiometric composition of $AuSb_2$. However, "highly disordered ultra-thin grain phase" or "amorphous-like" phase constituted NPs with a diameter smaller than ~5 nm with the same nominal composition (as deduced from HREM micrographs showing almost random-like lattice fringes).

The findings are summarized in Fig. 2.6(c), where phase fields are drawn qualitatively for NPs less than 5 and ~10 nm diameter NPs (bottom and center panels, respectively) and are compared to the bulk phase diagram (top panel). Accordingly, the solubilities and the stoichiometry range of the intermetallic compound are greatly enhanced for NPs. For smaller NPs, the appearance of highly-disordered ultra-fine grain phase would agree with the occurrence of the amorphous NPs in the two-phase regions of Bi-Sn phase diagram, as observed by Allen and Jesser (1984) (Fig. 2.6(a)).

When measuring the Sb content in a NP, the authors did not quote an uncertainty. Although the intensity axis shown in the EDX spectra of Fig. 2.7 are set in "arbitrary units", it is clear that the counting statistics are extremely low, given the

**Although unreferenced by the authors, the identical HREM image and corresponding EDX spectrum shown in Fig. 2.7(a) were also published in a paper by the same authors (Mori and Yasuda 1996, Fig. 3), where similar conclusions were drawn.

discrete nature of the background. For instance, the EDX spectra shown in Fig. 2.7(b) shows that at most 4–6 counts are included in the Au $L_{\alpha 1}$ peak (after background subtraction) and not much can be found to constitute the Sb $L_{\alpha 1}$. Given that the X-ray emission events follow a Poissonian distribution, the uncertainty scales as the square root of the total number of counts making questionable the conclusion that the measured composition of 77% is significantly higher than 67%, the stoichiometric composition.

Catalysis is an extremely active area of research for noble metal clusters. The clusters are often supported by alumina or other types of ceramics and are generally calcinated at high temperature, thus allowing them to be studied in an equilibrium state. Although internal segregation becomes challenging to rule out for clusters with diameters below 5–7 nm, many reports claim that a composition-size scatter plot would delimit possible size-dependent phase boundaries. For example, it was shown using precise EDXS performed on sub-10 nm Pt-Rh clusters, that a bimodal composition distribution existed at room-temperature (Lakis et al. 1995; Lyman et al. 1995), while alloyed NPs would be observed at higher temperatures. This would be in agreement with the presence of a miscibility gap in the Pt-Rh phase diagram, which is predicted but not experimentally demonstrated, in bulk alloys due to kinetic restrictions (Fig. 2.8(a)). The EDXS analysis lead to the concept of composition-size diagrams which plots the composition of individual NPs (with the corresponding error estimate) as a function of the NPs diameter. On the other hand, Luo et al. (2005) demonstrated by X-ray diffraction (XRD) techniques that annealed, 2–3 nm diameter Au-Pt clusters are in an alloyed state over the whole composition range, as shown in Fig 2.8(b), in spite of the presence of a known miscibility gap in the bulk phase diagram. It should be noted that the results were not confirmed by the measurement of the composition of individual NPs, as the conclusions were drawn on the basis of the XRD data.

It should be mentioned that, in all these studies, the clusters are dispersed on or (within) a (porous) support such as γAl_2O_3 or MgO. The interaction between the support and the cluster will probably affect the stability and the structure of these clusters. For example, following a study by Molenbroek et al. (1998), it was concluded from extended X-ray absorption fine structure spectroscopy that 2–6 nm diameter Cu-Pd clusters exhibit surface segregation when supported by alumina, while presenting signs of random alloying when supported by silica.

2.5 Conclusion

This review focused on the theoretical models and experimental reports of the effect of size on the phase diagram of isolated, binary NPs. The main conclusions from theoretical and experimental observations can be summarized as follows:

- Melting point and phase transition point usually decrease with size;

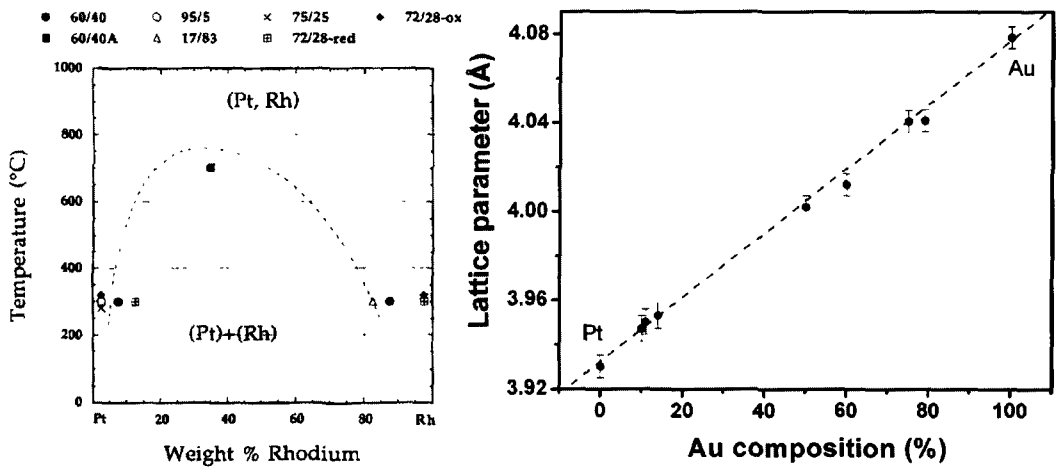

FIG. 2.8: Data points correspond to the composition of Pt-Rh clusters and are overlaid to the bulk phase diagram. Reproduced from Lakis et al. (1995, Fig. 15). (b) Lattice parameter dependence on the nominal Au content of clusters. Reproduced from Luo et al. (2005, Fig. 5).

- Solubility is generally enhanced and complete miscibility can be expected, and has been observed, below a critical size;
- Disordered or amorphous phases can be stabilized within NPs;
- Surface segregation (or a core-shell configuration) becomes important as size decreases.

We compared various approaches that were used in the literature to evaluate the effect of size on the phase diagram. There exist two complementary methods to describe the state of an ensemble of atoms. The first one is to optimize a thermodynamic function under a variety of constraints (Gibbsian approach) and the second one minimizes the energy of an ensemble of atoms by atomistic simulation (molecular dynamics). It would be advantageous if the two methods could be reconciled with themselves and with experimental data at the 10–100 nm scale to explain the stability of NPs.

We noted that most theoretical models were not supported by experiments. On the other hand, there exists many pieces of evidence of size-related phenomena on thermodynamically equilibrated NPs not explained in terms of phase stability. Therefore there is a definite need to bridge the various models to the experimental data in a systematic and coherent manner.

Chapter 3

Stability Analysis of the Au-Pt Binary Nanosystem

3.1 Introduction

Several temperature-dependent properties of a multi-component system can be deduced from thermodynamically-derived tools such as phase diagram, usually valid for bulk materials at equilibrium. As we reviewed in the previous Chapter, adding the surface or interface energy to the thermodynamic description of a system can alter the landscape of a phase diagram: it usually lowers the melting points, can stabilize or repress certain phases or phase transformations, etc. Apart from the scientific interest, there is an obvious technological incentive to predict the state of multi-component nanoparticles (NPs) of a given size.

We have chosen to explore the effect of size on Au-Pt NPs for many reasons. Firstly, it pertains to the experiments discussed in Chapter 6. Furthermore, the Au-Pt phase diagram contains many features arising from the positive enthalpy of mixing of the solid and the liquid phases, such as a miscibility gap in the solid and a large solid–liquid partitioning. The scientific interest lies in the study of the impact of size on such phase diagram particularities.

The purpose of this Chapter is two-fold: *(i)* explore the effect of particle size on the phase diagram of isolated Au-Pt NPs and *(ii)* provide some theoretical basis for the experiments reported in Chapter 6, where we investigate the phase stability of solid Au–Pt NPs. We will treat the solid-liquid equilibrium and the miscibility gap, using two separate approaches, both of which are inspired by those reviewed in Chapter 2.

The solid-liquid equilibrium will be recomputed under the constraint of mass balance assuming the system adopts a single phased configuration or one composed of a solid core surrounded by a liquid shell. As mentioned in the previous Chapter, this core-shell geometry was observed experimentally (Jesser et al. 2004) for other system of bimetallic NPs upon heating and cooling. The method is based on a simplified version of Jesser's (2004) approach. In particular, we will consider the surface energy to be a linear function of composition and ignore surface segregation.

The dependence of the miscibility gap on size will be calculated using Tanaka's (2001a, 2001b) method that we have adapted for miscibility gaps. In this case, the composition dependence of the surface energy is of key significance and is evaluated using Butler equations, as discussed in Section 2.3.2. In contrast to the solid-liquid equilibrium, we will explore the stability region of the single-phase NP, hence conveniently avoiding the consideration of the creation of an inner boundary.

3.2 Solidus and Liquidus

3.2.1 Model and Governing Equations Let us first consider an $A-B$ spherical particle of radius R_0 and nominal molar B content, X_0^B. Suppose that the initially homogeneous alloy transforms into a solid core of radius r and composition X_S^B surrounded by a liquid sheath of radius R and composition X_L^B. We consider a closed system with two constituents where the number of atoms is finite. The total number of moles of species A and B, n^A and n^B, respectively can be written as:

$$n^i = C^i\Gamma \tag{3.1a}$$

$$n^i = X_0^i\frac{\Gamma}{V} \quad i=A,B, \tag{3.1b}$$

where C^i is the number of moles of species A or B per unit volume of the alloy, X_0^i its molar fraction, and Γ the volume of the alloy and V its corresponding molar volume. For a binary system, $X^B = 1 - X^A = X$, where we now drop the superscript; X will hereafter refer to the molar fraction of B.

Using Eqs. 3.1, geometric considerations require that

$$X_S\, r^3/V_S + X_L\,(R^3 - r^3)/V_L = X_0\, R_0^3/V_0 \tag{3.2a}$$

$$r^3/V_S + (R^3 - r^3)/V_L = R_0^3/V_0, \tag{3.2b}$$

where the V's are the temperature-dependent molar volumes of the solid and the liquid phases. The molar volumes are approximated by a linear combination of the molar volumes of the pure species:

$$V_j = (1-X_j)V_j^A + X_jV_j^B \quad j=L,S \tag{3.3a}$$

$$V_0 = (1-X_p)V_p^A + X_pV_p^B \quad p=L\,\text{or}\,S, \tag{3.3b}$$

where the subscript p refers to either solid or liquid, depending on the starting phase of the homogeneous particle. Furthermore, we consider that the molar volume of the liquid varies linearly with temperature:

$$V_L^i = V_{mp}^i[1+\alpha^i(T-T_{mp}^i)] \quad i=A,B, \tag{3.4}$$

where T is the temperature, T^i_{mp} is the melting temperature of the pure bulk component, α^i is the thermal expansion coefficient and V^i_{mp} is the molar volume at the melting point, for $i = A, B$. We approximate the molar volume of the pure solid components to be proportional to their respective liquid counterparts:

$$V^i_S = V^i_L/(1+\beta^i) \qquad i = A, B, \tag{3.5}$$

where β^i can be viewed as a contraction coefficient upon solidification of metals (Wittenberg 1972).

We wish to find the temperature and nominal composition ranges at which a configuration composed of a solid core and a liquid shell is thermodynamically stable, with respect to a completely solid or liquid NP. At a given R_0, X_0 and T, r and R are determined by the equilibrium between the solid and liquid phases through Eqs. 3.2-3.5.

We denote the molar Gibbs energy of the liquid G_L. The molar Gibbs free energy of a completely solid NP is referred to as G_{S1} (which implies a one-phase NP), while that of the solid core, G_{S2} (which implies a two-phase NP). These molar free energies are equal to:

$$\begin{aligned} G_L &= G^M_L + S_{LV} + G^A_L(1-X_L) + G^B_L(X_L) && \text{(3.6a)}\\ G_{S2} &= G^M_S + S_{SL} + G^A_S(1-X_S) + G^B_S(X_S) && \text{(3.6b)}\\ G_{S1} &= G^M_S + S_{SV} + G^A_S(1-X_S) + G^B_S(X_S), && \text{(3.6c)} \end{aligned}$$

where G^M_S and G^M_L are the energy of mixing of the solid and the liquid alloy, respectively. S_{LV}, S_{SL} and S_{SV} are the energy per mole of surface associated with a liquid-vacuum, a solid-liquid and a solid-vacuum interface, respectively. G^A_p and G^B_p are the lattice stability of element A and B respectively in phase p, (with respect to the liquid reference state):

$$\begin{aligned} G^i_L &= 0 && \text{(3.7a)}\\ G^i_S &= H^i_m + S^i_m T \quad i = A,\ B. && \text{(3.7b)} \end{aligned}$$

The molar energies of mixing of a regular solution are commonly written as the sum of an ideal term, G^{ID}_j, and an excess term, G^E:

$$\begin{aligned} G^M_j &= G^{ID}_j + G^E_j && \text{(3.8a)}\\ G^{ID}_j &= R_g T[X_j \ln(X_j) + (1-X_j)\ln(1-X_j)] && \text{(3.8b)}\\ G^E_j &= X_j(1-X_j)\Omega_j \quad j = L,\ S, && \text{(3.8c)} \end{aligned}$$

where R_g is the gas constant and Ω_j is the interaction parameter. The surface contributions S_{LV} and S_{SV} are easily deduced from Eq. 2.3, however, we will derive the expression of S_{SL}. Let us consider only half the composite solid(core) liquid(shell)

particle, as shown in Fig. 3.1. The net pressure applied on the outer surface of the particle is the difference between the external pressure, P_{ext} and the inner pressure P_L of the liquid phase. If we consider the horizontal projection of the pressure applied to the liquid surface, we obtain that the pressure $P_{ext} - P_L$ is exerted on a disc of radius R. The force resulting from the projected pressure in the horizontal direction is in equilibrium with the line tension σ_{LV}, applied on a circle of radius r. Since the membrane is at rest, we can write

$$(P_{ext} - P_L)\pi R^2 = 2\pi R\sigma_{LV}. \tag{3.9}$$

Similarly, considering a force balance on the inner surface leads to

$$(P_L - P_S)\pi r^2 = 2\pi r\sigma_{SL}. \tag{3.10}$$

Adding Eqs. 3.9 and 3.10 and simplifying gives

$$P_{ext} - P_S = 2\left(\frac{\sigma_{SL}}{r} + \frac{\sigma_{LV}}{R}\right). \tag{3.11}$$

Finally, by recognizing that the capillarity contribution can be expressed in terms of a pressure difference (e.g. only the two first terms of Eq. 2.8), we can write the molar surface energy contribution of the surfaces or interfaces as

$$\begin{aligned} S_{LV} &= 2\sigma_{LV}V_L/R & \text{(3.12a)}\\ S_{SL} &= 2\sigma_{LV}V_L/R + 2\sigma_{SL}V_S/r & \text{(3.12b)}\\ S_{SV} &= 2\sigma_{SV}V_S/R. & \text{(3.12c)} \end{aligned}$$

We approximate the surface energy of an alloy as a linear combination of the surface energies of its pure components:

$$\begin{aligned} \sigma_{LV} &= (1 - X_L)\sigma^A_{LV} + X_L\sigma^B_{LV} & \text{(3.13a)}\\ \sigma_{SL} &= (1 - X_S)\sigma^A_{SL} + X_S\sigma^B_{SL} & \text{(3.13b)}\\ \sigma_{SV} &= (1 - X_S)\sigma^A_{SV} + X_S\sigma^B_{SV}. & \text{(3.13c)} \end{aligned}$$

Since the surface energy is temperature-dependent and the available data on surface energy is usually given at the melting point of the metal, we will consider the following equations:

$$\sigma^i_{LV} = \sigma^i_{LV\,mp} - \kappa^i_{LV}(T - T^i_{mp}) \qquad i = A,\ B, \tag{3.14}$$

$\sigma^i_{LV\,mp}$ is the surface energy of component i at the melting point and κ^i_{LV} is a temperature coefficient. The solid-liquid interfacial energy are observed to be about 25% larger than their liquid-vapor counterpart (Allen 1972; Murr 1975; Kumikov and

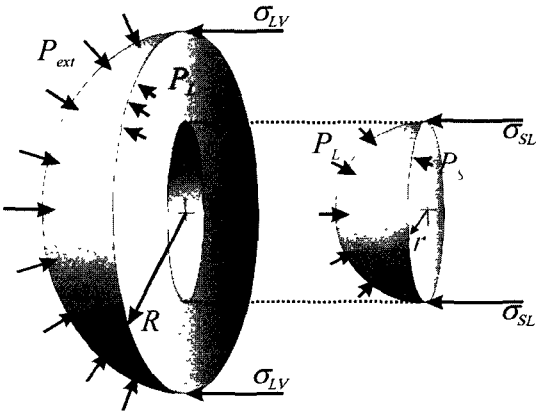

FIG. 3.1: Scheme of a composite NP cut in two hemispheres, where the core is detached. r and R, are the radii of the solid core and the liquid shell, respectively. σ_{LV} and σ_{SL} refer to the surface tension of the outer and inner shell, respectively. P_{ext} is the external pressure applied on the outer shell while P_L and P_S are the pressures within the liquid and the solid phases, respectively.

Khokonov 1983) and are considered to follow the same temperature dependence as their liquid counterpart. Therefore, we can write

$$\sigma^i_{SL} = 1.25\sigma^i_{LV} \qquad i = A,\, B. \tag{3.15}$$

Finally, we will consider that the surface energy of the pure solid component, σ^i_{SV}, is temperature-independent.

We demonstrate that there exists a limited range of temperatures and nominal compositions over which the core-shell configuration is stable. The core-shell configuration must fulfill the following conditions to be stable (we will subsequently refer to these conditions by their number):

1. The phases must be in equilibrium, i.e., the chemical potential must be equal for both phases (one can draw a common tangent);

2. Mass balance (Eqs. 3.2) must be fulfilled with a core radius that is strictly positive and smaller than the shell radius (i.e., $0 < r < R$). Furthermore, the nominal composition of the NP, X_0, must be within the range defined by the composition of the liquid shell, X_L, and that of the solid core, X_S;

3. The Gibbs free energy of the core-shell system, G_{S2}, must be lower than that of a completely solid (G_{S1}) or liquid (G_L) NP. In other words, a two-phase NP must be more stable than a single-phase NP.

The main assumptions are listed as follows:

- The NP properties are isotropic which is reasonable for the liquid phase and for solids at high temperatures. This approximation can be relaxed by considering a surface torque term. This would also allow one to estimate the contribution of faceting, expected to be important for small NP (for R typically below 10 nm, at low temperatures);

- The core is not considered under compression and the overall stress state of the NP does not affect the equilibrium. The model can be further refined by following, for example, the method described by Huh et al. (2005);

- No nucleation barrier is set for the formation of a solid core. However, if the core is too small, the surface contribution of the solid eventually raises the Gibbs energy curve of the solid phase to a point where only a single-phase NP is stable (either G_L or G_{S1}). This phenomenon indirectly acts as a "nucleation barrier";

- Surface or interface segregation are not considered, for simplicity. These could be added to the computation by considering the Gibbs adsorption isotherm as described, for example, by Jesser et al. (2004);

- The phases are homogeneous and the solid-liquid interface is sharp (Howe and Saka 2004);

- The surface energy of the alloy is a linear combination of the surface energy of the pure component. This can be further refined by the use of Butler equations (Butler 1932; Tanaka and Hara 2001a; Tanaka and Hara 2001b) that can be computed *via* the thermodynamic properties of a liquid alloy. Note that Butler equations are not experimentally verified for solids.

We apply this method to the solid-liquid equilibrium within a Au-Pt NP. Okamoto and Massalski (1985) have provided the most up-to-date thermodynamic assessment of the Au-Pt system. The thermodynamic parameters of the system are listed in Table 3.1. All the additional parameters and physical properties are listed in Table 3.2.

The objective of these simulations are to *(i)* explore the limits of stability of a core-shell configuration in terms of temperature and composition with respect to a single-phase NP (either liquid or solid) and *(ii)* for conditions (T, X_0 and R) in which the core-shell configuration is stable, determine the composition and the radius of the solid core (X_S) and the liquid shell (X_L).

3.2.2 Gibbs-Thomson Curves and Phase Equilibria (Condition 1) We shall first consider the Gibbs energy curves related to a 50 nm radius NP at 1400 K (Fig. 3.2). The curve labeled G_L is associated with the liquid phase and is invariant to the size of the solid core. The other curves (black) are associated with the solid and can be used to demonstrate the Gibbs-Thomson effect. $G_{S2}, r \rightarrow R$ represents the case

TABLE 3.1: Thermodynamic functions for the liquid and solid Au-Pt phases and lattice stability of solid Au and Pt with respect to the liquid state (Okamoto and Massalski 1985).

Phase	**Enthalpy of mixing,** $\frac{\Delta H}{X(1-X)}$, J/mol	**Entropy of mixing,** $\frac{\Delta S^E}{X(1-X)}$, J/mol·K
Liquid	$23\,500 + 4\,000X$	0
Solid	$30\,000X$	$-13.00 + 14.183X$
Element	**Lattice stability** G_s^0, J/mol	
Au	-13 000 + 9.7190 T	
Pt	-19 650 + 9.6224 T	

TABLE 3.2: Au and Pt physical properties and parameters used in the computation of equilibrium.

Parameter	**Symbol**	**Value**	**Reference**
Melting temperature (K)			
Au	T_{mp}^{Au}	1336.15	(Okamoto and Massalski 1985)
Pt	T_{mp}^{Pt}	2047.15	(Okamoto and Massalski 1985)
Thermal expansion coefficient (K^{-1})			
Au	α^{Au}	6.9×10^{-5}	(Iida and Guthrie 1988)
Pt	α^{Pt}	15.2×10^{-5}	(Iida and Guthrie 1988)
Molar volume at melting point (m^3/mol)			
Au	V_{mp}^{Au}	11.3×10^{-5}	(Iida and Guthrie 1988)
Pt	V_{mp}^{Pt}	10.3×10^{-5}	(Iida and Guthrie 1988)
Contraction coefficient			
Au	β^{Au}	0.055	(Wittenberg 1972)
Pt	β^{Pt}	0.063	(Wittenberg 1972)
Surface energy temperature coefficient (J m^{-2}·K^{-1})			
Au	κ^{Au}	2.5×10^{-4}	(Kasama et al. 1976)
Pt	κ^{Pt}	1.2×10^{-4}	(Allen 1972; Morita 1976)[a]
Liquid surface energy at melting point (J/m^2)			
Au	$\sigma_{LV\,mp}^{Au}$	1.169	(Kasama et al. 1976)
Pt	$\sigma_{LV\,mp}^{Pt}$	1.8	(Allen 1972)
Solid surface energy at melting point (J/m^2)			
Au	σ_{SV}^{Au}	1.39	(Jones 1971)
Pt	σ_{SV}^{Pt}	2.28	(Jones 1971)

[a]average between experimental data: 1.7×10^{-4}(Allen 1972) and 0.7×10^{-4}(Morita 1976).

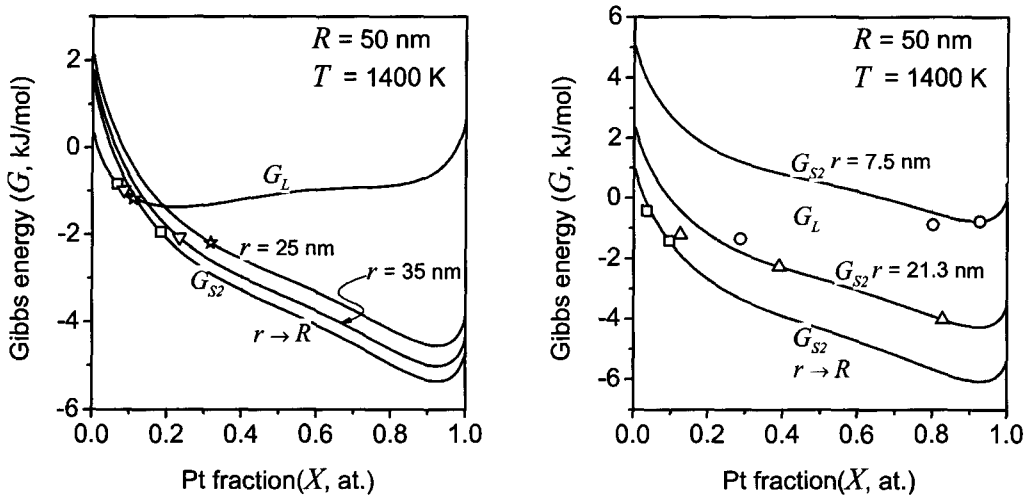

FIG. 3.2: Demonstration of the Gibbs-Thomson effect with Gibbs energy curves associated with a 50 nm radius NP at 1400 K. Liquid: G_L, grey line. Solid core: G_{S2}, $r \rightarrow R$, bottom black line. (a) G_{S2} is also plotted for a solid core with inner radius of (r) 35 nm and 25 nm: center and upper black curves, respectively. Symbols correspond to the equilibrium composition between the energy curves of the solid and the liquid, as specified by the common tangent construction. By decreasing the inner radius of the solid phase, the energy curve rises to increase the equilibrium composition of both the liquid and the solid phases (indicated by squares, down triangles and stars, for $r \rightarrow R$, 35 and 25 nm, respectively). (b) The values of the inner radius were chosen to match the particular case of a peritectic ($r = 21.3$ nm, triangle) and monotectic ($r = 7.5$ nm, circle) transformation.

where the NP is almost completely solid but still shares an interface with an infinitely thin liquid shell. Should the NP adopt this core-shell configuration, the open squares in Fig. 3.2(b) indicate the equilibrium composition of the liquid and the solid phases. As the inner core radius, r, decreases, the Gibbs energy curve associated with the solid will rise to higher energies. Consequently, the equilibrium composition of both the liquid and the solid will shift to higher Pt fractions, as determined by the common tangent construction. The intercepts of the common tangents are respectively marked by open down triangles and stars for r= 35 nm and 25 nm.

The thermodynamic functions of the liquid and the solid phases both exhibit a double well (at low temperatures) as a consequence of their large and positive enthalpy of mixing. Consequently, as the Gibbs energy curve of the solid is increased and the compositions shifted to higher Pt content, there will exist two critical inner radii corresponding to a monotectic and a peritectic transformation. The case where $r = 21.3$ nm, in Fig. 3.2(b) illustrates a peritectic transformation: the tangent construction intercepts twice the solid phase curve and once the liquid phase curve (open triangles). Similarly, a monotectic transformation is reached for $r = 7.5$ nm:

an equilibrium is obtained between the solid and the liquid phases with two possible compositions (open circles).

The variation of the composition of the solid (X_S) and liquid (X_L) phases as a function of inner core radius, (r) are plotted in Fig. 3.3 for a 50 nm radius NP. We will subsequently refer to these types of curves as "Gibbs-Thomson curves" or "Gibbs-Thomson branch", when referring to either curve. The radius at which discontinuities occur are marked by open squares and triangles symbols which correspond to those of Fig. 3.2(b). The other symbols refer to those of Fig. 3.2(a). For any given temperature or NP size, X_S and X_L form a pair of Gibbs-Thomson curves that merge for a small value of r, r_{min}, at which $X_S = X_L = 1$. This corresponds to the case where the Gibbs energy curve associated with the solid core raises to a point where it only intersects the liquid phase curve at X=1.

The Gibbs-Thomson branches are composed of segments, each roughly following an exponential decay, in agreement with Eq. 2.5. If the axes of the Gibbs-Thomson curves were interchanged, X_S and X_L curves could be considered as a liquidus and solidus lines. This would result in a meaningless exercise, unless we take into account mass balance, as it will be demonstrated.

The Gibbs-Thomson curves are drawn at various temperatures (Fig. 3.4) for a 50 nm (a) and 20 nm (b) radius NP. As the temperature is increased, the discontinuities disappear above a critical temperature which corresponds to the consolute point (temperature and composition above which the two inflexion points of the double-well Gibbs energy curve degenerate). At higher temperatures, we also note that the curves shift to larger inner radii and higher compositions. Indeed, at high temperature, the Gibbs energy curve of the liquid phase is stabilized with respect to that of the solid phase. Therefore, at high temperatures, the interfacial energy can easily promote the Gibbs energy curve of the solid core to higher energies where equilibrium with the liquid is forbidden (i.e. $G_{S2} > G_L$ for the whole composition range).

When the size of the NP is decreased to R=20 nm, (Fig. 3.4(b)), the Gibbs-Thomson curves remain unchanged but are truncated at a smaller inner radius, since r must be lower than R (note the abscissa scale change). This can be understood by inspection of Eqs 3.12a and 3.12b. When decreasing the overall size, R, of the NP, a common term, $2\sigma_{LV}V_S/R$, raises both the liquid and the solid Gibbs energy curves by the same amount, leading to an unchanged equilibrium. The consequence of such a construction is that the liquid phase can be stabilized even at very low temperatures, as seen in Fig. 3.4(b) at 1000 K. At this temperature, the Gibbs energy curve associated with a solid core with an inner radius smaller than ~4 nm will be higher than that of the liquid for all X, thus stabilizing the liquid phase for such a low temperature (as we will discuss subsequently, this situation will be prevented by invoking Condition 3). Alternatively, at 1000 K, for a solid core with an inner radius larger than ~10 nm, the Gibbs energy curve of the solid is lower than that of the liquid for all X. In this situation we can define an upper limit for the inner radius, r_{max}, at which $X_S = X_L = 0$. If the core-shell geometry of a NP is fixed with

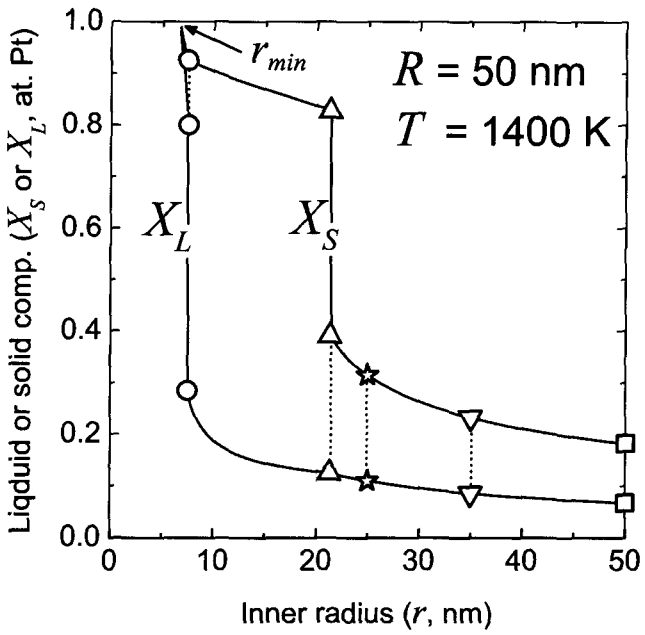

FIG. 3.3: Variation of the equilibrium composition of the liquid (X_L) and the solid (X_S) with the inner core radius (r) at various temperatures for a R=50 nm NP. These types of functions are referred in the text to as "Gibbs-Thomson curves". The discontinuities in the variation of the liquid phase composition are associated with a monotectic transformation while those on the solid phase are attributed to a peritectic transformation. Open symbols (square, down triangles, stars, up triangles and circles correspond to $r \rightarrow R$, 35 and 25, 21.3 and 7.5 nm, respectively) refer the tangency points of the solid and liquid phases energy curves shown in Fig. 3.2(b). The dotted line between the symbols can be considered as tie-lines.

an inner radius above r_{max}, the NP will be completely solid at 1000 K. As we will discuss subsequently, this situation will never be encountered as we demonstrate that a core-shell configuration is not stable for such small NPs (R=20 nm). The existence of r_{min} and r_{max} will not be referred to subsequently but are discussed for sake of completion.

3.2.3 Mass-Balance Restriction (Condition 2) The restriction of mass balance is demonstrated by first expressing X_L as a function of r through the mass balance equation (Eqs. 3.2) and comparing it with the Gibbs-Thomson X_L branch. Fig. 3.5 shows the Gibbs-Thomson curves for a 50 nm NP at 1650 K together with X_L (as defined by Eqs. 3.2) plotted for various nominal compositions (inward curves). When X_L is plotted for a nominal composition $X_0 = 0.55$ (dotted curve), it intersects the Gibbs-Thomson X_L branch at two positions marked by open squares. This implies that there exist two possible configurations which satisfy both the mass balance and

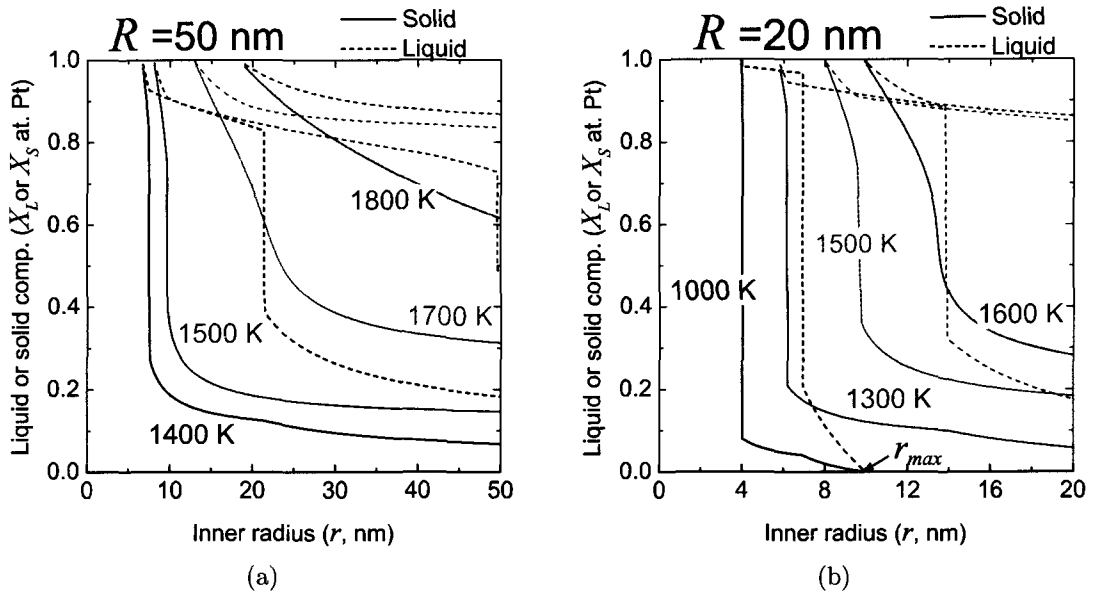

FIG. 3.4: Variation of the equilibrium composition of the liquid (X_L, full lines) and the solid (X_S, dashed lines) with the inner core radius (r) at various temperatures for a 50 nm (a) and a 20 nm (b) NP. These types of functions are referred in the text to as "Gibbs-Thomson curves". The discontinuity in the liquid branch is associated with a monotectic transformation while the one in the solid branch is attributed to a peritectic transformation. Symbols in (a) refer to those in Fig. 3.2(b)

the equilibrium restrictions for a 50 nm NP at 1650 K: *(i)* r = 17.05 nm with X_S = 0.53 and X_L = 0.88 and *(ii)* r = 37.5 nm with X_S = 0.27 and X_L = 0.83. It is important to note that the solution with the largest inner radius is always the most stable one, as its total energy is lower. As the nominal composition decreases, the two solutions move closer together and eventually become degenerate. For X_0 = 0.398, defined hereafter as X_0^{min}, there exists only one solution that satisfies both restrictions imposed by mass balance and phase equilibrium which is described by: for r = 23.8 nm, $X_S = 0.86$ (X_S^{min}) and $X_L = 0.33$ (X_L^{min}). For values of $X_0 < X_0^{min}$ the coexistence of liquid and solid is impossible since the amount of Pt in the system is not sufficient for the core-shell configuration to exist.

The solid, X_S^{min}, and liquid, X_L^{min}, composition (open circles) corresponding to the case $X_0 = X_0^{min}$ (closed circle) are plotted on a phase diagram in Fig. 3.6(a), for a 50 nm radius at 1650 K. The bulk liquidus and solidus of the Au-Pt system are also displayed in light grey as a reference. Note that the phase diagram serves two purposes here: for a given temperature, it displays the minimal nominal composition that a core-shell configuration can sustain and shows the corresponding composition of the liquid shell and the solid core.

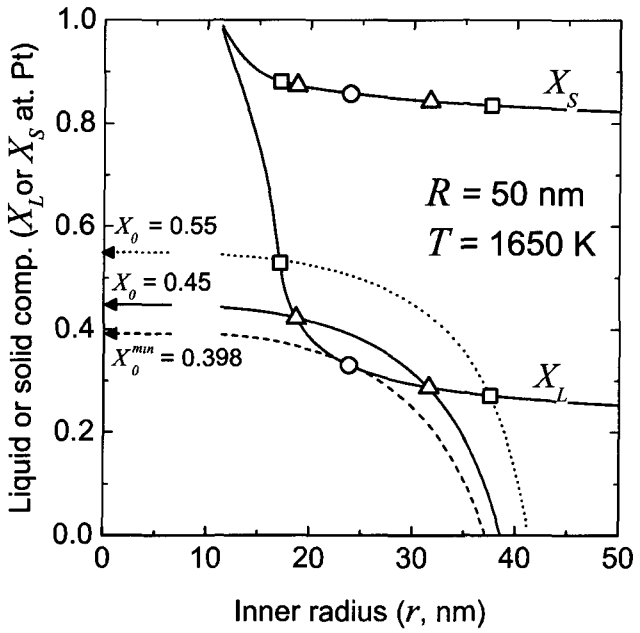

FIG. 3.5: Variation of the equilibrium composition of the liquid phase (X_L) and the solid phase (X_S) with the inner core radius (r) at 1650 K for a 50 nm radius NP. The composition of the liquid (X_L), as derived from the mass balance (Eqs. 3.2) is plotted for nominal compositions of $X_0 = 0.55$ (dotted line), 0.45 (full line) and 0.398 (dashed line). The intersection of these curves with the equilibrium liquid composition (as specified by the double tangent construction) are marked symbols. For $X_0 > 0.398$, two solutions exist while for $X_0 = 0.398$, these solutions become degenerate. For $X_0 < 0.398$, the amount of Pt in the system is not sufficient for the liquid(shell)/solid(core) configuration to exist.

We can construct a "mass balance phase boundary" by computing X_0^{min} for an array of temperatures (closed circles, Fig. 3.6(b)). If the nominal composition is below X_0^{min}, the NP will be in the liquid state. If $X_0 = X_0^{min}$, the NP will adopt the core-shell configuration with a solid core and a liquid shell having a composition X_S^{min} and X_L^{min} (open circles), respectively.

3.2.4 Relative Stability of a Two-Phase with Respect to a Single-Phase NP (Condition 3) Condition 3 requires that the core-shell configuration must have a lower energy than a single-phase NP. This condition is illustrated in Fig. 3.7(a) which displays the Gibbs energy curves of the possible phases associated with a 50 nm radius NP at 1650 K with an inner radius of 32.8 nm. The equilibrium compositions between the liquid shell and the solid core (upper black line) are dictated by the double tangent construction (grey line) and are marked by open circles. X_0^{max} is defined as the composition where the Gibbs energy curve of the solid NP (G_{S1}, black

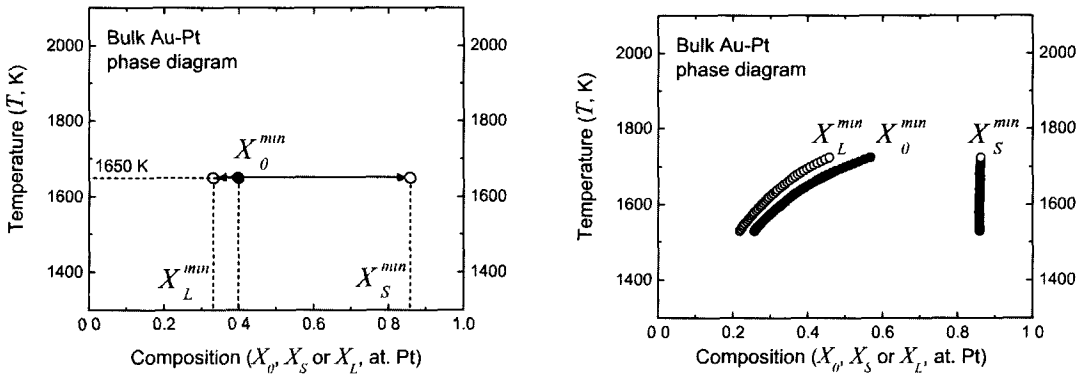

FIG. 3.6: (a) Temperature-composition graph showing the minimal nominal composition (X_0^{min}) necessary for a core-shell configuration to exist for a 50 nm radius NP at T=1650 K (closed circle, $X_0 = 0.398$ see Fig. 3.5). For this nominal composition, the corresponding composition of the solid (X_S^{min}) and liquid (X_L^{min}) partitions are shown (open circles). (b) The minimal nominal composition, X_0^{min} (closed circles) calculated at various temperatures for a 50 nm NP with corresponding partition composition (open circles). The bulk liquidus and solidus are shown for comparison purposes (grey lines).

curve) intersects the double tangent (marked by a closed circle). A common tangent construction cannot be drawn between G_{S1} and G_L, since this implies equilibrium between the two phases. As noted previously, equilibrium between solid and liquid necessarily creates an interface which raises the Gibbs energy curve associated with the solid core. Consequently, the solid-liquid equilibrium can only be considered between G_{S2} and G_L. As seen from Fig. 3.7(a), for $X_L^{max} < X_0 < X_0^{max}$, the energy of a solid or liquid NP is higher than that of a core-shell NP of the same nominal composition (downward arrow). Alternatively, for $X_0 > X_0^{max}$, the most stable configuration is a single-phase solid solution.

The exact composition of X_0^{max} is found by successive iterations since it varies with r. We start the iteration process with X_0 slightly larger than X_0^{min} and find the radius at which the Gibbs-Thomson liquid curve intersects X_L as computed using the mass balance equation. Gibbs energy curves are then generated with those conditions and the intersection point between the double tangent and G_{1S} becomes the new X_0 and the process is repeated until convergence. This iterative procedure is then finally carried out for an array of temperatures. Another phase boundary can be constructed with the values of X_0^{max} (closed circles), as shown in Fig. 3.7(b) in which the corresponding values of X_L^{max} and X_S^{max} are also reported.

For the situation where $X_0 < X_0^{min}$ or $X_0 > X_0^{max}$, the NP can either be completely liquid ($G_L(X_0) < G_{S1}(X_0)$) or a completely solid phase ($G_{S1}(X_0) < G_L(X_0)$).

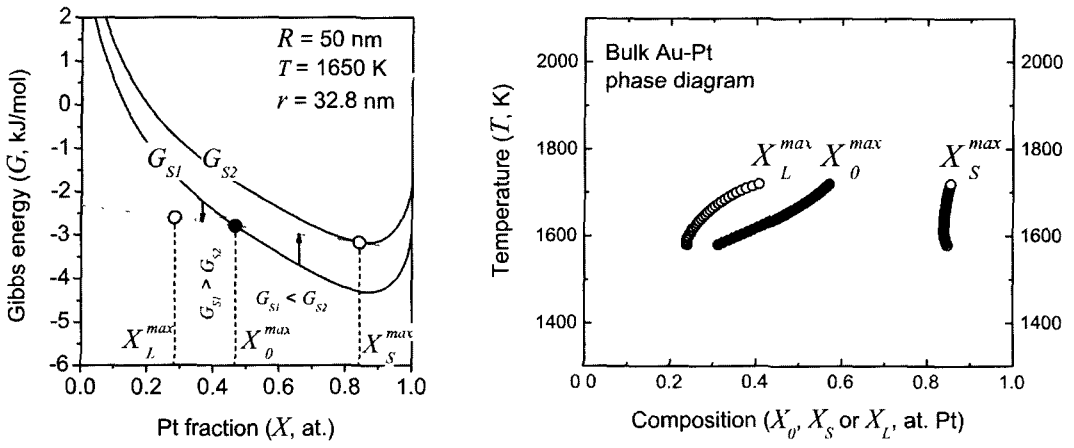

(a) (b)

FIG. 3.7: (a) Gibbs energy curves computed for a 50 nm radius NP at 1650 K for the liquid phase (G_L, grey curve), a solid NP (G_{S1}, lower black curve) and a solid core having a 32.8 nm radius (G_{S2}, upper black curve). The double tangent (grey line) specifies the composition of the solid core and a liquid shell (open circles). The intersection between G_{S1} and the double tangent (closed circle) marks the composition above which the energy of a single solid phase is more stable, X_0^{max}. For a NP having an overall content $X_L^{max} < X_0 < X_0^{max}$, a core-shell configuration is stabilized when the solid and liquid phase compositions are X_S^{max} and X_L^{max}, respectively. (b) X_0^{max} (closed circles) calculated at various temperatures with corresponding X_S^{max} and X_L^{max} (open circles). The bulk liquidus and solidus are shown for comparison purposes (grey lines).

For example, Fig. 3.8(a) shows the Gibbs energy curves associated with a 50 nm radius NP at 1500 K with an inner radius core of 19.6 nm. In this situation, the intersection between G_L and G_{S1}, hereafter defined to as X_0^{SL}, occurs at a composition smaller than X_L (as defined by the double tangent construction between G_L and G_{S2}). If $X_0 < X_0^{SL}$, the NP is either completely liquid or solid otherwise, since the G_{S1} energy curve is lower than the double tangent for any composition between X_0^{SL} and 1. Fig. 3.8(b) plots X_0^{SL} for the whole composition range. The molar energy of the alloy can therefore be regarded as a lower envelope of G_L, G_{S1} and the common tangent between G_L and G_{S2}. For the case of pure components, this curve appropriately describes the melting point depression expected when decreasing the size of NPs (Buffat and Borel 1976). However, it should be noted that the model does not predict the appearance of a liquid sheath upon melting of pure NPs.

3.2.5 Temperature-Composition Diagram of Au@Pt NPs We can now combine on the same plot (Fig. 3.9(a)) all the constraints (Conditions 1 to 3) and infer on the stability of a core-shell configuration. It is surprising to realize that the only region of the phase diagram where a liquid and a solid phases can coexist in a core-shell

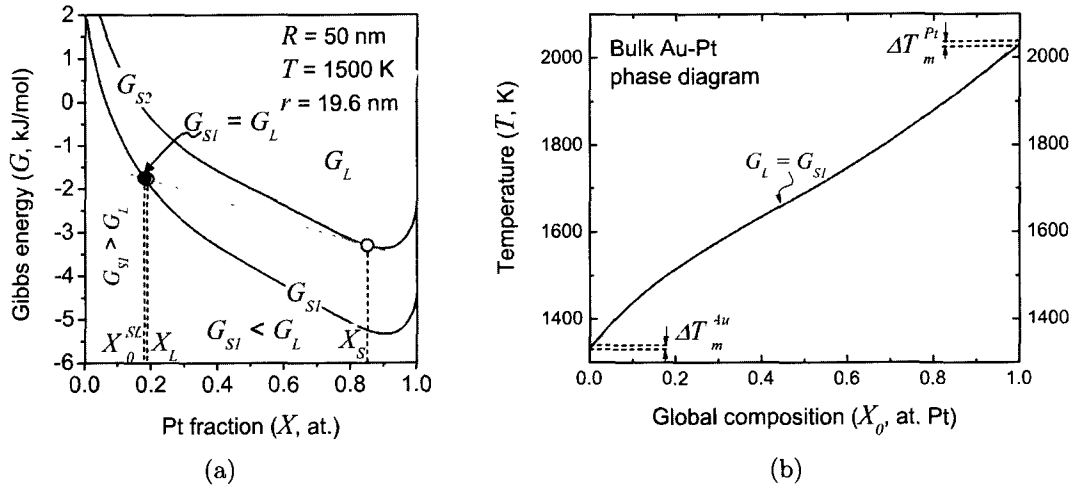

FIG. 3.8: (a) Gibbs energy curves associated to a 50 nm radius NP at 1500 K. Grey line: G_L, liquid phase. Lower black line: G_{S1}, single phase NP. Upper black line: G_{S2}, 19.6 nm radius solid core. Open circles marks the solid (X_S) and liquid (X_L) composition of the liquid (G_L) and the solid core (G_{S2}), as specified by the double tangent construction (grey line). Since the composition at which G_L intersects G_{S2} (X_0^{SL}) is lower than X_L, the solid(core)/lquid(shell) configuration cannot be stable. In this case, the solid and liquid phases shall not coexist within the same NP: the NP is in a liquid state for $X_0 < X_0^{SL}$, and completely solid otherwise. (b) The critical point X_0^{SL} is calculated by letting $G_{S1} = G_L$ for the whole temperature range of interest. The magnitude of the melting points depression of Au (T_m^{Au}) and of Pt (T_m^{Pt}) for a 50 nm radius NP are in agreement with experimental observations (Buffat and Borel 1976). The bulk liquidus and solidus are shown for comparison purposes (grey lines).

configuration for a NP having a 50 nm radius is contained in a small lens-shaped region defined by X_0^{min} and X_0^{max}. Note that the phase boundary, X_0^{SL}, is meaningless in the two-phase region. The inset of Fig. 3.9(a) shows a magnified view of a region of the phase diagram where the phase boundaries appear to intersect. One can note that the phase boundary defined by X_0^{SL} is secant with the phase boundary defined by X_0^{min}. This implies that if the temperature of a NP having a nominal composition of 0.57 decreases from the liquid phase, it will transform first to the solid phase over the small temperature range X_0^{SL}–X_0^{min} (1726–1730 K). Lowering the temperature further in the range 1720–1726 K will stabilize the solid(core)-liquid(shell)configuration. The NP would be solid for lower temperatures. This counterintuitive transformation (Liquid → Solid → 2 phases → Solid) is not a consequence of numerical instabilities or precision but is a phenomenon that is predicted on the basis of this model.

The transformation sequence related to a partionless transition* from liquid to solid would be kinematically forbidden at the predicted temperatures. We rather expect an undercooling associated with the solidification of a NP. Consequently, a

*Which occurs without the coexistence of two or more phases.

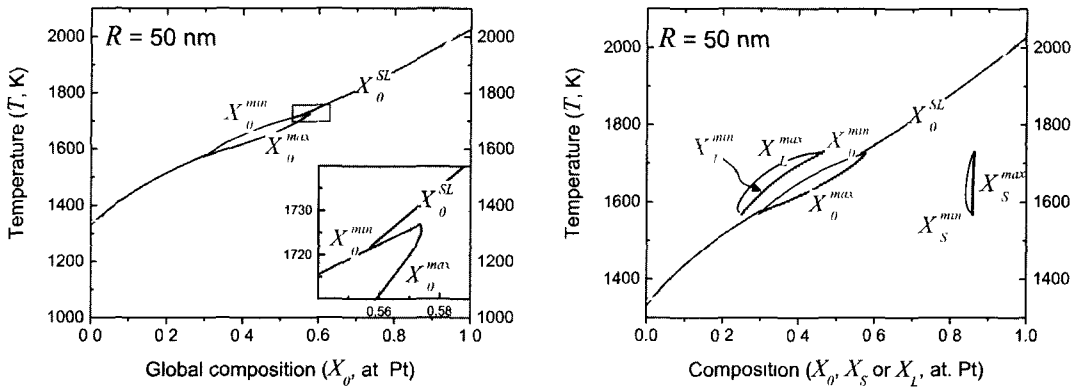

FIG. 3.9: (a) Stability limit of a core-shell configuration of a 50 nm radius NP. The solid and the liquid phases can coexist in a core-shell configuration only for temperatures and compositions of the phase diagram enclosed within X_0^{min} (red) and the X_0^{max} (blue) curves. For other regions of the phase diagram, the NP will be completely liquid for $X_0 < X_0^{SL}$ or solid for $X_0 > X_0^{SL}$. The inset shows the details of the intersection of the limiting curves. (b) Same as (a) but the extent of the new liquidus (bonded by X_L^{min} and X_L^{max}) and solidus (bonded by X_S^{min} and X_S^{max}) are shown. The bulk liquidus and solidus are shown for comparison purposes (grey lines).

smaller undercooling would be associated with smaller NPs, in agreement with the nucleation theory (see for instance Porter and Easterling 1992) and shares some similarity with the conclusions of Shirinyan's model, as discussed in Section 2.4. The kinetics of the transformation in small scale system is, however, outside this chapter's scope.

The stability limits of the core-shell configuration are drawn again in Fig. 3.9(b). Should the solid and liquid phases coexist within the NP, then the composition of the solid and liquid phases are expected to be included between X_S^{min} and X_S^{max} and between X_L^{min} and X_L^{max}, respectively. These can be understood as the liquidus and solidus of a NP in the sense that they predict the composition of the phases but are by no means considered as phase boundaries. We stress the fact that the phase boundaries are predicted by X_0^{SL}, X_0^{min} and X_0^{max}.

The effect of increasing the outer radius, R, is demonstrated in Fig. 3.10(a). The stability limits, X_0^{min} and X_0^{max}, of a 50 nm and a 100 nm NP are shown. The two-phase region of the 100 nm radius NP extends on a much larger composition and temperature range than for the 50 nm radius case. Note that the limit X_0^{SL} is slightly raised to higher temperatures, consistent with the small variation of the melting point of pure NPs that large. The liquidus and solidus corresponding to the 100 nm NP (blue curves, Fig. 3.10(b)) are compared with those of a 50 nm radius NP. Overall, for larger NPs, the liquidus and solidus borders those of the bulk, as

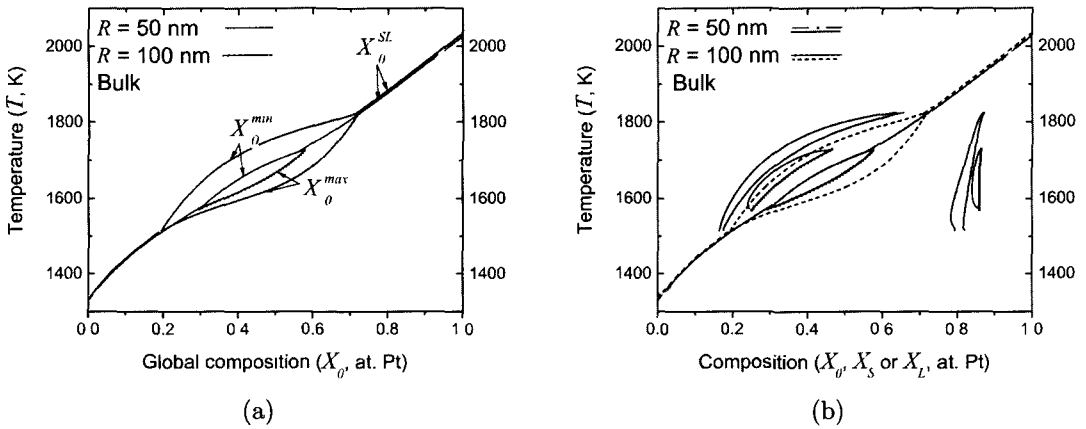

FIG. 3.10: (a) Phase diagram comparing the stability limits of the core-shell configuration of a 50 nm (red) and a 100 nm (blue) radius NPs. (b) Stability limits of the core-shell configuration of a 50 nm (black curve) and a 100 nm (dashed black curve) radius NPs along with their respective liquidus and solidus. The bulk liquidus and solidus are shown for comparison purposes (grey lines).

the NP stability limits is expected to approach the bulk liquidus and solidus. These trends are consistent with the expected asymptotic behavior: as $R \rightarrow \infty$, the stability limits X_0^{min} and limiting curves defined by X_L^{min} and X_L^{max} will all merge with the bulk liquidus. Similarly, X_0^{max} and the limiting curves defined by X_S^{min} and X_S^{max} will merge with the bulk solidus.

As the NP size decreases, X_0^{min} and X_0^{max} will collapse to a single point where the coexistence of liquid and solid in a core-shell configuration within a NP will not be possible for sizes smaller than a critical radius. This critical radius is estimated to $R \sim 41.5$ nm and, for this radius, a core-shell configuration is only possible at a temperature of 1645 K. At this temperature, the NP will partition into a 86.4% Pt core with a radius of 21.5 nm and a 35.6% Pt-rich shell.

3.3 Miscibility Gap

The last Section focused on the calculation of the equilibrium between the liquid and the solid phases in a core-shell configuration while ignoring the rest of the Au-Pt phase diagram. In particular, it was forbidden for the system to further phase segregate within individual phases as it would be the case in a monotectic or peritectic reaction. In this Section, we explore the effect of size on the miscibility gap of the Au-Pt system. In contrast with the last Section, we shall be only concerned with the stability conditions of a single-phase particle. Therefore, no geometry is imposed on the system, hence eliminating the need to consider the effect of interfaces other than

the particle surface. As a consequence of such a simplification, the miscibility gap boundary will no longer correspond to the composition of the segregated phases: it will rather reflect the single-phase stability limit for a given particle size.

A miscibility gap is present in a system at a given temperature if its corresponding Gibbs energy curve exhibits a double welled shape. An homogeneous alloy quenched at a given temperature within the heart of the miscibility gap will phase separate into α_1 and α_2 phases. The terminal composition of each phase, X_1 and X_2, are determined by the common tangent construction.

3.3.1 Linear Dependence of the Surface Energy with Composition Let us first recall that the intercepts (X_1 and X_2) of the common tangent with the Gibbs energy curve of the solid phase (G_{S1}) can be expressed as the solution of a system of equations:

$$\left.\frac{\partial G_S(X)}{\partial X}\right|_{X=X_1} = \left.\frac{\partial G_S(X)}{\partial X}\right|_{X=X_2} \tag{3.16a}$$

$$\frac{G_S(X_1)-G_S(X_2)}{X_1-X_2} = \left.\frac{\partial G_S(X)}{\partial X}\right|_{X=X_1}, \tag{3.16b}$$

where $G_S(X)$ now replaces G_{S1} for convenience. If a polynomial of the nth degree, $\sum_{i=0}^{n} a_i X^i$, is added to $G_S(X)$, one can rewrite Eqs. 3.16 as

$$\left.\frac{\partial G_S(X)}{\partial X}\right|_{X=X_1} + \sum_{i=1}^{n} i\, a_i X_1^{i-1} = \left.\frac{\partial G_S(X)}{\partial X}\right|_{X=X_2} + \sum_{i=1}^{n} i\, a_i X_2^{i-1} \tag{3.17a}$$

$$\frac{G_S(X_1)-G_S(X_2)}{X_1-X_2} + \frac{\sum_{i=0}^{n} a_i X_1^i - \sum_{i=0}^{n} a_i X_2^i}{X_1-X_2} = \left.\frac{\partial G_S(X)}{\partial X}\right|_{X=X_1} + \sum_{i=1}^{n} i\, a_i X_1^{i-1}. \tag{3.17b}$$

If n=0 or 1, Eqs. 3.17 reduce to Eqs. 3.16, demonstrating that adding a constant or a linear term leaves X_1 and X_2 unchanged. Therefore the third and fourth terms of Eq. 3.6c related to the lattice stability can be dropped from the computation of X_1 and X_2 since they vary linearly with composition. The miscibility gap is now dependent on the contributions of the Gibbs energy of mixing (Eq. 3.8) and the surface energy (Eq. 3.12c). If the surface energy contribution (Eq. 3.12c) is either independent of, or is a linear function of composition, the miscibility gap will be independent of the particle radius (if the liquid phase is ignored).

Inspection of Eq. 3.12c reveals that the surface energy term has a quadratic dependence with the composition, X. Indeed, the surface energy σ_{SV} and the molar volume, V_S, each bear a linear dependence on the composition X. The surface energy can be rearranged to highlight its parabolic dependence with respect to the composition:

$$S_{SV} = a_0 + a_1 X + a_2 X^2 \tag{3.18}$$

with the coefficients being temperature-dependent parameters. After some algebra with Eqs. 3.3-3.4, 3.12c and 3.13c, the coefficient of interest, a_2, is found equal to

$$a_2 = \frac{2}{R}(\sigma_{SV}^{Pt} - \sigma_{SV}^{Au})\Delta V_S \tag{3.19}$$

where ΔV_S is the molar volume difference between Pt and Au at a given temperature and can be written in full as

$$\Delta V_S = \frac{V_{mp}^{Pt}\left[1+\alpha^{Pt}(T-T_{mp}^{Pt})\right]}{1+\beta^{Pt}} - \frac{V_{mp}^{Au}\left[1+\alpha^{Au}(T-T_{mp}^{Au})\right]}{1+\beta^{Au}}. \tag{3.20}$$

For $n = 2$, Eqs. 3.17 reduce to:

$$\left.\frac{\partial G_S(X)}{\partial X}\right|_{X=X_1} + 2a_2(X_1 - X_2) = \left.\frac{\partial G_S(X)}{\partial X}\right|_{X=X_2} \tag{3.21a}$$

$$\frac{G_S(X_1) - G_S(X_2)}{X_1 - X_2} - a_2(X_1 - X_2) = \left.\frac{\partial G_S(X)}{\partial X}\right|_{X=X_1}. \tag{3.21b}$$

To plot the miscibility gap for a given radius, R, one must solve Eqs. 3.21 for X_1 and X_2 for an array of temperatures. We can select an array of temperature from an arbitrary lower temperature, say 800 K to the top of the miscibility gap, commonly referred to as "consolute point". The consolute temperature and composition of a bulk system can be determined by solving the system of equations formed by letting the second and the third derivatives of the Gibbs energy curves equal to 0. When the surface energy is taken into account, the consolute point can be solved with the following set of equations:

$$\frac{\partial^3 G_S(X)}{\partial X^3} = 0 \tag{3.22a}$$

$$\frac{\partial^2 G_S(X)}{\partial X^2} = 2a_2. \tag{3.22b}$$

Note that the quadratic terms of the surface energy did not survive the third derivative. However, the composition and the temperature of the consolute point will exhibit a dependence on the radius through a_2 (Eq. 3.19).

An example of the numerical computation of the miscibility gap at 1000 K is illustrated in Fig. 3.11(a). The energy curves of the bulk (grey line) and of a 10 nm radius NP (black line) their corresponding common tangent were calculated only with the relevant terms pertaining to the computation of the miscibility gap, namely the Gibbs energy of mixing and the contribution of the quadratic terms of the surface energy, a_2X^2. The fact that the surface contribution *decreases* the value of the molar energy is irrelevant, since constant and linear terms were omitted. The solubilities at a given temperature are found by the intersection of the common tangent with

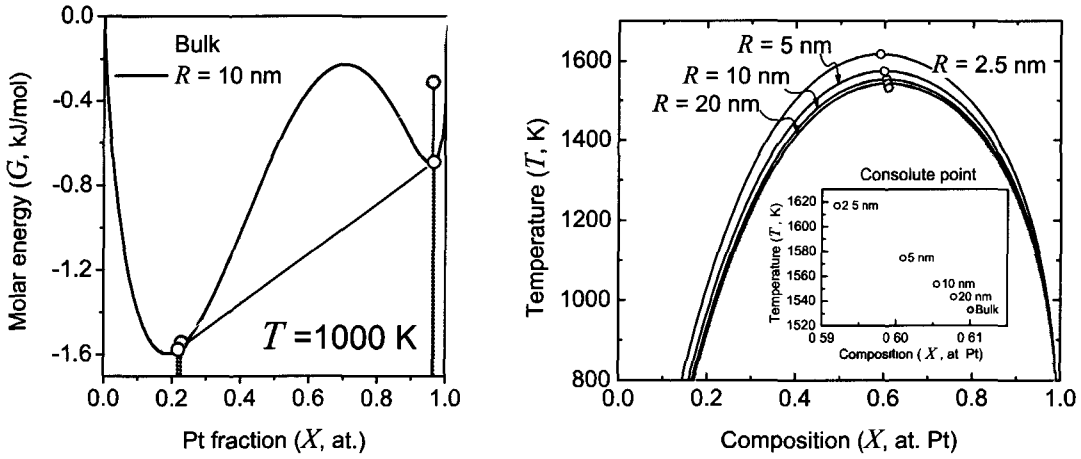

FIG. 3.11: (a) Effect of the quadratic terms of the capillarity term on the Gibbs energy curve. Gibbs energy curve of a 10 nm radius solid Au-Pt alloy (black line) compared to the bulk alloy (grey line). (b) Miscibility gap of a bulk Au-Pt alloy (grey line) and of NPs of various radii, computed with Eqs. 3.21. The consolute points (Eq. 3.22), are marked by open circles on the miscibility curves and are plotted again in the inset graph.

the two wells of the energy curve (indicated by circles in Fig. 3.11(a)). Calculated miscibility gaps for 2.5, 5, 10, 20 nm radii NPs (black lines) are compared to the bulk (grey line) in Fig. 3.11(b). The consolute points calculated for the NPs are marked by open circles (bulk: grey circle) at the apogee of their respective miscibility gap and appear again in the inset at a magnified scale.

Surprisingly, smaller radii shift the consolute point to *higher* temperatures and decreases the solubility of Pt in Au. The solubility of Au in Pt remains unchanged largely because of the much smaller curvature of the Pt-rich well compared to the Au-rich well of the Gibbs energy curve. The notion of increased solubility with decreasing size is usually understood in terms of the Gibbs-Thomson effect, where the solubility of the matrix is increased by the interaction with a small precipitate. The situation here is different inasmuch that a single energy curve is in equilibrium with itself. In this situation, the magnitude and the direction of the shift of the miscibility gap and the consolute point are largely determined by a_2, itself proportional to the difference of molar volume and surface energy between the pure constituents, at a given temperature.

We stress the fact that the computed phase diagrams in Fig. 3.11 represent the stability limit of single-phased NPs. For example, the stability limit of a bulk homogeneous alloy at 1000 K is ~22.8% at. Pt. For a 10 nm radius NP, this limit is evaluated to ~21.8% at. Pt. However, if an infinitesimal amount of Pt is added

to such a NP, then a new phase precipitates and will be sharing an interface with the parent phase. The equilibrium is now modified with respect to a single phased system since a new phase and an interface are now interacting with the parent phase. Therefore, the concepts developed in this Section do not render the equilibrium of a particle having a nominal composition in the vicinity of the (recalculated) miscibility gap. Another consequence of restricting the computation to a single phase is the inability to consider the equilibrium with other phases, such as the liquid, since this implies the coexistence of solid and liquid –and thus, the presence of an interface.

Inspection of the liquid energy curve also reveals the presence of a double-well structure at low temperatures. In the bulk phase diagram, the liquid miscibility gap is repressed by the stability of the solid phase at the same temperature range. The method introduced in this Section can also be used to recompute the miscibility gap of a liquid droplet on the verge of a monotectic transformation.

3.3.2 Nonlinear Dependence of the Surface Energy with Respect to Composition We can propose a further refinement to the miscibility gap computation. So far, we have considered a surface energy which varies linearly with composition. This is an oversimplification as a deviation is often observed due to the surface enrichment (usually, a few monolayers) with the component having the lowest surface energy. By considering the equilibrium between the surface of an alloy and the bulk phase, Butler (1932) showed that the surface tension of an alloy, σ_{SV}, can be estimated at a given temperature and nominal composition from its thermodynamic parameters. The surface energy can then be defined by the following system of equations:

$$\sigma_{SV} = \sigma_{SV}^{A} + \frac{R_g T}{\omega^A} \ln \frac{a^A_{\text{Surf}}}{a^A_{\text{Bulk}}} \tag{3.23a}$$

$$\sigma_{SV} = \sigma_{SV}^{B} + \frac{R_g T}{\omega^B} \ln \frac{a^B_{\text{Surf}}}{a^B_{\text{Bulk}}}, \tag{3.23b}$$

where ω^i ($i = A$ or B) is the molar area of component i and can be written as

$$\omega^i = f V^{i\,2/3} N_{Av}^{1/3} \quad i = A, B, \tag{3.24}$$

where N_{Av} is Avogadro's number and f, a constant related to the coordination number at the surface and is equal to 1.06 (Kaptay et al. 2000). The a^i_j's are the activities of the pure constituents components on the surface and in the bulk (j=Surf or Bulk, respectively). The activities can be expressed as:

$$a^i_{\text{Bulk}} = \gamma^i_{\text{Bulk}} X^i_{\text{Bulk}} \tag{3.25a}$$

$$a^i_{\text{Surf}} = \gamma^i_{\text{Surf}} X^i_{\text{Surf}} \quad i = A, B, \tag{3.25b}$$

where γ_j^i's are the activity coefficients and are defined as:

$$\gamma^i_{\text{Bulk}} = \exp\left(\frac{G^{E,i}_{\text{Bulk}}}{R_g T}\right) \tag{3.26a}$$

$$\gamma^i_{\text{Surf}} = \exp\left(\frac{G^{E,i}_{\text{Surf}}}{R_g T}\right) \quad i = A, B. \tag{3.26b}$$

The excess energies, $G_j^{E,i}$, are derived from the interaction parameters, Ω_j:

$$G^{E,A}_{\text{j}} = X_j^2 \Omega_j \tag{3.27a}$$

$$G^{E,B}_{\text{j}} = (1 - X_j)^2 \Omega_j \quad j = \text{Bulk, Surf}, \tag{3.27b}$$

where

$$\Omega_{\text{Surf}} = \eta \Omega_{\text{Bulk}}. \tag{3.28}$$

η can be considered as the ratio of the surface to the bulk coordination number, taken here as 0.83 (Tanaka and Hara 2001a). Ω_{Bulk} can be found in thermodynamic databases and is listed for a solid Au-Pt alloy in Table 3.1. Let A represent Au and B Pt, then σ_{SV} is computed at a given temperature by solving Eqs. 3.23-3.28 for the equilibrium composition of the surface and the bulk, X_{Bulk} and X_{Surf}, respectively. To avoid confusion, the NP nominal composition will be referred to as X_0 instead of X_{Bulk}.

These set of equations were derived from studies of liquid metals and salts but were never experimentally challenged for solids. Some authors have nevertheless adapted these concepts to predict the surface tension of solids (Tanaka and Hara 2001b; Jesser et al. 2004) in order to derive nanophase diagrams, as discussed in Section 2.4. In the following discussion, we consider that the number atoms contributing to the surface enrichment is insignificant with respect to those in the rest of the NP.

Equations 3.23 are plotted in Figs. 3.12 (grey and black lines are associated with Eqs. 3.23a and 3.23b, respectively) as a function of the surface composition (X_{Surf}) for T = 1000 K and a bulk composition, X_{Bulk}=0.5 (a), 0.99 (b) and 0.9996 (c). The intersection of the two curves can be computed numerically and corresponds to the solution(s) of Eqs. 3.23 yielding the surface tension, σ_{SV} for a given X_{Bulk}. This calculation is then repeated for an array of values of X_{Bulk} (Fig. 3.12(d)) to show the dependence of σ_{SV} on the composition, at T = 800, 1000 and 1200 K (dotted, solid and dashed lines, respectively). The open circles on the T=1000 K curve in Fig. 3.12(d) refer to the solutions computed in Figs. 3.12(a)–3.12(c).

Both curves related to X_{Surf} evolve in a non-trivial manner with X_{Bulk}. The dependence of σ_{SV} with composition greatly contrasts with the linear approximation (Fig. 3.12(d), grey line). According to Fig. 3.12(d), the surface tension of an alloy plateaus at a value close to that of Au (~1.39 J/m^2) up to a bulk composition

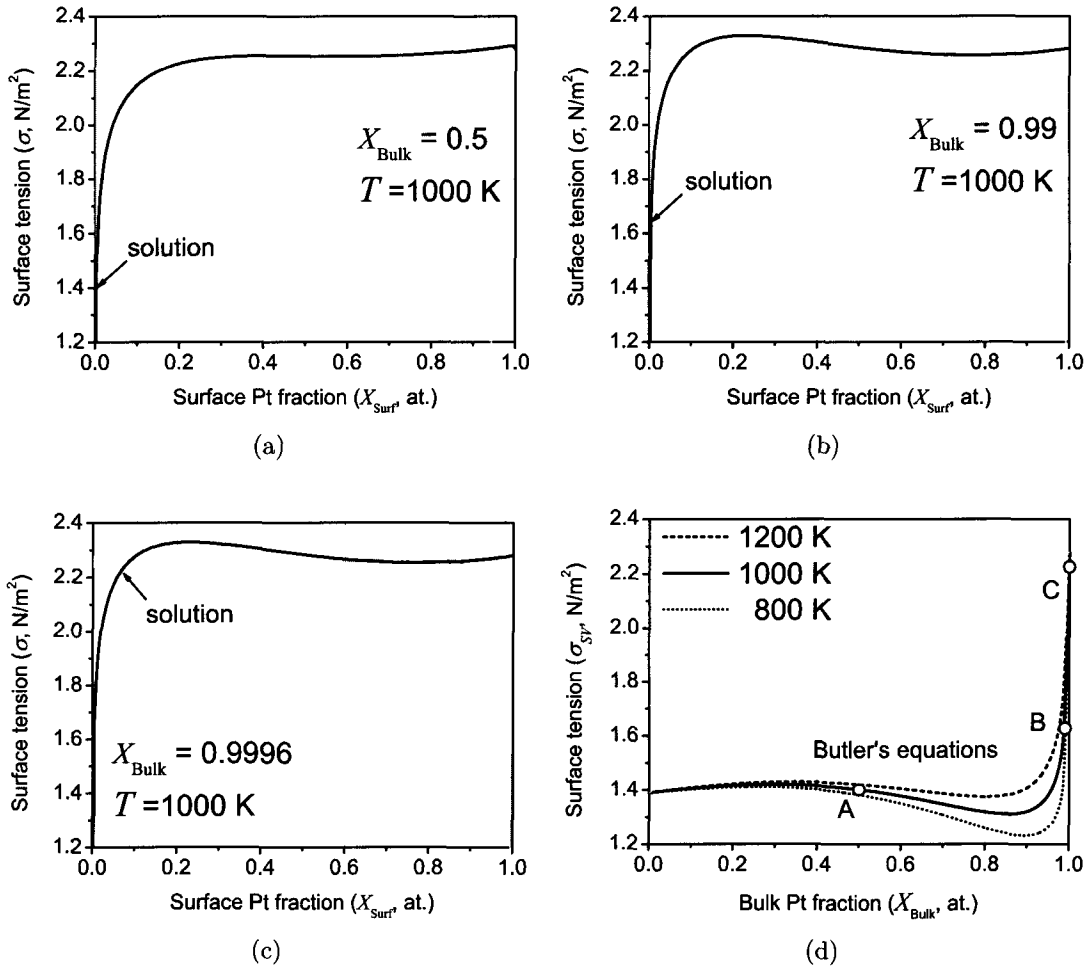

FIG. 3.12: Examples of solutions to Butler equations (grey and black curves correspond to Eq. 3.23a and Eq. 3.23b, respectively) at a temperature T=1000 K for bulk Au-Pt alloy of various compositions: X_{Bulk}=0.5 (a), 0.99 (b) and 0.9996 (c). (d) Calculated surface energy, σ_{SV}, as a function of X_{Bulk} for various temperatures: T=800 (dotted curve), 1000 (solid curve) and 1200 K (dashed curve). The linear approximation (grey line) is shown for comparison. The open circles refer to the solution of the examples of calculation in (a), (b) and (c).

of ~0.5% at. Pt, then dips to lower values and abruptly reaches that of pure Pt (~2.28 J/m^2) for a bulk composition greater than ~90% Pt. The magnitude of the dip increases for lower temperatures and can be attributed to the temperature dependence of the interaction parameter (Table 3.1).

The Au-Pt system exhibits a large and positive mixing energies. As a consequence, for a specific range of temperature and composition, the curves will intersect at more than one points. In such a specific situation[†], the lowest surface energy will be selected (Kaptay 2005). This only occurs for extremely narrow range of composition close the Pt-rich side of the miscibility gap, as depicted in Fig. 3.12(d).

Knowing $\sigma_{SV}(X_0)$, the miscibility gap can be computed for various radii, as described above. Fig. 3.13 compares the bulk miscibility gap with those computed for various NPs radii (2.5, 5, 10 and 20 nm), computed using Butler equations. The chief difference with the miscibility gaps computed with the linear approximation (Fig. 3.11(b)) lies in the behavior of the Pt-rich branch. When the surface energy is computed with Butler equations, both branches of the miscibility gap are significantly shifted towards the Au-rich side of the phase diagram.

3.4 Conclusion

In this Chapter, we have explored the effect of size on the various possible equilibria of the Au–Pt system. The size-dependent solid-liquid equilibrium was calculated using a different approach than for the miscibility gap. Each of the methods proposed to compute sections of the size-dependent phase diagram can be considered as a hybrid of Tanaka and Jesser's approaches (Section 2.4), as summarized in Table 3.3.

Special consideration was given to illustrate in a graphical manner the effects of surface energy on the Gibbs energy curves. Using "Gibbs-Thomson" curves, the size-induced phase transition and the constraint of mass balance could be described in an intuitive and graphical approach. We have also identified the main contributions to the size-dependent shift of the miscibility gap using a mathematical approach.

Given the high energy cost of the interface, it was found that the solid and liquid phases could not coexist in a core-shell configuration within a NP whose diameter is below ~42 nm. The phase boundaries of the stability region on a temperature-composition diagram for which a solid core could coexist with a liquid shell would approach those of the bulk phase diagram as the size of the NP increased. However, the liquid and solid phase composition, for a given size and nominal composition, are expected to be substantially lower than those of the bulk.

In retrospect, we can state that the Au-Pt system was the ideal example to demonstrate the concepts introduced in this Chapter. Indeed, this system allows one to

[†]The presence of multiple solutions indicates the existence of a first-order surface phase transition (Kaptay 2005).

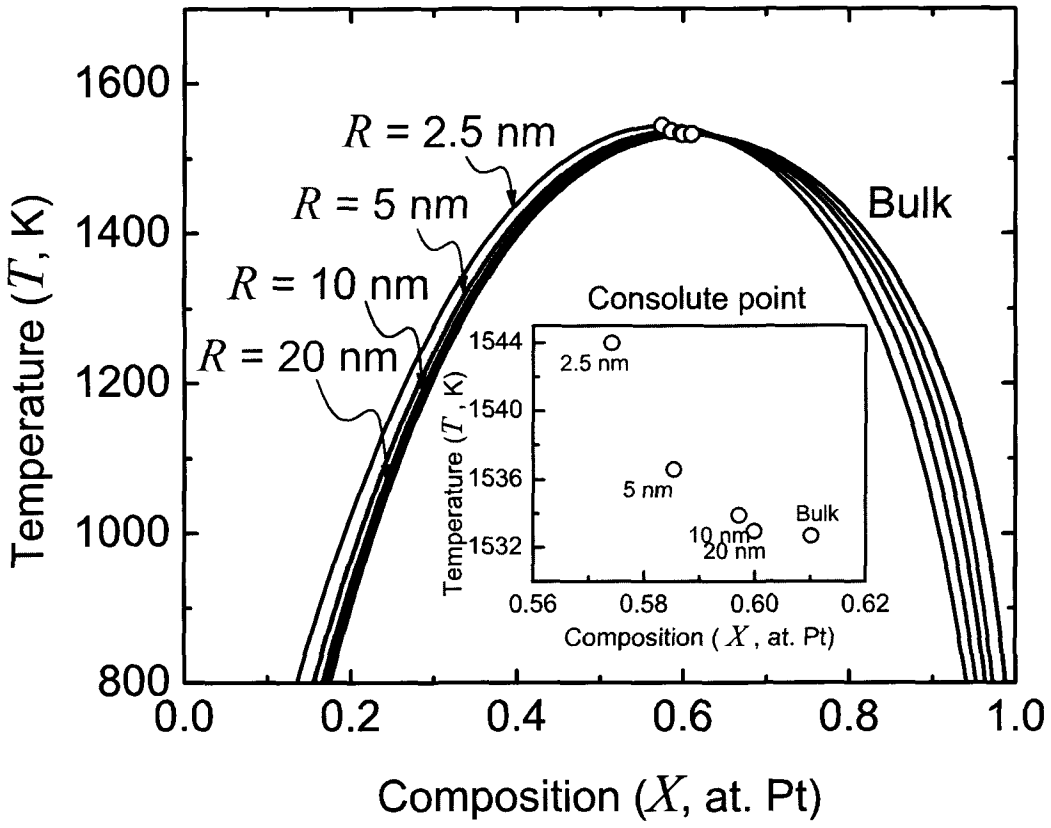

FIG. 3.13: Miscibility gap calculated for Au-Pt NPs of various radii using Butler equations (i.e. the surface energy dependence on composition is computed using Eqs. 3.23). The miscibility gaps are computed for R=2.5 (red), 5 (green), 10 (blue) and 20 nm (magenta) and compared with the bulk phase diagram (black line). The consolute points appear on the top of the respective miscibility gaps (open circles) and again in the inset, to highlight the composition and temperature shift of the consolute point with size.

explore the effect of size on the occurrence of various phase transformations that are highlighted by the discontinuities in the Gibbs-Thomson curves. The large partition of the solidus and liquidus facilitates the display of the phase diagram topological changes associated with the size of the system. In addition, the calculations presented in this Chapter showed that the concepts can be applied to system having a complex thermodynamic description.

Suggestion of further work includes using Butler equations to compute the solid-liquid equilibrium. In general, it would be of use to evaluate the stability of a system in another configuration than a core-shell, as suggested by (Weissmüller et al. 2004). For example, we can imagine an $A - B$ particle where each phase (α and β) is

TABLE 3.3: Features of the proposed method to calculate the size-dependent phase diagram compared to selected works from the literature. $\sigma(T)$: surface energy dependence on the temperature (linear or constant). $\sigma(X)$: surface energy dependence on composition (linear or computed using Butler equations). $V(T)$ and $V(X)$: molar volume dependence on temperature and composition, respectively (constant, linear, or quadratic). *Surface segregation* indicates whether this feature was taken into account and if so, the model used to estimate the effect. *Mass conservation* indicates whether this feature was taken into account or not. *Juxtaposition* refers to the geometry assumed by the model.

	Tanaka	**Jesser**	**Liquidus-Solidus**	**Miscibility Gap**
Reference	2001a 2001b	2004	This work	
$\sigma(T)$	Linear	Linear	Linear	Linear, Butler
$\sigma(X)$	Butler	Butler	Linear	Linear, Butler
$V(T)$	Linear	Linear	Linear	Linear
$V(X)$	Linear	Quadratic	Linear	Linear
Surface segregation	No	Gibbs adsorption	No	No
Mass conservation	No	Yes	Yes	No
Juxtaposition	Single phase	$\text{Solid}_{\text{core}}$-$\text{Liquid}_{\text{shell}}$	$\text{Liquid}_{\text{core}}$-$\text{Solid}_{\text{shell}}$	Single phase

segregated in two spherical caps separated by an interface, ω. If the system is subject to the constraint of mass balance and adopts an equilibrium shape, it is possible to demonstrate that the curvature of the two phases and the interface will be determined by the relative surface energy: $\sigma_\alpha/\sigma_\omega$ and $\sigma_\beta/\sigma_\omega$. Once the curvatures are known, then the capillarity terms would need to be determined by variational calculus (as opposed to simply taking the product of the area of the spherical cap and the surface energy per volume of molecules). The capillarity energy of each phase could then be added to their Gibbs energy and the contribution of the interface can be treated as an energy penalty to the molar energy, referred to a standard state of an equilibrium two-phase mixture.

Chapter 4

TEM Characterization Methods

4.1 Introduction

Bulk characterization techniques such as UV-visible-infrared spectroscopy, X-ray diffraction, and X-ray photoelectron spectroscopy are routinely used to probe collective properties of nanoparticles (NPs) samples. Such measurements must be complemented and validated by the characterization of individual NPs. in this regard, transmission electron microscopy (TEM) and the related suite of analytical tools, such as energy-dispersive X-ray spectroscopy (or spectrometry, EDXS) and electron energy-loss spectroscopy (or spectrometry, EELS) not only offer the means to characterize individual NPs, but can provide information with high spatial resolution and elemental selectivity from *within* these nanostructures.

The small size of NPs offers both advantages and challenges to analytical TEM. On one hand, it limits electron beam spreading, X-ray absorption and multiple scattering and therefore facilitates the measurement of EDXS and EELS spectra and their interpretation. On the other hand, the signal strength of a NP is generally low, as it is roughly proportional to the interaction volume defined by the NP and the electron beam. Longer acquisition times are generally required to obtain meaningful quantitative results, but electron beam damage or drift then becomes an issue. The signal-to-noise ratio can also be increased by summing the regions containing similar information within a NP. This data reduction technique is usually done at the expense of spatial resolution. For all these reasons, quantitative maps of NPs are seldom performed and are prone to many artifacts related to the poor counting statistics.

For the study of binary NPs, analytical TEM was extensively used to measure the composition of clusters, or the composition of the phase(s) constituting NPs, as discussed in Section 2.4.3. Typically, the electron probe is positioned on the cluster or the phase while characteristic signal is collected by an EDX spectrometer. The spectrum is then processed to yield a composition, where the measurement of the uncertainty is seldom given. Furthermore, the composition of each phase is given under the assumptions that the NP did not drift during the measurement and that the phase is homogeneous and representative of the rest of the NP or the cluster. However, the characteristic signal of a nanostructure is intrinsically weak, and therefore, longer acquisition times are necessary to record a significant level of counts, thus increasing the probability of a substantial drift to occur during the analysis. Furthermore, the

presence of a surface or an interface could induce segregation, making the assumption of homogeneity uncertain, unless verified. For the study of phase stability of NPs, it is thus paramount to assess the spatial resolution, establish the assumption of homogeneity (whenever possible) and evaluate the uncertainty of any measurement recorded from a nanostructure.

In this Chapter, we develop some of the TEM analytical tools adapted specifically to the analysis of NPs and use them throughout the body of this work. We propose to combine various types of signals from a NP and take advantage of an axis of symmetry, if present, to enhance the quality and the interpretability of a spatially resolved quantitative signal.

The proposed post-processing techniques are first explained and subsequently tested on NPs of known structure. We start with a brief review of image formation in a TEM and the related analytical techniques, namely EELS and EDXS. Some statistical tools used to analyze low-counts EDX spectra are then discussed. We next show how to generate quantitative EDX maps and introduce a method to increase their interpretability. Lastly, we present techniques to find the radial composition of a spherical NP given its projection.

4.2 TEM Basics

Electron sources for modern TEMs can either be a LaB_6 cathode or a field-emission gun, the latter being brighter and more coherent. The electrons are then accelerated in the order of hundreds of kV and travel through successive sets of deflector coils, apertures and magnetic lens, which control the final electron beam characteristics, such as the convergence angle, probe size and current. When working in conventional TEM (CTEM), the lens system is set to generate an electron beam having a parallel illumination with respect to the specimen (Fig. 4.1(a)). The electron beam scatters through the thin specimen and exits with a wave function that is modified by the inner potential of the specimen and its thickness. The multiple diffracted or scattered electrons composing the exit wave function, then run through the objective lens and are converged to a back focal plane, situated below the specimen. The intermediate and projector lens can then be set to either magnify the diffraction pattern formed in the back focal plane (i.e. to obtain the diffraction pattern) or the image in the object plane. If the back focal plane is chosen for viewing, the region of interest contributing to the diffraction pattern can be isolated by using the selected area aperture (Fig. 4.1(a), left). Alternatively, an objective aperture placed in the back focal plane can be used to select the transmitted and/or diffracted beams that will contribute to the image (Fig. 4.1(a), right). In conventional TEM, contrast will therefore be a function of the specimen properties (i.e., density and thickness), and the diffraction effects, set by the crystal symmetry, orientation with respect to the beam, presence of defects, etc.

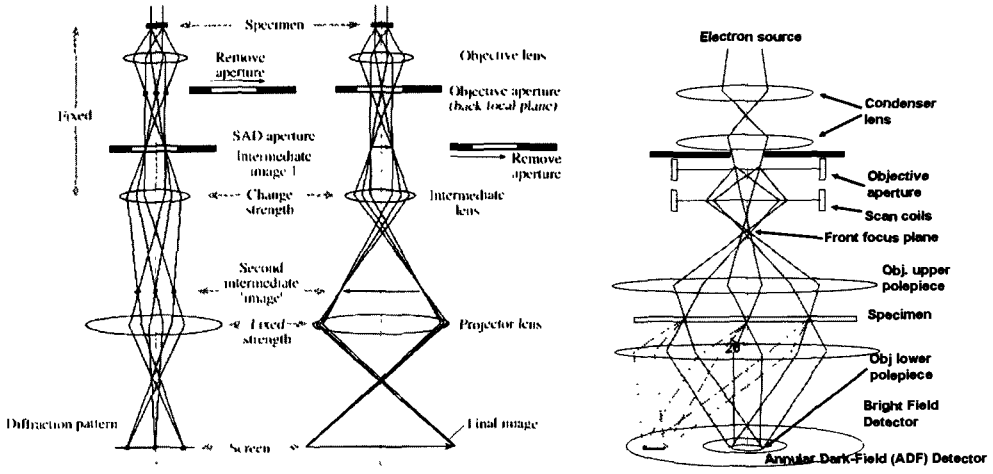

(a) (b)

FIG. 4.1: (a) Image formation in conventional TEM when forming a diffraction pattern (left), an image (right) (Williams and Carter 1996, p47). (b) Ray path showing the lens and detector configuration in HAADF-STEM mode (Courtesy of Ye Zhu).

Atomic resolution images are obtained in high-resolution (HR)TEM mode, by selecting a number of diffracted beams with the objective aperture and are allowed to interfere with the transmitted beam. In this condition, the objective lens can be set in the so-called Scherzer defocus, which allows the image to be directly interpretable (provided, once again, that the specimen is "thin"). Further combination of objective lens and defocus values can be used to extract information on the atomic structure using reconstruction techniques (Coene et al. 1996).

In scanning TEM (STEM) (Fig. 4.1(b)), the electron beam is converged to a small probe onto the specimen. The diffracted beams form discs in the back focal plane rather than sharp spots. These discs contain information on the crystal symmetry and also on the space group. Imaging these discs when the beam is still and centered provides a convergent beam electron diffraction (CBED) pattern. If the beam is scanned onto the specimen and the intensity of the transmitted beam is recorded as a function of its position, then the "bright field" signal is detected (BF-STEM). The diffraction contrast information is carried by electrons scattered at small angles ($\lesssim$10 mrad), while electrons are scattered incoherently at larger angles. By using an annular detector and by adjusting the camera length accordingly, an image can be formed using the intensity of the scattered electrons falling in a given angular range (ADF-STEM). At high angles (typically $\gtrsim$50 mrad), the contrast becomes nearly a strict function of mass and density. This technique is particularly suitable for imaging very small clusters of heavy elements ($Z \gtrsim 20$), provided that the clusters are supported by a thin and low Z film, such as amorphous carbon, alumina or silicon nitride.

4.3 Analytical TEM

Upon interaction with the specimen, electrons undergo elastic and inelastic scattering processes. The emission of characteristic X-rays is a typical inelastic process between fast electrons and matter. It occurs when a fast electron ionizes an inner shell electron and X-rays radiation are emitted upon transition of an electron from a higher energy shell to the electron hole. By measuring the number of emitted X-rays as a function of their energy (using a Si(Li) reverse-biased p-i-n diode detector) an energy dispersive X-ray spectrum is generated. The energy and relative intensity of the characteristic peaks constitutes the fingerprint of an element. If more than one element is present, the intensity ratio of the peaks provides quantitative information on the relative amount of the elements. The analysis of a standard of known composition in the same acquisition conditions as the specimen is required for precise measurements (Cliff and Lorimer 1975).

The processes by which electrons can lose energy via the interaction with the specimen can typically be categorized in two classes (Fig. 4.2):

- Plasmon generation occurs when a small fraction of the electrons energy is transmitted to collective electron oscillations, therefore creating a series of structures at low loss energies;
- Ejection of core-shell electron to the unoccupied density of states, therefore creating an edge at a set of energies typical of the element.

The edge shape bears the signature of the electronic structure, since it probes the unoccupied density of states. The post-edge spectrum details are referred to as energy-loss near-edge structure (ELNES). Small oscillations of the spectra occurring at energies ~50 eV greater than the edge are due to local diffraction effects caused by the neighboring atoms and are referred to as extended energy-loss fine structure (EXELFS).

By integrating the edges of the different elements present in the structure, the relative amount of each element can be extracted (as in EDXS, precise work requires a standard). The edge intensity extraction is somewhat more complicated than for the EDX spectra:

- The background must first be extracted using a power-law model of the type AE^{-r}, with E being the energy loss, A and r being constants;
- Plasmon losses for "thick" samples must be deconvoluted from the edge;
- To perform quantitative analysis, the EELS spectra of a standard of known composition must be obtained in the same operating (convergence and collection angles) and processing (background subtraction procedure, slit width) conditions as the unknown;

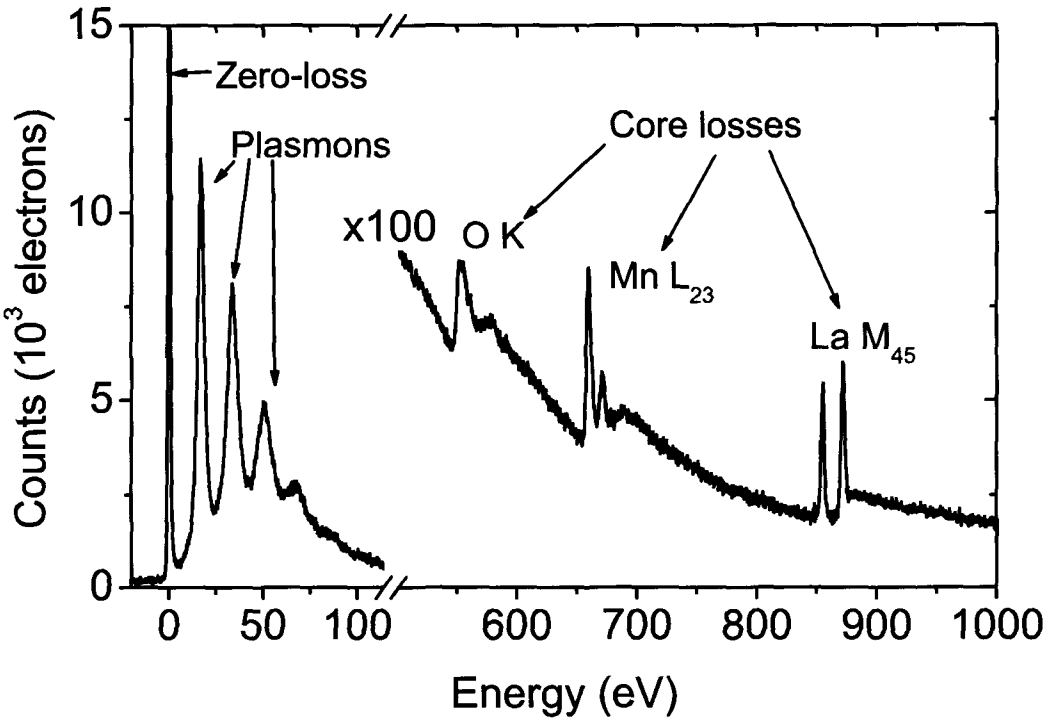

FIG. 4.2: Montage of spectra recorded from the low-loss of Si, and from the core-losses of $La_xSr_{1-x})MnO_3$, (specimen courtesy of B. Martin). The low-loss spectrum is dominated by an intense zero-loss peak followed by plasmon oscillations. The weaker, core-loss signal modulates the exponential background with features associated to the unoccupied density of states of the elements and are referred to as "edges".

- Thickness, orientation, valency of the elements under investigation, amongst other specimen characteristics, have all been shown to introduce a bias in the quantification (Egerton 1996). The strategy to avoid their effect is either to make the reference as close as possible to the specimen, set up the instrument and the processing parameters in a configuration that minimizes their impact or apply the appropriate post-processing corrections.

Provided that the specimen can be made thin, EELS is generally the method of choice for the analysis of light elements and many transition metals, rare-earth elements and oxides. For all other elements, including semi-conductors and noble metals, EDXS would generally be preferred (depending on the exact nature of the work to be carried out) as their EELS edge is not sharp. In practice there is much overlap and combining both methods allows one to extract complementary signals (Leapman and Hunt 1991).

4.4 Specimen Preparation

Novel TEM-related techniques adapted to NPs will be discussed in the next Section. These techniques are tested for EDXS and EELS using Au@Pt and Co@CoO NPs, respectively since they can be considered as NPs of known composition and structure. In this Section, we describe the steps involved in the preparation of these nanostructures and briefly discuss specimen preparation techniques.

One of the most popular method to synthesize Au NPs in aqueous solution is the technique developed by Frens (1973). The procedure consists of adding the reducing agent, (9 mL of trisodium citrate 1 % wt.) preheated to 80 °C to 300 mL of boiling chloroauric acid (10^{-2} % wt.). Seconds after, the solution becomes purple (formation of Au clusters) and evolves within ~30 min to a bright red solution (growth of the Au clusters). The size of the NPs is governed by the nucleation rate, and can be controlled within a limited size range (from ~12 nm to ~150 nm) by varying the amount and concentration of citrate. Fig. 4.3(a) shows a TEM micrograph of Au NPs having a narrow size distribution centered, at about 16 nm. Note that the NPs are prevented from coalescence by electrostatic interaction of ionic species at the NPs surface. When the solution dries on a TEM grid, for instance, the NPs will sinter* with neighbors.

To coat the NPs with Pt, we follow the procedure developed by Schmid et al. (1991), adapted to Au@Pt by Lu et al. (2004). 9.6 mL of the Au NPs solution is mixed with 10 mL of chloroplatinic acid (4.8×10^{-4} % wt.) and 1.5 mL of ascorbic acid (1.76 %wt.) in an ice bath. Following a reaction time of 90 min, Pt clusters precipitate and form a layer around the Au NPs, acting as nucleation sites. The thickness of the layer can be controlled by the amount of chloroplatinic solution added.

Fig. 4.3(b) shows a TEM micrograph of Au@Pt NPs having a diameter between ~19 and ~21 nm. The shell thickness is thus estimated to ~1.8-2 nm. From the ratio of the volumes of the core and the shell, the average Pt composition is estimated to ~45-50% at. Pt, which is confirmed by EDXS measurements performed over NPs-dense areas.

Co NPs were prepared by S. Behal, from the Chemistry Department of McMaster University following the procedure developed by Puntes et al. (2001). Typically, $Co_2(CO)_8$ is reduced with *o*-dichlorobenzene in the presence of oleic acid and trioctylphosphine oxide (TOPO) at 182 °C for 30 minutes. This results in the synthesis of Co NPs having a diameter (standard deviation) of 18(3) nm (Fig. 4.4(a)). According to Puntes et al. (2001), TEM, EELS and EDX measurements have shown that the Co NPs adopt the ϵ phase and are free of defects or oxides. It can be shown however, that some Co NPs nevertheless exhibit a thin 1.5-2 nm CoO (rock salt) shell (Braidy et al. 2007). For the discussions in Section 4.6.3, it will suffice to show a TEM micrograph (Fig. 4.4(a)) and corresponding EFTEM composite image

*A neck is often observed between two adjacent Au NPs, suggesting the occurrence of room-temperature sintering.

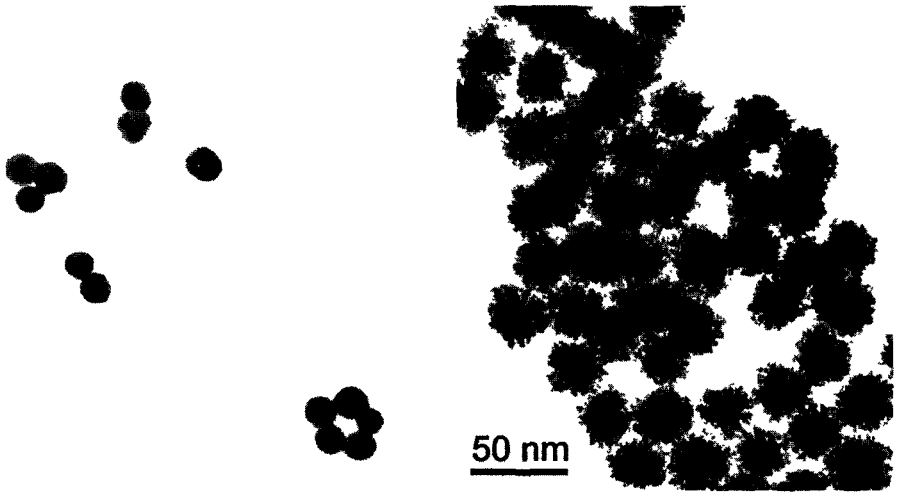

FIG. 4.3: (a)15–17 nm diameter Au NPs prepared by the Frens (1973) method. NPs naturally sinter when the solution dries. (b) A 2–5 nm-thick layer composed of 1–3 nm clusters surrounds the Au NPs after reduction of the chloroplatinic acid.

TABLE 4.1: Energy-filtered transmission electron microscopy acquisition parameters for C, O and Co maps (shown in Fig. 4.4(b)).

	C	O	Co
Pre-edge 1 (eV)	251–266	482–502	724–744
Pre-edge 2 (eV)	268–283	507–527	749–749
Post-edge (eV)	284–299	522–552	779–799
slit width (eV)	15	20	20
Acquisition time (s)	15	2×40^{a}	40

[a]Sum of two cross-correlated energy-filtered images to reduce drift.

(Fig. 4.4(b) acquired with the parameters listed in Table 4.1, Co(blue), C(green) and O(red)) where a 1.5-2 nm oxide shell is evident.

Two types of TEM grids were typically used in the body of this work: conventional TEM mesh grids and silicon nitride membranes. A conventional TEM grid consists of an amorphous carbon thin film supported by a Ni, Ti or Mo 200 mesh grid. The TEM grids were purchased with and without an a-C thin film from SPI Supplies. The following procedure was used to coat the grids with a thin (10–30 nm) film of a-C:

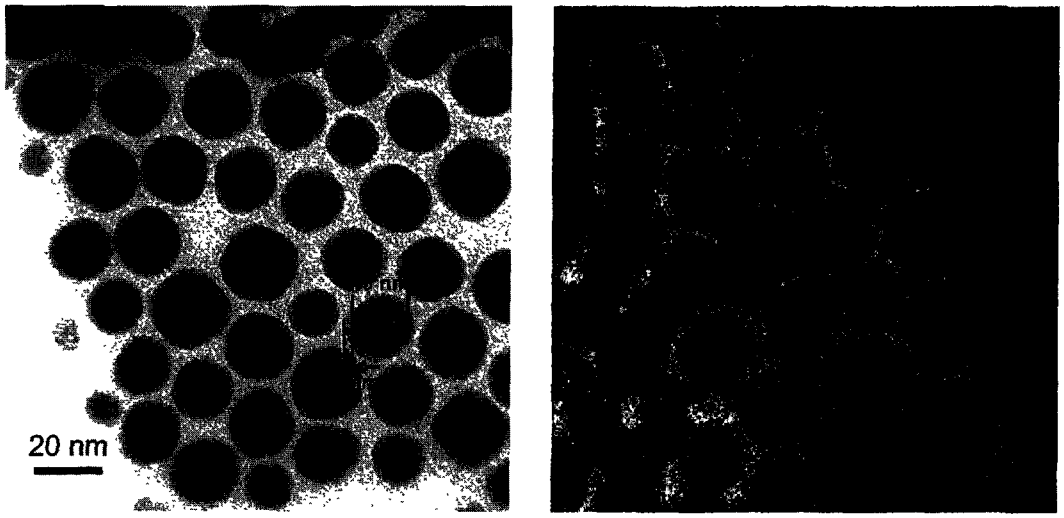

(a) (b)

FIG. 4.4: (a) TEM bright-field image of Co NPs exhibiting an oxide over-layer. (b) Composite image constructed with Co (blue), C (green) and O (red) elemental maps acquired by EFTEM using the 3 windows method with the parameters listed in Table 4.1 (different area than (a)).

1. A clean glass slide is dipped and slowly pulled out of a Formvar solution (3–5% wt 1,2 dichloroetyane) (SPI Supplies) and left to dry in a dust-free environment;

2. The edges of the coated glass slide are then scored with a razor blade knife;

3. The film is then floated on distilled and deionized water by carefully and slowly dipping the slide into the water at a grazing angle, while avoiding cracking of the film;

4. An array of previously ultrasonic cleaned Ni, Mo or Ti TEM grids is carefully placed upsidedown on the floating Formvar film. The grids and the film are then transferred out of the water all at once using a large piece of wax paper. This is done by laying the wax paper on top of the floating grids to which they will adhere and then slowly "peeling" the wax paper off the water and out of the dish;

5. The grids are now sandwiched between wax paper and the thin Formvar film. Using a sharp scriber or tweezer, the grids are then released by poking the film around the grid;

6. Ten to 30 nm-thick a-C thin film is then sputtered onto Formvar-coated grids using a carbon arc-evaporator;

7. The grids are then transferred into a petri dish where a filter paper soaked with 1,2–dichloroetyane is placed on the bottom plate. The vapor dissolves the Formvar, leaving only a thin a-C film supported by the mesh.

A drop of a NP suspension was then left to dry on the grid. Once on the grid, a large fraction of the drop was blotted away using the edge of a piece of filter paper, to avoid aggregation or coalescence while drying. The concentration and amount were chosen to ensure that NPs were well separated from each other.

The silicon nitride membranes are fabricated by depositing 30-50 nm-thick silicon nitride on monocrystalline silicon. The silicon nitride window is then exposed by etching the back of the silicon. These were purchased from SPI Supplies (catalogue number 4124SN-BA).

4.5 Spatial Resolution of Analytical Techniques

The spatial resolution of EDX maps is limited by the probe size and the electron beam broadening within the specimen. The probe size is determined by the probe forming lens and is a function of the electron beam brightness, current, spherical aberration and convergence angle. Scattering within the specimen will broaden the distribution of electrons. This broadening, b_s (cm), can be empirically estimated for various conditions using (Goldstein et al. 1977):

$$b_s = 721 \frac{Z}{E_0} \sqrt{\frac{\rho}{A} t^3}, \tag{4.1}$$

where Z is the atomic number, E_0, the electron energy (keV), ρ, the density (g/cm^3), A, the molar mass (g/mol) and t, the thickness (cm). A 200 keV electron beam will broaden to 2.5 nm at the exit of a 20 nm-thick Au foil. The size of an electron beam is commonly taken as the diameter containing 50% of the electron, d_{50}. The total resolution is the quadratic sum of the intrinsic probe size and the broadening. For a 0.7 nm probe, adding the broadening in quadrature results into a 2.6 nm resolution. Michael and Williams (1987) found Eq. 4.1 to overestimate the true broadening and rather proposed

$$d_{50}^{\mathrm{EDXS}} = \frac{d_{50} + \sqrt{d_{50}^2 + b_s^2}}{2\sqrt{2}}. \tag{4.2}$$

For the same conditions, the resolution of a 200 keV electron probe on a 20 nm-thick foil would rather be ~1.2 nm, according to Eq. 4.2.

EDXS, high-resolution transmission electron microscopy (HRTEM) and annular dark field (ADF) observations were carried with a JEOL 2010F field emission electron microscope operated at 200 kV and equipped with a Si(Li) Ultrathin polymer

(Moxtek™ AP3.3, active area: 30 mm^2 solid angle: 0.114 sr) window energy dispersive detector (Oxford Instruments). The spectrum or maps were acquired with INCA (Oxford Instrument) using the highest energy resolution (time constant set to 6). The SiteLock™ was enabled at all time, allowing a drift correction algorithm (based on images cross-correlation) to be applied every 10 s. EDX maps with drift in excess of 1Å/s were discarded. This precaution ensures that the contribution of drift to the spatial resolution degradation is at most 1 nm.

Electron beam broadening does not affect the spatial resolution of EFTEM in the same way as EDXS. The estimation of the spatial resolution of EFTEM includes the contributions of *(i)* spherical and *(ii)* chromatic aberration, *(iii)* diffraction and *(iv)* delocalization. Their individual contribution to the final resolution can be understood with the concept of the point spread function (PSF), (Egerton 1996; Egerton and Crozier 1997). A point spread function describes mathematically the radial distribution of the broadening of a point source, often unjustly simplified as a Gaussian. For each of the contributions listed above, there exist a corresponding PSF from which a diameter including 50% of the electrons can be defined.

Adding these terms in quadrature yields an estimate of the final resolution, given a set of operating parameters. These estimates were computed with EFTEM Assistant v1.1 (Lozano-Perez and Titchmarsh 2007), a free add-on to Digital Micrograph™ downloadable from the DM Script Database from the Graz University of Technology (Mitchell and Schaffer 2005). The "Egerton thin film" option was selected to generate the PSFs of the various sources of image blurring (spherical and chromatic aberrations, diffraction and delocalization) based on the formulation of Egerton and Crozier (1997), for a thin specimen. Given the parameters of operation listed in Table 4.1 and in this Section, the spatial resolution of an O K and Co L_{23} EFTEM maps were both theoretically evaluated to ~0.4 nm.

Realistically, the spatial resolution of Fig. 4.4(b) should also include the pixel size, drift and the consequence of having a low signal level. It should be mentioned that the pixel size alone in Fig. 4.4(b) is almost twice as large as the total resolution limit computed in Table 4.1. In this case, the limiting resolution factor was drift and electron beam damage, as the oxide surrounding the Co NPs would disintegrate *via* radiolysis[†] following approximately 5 min exposure to an electron beam of 10 nA roughly converged to a 150 nm diameter probe (current density estimated to ~60 A/cm^2). In Chapter 5 we discuss the delicate compromise between acquisition of sufficient signal and electron beam damage and its consequence on the analysis limits. Alter-

[†]Radiolysis of metal oxides occurs by a Knotek-Feibelman mechanism (Knotek and Feibelman 1978): a core-hole in a metal atom is first created and decays using the electron(s) from a neighboring O atom at the surface (interatomic Auger) which then becomes neutral and desorbs from the surface. This process is often referred to as "Electron-Stimulated Desorption", (ESD) or "Damage-Induced Electronic Transition", (DIET). Prolonged exposure at high current density induces amorphization and pitting of the oxide. Furthermore, the oxide is found to reduce to its monoxide and, in extreme cases, leads to the formation of the base metal (McCartney et al. 1991). In our case, the strategy was thus to acquire the O map first, before damage occurred to the oxide shell.

natively, Egerton (1999) evaluated the spatial resolution limits on the interpretable signal image given a damage cross section and a signal-to-noise threshold.

4.6 Novel Post-Processing Methods

4.6.1 Statistical Analysis There exists two common methods to extract quantitative information from an EDX spectrum given a set of sensitivity factors. In the first method, hereafter referred to as the "Gaussian method", the concentration ratio of element A to B, C_A/C_B, is given by the ratio of the area of the background-subtracted peaks, I_A/I_B, times a previously determined sensitivity factor k_{AB} (Cliff and Lorimer 1975):

$$C_A/C_B = k_{AB} I_A/I_B \tag{4.3a}$$

$$C_A = k_{AB} I_A/(k_{AB} I_A + I_B). \tag{4.3b}$$

Eq. 4.3b is simply deduced for binary systems where $C_B = 1 - C_A$. The magnitude of the background under the peak of interest can be extrapolated from neighboring channels. Since the X-ray emission probability follows a Poissonian distribution, the standard deviation of an EDX peak is simply equal to the square root of its intensity. The error on the concentration ratio can be computed by standard propagation error techniques. It is easy to demonstrate, when the uncertainty on k_{AB} is negligible, that the standard deviation of the concentration ratio, σ_{C_A/C_B} is

$$\sigma_{C_A/C_B} = C_A/C_B \sqrt{I_A^{-1} + I_B^{-1}}, \tag{4.4}$$

In the second method, hereafter referred to as the "Top Hat method", a numerical filter (a kernel with the shape of a hat) is first applied to the *whole* spectrum, S. This acts as a numerical second derivative and removes the background. The transformed spectrum, S', is then fitted against references, $S'_A, S'_B, \ldots$ acquired or simulated using similar experimental conditions and processing:

$$S' = I_A S'_A + I_B S'_B + \ldots \tag{4.5}$$

The coefficients, $I_A, I_B, \ldots$ can be determined using multiple linear least-squares fitting. The concentration ratio is then deduced using Eq. 4.3. The top hat filter and the fitting procedure will both contribute to the error, which can be computed by following an approach proposed by Statham (1977).

The Gaussian method can only be used when the shape of the EDXS signal is indeed a gaussian and therefore fails for peak bundles. The Top Hat approach can be

employed to any peak shape and is the method of choice in commercially-available softwares. If the EDXS signature of an element exhibits several strong peaks, then it is beneficial to use the Top Hat technique to compute the concentration ratio. However, for low-counts spectrum where the secondary peaks of an element are very weak, then it is best to apply the Gaussian method only to the strongest peaks to deduce C_A/C_B. In this case, the main advantage of the Gaussian method lies in its simplicity and fewer number of operations, which generally leads to a better precision, especially for low-counts spectra.

The EDX spectra of Au and Pt will often be encountered in the body of this work. There are many advantages to perform a gaussian fit over the Au and Pt L_α peaks rather than simply integrating the counts over an given energy range. First and foremost, it avoids the self-interference of the peaks due to partial overlap of the Au and Pt L_α lines by separating their individual contributions. Fitting a Gaussian also reduces the variability associated with noise in the same way multivariate statistical analysis would, and hence, provides better estimates of the true intensity (area) of a peak. Finally, as we will describe in the next few paragraphs, many useful parameters, such as the detectability limit and the measurement uncertainty, can be readily deduced from gaussian statistics.

The elemental quantities in the body of this work are not always expressed as ratios but often in terms of atomic fractions, so that Eq. 4.4 no longer holds. Using standard error propagation, it can be shown that the standard deviation of the elemental fraction, C_A, can be written as:

$$\sigma_{C_A} = C_A \sqrt{\frac{I_B}{I_A} \frac{(I_A + I_B)}{(k_{AB} I_A + I_B)^2}}, \tag{4.6}$$

where I_A and I_B are the background-subtracted integrated areas of the gaussians associated to the element A and B, respectively. The total integrated intensity of a gaussian, having a known full-width at half maximum (FWHM) and amplitude, H is calculated in the following manner:

$$I_i = \sqrt{\frac{\pi}{4\ln(2)}} \mathrm{FWHM}_i H_i, \quad i = A, B. \tag{4.7}$$

Each peak must also satisfy the detectability criteria:

$$I_i > C_L \sqrt{2 I_b} \quad i = A, B, \tag{4.8}$$

where C_L is the confidence level ($C_L = 1, 2 \ldots$ corresponds to a $1\sigma, 2\sigma \ldots$ confidence level), I_b is the background under the peak, defined over a given energy range, w. It is possible to demonstrate (García and Puimedín 2004) that the optimal range for inte-

gration of a Gaussian peak is equal to ~1.189FWHM. Consequently, the background intensity corresponding to an EDXS peak is:

$$I_i^b = C_L \frac{\sqrt{2I_b\, 1.189\ \mathrm{FWHM}_i}}{w} \quad i = A, B. \tag{4.9}$$

The corresponding area of a Gaussian integrated over this range becomes:

$$I_i' = I_i \,\mathrm{erf}(1.189\sqrt{\ln 2}) \quad i = A, B, \tag{4.10}$$

and the condition of visibility is expressed as:

$$I_i' > I_i^b \quad i = A, B. \tag{4.11}$$

If either I_A (or I_B) is identified as undetected, then C_A is set to 0 (1) with an upper (lower) confidence interval computed by substituting I_A (I_B) with I_A^b (I_B^b). The data in this thesis will be expressed as an elemental fraction of A with an error bar corresponding to $\pm C_L \sigma_{C_A}$, where C_L is generally set to 2 (95% confidence level), unless otherwise stated. A last remark on the validity of Eq. 4.6: for very low values of either I_A or I_B, the error bar can extend above unity or into negative concentrations. In such circumstances, the confidence interval is clipped to values contained between 0 and 1 and the data point becomes flagged.

4.6.2 Novel Functions for EDX Quantitative Mapping In most EDXS commercial softwares, an EDX map consists of a sequence of images, each corresponding to the spatial distribution of an element within a given region of interest. The software defines an energy window corresponding to a characteristic X-ray peak. The intensity of the pixel on the elemental map is set to the number of characteristic X-rays detected in this energy range. These maps are at most qualitative since the background is not subtracted. Furthermore, peak overlap, if present, will prevent any attempt of forming a truly quantitative map.

With improvement of electron sources and detector systems, it has been shown that, given sufficient counts per pixel, a quantitative map can be generated (Williams et al. 2002, for instance). The post-processing methods are not yet available in commercial softwares but their algorithm follow the same axioms (namely, background subtraction, peak extraction, fitting, error estimation). Nevertheless, the main limitation remains the low level of counts. If a dedicated system is not available (e.g. dual detector, dedicated STEM, etc.), one must rely on post-processing techniques to improve the counting statistics.

"Binning" (e.g. adding the information of neighboring pixels), is a method used to improve the chemical resolution of a concentration map by sacrificing spatial resolution. Alternatively, whenever the symmetry of the object allows, projection along

an axis of symmetry should rather be carried out. The challenge lies in improving the chemical resolution to a point where meaningful quantitative information can be extracted, while conveying significant spatially-resolved elemental information.

The projection of an EDX map carried out with a commercial softwares is usually done along an orthogonal axis. If the symmetry of the object is of radial nature, the result of a projection convolves the data and complicates its analysis (the mathematical description of such a projection is the object of the next Section). In this Section, we describe two new and simple methods specifically designed for NPs. The first method proposes to apply an angular projection to express the data as a radial profile, which is especially useful for nano-objects having a spherical symmetry. The second method allows the intensity of a STEM image acquired in parallel to an X-ray map or profile to act as a mask and helps determine the edge of a nanoobject, often ill-behaved following the operation involving low counts pixels.

The various steps involved in the generation of a concentration map or radial profile from a raw spectrum image are explained in the flow chart of Fig. 4.5. The flow chart starts with a representation of an X-ray map acquired over an 18 nm diameter Au@Pt NP. The first step involves increasing the signal-to-noise level in each pixel. This is done either by binning (left) or projecting the data along an axis of symmetry (right). Because of the spherical symmetry of the Au@Pt NP, the 3D data cube can be collapsed using an angular projection. The resulting "image" is a stack of EDXS spectra having the displayed intensity set to the number of X-rays acquired per energy channel (abscissa). The radius appears on the ordinate, making the top spectra correspond to the central pixel and the bottom one to the sum of the pixels along the outer edge of the NP.

A quick note on the color look-up tables used to display the color maps. The temperature scale used is inspired from the perceived color of a glowing object. Supposing a linear greyscale with black assigned to 0 and white to 100%, then a blue, green, red and yellow will correspond to 20, 40, 60 and 80% grey level, respectively. Similarly, royal blue, brown and orange correspond to a grey level of 25, 50 and 75%, respectively. Table 4.2 gives the exact functions used to generate the red, green and blue channels of a grey level image which display is set to "temperature", in DM.

Background-subtracted elemental maps and radial profiles (Fig. 4.5, second row) are generated by fitting a Gaussian on the Lα peaks of Au (red) and Pt (blue) and subtracting from them the corresponding normalized background (green). A Au concentration map or profile is then simply generated using Eq. 4.3b (Fig. 4.5, third row). To avoid negative counts resulting from the possibility of subtracting a background larger than the elemental intensity (this may occur for low-count pixels), negative counts in the background-subtracted maps were clipped to 0.

Many pixels in the background of the concentration map are undetermined: this results from the division of Au and Pt intensities that are both null. Moreover, some pixels in the background are ill-behaved (mostly white) due to the division operation

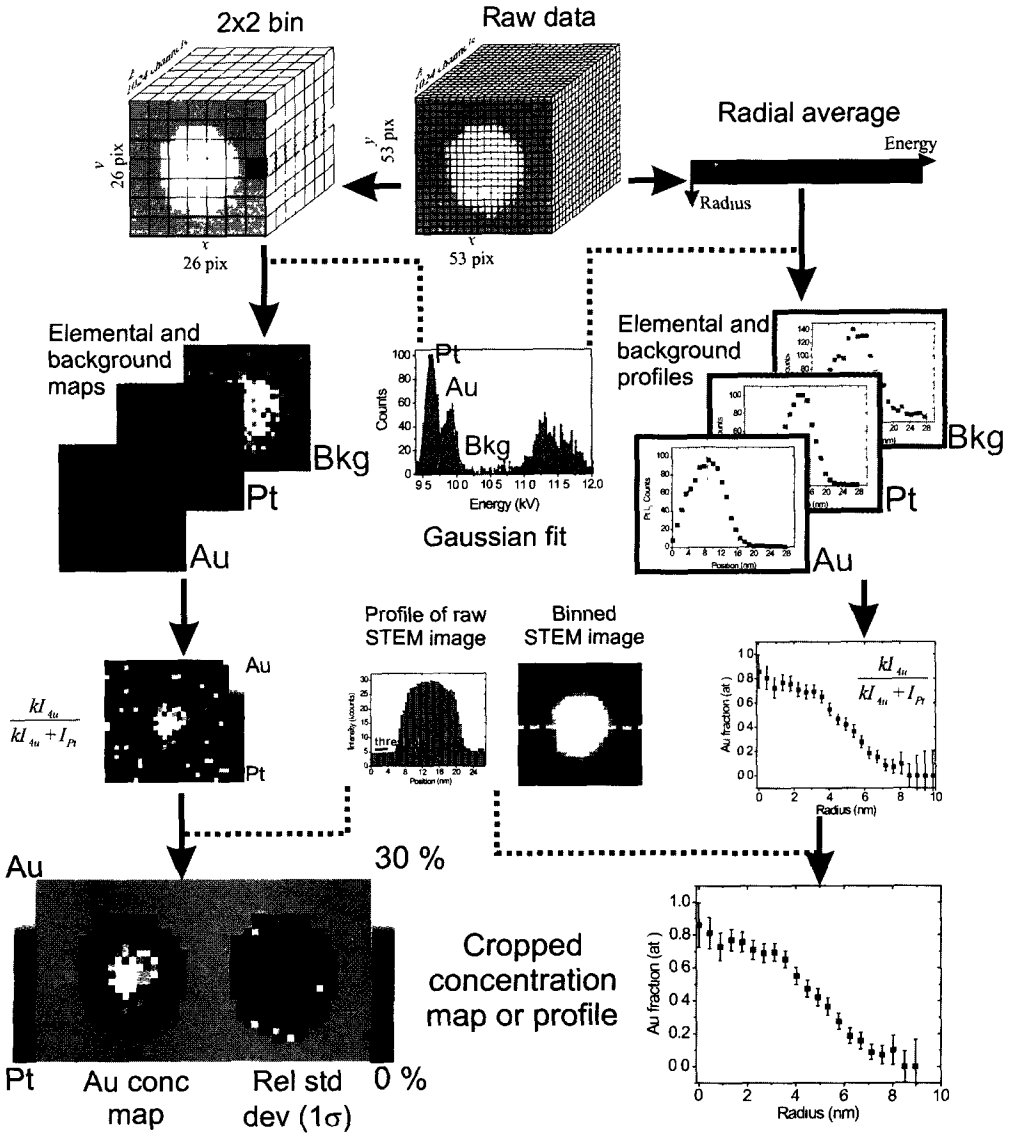

FIG. 4.5: Flow chart of the proposed method to construct a quantitative EDX map or profile. The data acquisition software outputs a data cube where each pixel contains the whole EDX spectrum. The dataset is either binned (left) or projected following an angular axis (right). Elemental maps or radial profiles of Au and Pt are generated by fitting Gaussians to the Au and Pt Lα peaks of each resampled pixel. A concentration map or profile of Au is computed with the background subtracted elemental maps of Au and Pt. The maps and corresponding 1σ relative standard deviation are displayed using a temperature scale while the profile appears in a graph where the error bars refer to the 2σ standard deviation of the Au fraction. The intensity of the STEM image acquired in parallel is used to define a mask that determines the background (grey shade) or crops the radial profile outside the NP boundary.

TABLE 4.2: Functions used for the temperature scale color-lookup tables used to display color maps (implemented as the "temperature" scale in the display options of Digital Micrograph™). Depending on the value of the normalized grey intensity, g, the red, green and blue channels are assigned a given function of x, where $x = \frac{g-a}{b-a}$, and a and b define a range of grey intensity.

$a \leq g < b$		**Red**	**Green**	**Blue**
0	0.2	0	0	x
0.2	0.4	0	$2/3x$	$1-x$
0.4	0.6	x	$2/3(1-x)$	0
0.6	0.8	1	x	0
0.8	1	1	1	x

performed on low-counts background pixels. As a result, the edge of the NP on the concentration map (third row, Fig. 4.5) is poorly defined. One way to distinguish the background from the NP is through statistical testing of the signal level. However, a technique to discriminate between the absence or the presence of signal has two main artifacts that can be understood in terms of Bayesian statistics: *(i)* a pixel on the edge of the particle is pure Pt (thus $C_{Au} = 0$) but the method flags it as being undetermined (false positive) or *(ii)* a pixel outside the particle does not contain any meaningful signal and the random noise was interpreted as a signal (false negative). The former will result in a badly defined edge while the latter will generate ill-behaved pixels in the background, both of which are characteristic of the raw composition map in the third row of Fig. 4.5. Clearly, a discriminant of a different nature is required to remedy the situation.

We propose to use the intensity of the STEM image acquired in parallel as a spatial filter to discriminate between the background and the NP, hence using an independent signal to fix the NP boundary. There are two requirements for this procedure to be carried out successively: *(i)* the sampling size and the position with respect to a given spatial reference of both the X-ray map and the STEM image should coincide; *(ii)* no clipping should occur in the STEM image (i.e. the intensity of the particle should not saturate and that of the background not be null).

The STEM micrograph in Fig. 4.5 (center of third row) was acquired with the X-ray map shown in the same figure. A STEM intensity profile generated along the grey dotted line (extracted from the raw STEM image) is then used to identify a signal threshold, in this case, 6500 electrons. Pixels in the X-ray map having a corresponding STEM intensity lower than the defined threshold are attributed a grey shade. The cropped composition map in Fig. 4.5 was generated using this approach. In comparison to the raw concentration map, the edge of the particle and the background are much better defined. The same method was also used to crop the radial profile from the data outside the average radius of the NP.

In addition to the cropped composition map, we have also computed (and cropped accordingly) the accompanying relative standard deviation map. The composition and *relative* standard deviation ($\sigma_{C_{Au}}/C_{Au} \times 100\%$) of a given pixel is read off the temperature scale provided with the color maps (bottom row, Fig. 4.5). The 2σ standard deviation was also computed for the radial profile and is set as the error bar. Both uncertainties were computed with Eq. 4.6. The relative standard deviation of the concentration map varies between 5% (center) and 20% (edge of the NP). This is to be expected from the fact that a stronger signal originates from the center of the particle than from the edge. Alternatively, the uncertainty of the radial profile increases towards the center as smaller number of pixels are being summed close to the NP origin.

Given the complexity of the procedure for generating a quantitative map, it was partly implemented in a script working with DM. The script is listed in Appendix C with detailed instructions. The script prompts the user for elemental maps, background map and a corresponding STEM image. The user then enters the computation parameters (FWHMs, STEM intensity threshold, confidence interval, k-factor, etc.) and outputs the concentration maps with corresponding upper and lower uncertainty. Other utility functions are listed in Appendix E which executes rotational averages and various operations on maps and linescans.

4.6.3 Radial Concentration Profile Reconstruction Any information provided by TEM-related techniques is intrinsically the result of an average performed along the electron path. Indeed, the materials properties are averaged along the thickness of the specimen by the transmitted electron beam. The information from the third dimension can be reconstructed using tomography, a technique pioneered a decade ago by (Frank 1992) to obtain structural information from protein complexes and recently adapted for materials science (Kubel et al. 2005, and references therein). Tomography is a technique by which a series of projections is first recorded over a large tilt range ($> \pm 55$ deg). The reconstruction algorithms are based on a numerical Radon transform, to retrieve the 3D information. Although tomography techniques have evolved rapidly, they are still not adapted to reconstruct the internal structure of a 20 nm diameter NP from an EDXS tilt series. There are various technological limitations for such a task to be performed. The main challenge takes origin in the strong anisotropy of the X-ray angular distribution. This prevents high tilts measurement from being performed and deprives the reconstruction from essential information. However, if a spherical symmetry can be assumed, such as for NPs, then theoretically, only one projection is sufficient to retrieve the radial profile of the NP.

In this Section, we first familiarize ourselves with the mathematical nomenclature involved when performing the projection of a function in a spherical environment. We then explore the applicability of some reconstruction algorithms to retrieve the

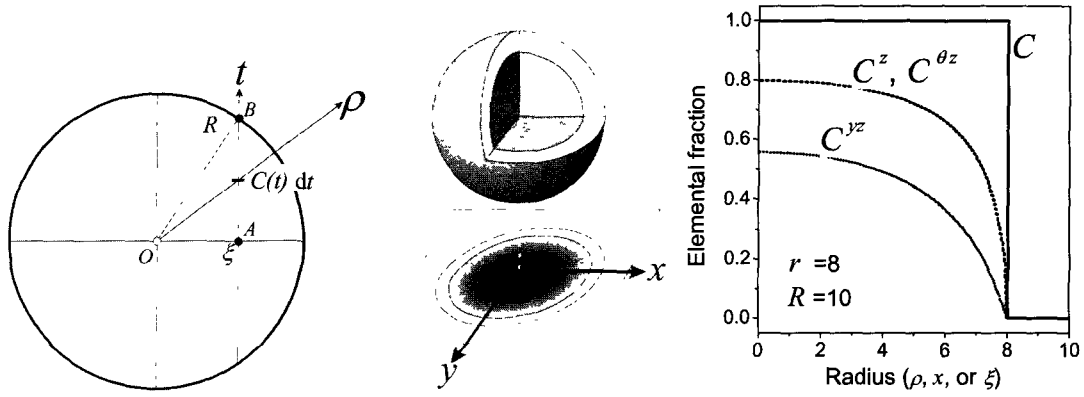

(a) (b) (c)

FIG. 4.6: (a) Circular slice of the NP with radius R and origin O. The electron probe path is indicated by the vertical axis t and intersects the circle at a point B and the circle abscissa at a point A, at a position ξ, away from the origin. The axis ρ is defined by the origin and an elemental slice along the thickness axis, $C(t)\mathrm{d}t$. (b) Illustration showing the projection of the composition of a core-shell sphere onto an xy plane. (c) C: radial composition of a composite sphere; C^z: composition profile following a projection along z axis, equivalent to its angular projection $C^{\theta z}$ (Eq. 4.17); C^{yz}: projection along y axis of C^z (Eq. 4.18).

radial concentration profile of a NP given its projection. These algorithms are then tested with EDXS and EELS datasets of NPs of known structure.

As it is common to all TEM imaging methods, the information in the spectrum image is already averaged along the thickness of the sphere. The circle in Fig. 4.6(a) represents the center slice of a sphere of radius R. Let the electron beam probe the NP along the thickness of this slice, parallel to the line AB at a position ξ, away from the center. The average composition, $C(\xi)$, at point ξ on the abscissa, can be computed by integrating $C(t)$, the composition, at a given thickness from A to B and dividing by the length between A and B, $\|AB\|$:

$$C(\xi) = \frac{1}{\|AB\|} \int_A^B C(t)\mathrm{d}t. \tag{4.12}$$

By trigonometry, $\|AB\| = \sqrt{R^2 - \xi^2}$ and by changing the integration bounds accordingly, the integral of Eq. 4.12 is rewritten as:

$$C(\xi) = \frac{1}{\sqrt{R^2 - \xi^2}} \int_0^{\sqrt{R^2-\xi^2}} C(t)\mathrm{d}t. \tag{4.13}$$

Introducing a change of variable, $t = \sqrt{R^2 - \rho^2}$, the integral becomes:

$$C^z(\xi) = \frac{1}{\sqrt{R^2 - \xi^2}} \int_{\xi}^{R} \frac{\rho}{\sqrt{\rho^2 - \xi^2}} C(\rho) \mathrm{d}\rho. \tag{4.14}$$

$C^z(\xi)$ is now the projected concentration profile on a plane xy resulting from the averaging operation along the thickness z. The superscript z refers to a projection along the z axis. Here, we stress on the change of variable from $\rho \rightarrow \xi$, the former referring to an axis defined by the radius of the sphere and the latter to an axis defined by the radius of the *projected* sphere. Eq. 4.14 can be expressed in terms of an Abel transform, $\mathcal{A}$:

$$C^z(\xi) = \frac{\mathcal{A}\{C(\rho), \xi\}}{2\sqrt{R^2 - \xi^2}}, \tag{4.15}$$

where the operator $\mathcal{A}$ is defined as an integral transform of the type (Bracewell 1986, p262):

$$g(u) = \mathcal{A}\{f(t), u)\} = \int_{u}^{\infty} \frac{2t}{\sqrt{t^2 - u^2}} f(t) \mathrm{d}t, \tag{4.16}$$

where $f(t)$ is the function, t, the variable of integration, u, the new variable of the resulting function $g(u)$. In our case, the function is undefined beyond R, so that the upper integration bound of the Abel transform can always be substituted with the radius of the sphere, R.

Now, assume an object with a spherical symmetry having an outer radius R and a radial composition profile, $C(\rho)$. Fig. 4.6(b) shows, for example, a composite sphere having a pure A core and B shell. For the case of a composite sphere, $C(\rho)$ represents the radial fraction of A expressed as a step-like function (full line, Fig. 4.6(c)). Following this projection, the step function defining the composition profile of the composite sphere reduces to (dashed line, Fig. 4.6):

$$C^z(\xi) = \frac{\sqrt{r^2 - \xi^2}}{R^2 - \xi^2}, \tag{4.17}$$

where r is the radius of the inner core.

A common microscopy technique is to acquire a linescan across the central region of a NP. If the width of the linescan is too thick, the substructures, if present, will be further convolved. For the extreme case, when the thickness of the linescan is equal to the diameter of the NP, $C^{yz}(x)$ will have suffered the effect of two successive Abel transforms. If an orthogonal projection is applied again, for instance along the y direction, the final profile will be written as:

$$C^{yz}(x) = \frac{\mathcal{A}\{C^z(\xi), x\}}{2\sqrt{R^2 - x^2}}. \tag{4.18}$$

In this case, x is chosen as the variable of integration, since it is orthogonal to the axis of projection, selected as y.

Following two successive projections the resulting integral must be solved analytically and is plotted as the dotted line in Fig. 4.6. Following an *angular* projection, the concentration profile, $C^{\theta z}(\xi)$ is essentially the same as $C^{z}(\xi)$. In comparison to the orthogonal projection, it is therefore much easier to interpret the data resulting from an angular projection. From an experimental point of view, acquiring a linescan through the central region of the particle could avoid having to perform a radial average. However, this can only be done only if prior measurements confirms the spherical symmetry of the NP and secondly, the thickness of the linescan must be small with respect to the diameter of the object. When these conditions are not met, it is proposed to check these assumptions by performing the acquisition of the whole map.

It is possible to demonstrate that the inverse Abel Transform, $\mathcal{A}^{-1}$, can be written as (Bracewell 1986, p262-3):

$$f(t) = \mathcal{A}^{-1}\{g(u), t\} = \frac{-1}{\pi}\int_{t}^{\infty} \frac{g'(u)}{\sqrt{u^2 - t^2}} du. \tag{4.19}$$

Eq. 4.19 provides the means to deduce $C(\rho)$ given $C^{rz}(\xi)$, which is a useful but challenging problem:

$$C(\rho) = \mathcal{A}^{-1}\{2C(\xi)\sqrt{R^2 - \xi^2}, \rho\} \tag{4.20}$$

The main challenge lies in the application of the numerical inverse Abel transform to a set of data. Inspection of Eq. 4.19 reveals a discontinuity at the lower integration bound. In addition, integrating a numerical derivative is prone to noise amplification.

There has been a plethora of techniques developed in many areas of physics, namely optics (e.g. Montarou et al. 2006, and references therein) and plasma diagnostics (Park 1989; Kalal and Nugent 1988; Ha et al. 2004, for instance), astronomy (Bracewell 1956; Craig 1979) and geoplanetary science (Hajj and Romans 1998) to perform a *numerical* inverse Abel transform to retrieve the radial profile projection. Bracewell (1986, p262-6) have proposed a simple approach to perform an Inverse Abel transform while avoiding both the singularity and the use of a numerical derivative. Briefly, the author reduces the Abel transform to a convolution integral following a change of variables. The details of his clever demonstration will not be repeated here, but we will provide a simple and intuitively understandable description of the proposed method.

Let us consider one quadrant of a spherical particle subdivided into shells having the width corresponding to the sampling size of the map (Fig. 4.7). The radial profile (solid line) can be deduced recursively from the data of the projection (dotted line). The composition of the first shell (bold segment), C_1^r, is equal to that of the first bin, C_1^x. The composition of the second outermost shell (solid line at bin #2) can be

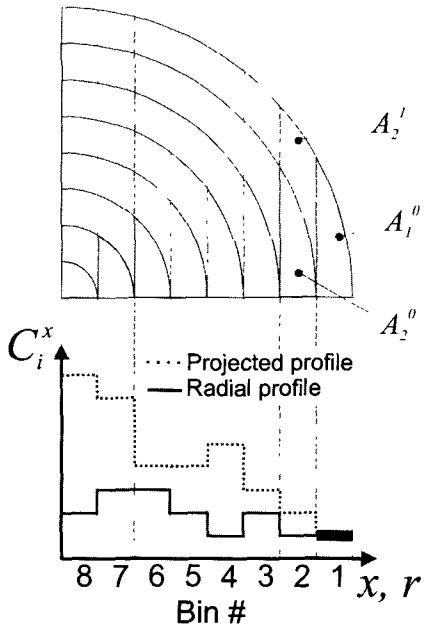

FIG. 4.7: Scheme explaining Bracewell's algorithm to perform a radial reconstruction from a projection. A quadrant of a sphere is first divided in layers corresponding to the sampling size (top panel). Given the projection (dotted broken line, bottom panel), one seeks the radial profile (full line). The radial composition of the first bin is equal to the projected one (bold line). The radial composition of the second bin is obtained by subtracting the contribution of the first one (whose composition is now known, C_1^r), normalized by a factor, A_2^1, related the thickness of the sphere at that position along the radius. The whole radial composition is retrieved by applying this method recursively (full details in the text).

found by removing the contribution of the outer shell and normalizing with a factor related to the electron beam path length, A_2^0:

$$C_2^r = \frac{C_2^x - \frac{A_2^1}{A_1^0} C_1^x}{A_2^0} = \frac{C_2^x - A_2^1 C_1^r}{A_2^0} \tag{4.21}$$

The values of the A's can be computed from simple geometry and stored in a lookup table, as they are independent of the profiles. One can retrieve the radial composition by recursively applying this method from the edge to the center of the particle:

$$C_i^r = \frac{C_i^x - \sum_{j=1}^{i-1} A_i^{i-j} C_j^r}{A_i^0} \tag{4.22}$$

The recursive nature of the method is responsible for the noise amplification as i increases from the edge to the center.

Another approach is to fit the data to one or several functions having an analytical solution when substituted into Eq. 4.20. Cubic splines are such functions and are conveniently used to fit to data. A computer code was developed by Beniaminy and Deutsch (1980), which first fits the data with a set of cubic splines where the number and the spacing of the knots have been optimized (Deutsch and Beniaminy 1982)[‡]. Since there exist an analytical solution to the integral of Eq. 4.20 when the integrand is a polynomial of the third degree, the Abel inversion is computed on each segment approximating the dataset. The programs outputs the reconstructed profile with a set of piecewise functions having the same set of knots as the fitted profile.

Here, we adapt and compare both Bracewell's and Beniaminy's treatment to retrieve the radial profile of a nanoparticle from EDXS and EELS measurements. For EDXS, Au@Pt NPs are used a benchmark while for EELS, Co NPs having a thin oxide layer will be used to test and compare both methods.

There exist two ways to reconstruct $C(\rho)$ from the projected data. The first one consists of applying the inverse Abel transform directly to $C^{\theta z}(\xi)$. The second method consists of applying the inverse Abel transform to the elemental profiles and then combining the individual reconstructions into a concentration profile. The latter method is preferred to the direct reconstruction from the profile of $C^{\theta z}(\xi)$ since this avoids the amplification of the noise introduced by the division operation.

Bracewell's algorithm for numerical Abel and inverse Abel Transforms were implemented in DM scripts which codes are listed in Appendix D. The FORTRAN 77 source code of Beniaminy can be downloaded from the Computer Physics Communications web site.

Radial reconstruction from EDXS maps

An EDX map was acquired from an 18 nm diameter Au@Pt NP having an overall composition of 49% Au (the same as in Fig. 4.5). From the size and the global composition, we deduce that the NP has a 14.4 nm diameter Au core and a 1.8 nm-thick Pt shell. Since the structure of the NP is known, it will be used as a benchmark to test Bracewell's and Beniaminy's reconstruction algorithms on a hypothetic and an experimental dataset.

Figure 4.8(a) shows the idealized Au and Pt intensity profiles expected from a 7.2 nm radius Au core surrounded by a 1.8 nm-thick Pt shell with the same number of data points as its experimental counterpart (Fig. 4.8(b)). Although the experimental profiles suffer from a diffuse interface and from an increasing noise towards the center, it reproduces the main features of its theoretical equivalent. Following the reconstruction of the idealized case (Fig. 4.8(c)), a "ringing artifact" is introduced at the interface which is apparent to the so-called Gibbs phenomenon encountered in

[‡]The portion of the code which optimizes the number of knots to fit a set of data is based on the program available in the Harwell Subroutine Library (see reference by Powell 1967).

numerical transforms[§]. These artifacts distort much more severely the spline-based profile (Beniaminy's) than the one generated using Bracewell's method. In contrast to the simulation, the reconstructed experimental profiles (Fig. 4.8(d)) do not exhibit such artifacts. These are likely overwhelmed by noise amplification, especially near the center, as the scatter in Bracewell's reconstruction suggests. Beniaminy's reconstruction method is much more insensitive to such scatter, as a smooth curve was obtained. Note that negative values in the experimental reconstructed profiles were clipped to 0.

The ringing artifacts in the reconstructed profiles persist through the computation (Eq. 4.3b) of the concentration profile (Fig. 4.8(e)). Bracewell's method reproduces the width of the interface of the simulated data with much more fidelity than Beniaminy's. Although the thickness of the Pt shell is retrieved, none of the reconstruction techniques show a sharp interface in the experimental dataset (Fig. 4.8(f)).

We can list two main contributions to the failure of the algorithm to retrieve a sharp interface from the experimental data. The dominant contribution stems from the slightly elongated aspect of the NP (refer to the Au concentration map in the bottom-right corner of Fig. 4.5). The spherical reconstruction of the projection of a composite *ovoid* will give similar result: namely the width of the shell could in principle be retrieved, but will render a "dull" interface. The other contribution is the rough aspect of the shell arising from the presence of the fine Pt clusters or faceted Au core. The angular projection will obviously suffer from these imperfect physical characteristics.

In Section 4.5, the expected spatial resolution of an EDX map of a 20 nm-thick Au foil was estimated to $\sim$1.2 nm. This sets an upper limit to the electron beam broadening. An average and more realistic estimate of the beam broadening present in a 20 nm diameter Au-Pt NP would be closer to 1 nm (average "thickness" of a sphere). If we add in quadrature the contribution of the drift (the maximum drift between two successive cross-correlations was kept below 1 nm), then the maximum (average) broadening due to acquisition and the instrumental contribution is estimated to 1.6 (1.4) nm. The sampling of the EDX map was performed at every 0.3 nm. Following a 2x2 binning, the sampling size is still well below the expected resolution and satisfies the oversampling criteria[¶].

[§]The Gibbs phenomenon occurs upon approximating a discontinuous function with a truncated sum of Fourier components. The artifact takes the shape of an overshoot accompanied by damped oscillation near the discontinuity. As the number of Fourier components increases, the oscillations weaken but the overshoot remains and asymptotically tends towards $\sim$1.18 times the height of the step. Here, we simply report the similarity between the numerical artifact observed following a numerical inverse Abel transform and the Gibbs phenomenon without attempting a formal demonstration. Note that English mathematician Henry Wilbraham (1825-1883) (Wilbraham 1848) observed and explained the phenomenon nearly 50 years before J. Willard Gibbs did, in 1889.

[¶]Given a probe size d, the minimum sampling –the distance between two successive measurements– should be smaller than $d/2$.

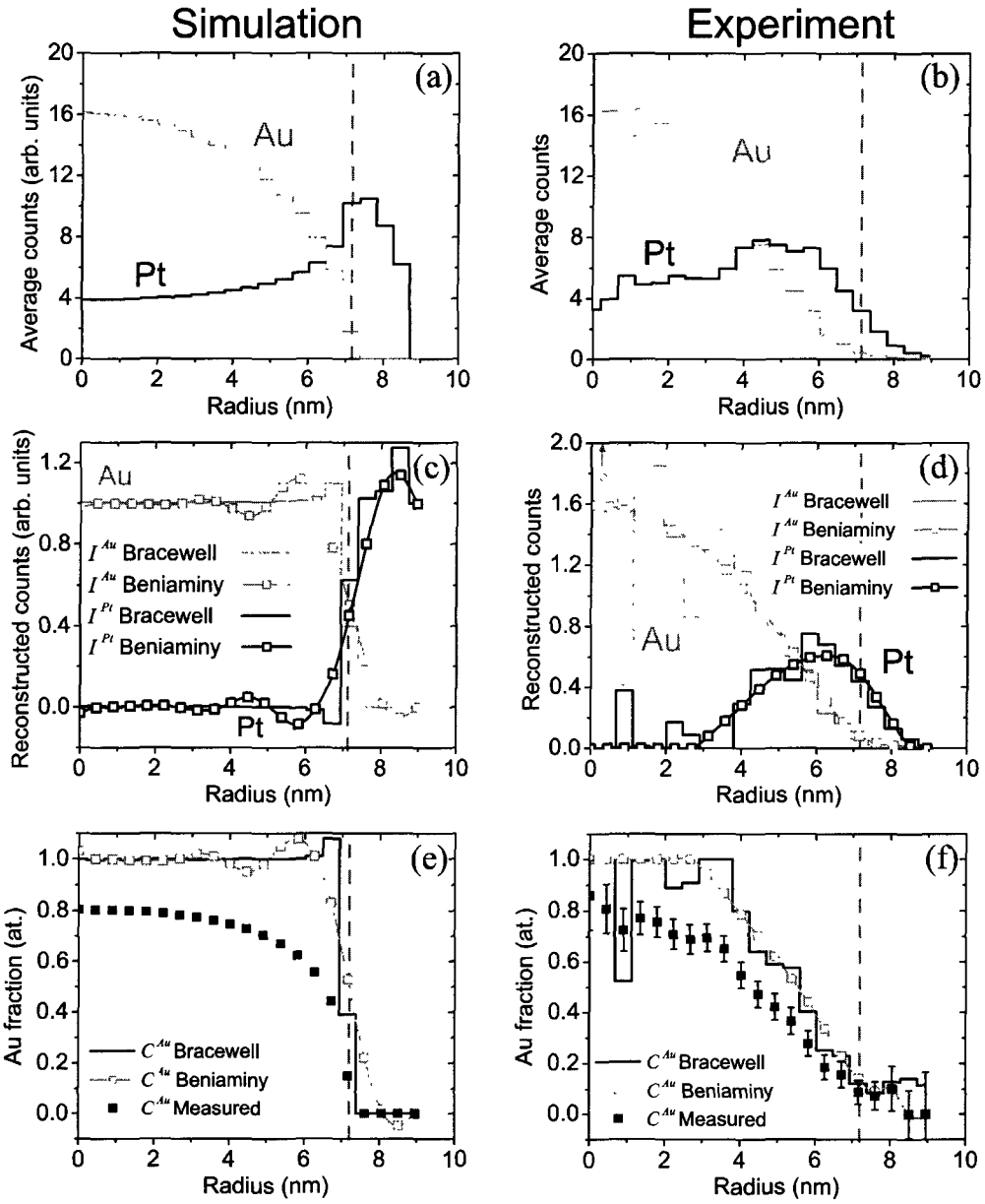

FIG. 4.8: Simulated (left panels) and experimental (right panels) data of the projected and reconstructed EDXS signal from a NP having an 14.4 nm diameter Au core and a 1.8 nm-thick Pt shell. The radial profiles are first generated using an angular projection of the simulated (a) and experimental (b) Au (grey line) and Pt (black line) background subtracted intensities. Reconstructed radial profiles of the Au (grey lines) and Pt (black lines) counts using the numerical-based approach developed by Bracewell (step line) and the splines-based method from Beniaminy (lines + squares) for the simulation (c) and the experimental (d) data. Simulated (e) and experimental (f) Au radial composition computed with the data generated in (c) and (d), respectively using Bracewell's (black, step line) and Beniaminy's (grey line + squares) reconstruction methods. The projected Au concentration profiles are also shown with their respective reconstruction. The vertical dashed grey line marks the position of the interface.

We can estimate the total spatial resolution of the radial reconstruction technique using the Au@Pt NPs as a benchmark. From the reconstruction of Fig. 4.8, the width of the reconstructed interface is about 3 nm. Assuming a resolution of 1.4 nm, the data processing and imperfection in the spherical symmetry would account for a ~2.7 nm broadening (if the contributions are added in quadrature).

Radial reconstruction from EFTEM measurements

The reconstruction methods can easily be extended to EELS spectrum images or EFTEM micrographs. We demonstrate this using the EFTEM images acquired over Co@CoO NPs with the acquisition parameters listed in Table 4.1. To increase the signal level, the O and Co maps of four ~ 23.4 nm diameter NPs were added. From the EFTEM image, we can estimate the shell width to ~1.8 nm and calculate the theoretical projection of the O and Co signal, plotted in Fig. 4.9(a) (the ratio of the partial cross sections of O to Co was artificially set to 3). Each of the experimental maps was radially averaged to generate the projected signal of O (dotted line) and Co (full line) (Fig. 4.9(b)). Note that O and Co are both present in the shell. Knowing that the shell has a Co:O 1:1 stoichiometry, the ratio of the partial cross sections of Co and O could be deduced from the data points on the edge of the NP.

The hypothetical (Fig. 4.9(c)) and experimental (Fig. 4.9(d)) O and Co radial profiles were reconstructed using the Beniaminy's (full line) and Bracewell's (dotted line) approaches. The same types of numerical artifacts as in the example of the Au@Pt appear in the reconstruction of the simulation, namely the overshoot at the interface. Again, we can recognize the better performance of Bracewell's algorithm for idealized dataset. In contrast to the case of Au@Pt , both reconstruction profiles reproduce well the Co core but fail to show a plateau of constant Co:O 1:1 composition at the edge of the NP.

It is clear from the figures given in Section 4.5 that the EFTEM resolution is not the limiting factor for the spatial resolution of the reconstruction technique. Given the higher spatial resolution for EFTEM, the width of the reconstructed interface is expected to be ~2.5 nm (estimated from Fig. 4.9(d)).

The sources of error in the reconstruction are summarized in Table 4.3. As discussed, the reconstruction procedure may fail because of an imperfect spherical symmetry. Conceptually, there exists an optimal size range where the performance of the reconstruction is maximized. Indeed, if the NP is too small, then insufficient signal may be the limiting factor in the reconstruction. If the NP is too large, then electron beam spreading and absorption (EDXS) or multiple scattering (EELS) will degrade the quality of the reconstruction.

When comparing both reconstruction methods, in the absence of noise, Bracewell's algorithm is more reliable than Beniaminy's, especially in the presence of a sharp discontinuity such as in a core-shell or onion-type configuration. Alternatively, Beniaminy's spline-based reconstruction is much better suited to avoid noise amplification problems. Note that if one can assume a composite sphere geometry, then the prob-

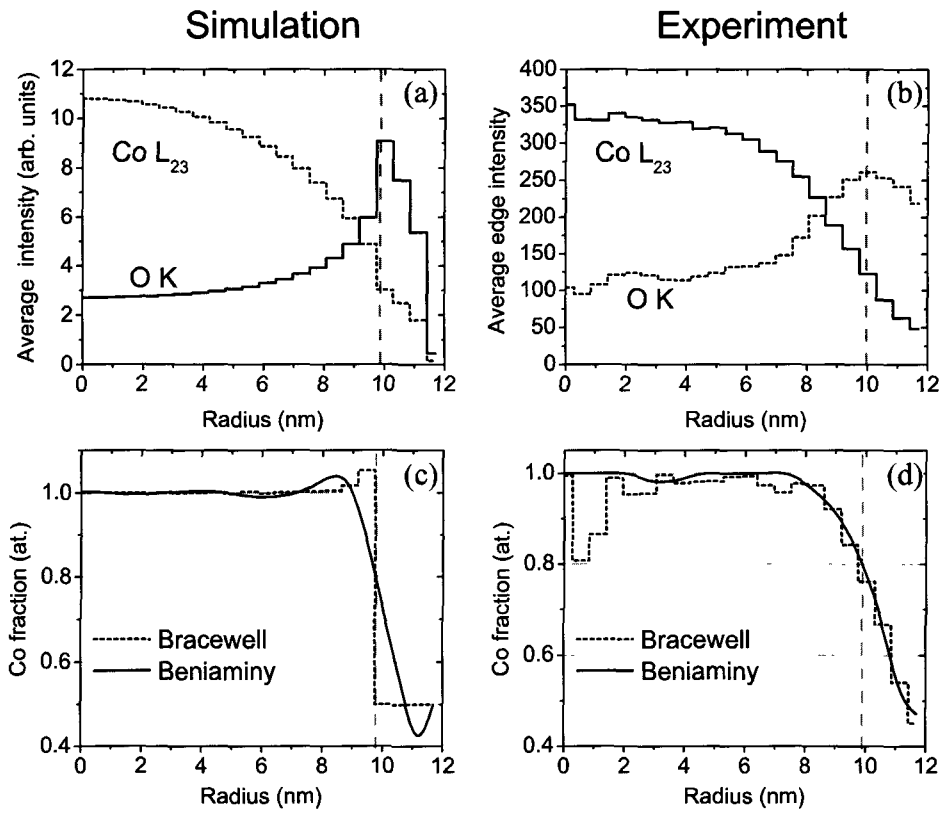

FIG. 4.9: Hypothetical (left panels) and experimental (right panels) data of the projected and reconstructed EELS signal from a NP having an 23.4 nm diameter Co core and an 1.8 nm-thick CoO shell. The radial profiles are first generated using an angular projection of the simulated (a) and experimental (b) Co L_{23} (solid line) and O K(dashed line) background subtracted edges intensities. Simulated (c) and experimental (d) Co radial composition using Bracewell's (dashed step line) and Beniaminy's (solid curve) reconstruction method. The vertical dashed grey line marks the position of the interface.

lem reduces considerably. Indeed, the only variables describing a composite geometry are the number of shells, their respective composition and thickness and the positions of the interfaces. Deutsch et al. (1989) devised a numerical procedure to perform such a task, which can be used on objects assuming a composite geometry. When such a configuration cannot be assumed, it is suggested that Beniaminy's method should be employed for the reconstruction of EDX or EELS data.

4.7 Conclusion

In this Chapter, we have described some of the analytical techniques employed to characterize nanostructures. Particular attention was given to deal with the in-

TABLE 4.3: Sources of error in the radial profile reconstruction from projected EDXS or EELS data.

Data processing	Data acquisition	Instrumental contribution
Poorly defined center	Drift during acquisition (lateral and depth)	Size of the probe
Imperfect particle roundness	Low signal-to-noise ratio	Electron beam broadening
Insufficient data points	Electron beam damage	Absorption (EDXS) or multiple scattering (EELS)
Sharp discontinuities		Delocalization (EELS)

trinsically weak analytical signal of NPs. Post-processing methods to improve the signal-to-noise level such as binning and projection along an axis of symmetry were introduced and compared with benchmarks specimen, namely, Au@Pt and Co@CoO NPs. The same NPs were also used to compare the performance of two reconstruction algorithms to retrieve the radial profiles from an EDXS and EELS projection. The performance of each reconstruction scheme depended mainly on the quality of the projected data. It was preferable to use Beniaminy's method with a noisy dataset, since the spline fitting step would avoid noise amplification. Alternatively, for a low-noise data, such as for simulated ones, Bracewell's algorithm was more efficient, as it would minimize the numerical artifacts. Finally, we have discussed the limits of the technique together with sources of errors affecting the spatial resolution. For the Au@Pt NPs, the imperfect NP spherical symmetry was the main factor degrading the spatial resolution of the technique. For the case of Co@CoO NPs, the limiting factors was rather specimen-related phenomena such as drift and electron-beam damage.

The concept of spatial resolution can often be misleading, especially in the field of electron microscopy, since it is often perceived to be linked solely to the capability of the instrument. In this Chapter, the main focus was to find the best compromise between chemical sensitivity or precision and spatial resolution, given a set of constraints related to the instrument and specimen stability. The microscopy community would gain from exploring quantitatively the chemical–spatial resolution relationship. This would allow the experimentalists to predict the spatial or chemical resolution given a set of requirements. In the next Chapter, we explore a similar concept, that of the analytical sensitivity given the size and the composition of electron beam-sensitive NPs.

Chapter 5

Electron Beam Damage and Detectability Limits

5.1 Introduction

The various sizes and temperature-dependent structural and thermodynamical properties of nanoparticles (NPs) can either be probed using bulk or local characterization techniques. For example, bulk methods, such as differential calorimetry or X-ray diffraction are commonly used to detect the average phase transition temperature of an *ensemble* of NPs. The results are interpreted under the assumptions that the particles are and remain identical to each other during the analysis. However, it is common for NPs to exhibit a natural size or composition distribution. Moreover, it is known that NPs have a natural tendency to agglomerate and sinter upon heating. Local characterization methods, namely transmission electron microscopy (TEM)-related characterization techniques, can be used to validate these assumptions and also confirm some of the measurements provided by bulk analysis methods. As reported in Chapter 2, hotstage TEM experiments were extensively employed to determine the phase of NPs at a given temperature and deduce the trends of the transition point with size with the advantage of providing precise structural and chemical information from within *individual* NPs.

With the advent of field-emission guns and aberration correctors, the instrument is no longer the limiting factor for high analytical accuracy and low detection limits. Radiation damage in the TEM is becoming a growing matter of concern as the current density of the electron beam increases with smaller probes and higher brightness and acceleration voltages. This is especially the case with the analytical characterization of nanostructures such as NPs. If one or more components of the NP is sensitive to electron-beam irradiation, the EDXS results can be deceiving if the technique is improperly applied, especially if one element is selectively lost during the analysis. In such a situation, long acquisition times required to obtain high statistical precision and low detection limit may therefore lead to considerable loss of the sensitive element, resulting in erroneous analysis. In cases where selective beam-damage is unavoidable, one can overcome the problem by acquiring a series of spectra and deducing the unexposed sample composition based on the depletion rate (Shuman et al. 1976; Hren 1986; Egerton and Rauf 1999). While this method has found use in the characterization of some sensitive materials, several issues arise with beam-sensitive

NPs. For instance, what precision level is expected if such a procedure was to be used to determine the beam-sensitive NP composition? What would be the expected detectability limits? How would these two benchmarks be influenced by experimental conditions? Finally, what is the impact of electron beam damage on the experimental investigation of a nanophase diagram?

In order to address these questions, we have developed a systematic method to determine the composition of an electron-beam sensitive NP, where one element is selectively removed, along with the corresponding precision from the analysis of the element removal rate. The method is demonstrated with the analysis of alloyed Ag-Au NPs produced by laser ablation of a micrometer-sized powder mixture with various initial Ag:Au ratios (Zhang et al. 2003). We present experimental evidence for Ag depletion and discuss the possible damage mechanisms. We investigate in detail 30 selected NPs of various sizes and composition and analyze the loss rate and radiation-damage cross-section. Using the software DeskTop Spectrum Analyzer (Fiori et al. 2003), we performed a series of spectra simulations in order to predict the limit of the measurements as a function of NP size and acquisition time.

The main findings reported in this Chapter were accepted for publication (Braidy et al. 2007), but we will nevertheless provide supplementary data, equations and discussions. In Section 5.2, we combine the theories of X-ray generation from a NP and knock-on damage to develop a model later used to analyze our experimental data. The synthesis technique of Au-Ag NPs and general specimen characterization follows in Section 5.3. The methodology used to acquire a sequence of spectra necessary to determine the zero-exposure composition of a NP and perform the simulations is introduced in Section 5.4. The analysis of the X-ray measurements and the DTSA simulations results are then described in Section 5.5. A discussion on possible damage mechanisms and on the expected detectability limits of the technique is presented in Section 5.6, were we also discuss the hypothetical consequences of selective electron beam damage on the investigation of the Au-Ag nanophase diagram.

5.2 Theory

When performing EDXS acquisition on a NP in conventional TEM mode, the electron beam diameter is often larger than the NP diameter. In this situation, if absorption and fluorescence are negligible, it is convenient to write the detected intensity of a particular X-ray line family of an element A (Goldstein et al. 1986) in terms of NP size and beam diameter. If the electron beam diameter, B_d, is larger than the NP diameter, D, the detected X-ray intensity, I_A^{NP}, will be reduced (compared to that detected from a foil geometry, I_A^f) by a factor corresponding to the ratio of the NP volume and that of a cylinder defined by the intersection of the parallel electron beam and a hypothetical foil of thickness t:

$$I_A^{NP} = I_A^f \frac{\pi D^3/6}{\pi t B_d^2/4} = \frac{2}{3} C_A^{wt} \frac{D^3}{B_d^2} \frac{\rho N_0}{A_A} \frac{\tau i}{e} \omega a \eta \varepsilon Q_A, \tag{5.1}$$

where τ is the acquisition real time (s) (for low counting rates, the real time is approximated as the live time), i is the current (A), e is the electron charge (C), C_A^{wt} is the weight concentration of A, ρ is the NP density (kg/m^3), N_0 is the Avogadro number (atoms/mol), A_A is the atomic mass of element A (kg/mol), ω is the fluorescence yield of a particular X-ray family, a is the relative transition probability of a line from the same X-ray family, η is the detector collection efficiency, ε is the detector absorption efficiency, Q_A is the ionization cross-section. Since the number of A atoms, n_A is related to the NP volume, Eq. 5.1 can be reduced to

$$I_A^{NP} = \frac{4 n_A}{\pi B_d^2} \frac{i\tau}{e} \omega a \eta \varepsilon Q_A. \tag{5.2}$$

Inversely, I_A^{NP} can be used to determine $\omega a \eta \varepsilon Q_A$ by recording several spectra of NPs of known sizes if the current, live time and electron beam diameter are known.

The rate at which the A atoms are depleted from an irradiated region is proportional to the number of remaining atoms, n_A, the displacement cross-section, σ_d, and the current density (expressed in electrons m^{-2}s^{-1}) (Howitt 1986). In this case, the number of remaining atoms as a function of the beam size and the initial number of atoms, n_A^0, can be expressed after integration as

$$n_A = n_A^0 \exp\left(-\sigma_D \frac{i/e}{\pi B_d^2/4} \tau\right). \tag{5.3}$$

If n_B remains unchanged during the analysis, we can use Eq. 5.2 in conjunction with Eq. 5.3 to express the instantaneous NP concentration ratio as a function of cumulated X-ray intensity of B, I_B

$$(C_A/C_B) = (C_A/C_B)_0 \exp(-R \cdot I_B), \tag{5.4}$$

where $(C_A/C_B)_0$ is the non-exposed NP *atomic* concentration ratio and R is a constant proportional to the displacement cross-section and is defined as

$$R = \frac{\sigma_d}{n_B \omega a \eta \varepsilon Q_B}. \tag{5.5}$$

The number of B atoms, n_B, can be determined from the knowledge of the NP size and composition using Eq. 5.2. The term $\omega a \eta \varepsilon Q_B$ can be deduced from pure B nanoparticles. Therefore one can determine R from an acquisition sequence and calculate σ_d. Finally, the ratio C_A/C_B is calculated from the extrapolation of EDX spectra acquired

sequentially using the Cliff-Lorimer equation (Cliff and Lorimer 1975) (Eq. 4.3a) with suitable $k_{A/B}$-factor.

By applying a logarithmic transform to Eq. 5.4, our data can be expressed as

$$\ln(C_A/C_B)_i = \ln(C_A/C_B)_0 - R \cdot (I_B)_i + \epsilon_i, \tag{5.6}$$

where ϵ_i is an error term. The exponential decay of the ratio could be fitted (Wonnacott and Wonnacott 1981) by applying a logarithmic transform and using a linear regression weighted by the relative statistical error of the ratio (found by using standard error propagation techniques, (Williams and Carter 1996)) to obtain the depletion rate and the initial ratio of each NP with their corresponding 95 % confidence interval. This technique is applicable only in the case where element B does not deplete during the experiment, unless the mass-loss behavior of element B is known.

The EDXS minimum detectability fraction (MMF) can be expressed as (Ziebold 1967)

$$MMF = \frac{F}{(\frac{P}{B} \cdot P \cdot \tau)^{1/2}}, \tag{5.7}$$

where P/B is the integrated peak-to-background ratio of the pure element, P, is the pure element counting rate, and τ , is the acquisition live time, and F (counts$^{1/2}$ s$^{1/2}$) is a constant. We can express Eq. 5.7 in terms of NP diameter, D as

$$MMF = \frac{a}{\tau^b D^c}, \tag{5.8}$$

where τ and D are the acquisition live time (s) and NP diameter (nm), respectively, $a = F/(P/B)$, $b = 1/2$. From Eq. 5.1, $P \propto D^3$ and $c = 3/2$.

We can define a "practical MMF", $C_{A,0}^{\mathrm{MMF}}$, as the starting concentration of element A in a NP which has decreased, due to preferential mass loss, to the value of the MMF after the acquisition of k spectra. An expression for $C_{A,0}^{\mathrm{MMF}}$ as a function of exposure to the electron beam, $k\tau$, can be obtained by first rewriting Eq. 5.3 in term of concentration ratio

$$C_A/C_B = C_A^0/C_B^0 \exp\left(-\sigma_D \frac{i/e}{\pi B_d^2/4}\tau\right). \tag{5.9}$$

We then substitute C_A^0 and C_A for $C_{A,0}^{\mathrm{MMF}}$ and MMF, respectively. Writing C_B^0 and C_B in terms of C_A and solving for $C_{A,0}^{\mathrm{MMF}}$ finally yields,

$$C_{A,0}^{\mathrm{MMF}} = \frac{MMF}{MMF[\exp(-\mu k\tau) - 1] - \exp(-\mu k\tau)}, \tag{5.10}$$

where

$$\mu = \sigma_d \frac{4i}{\pi e B_d^2}. \tag{5.11}$$

In other words, after an exposure to the electron beam of $k\tau$ seconds, the composition of a NP of a given diameter (D) would fall below the predicted detectability limit. Although one should consider the evolution of the particle size with mass loss numerically, for simplicity and as a first approximation, we consider the diameter of the particles (and consequently, the MMF) as constant throughout the analysis to give an estimate of the $C_{A,0}^{\mathrm{MMF}}$.

5.3 Materials

In this Section, we describe the synthesis of Au-Ag bimetallic NPs with various Ag:Au ratios. We first review the influence of each of the synthesis parameters. Details pertaining to the synthesis and TEM analysis of Au-Ag NPs are given followed by a TEM and EDXS investigation of the average composition and internal homogeneity.

5.3.1 Literature Review Henglein's (Henglein 1993; Fojtik and Henglein 1993) and Cotton's group (Sibbald et al. 1996; Heddersen et al. 1993) demonstrated that laser ablation is applicable to targets in solutions to produce colloids. This physical method allows the simple preparation of a high yield of alloyed nanoparticles without the contamination of the reducing agent. The experimental setup involves shining a laser onto metals immersed in an aqueous solution of surfactant or stabilizer. Several studies have appeared on the influence of the process parameters (laser beam parameters, type of solution, type and concentration of stabilizer agent, starting material) on the properties of the colloids (size distribution, shape, composition, etc.). The dynamics of the formation of the nanoparticles within a liquid is explained in the following chronological steps (Mafune et al. 2000a; Mafune et al. 2000b; Lee et al. 2001; Mafune et al. 2001; Mafune et al. 2002a; Mafune et al. 2002b; Mafune et al. 2003a; Mafune et al. 2003b; Mafune and Kondow 2004; Inasawa et al. 2003; Kabashin et al. 2003):

1. Above a certain laser power threshold, the metal is ablated and atomic species are ejected into a dense cloud. At that stage, the nucleation of small clusters takes place within a bubble, via the aggregation of neighboring species as fast as the atoms are supplied. As a result, embryonic NPs become surrounded by regions void of atoms;

2. This fast growth is followed by a period of slow growth within the liquid, where atoms diffuse from outside the region to the particle: the growth is controlled

by Ostwald ripening and is terminated when the particle is fully coated by the stabilizer.

Provided that the laser radiation is not absorbed by the NPs, the abundance of NPs will increase linearly with the ablation time (or the number of shots delivered by a pulsed laser) and the NP size distribution will shift towards smaller values as the laser intensity is increased (Mafune et al. 2001; Mafune et al. 2003a; Mafune et al. 2003b; Mafune and Kondow 2003c; Tsuji et al. 2001; Jiang et al. 2001). However, when one of the NPs absorption band coincides with the laser wavelength, two effects are observed (Inasawa et al. 2003; Mafune and Kondow 2003c; Tsuji et al. 2001; Tsuji et al. 2000; Ah et al. 2000): *i)* the NPs produced progressively prevent the laser from reaching efficiently the target and the production levels off and *ii)* the absorption of the laser energy induces photofragmentation leading to a smaller size distribution.

Effect of stabilizer. The presence of a stabilizer such as sodium dodecyl sulfate (SDS), $C_{12}H_{25}SO_4Na$, is often necessary to assist the growth of NPs. Aggregation is prevented by the steric repulsion of micelles (Chen et al. 2002): the micelles would have their hydrophilic end $-SO_4^-$ weakly bound to the nanoparticle while their hydrophobic tail $-C_{12}H_{25}$ points outward. Accordingly, the minimal concentration of surfactant is a function of the concentration and the size distribution of the nanoparticles. It was demonstrated (Mafune et al. 2000b) that a sodium based surfactant, ($C_nH_{2n+1}SO_4Na$) is an effective stabilizer only when $n \geq 12$. Otherwise, the surfactant will not possess a sufficient hydrophobic interaction. By considering stage 2 of the NP formation, a higher stabilizer concentration will generally terminate the NP growth early in the process and the size distribution will decrease to smaller values. The type of stabilizer is function of the nature of the metals: SDS was mainly used for Au and Ag but stabilizer such as cetyltrimethylammonium bromide (CTAB) and n-dodecanethiol are also reported to be effective stabilizer for these noble metals (Chen et al. 2002).

Effect of solvent. The nature of the solvent has a determinant effect on the process. Noble metals NPs such as Au and Ag can be easily produced in water, or anaerobic environment. Yeh et al. (1999) reduced CuO powder in 2-propanol to produce Cu colloids using a 1064 nm-wavelength laser. It was demonstrated that smaller NPs were generated but easily oxidized in an aerobic environment when using a 532 nm or 355 nm lasers. The laser ablation often induces a chemical reaction between the NPs and the solvent. For instance, it was shown (Compagnini et al. 2003) that the ablation of Au or Ag in chlorinated species ($CHCl_3$ or CCl_4) leads to the formation of $AuCl_x$ and $AgCl_x$ compounds because of the strong affinity between chlorine and metal. On the other hand, Bae et al. (2002) reported that the presence of 5 mM of NaCl promotes the formation of Ag NPs but reduces the long term stability of the NPs when compared to those formed in neat water. The viscosity of the liquid medium has an impact on the shape and the rate of formation of the NPs. It was shown by Compagnini (2003) that by using alkanes of different weight a higher solvent

viscosity will increase the NPs aspect ratio most likely by modifying the plume-liquid interaction. Anikin et al. (2002) reported on the production of ZnSe and CdS quantum dots via laser ablation of their respective crystal in various liquids transparent to the Cu vapor laser (which has a photon energy close to the band gap of the quantum dot): isobutanol, diethyleneglycol (DETG), ethanol, water and dimethylsulfoxide. Only DETG and isobutanol yielded good results for reasons not mentioned by the authors. Finally, Ag_2Se was produced in a mixed solvent of 2-propanol and ethylenediamine from Se powder and Ag nitrate.

It appears from the literature that no effective guidelines exist for the choice of an appropriate combination of solvent/stabilizer (except avoiding the choice of a solvent that would react with the metal or the laser). Recipes exist for common NPs produced by the "wet" laser technique, but for other kinds of NPs, the best solvent/surfactant combination should be determined by trial and error.

Effect of the nature of the elements and the form of starting material. Au, Ag and Pt NPs were easily produced from the laser ablation of a plate or a rod, mainly because of their inertness. A smaller size distribution and a higher efficiency were achieved when the process was carried in two steps: A solution of large Au NPs was first prepared by laser ablation at 1064 nm and size-reduction was subsequently accomplished using a 532 nm laser (Mafune et al. 2001). It is worth mentioning that rather large particles of agglomerated Ag NPs were provided by the laser irradiation of an $AgNO_3$ solution. The laser ablation of Cu in water has also been demonstrated but the NPs were easily oxidized or hydroxilized in water (Heddersen et al. 1993). As mentioned above, Cu NPs synthesis can be achieved by laser ablation of CuO in 2-propanol (Yeh et al. 1999). Nanocrystalline diamond was synthesized by laser etching graphite in water (Yang et al. 1998).

Stoichiometric bicomponent NPs were also produced by this technique. AgSe NPs were produced by laser irradiation of Se powder in an $AgNO_3$ solution (Jiang et al. 2001). CdS and ZnSe NPs were produced by laser fragmentation of the corresponding crystal (Anikin et al. 2002). It is interesting to mention that the ZnSe crystal was doped with Ni (0.3 %) to increase the absorption of the laser (Cu vapor laser). Bimetallic NPs were also produced by the solid-liquid-vapor technique in system with complete miscibility. Au-Ag alloyed NPs were prepared by the laser ablation of various types of starting material: bulk alloy (Mafune et al. 2001) but a much higher yield could be achieved with micron-sized powder (Zhang et al. 2003), chemically-prepared core-shell (Au-Ag) NPs (Hodak et al. 2000), solution of chemically-prepared Au and Ag NPs (Chen and Yeh 2001) or Au_xPd_{1-x} and Ag_xPd_{1-x} NPs were prepared in the same fashion using colloidal species of the same composition (Chen et al. 2002).

5.3.2 Experimental Details: Synthesis of Au-Ag NPs The alloyed bimetallic Au-Ag NPs were synthesized using a novel and versatile approach (Zhang et al. 2003), which facilitates the production of small amounts of a broad composition range of al-

TABLE 5.1: Au-Ag NPs statistical parameters (D = mean diameter; σ = standard deviation; n = number of measured NPs) of samples prepared with different Ag to Au starting powder ratio (Ag:Au).

Ag:Au	D, nm	σ, nm	n
Ag	13.0	3.6	99
3:1	9.0	3.6	112
1:1	10.5	4.5	113
1:3	7.4	2.2	111
Au	6.5	1.5	108

loyed NPs. A summary of the technique and conditions of the synthesis are presented below. The Au-Ag NPs were produced by laser (wavelength: 532 nm, repetition rate: 30 Hz, fluence: 590 mJ/cm^2/pulse) vaporization of water-suspended mixtures of Au (Alfa Aesar, APS 0.8-1.5 μm, 99.96%) and Ag (Alfa Aesar, APS 0.5-1 μm, 99.9%) powders in the following atomic Ag:Au ratios: pure Ag, 1:3, 1:1, 3:1 and pure Au. The anionic surfactant sodium dodecyl sulphate (SDS, Aldrich, 99%, 5 mM) was added to the suspension to assist NP growth and prevent their coalescence and aggregation. The suspension was then centrifuged (Cole-Parmer, #17250-10; 15 min at 3400 RPM) to remove the remaining powder particles. A drop of the resulting supernatant diluted in water was left to dry on a holey amorphous carbon film supported on a copper-mesh TEM grid.

5.3.3 Overall Composition, Size Distribution and Homogeneity The bright-field TEM micrographs of typical regions of the Au, Ag and Ag:Au (1:1) samples (Fig. 5.1) show different distribution of sizes and shapes. Pure Au NPs (Fig. 5.1(a)) are essentially spherical and well-separated from each other by at least a 1-2 nm gap attributed to the presence of SDS molecules on their surfaces. On the other hand, partial coalescence is apparent in the micrograph of the pure Ag NPs (Fig. 5.1(c)). The Ag:Au (1:1) sample shows (Fig. 5.1(b)) a combination of the well-separated smaller spheres found in the pure Au NPs sample and the larger partly coalesced NPs observed for the pure Ag NPs sample. The mean size of NPs decreases from 13(4) nm to 7(2) nm and the size distribution becomes narrower (Table 5.1 and Fig. 5.2(a)) with increasing amount of Au in the powder mixture. NPs with a diameter smaller than 3 nm are unaccounted for in the histogram of the pure Au NPs sample since the bright field contrast of these NPs with respect to the carbon film is too low. When imaged in annular dark field in STEM mode (Fig. 5.2(b)), the pure Au NPs sample reveals the presence of numerous small Au clusters amounting to up to 75% of the sample volume, (as estimated by image analysis).

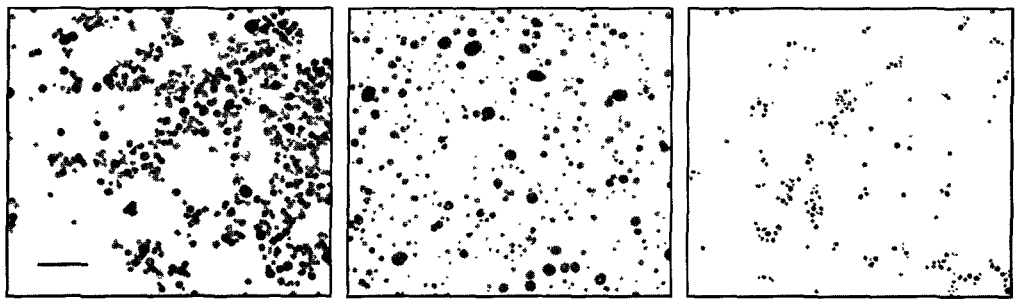

(a) (b) (c)

FIG. 5.1: Au-Ag alloyed NPs synthesized using the laser-liquid method with a Au:Ag ratio initial powder content of (a) 1:3 (b) 1:1 and (c) 3:1. Scale bar: 100 nm.

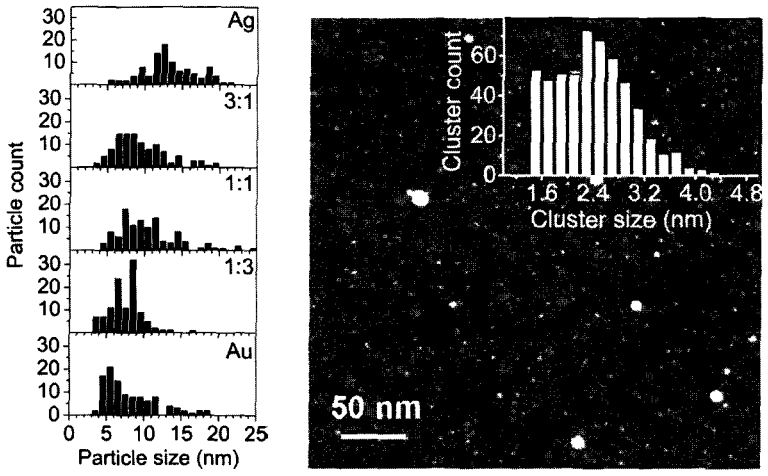

(a) (b)

FIG. 5.2: (a) Size distribution histograms for samples produced with different Ag:Au atomic ratios in starting powder mixture (shown in each panel). High magnification ADF-STEM image of Au NPs and clusters with corresponding size distribution histogram in inset (target was pure Au powder).

The average composition of each bimetallic sample was measured by acquiring several EDX spectra using a large beam spread out over regions with a high density of NPs to maximize the counting rate. During the analysis, the sample was continuously translated under the electron beam to avoid beam damage of the NPs. A typical spectrum of the Ag:Au (1:1) sample (Fig. 5.3(a)) shows the characteristic carbon and copper peaks originating from the carbon support and the grid, respectively (including Si peak from the carbon film and spurious Cu peaks from the grid bars). Au and Ag are both present in the NPs as evident from the appearance of the Ag L lines (L_α and L_β) and the Au L (L_α, L_β and L_γ) and Au M (M_α and M_β) lines. Quantitative analysis of this spectrum shows the Ag:Au ratio of 0.61(5), which is statistically different from the 1:1 composition of the starting material. For all the samples, quantitative analysis was performed on several regions and the average results of the analysis are shown in the inset of Fig. 5.3(b), where the measured Ag:Au ratio is plotted as a function of the Ag:Au ratio in the starting powder mixture. The broken line indicates the "reference" case, where the composition of the NPs is equal to that of the starting powder. For all three bimetallic samples, the measured Ag content is higher than that of the starting powder mixture. This is a surprising observation given the higher reflectivity and smaller absorbance length of Ag (~91% and ~14 nm, respectively) compared to Au (~47% and ~22 nm, respectively) at a laser wavelength of 0.5 μm (Bauerle 2000, p700, 703). If we postulate that Ag was preferentially ablated, we expect that the larger Au particles remaining from the powder were discarded during the centrifugation step.

Most of the EDX linescans performed across bimetallic NPs (two of which are displayed in Fig. 5.3(b)) show that Au and Ag are generally homogeneously distributed through the volume of the NP. This complete miscibility is in agreement with the Au-Ag bulk phase diagram. Partial segregation was nevertheless occasionally observed in some of the linescans performed on these NPs.

5.4 Methods

5.4.1 Instruments A Philips CM12 electron microscope operated at 120 kV was used to image NPs and to determine their size distribution. EDXS, high-resolution transmission electron microscopy (HRTEM) and annular dark field (ADF) observations were carried with a JEOL 2010F field emission electron microscope operated at 200 kV and equipped with a Si(Li) Ultrathin polymer (Moxtek™AP3.3, active area: 30 mm^2 solid angle: 0.114 sr) window energy dispersive detector (Oxford Instruments).

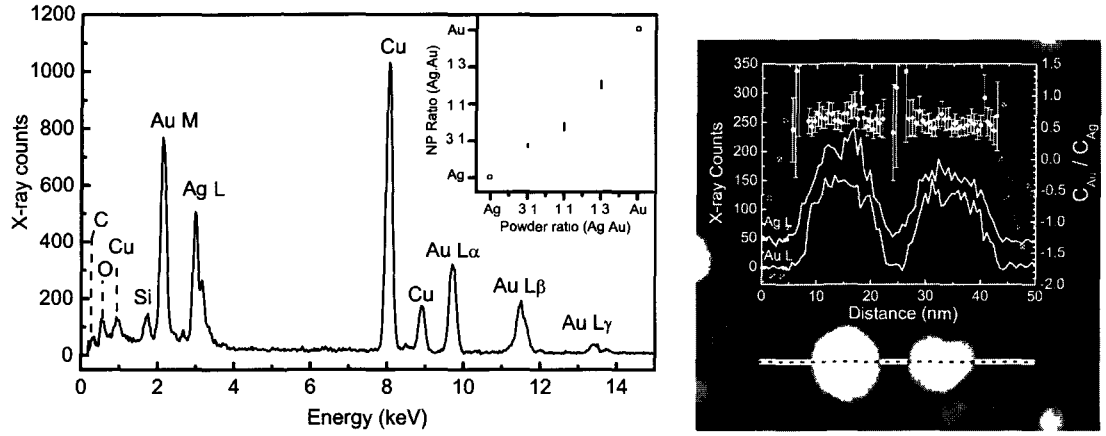

FIG. 5.3: (a) Energy dispersive X-ray spectrum acquired over several regions containing Ag-Au NPs produced with an equimolar powder mixture of Au and Ag. The results of the quantification performed on similar spectra recorded for samples produced with different starting Ag:Au powder ratios are shown in the inset. The dashed line indicates the situation of a congruent transfer powder stoichiometry to the average NP composition. (b)EDX linescan across two ~10 nm Au-Ag NPs from the Au:Ag (1:1) sample. Solid curves correspond to the background-subtracted X-ray signal from Au L and Ag L characteristic peaks (left scale, shifted 50 counts for clarity). Symbols with error bars refer to the C_{Ag}/C_{Au} atomic concentration ratio along with a 95% (2 standard deviation) confidence interval (right scale). Crossed off symbols data points have an statistically insignificant level of either Au L or Ag L counts.

5.4.2 k-factor Determination An Ag-Au standard (47.51 at.% Au) was prepared by arc melting high purity Au and Ag in controlled amounts and homogenized for 72 h. The sample was then microtomed to sections of 15-50 nm thick. Several EDX spectra were recorded for the different foil thicknesses from which the Au L and Ag L peak series were used for quantification. Since thicker foils were used to minimize the relative mass loss of Ag during the acquisition of the reference spectra, absorption correction were incorporated (Goldstein et al., 1977). The experimental Ag-Au k-factor was calculated by extrapolating the k-factor to zero-thickness (Horita et al. 1987). Using this approach, the k-factor at the 95% confidence level, $k_{AgL/AuL}(2\sigma)$, was found to be equal to 0.62(7) (atomic concentrations of Ag and Au were used), where the fluorescence factor was considered negligible. Considering a spherical geometry, absorption of the X-rays of interest within the studied NPs was found below 5% and was omitted from calculations (Kelly 1987; Zreiba and Kelly 1990). In cases where mass loss is unavoidable, the k factor can be determined by extrapolation, as described in this Chapter.

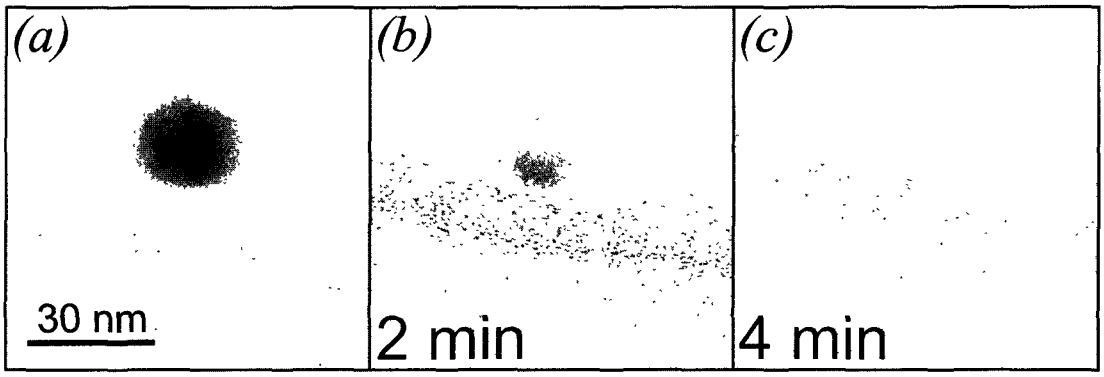

FIG. 5.4: (a) Unexposed Ag NP and following intense electron beam irradiation after (b) 2 and (c) 4 min. The 2.2 nA electron beam current was converged over the size of the remaining NP.

5.4.3 X-ray Generation from Pure Au and Ag Nanoparticles The term $(\omega a \eta \varepsilon)_{AuL} Q_{AuL}$ was evaluated to $0.7(3) \times 10^{-28} \mathrm{m}^2$ from the analysis of pure Au NPs in the range 6-15 nm. The electron beam diameter was fixed during the X-ray acquisition of one NP, but varied between 35 and 60 nm from particle to particle. For a fixed acquisition time of 400 s and a current of 2.2 nA, $\sim$ 2–9 $\times 10^3$ Au L counts could be accumulated, depending on the NP size and electron beam diameter.

The sensitivity of Ag NPs to the electron-beam irradiation is obvious from Fig. 5.4, showing a 30 nm diameter Ag NP (from the specimen prepared with the pure Ag NPs colloids) that is exposed to a converged electron beam after 2 (Fig. 5.4(b)) and 4 min (Fig. 5.4(c)). Following 2 min of intense electron-beam irradiation, half the volume of the NP is lost and the Ag NP is completely consumed after an exposure of 4 min.

The large mass loss rate of pure Ag NPs during electron beam irradiation prevented us from performing precise measurement of the loss rate, since no other element could be used to monitor the dose. The term $(\omega a \eta \varepsilon)_{AgL} Q_{AgL}$ could nevertheless be deduced (from the values measured for Au L using the k-factor) to be equal to $\sim 1.1(6) \times 10^{-28}$ m^2.

5.4.4 Minimal Detectable Fraction Simulation A set of standard spectra of Ag and Au was first generated with DTSA using the above parameters. An empirical k-factor ($\sim$0.63, in good agreement with the experimental one of 0.62, determined from standard) was then derived by least-squares fitting of a generated DTSA spectrum of known composition (Ag:Au, 1:1 at.) using the Au L and the Ag L lines. The expected value of the *MMF* and its corresponding error was computed on a set of 30 spectra simulated with a concentration corresponding to the *MMF*, according to the methodology described in the reference guide for DTSA (Fiori et al. 2003). Given the

intrinsic uncertainties associated with the experimental parameters, we have found a reasonable agreement between the value of the P/B (Eq. 5.7) of the simulated spectra and their experimental counterpart.

To investigate the effect of the substrate on the detection limits, the evaluation of the *MMF* of Ag in Au-Ag NPs was also performed with a 30 nm substrate of amorphous carbon. The relative compositions of Au, Ag and C together with the density and "film thickness" were adjusted to correspond to the situation where the electron beam interacts with a Au-Ag sphere and a 30 nm-thick carbon cylinder having a diameter 10 nm larger than the NP.

The DTSA simulations help quantify the relationship between *MMF*, the NP size and acquisition time. The procedure makes it possible to evaluate *a priori* P/B and the proportionality constant F in Eq. 5.7. The results are then fitted by multiple non-linear least-square regression to verify the expected proportionality of the *MMF* to $\tau^{1/2}$ and $D^{-3/2}$ (Eq. 5.8) as the exponents may slightly change with a bias introduced by adding Poisson noise to a low count spectrum.

5.4.5 Sequence Acquisition Procedure As it will be demonstrated in the DTSA simulations, long acquisition times are required for accurate EDXS measurements on NPs. However, since Ag is selectively removed at a rate that increases with electron dose, long acquisition times and high doses result in an apparent underestimation of the Ag content in the NPs. To circumvent this problem, we studied the evolution of EDX spectra to determine the elemental content of the NPs. For each NP, a sequence of spectra was recorded by focusing the electron beam over a small area containing the NP. For each individual spectrum, the collection of X-ray signal was stopped when ~800 counts under the Au M line (energy window corresponding to the 2.01-2.25 keV) were accumulated; longer times were used when dealing with low Ag fraction samples in order to improve the counting statistics. The choice of using the Au M peaks rather than the Au L peaks to terminate the acquisition is simply based on the fact that the Au M line is the strongest peak of the spectrum; it should be emphasized that the Au L peaks were subsequently used for the quantification of the spectra.

It is important to note that the Au count rate in the case of both pure Au and alloyed NPs did not decrease, even under a tightly focused electron beam. The acquisition time necessary to collect ~800 counts under the Au M line (shaded area in the spectra of Fig. 5.5 corresponding to the 2.01-2.25 keV energy window) varied between 10 s and 1 min, depending on the size of the NP (D) and the electron beam illumination (B_d). Using the Au L or M count scale as indicative of the given dose rather than a clock time scale made it possible to account for changes in the interaction volume, the focusing of the beam and the particle movement during analysis. This can be justified from Eq. 5.2: since n_{Au} can be determined and is constant throughout the time-series acquisition, the dose can be deduced from the cumulative Au L intensity

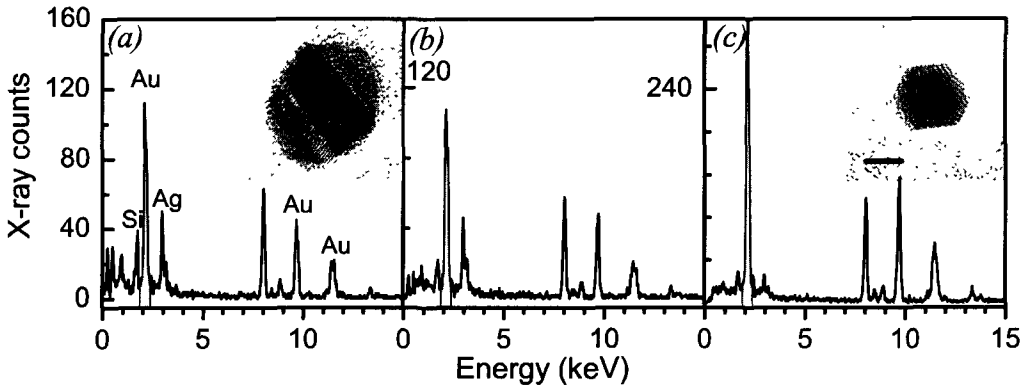

FIG. 5.5: The 1st (a), the 19th (b), and the last (c) spectrum from the sequence of 38 energy dispersive X-ray spectra recorded from the nanoparticle shown in the inset of the left panel. Inset of the right panel shows the beam-damaged nanoparticle after the acquisition of the series (scale bar = 2 nm) which exhibits faceting.

at any time. In other words, the dose given to the NP is related to the number of electrons impinging on the NP (rather than simply the beam current over the illuminated area) and thus, the generated X-rays. The acquisition of spectra was continued until the Ag peaks vanished or the Ag count rate reached a stable value.

For example, if we consider only the first spectrum of the sequence of 38 EDX spectra (displayed in Fig. 5.5(a)) recorded from the NP shown in the inset (from the Ag:Au (1:1) sample), quantification yields the Ag:Au ratio of 0.34(4). The nineteenth spectrum of the sequence (Fig. 5.5(b)), recorded after 18 spectra, each with ~800 counts under the Au M line, shows that the Ag:Au decreased to 0.25(3). The last few spectra of the sequence were acquired with an extended integration interval of ~2400 counts under the Au M peak in order to improve the counting statistics since the amount of Ag significantly decreased. The last spectrum of the sequence (Fig. 5.5(c)), recorded after ~48 800 counts under the Au M peak, reveals that the Ag:Au ratio decreased to 0.055(4) (still slightly higher than the *MMF* evaluated to 0.051, as computed with 2 confidence level of Ag in a Au matrix for these conditions of analysis).

The HRTEM micrographs in the inset of Figs. 5.5(a) and (c) show the same NP (from the Ag:Au (1:1) sample) before and after the acquisition of the EDX spectra sequence. Its shape appears slightly ellipsoidal with the minor and major axes of ~9 and 10 nm, respectively. The electron beam damage to the NP is evident from the micrograph taken following the acquisition of the last spectrum of the sequence (Fig. 5.5(c)). The approximate NP diameter decreased to ~5.8 nm, which corresponds to a volume loss of 75% (roughly estimated assuming that the NP is an ellipsoid with its two axes equal to the minor and the major axes of the projected ellipse and the third axis equal to the average of the other two). The NP shape also evolved from

TABLE 5.2: Fitted values of a, b and c (and corresponding standard errors) in Eq. 5.8 (where D is in nm) from the minimum detectability Ag fraction simulated with and without a 30 nm amorphous carbon (a-C) substrate.

	a	b	c
no a-C	31.4(3)	0.520(14)	1.52(4)
30 nm a-C	30.2(3)	0.48(10)	1.55(3)

ellipsoidal to faceted. This NP is viewed along the $<11\bar{1}>$ zone axis, as evident from the spacing and the direction of the HRTEM fringes as well as the elongated hexagonal shape.

It is apparent from the micrograph that mass loss also occurs in the carbon film. As the thickness of the film supporting the NP decreases with increasing electron beam exposure, the carbon and spurious Si peaks gradually disappear from the spectra (Fig. 5.5).

5.5 Results

5.5.1 Minimal Detectable Fraction The simulation results are summarized in Fig. 5.6, where both the *MMF* without substrate (open squares) and *MMF* with a 30 nm-thick a-C substrate (open circles) (expressed as an atomic Ag percent) are plotted for different NP sizes and counting times, when no damage is considered in the calculations. Not surprisingly, smaller NPs and shorter collection times both increase (degrades) the *MMF* (i.e. the numerical value increases) and its associated error. The Ag *MMF* for a spectrum of a 6 nm diameter NP acquired for 60 s is estimated to be as large as ~25% Ag at. with an absolute error of ~20%. Increasing the counting time to 900 s considerably reduces the *MMF* to 7(4)% Ag at. However, such a long collection time would result in selective beam damage, as demonstrated later. For the largest NPs (20 nm) the *MMF* improves (i.e. the numerical value decreases) from 1.3(1.3)% to 1.2(9)% with counting time increasing from 400 to 900 s. The presence of a substrate degrades the *MMF* by an average 12%. It can be seen that the difference between the *MMF* with and without the substrate becomes negligible for larger NPs and longer acquisition times.

The 16 simulated *MMF* were fitted to Eq. 5.8 using a non-linear multiple least-square routine. The fitted values of a, b and c and corresponding error appear in Table 5.2. The numerical values of b and c agree very well with the expected exponents of τ and D (1/2 and 3/2, respectively) in the expression of the *MMF* (Eq. 5.7), as discussed in Section 1. Interestingly, if we fix b and c, to 1/2 and 3/2, respectively, a

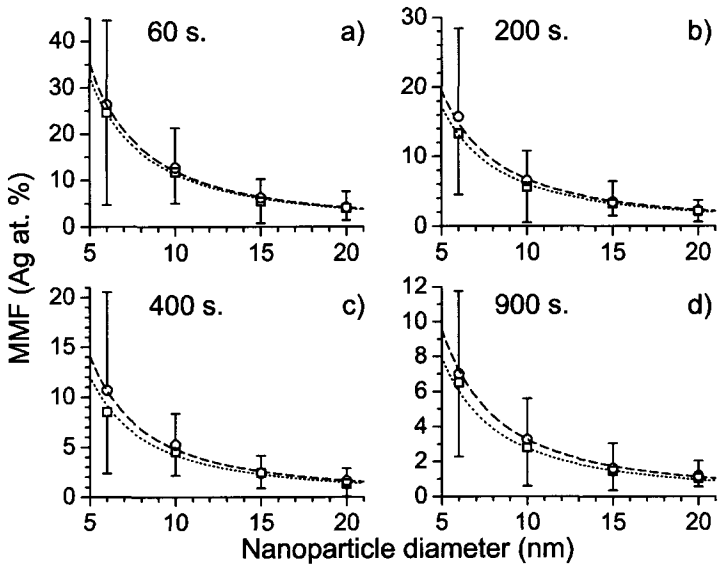

FIG. 5.6: Graphical representation of the estimated minimum detectable fraction (expressed in Ag at.% fraction) and associated error as a function of different nanoparticle sizes (6, 10, 15 and 20 nm) for the explored acquisition time (a) 60 s, (b) 200 s, (c) 400 s and (d) 900 s (note the vertical scale change). Circles and squares correspond to the simulations performed with and without the presence of a 30 nm amorphous carbon (a-C) substrate, respectively. Eq. 5.8 is plotted as dashed (with 30 nm-thick a-C substrate) and dotted (without substrate) curves with the fitted parameters (Table 5.2). Only half of the error bar is shown for clarity.

can be fitted to ~27.6(3) without the a-C substrate and 30.2(3) with the substrate (~11% relative difference). However, the goodness-of-fit of the non-linear regression decreases when b and c are fixed, so further discussion will only consider the fitted values indicated in Table 5.2. The values of these parameters are applicable only for the simulated conditions (i.e., for a given current density, probe size relative to the NP diameter, detector parameter, etc. and other parameters affecting the peak-over-background ratio).

5.5.2 Unexposed NP Composition and Damage Cross-Section Fig. 5.7 shows a log-linear plot of the Ag content of one NP from each sample as a function of dose measured in units of Au L counts. The linear segments at the beginning of the curves are indicative of the exponential behavior.

The curves eventually departed from the exponential trend and the data became scattered around a constant value, as exemplified by the 13.7 nm diameter NP in Fig. 5.7 after ~15 000 Au L counts. The plateau generally occurs after a drop of about ~90% from the initial value of the Ag:Au ratio regardless of the NP size and composition. This empirical criterion was used to exclude the plateau from the regression. For the confidence interval to be statistically well-behaved, we arbitrarily

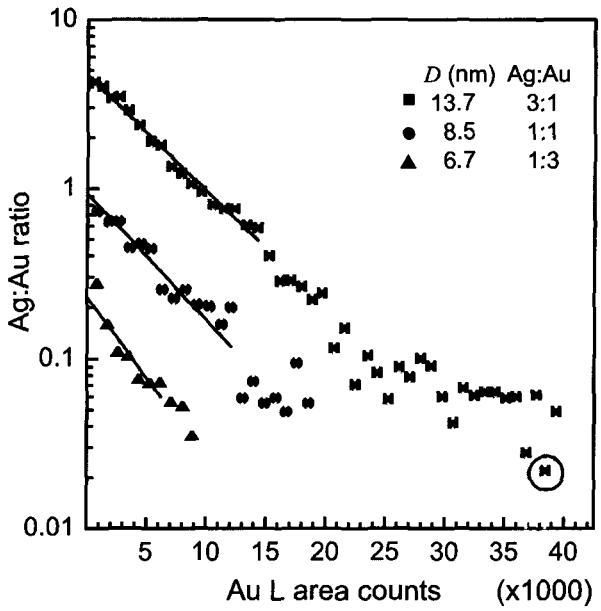

FIG. 5.7: Semi-logarithmic plot of the evolution of the atomic Ag:Au ratio with electron beam exposure as a function of the number of counts accumulated under the Au L peak. Evolution is plotted for one representative particle per bimetallic sample (average size based on the statistics presented in Table 5.1). The data point highlighted by a circle lies below the minimum detectable fraction computed for the corresponding condition of analysis. The curves were fitted according to Eq. 5.6 with the parameters indicated in Table 5.3.

set the minimum number of points for extrapolation to 5, which translates into only 3 degrees of freedom (in this case, the Student t value is ~3.2 and is already quite large, for a 95% confidence level). Sequences containing a smaller number of data points were discarded since they could not produce statistically significant data.

The fitted values of R (Eq. 5.6) and the NP Ag content, C^0_{Ag} (calculated from $(C_A/C_B)_0$), from the sequences displayed in Fig. 5.7, appear in Table 3. The full regression results of all the acquired sequences are shown in Fig. 5.8. Fig. 5.8(a) shows the 95% confidence intervals of the unexposed NP composition for each of the studied sample. The fitted results of σ_d appear in Fig. 5.8(b) in terms of the corresponding NP size and sample.

5.5.3 One hundred kV Acceleration Voltage and Low-Temperature Experiments A simple experiment to test whether knock-on damage significantly contributes to the disappearance of Ag under the electron beam is to evaluate the Ag loss at a lower acceleration voltage. From the cohesive energy, E_c ~2.95 eV/atom

TABLE 5.3: Fitting parameters of the acquisition sequences displayed in Fig. 5.7. $C_{Ag}^{min} - C_{Ag}^{max} = 95\%$ confidence interval of the unexposed nanoparticle composition, R = slope of the fitted line of the log-linear regressions (from Eq. 5.6), n = number of fitted data points used in the regression, D = unexposed nanoparticle diameter and (Ag:Au) is the Ag to Au starting powder ratio of the sample from which the analyzed nanoparticle is taken from.

Ag:Au	D, nm	n	R, $\times 10^{-5}$ Au L counts $^{-1}$	$C_{Ag}^{min} - C_{Ag}^{max}$
3:1	13.7	18	15(1)	0.81 - 0.83
1:1	8.5	14	17(4)	0.40 - 0.56
1:3	6.7	8	21(8)	0.14 - 0.24

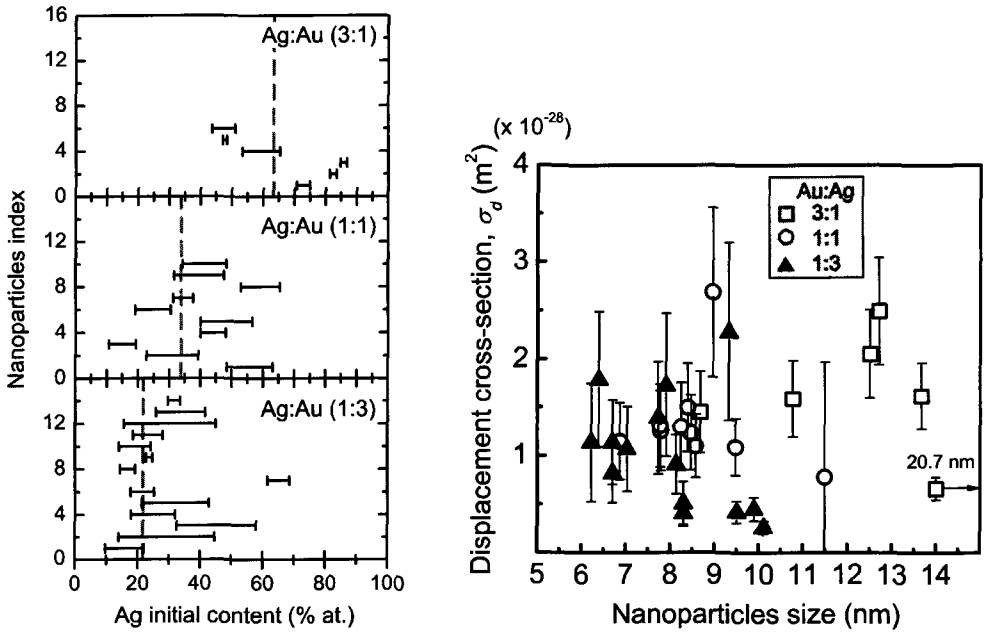

FIG. 5.8: (a) Zero-beam exposure confidence interval composition (in Ag % at.) of analyzed bimetallic nanoparticles. The index is for reference. The error bars represent the 95% confidence interval. The dashed lines indicate the composition measured over several regions containing Ag-Au nanoparticles. (b) Displacement cross-section obtained by regression analysis of the nanoparticles time-series against the analyzed nanoparticle size. Symbols refer to the identity of the sample of the analyzed nanoparticle [▲ 1:3, ○ 1:1 and □ 3:1 (Au:Ag)]

for Au and Ag, we can calculate the minimal knock-on threshold incident electron energies E_c for Ag and Au as ~127 keV and ~216 keV respectively (Oen, 1973). The same experiment was repeated on similar Au-Ag NPs in size and composition at 100 kV using the same current density (~10^6–10^7 A/m^2). Even after extended irradiation time (10^2–10^3 s), there was no noticeable loss of Ag.

Another common damage process found in transmission electron microscopy is radiolysis or etching, a phenomenon that occurs in the presence of residual water molecules commonly found in the microscope columns and as a residue in our sample. The etching rate is expected to be strongly enhanced at low temperature (Egerton and Rossouw 1976; Hren 1986). We performed the same experiments at 96 K using a liquid nitrogen cryogenic holder to verify if etching was occurring. The Ag loss rate was, however, not noticeably different at low temperature as compared with the room temperature EDXS measurements, which suggested that etching was unlikely to be responsible for the NP damage.

5.6 Discussion

5.6.1 NPs Composition Distribution Based on these measurements, we can discuss the relative merits of "bulk" EDXS analysis performed over areas containing a large number of nanoparticles, as compared with individual NP measurements. Fig. 5.8(a) displays the 95% confidence interval of the extrapolated composition of the NPs, prior to electron beam irradiation for each sample. The broken vertical lines reproduce the "bulk" EDXS C_{Ag} values found in the inset of Fig. 5.3(a). In all three cases, it is obvious that the spread in individual NP composition is larger than the uncertainty on the bulk EDXS measurements.

5.6.2 Damage Mechanism The phenomenon of beam damage of Ag with 200 keV electrons can easily be overlooked, especially if the dose is too low or the exposure to the electron beam too short to observe sensible change on the area of interest. We stress the fact that mass loss is not related to the preparation method of the NPs since the phenomenon was also observed for the thin Au-Ag standard after a prolonged exposure to a convergent beam (in TEM mode). Sputtering is likely to be the process by which Ag atoms are ejected from the surface of the Au-Ag NPs. Indeed, sputtering is the dominant damage mechanism in metallic systems (Howitt 1986; Egerton et al. 2004). This process is characterized by a minimum energy threshold above which damage can occur. This is in agreement with the 100 kV acceleration voltage experiments, where Ag depletion was not observed. This simple

model also explains why, at an acceleration voltage of 200 kV, Ag, but not Au, is removed from NPs.

Since sputtering is a surface phenomenon, a loss rate proportional to the number of beam-sensitive atoms on the surface is expected. However, in the present procedure, we suggest a simple model based on a loss rate proportional to the number of remaining beam-sensitive atoms (Eq. 5.3). While several phenomena are likely involved in the process of mass-loss in electron-beam sensitive NPs, it is reasonable to suggest that diffusion of the Ag atoms to the surface is the rate-limiting mechanism. Diffusion in our case can be assisted by "knock-on" or direct displacement (Hren 1986) by the incident electrons. If the speed by which Ag atoms replenish the surface layer is slower than the Ag removal rate, then the loss rate should be proportional to the Ag remaining in the *volume* of the NP. For the sake of completion, we derived a modified version of the surface-limited model for the Ag removal rate (see Appendix E). This version of the model is also capable of qualitatively describing the mass-loss behavior of the experimental data. However, the surface-limited model is mathematically and numerically much more complicated to handle than the simple exponential function we recommend in this Chapter (the extracted zero-exposure Ag fraction in individual NPs are essentially the same for both models).

The theoretical sputtering cross-section of Ag atoms, under an incident beam of 200 kV is estimated to be $\sim 483 \times 10^{-28}$ m^2 (Chadderton 1965; Oen 1973; Egerton and Rossouw 1976). The experimental σ_d values computed with Eq. 5.5 using the fitted sequences are plotted against the NP size in Fig. 5.8(b). σ_d exhibits no obvious dependency on NP size and composition, as expected from Eq. 5.5. Assuming that σ_d is independent of NP size and composition, a mean value of $\overline{\sigma_d} \sim 1.2(6) \times 10^{-28}$ m^2 is obtained using an average weighted by individual error over all the 30 available data points, (the error is the standard deviation of the set of σ_d). This is more than 2 orders of magnitude smaller than the theoretical prediction. This discrepancy between the theoretical sputtering cross-section and experimental values of σ_d supports the idea that, although sputtering is the mass loss mechanism, it is not the rate-limiting process underlying the Ag loss in Au-Ag NPs.

As a final remark, by comparing the value of $\overline{\sigma_d}$ with the effective Ag X-ray cross-section term ($(\omega a \eta \varepsilon)_{AgL} Q_{AgL} \sim 1.1 \times 10^{-28}$ m^2), it is interesting to note that for each Ag L X-ray detected, approximately one Ag atom is lost from the NP. If the data is fitted against the surface-limited model outlined in Appendix E, the extracted sputtering cross-sections are found to be ~1-5 times larger than those calculated on the base of the volumetric model, but still significantly smaller than the theoretical cross-section.

5.6.3 Practical Detectability Limits of the Nanoparticle Composition

The Ag *MMF* calculated in Section 5.4.4 (Fig. 5.6) and the corresponding semi-empirical relations derived from Eq. 5.2 are only valid for an individual spectrum

assuming no mass loss. The regression procedure described to extrapolate the initial Ag content C^0_{Ag}, however, requires 5 spectra, each having a calculated Ag fraction above the *MMF*. This requirement adds a constraint to the detectability limit of NPs. In this section, we evaluate the "practical" *MMF*, $C^{\mathrm{MMF}}_{Ag,0}$, as a function of NP size for sequences recorded with different collection times per spectrum (Eq. 5.10).

For example, consider a 6 nm diameter Au:Ag (1:1) NP supported by a 30 nm-thick a-C substrate probed by a 2.2 nA electron beam of 16 nm diameter (to allow for a 5 nm security ring around the NP). The detected number of Ag and Au counts accumulated in a 30 s live time spectrum would be ~639 and 508, respectively, according to Eq. 5.2 using the experimental values of $(\omega a \eta \varepsilon Q)$ for Au and Ag deduced in Section 5.4.3. This translates into an Ag composition contained in the 2 confidence interval 40-47% Ag at. which is slightly higher than the *MMF* determined by Eq. 5.8. This implies that the Ag peak would just satisfy the visibility criteria ($> 2 \cdot \sqrt{2 \cdot I^b}$, where I^b is the background intensity (Liebhafsky et al. 1960; Romig and Goldstein 1979)). If the analysis were continued for another 30 s the measured concentration would have dropped to the range 34-41% at. Ag, due to the expected mass loss of Ag (calculated with Eqs. 5.2 and 5.3). This concentration is now noticeably lower than the predicted *MMF*. Based on the Ag loss, there should be a minimum initial Ag concentration required to generate 5 spectra each having a calculated Ag content higher than the *MMF*. This happens to be 67% at. Ag for a 6 nm NP. Alternatively, the minimum particle size that can be analyzed for a Au:Ag (1:1) NP alloy using 5 spectra of 30 s acquisition time is ~7.5 nm.

Fig. 5.9 shows the "practical" detectability limit of a Au-Ag NP of a given size required to measure 5 statistically significant spectra as determined from Eq. 5.10. The curves in Fig. 5.9 were computed with operating conditions typical to this study (i =2.2 nA, $k = 5$, $B_d = 10$ nm larger than the NP diameter, $\sigma_d = 1.2 \times 10^{-28}\mathrm{m}^2$, *MMF* calculated with values in Table 5.2 considering a 30 nm a-C substrate) for different collection times per spectrum (τ = 15 s, 30 s, 60 s and 90 s). For a given NP size and collection time per spectrum, $C_{Ag,0}$ cannot be determined if it lies below the computed "practical" detectability limit, $C^{\mathrm{MMF}}_{Ag,0}$.

The curves displayed in Fig. 5.9 indicate that the determination of low Ag content is possible for larger NPs. Alternatively, for smaller NPs, the Ag content must be high enough to record sufficient Ag X-rays above the background in 5 consecutive spectra. Interestingly, a shorter collection time per spectrum generally extends the detectability range. Indeed one can benefit from the short acquisition time required to satisfy the Ag L peak visibility criteria and rapidly detect the Ag signal from smaller NP before the Ag content disappears below the *MMF*. On the other hand, an acquisition time too short (e.g. $\tau = 15$ s) will have the opposite effect since not enough X-ray counts will be accumulated per spectrum, regardless of the Ag loss. For a given a NP size, there appears to be an optimal acquisition time per spectrum to minimize $C^{\mathrm{MMF}}_{Ag,0}$. This value could be determined by taking the derivative of Eq. 5.10 with respect to τ and solving for τ. We calculated that the optimal acquisition time

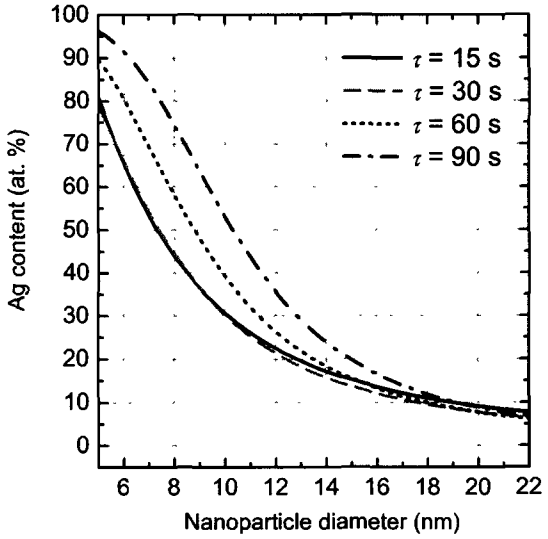

FIG. 5.9: Simulated practical minimum detectable Ag fraction (at.%), $C_{Ag,0}^{\mathrm{MMF}}$, as a function of nanoparticle size D (nm) for different acquisition times (Eq. 5.10). Solid, grey dashed, dotted and dash-dotted lines are computed with a collection time, τ = 15 s, 30 s, 60 s and 90 s per spectrum, respectively. Probe current i = 2.2 nA; Number of spectra per sequence k = 5; Probe diameter $B_d = D + 10$ nm; Displacement cross-section $\sigma_d = 1.2\times10^{-28}$ m^2; Values of a, b and c taken from Table 5.2 considering a 30 nm amorphous carbon substrate.

per spectrum is between 20 and 40 s for NPs in the 5-20 nm range and increases for larger NPs.

Eq. 5.10 was derived by assuming that the *MMF* remains constant throughout the experiment. However, the size of the NP decreases upon mass loss, therefore degrading (increasing) the *MMF*, and the corresponding $C_{Ag,0}^{\mathrm{MMF}}$, as it can be appreciated from Eqs. 5.8 and 5.10, respectively. The approximation is expected to break down for the Ag-rich part of the limiting curves of Fig. 5.9, where the relative mass loss due to electron beam damage would be highest. For example, according to Eq. 5.10, the $C_{Ag,0}^{\mathrm{MMF}}$ of an 8 nm diameter NP for τ =30 s is 44% Ag. By taking into account the variation of the *MMF* with mass loss, $C_{Ag,0}^{\mathrm{MMF}}$ can be evaluated numerically to ~51%. Typically, the relative difference in the values of $C_{Ag,0}^{\mathrm{MMF}}$ between the approximation (Eq. 5.10) and ones computed numerically is evaluated to ~20% for 5 nm diameter NPs but falls to below 5% for NPs larger than ~12 nm (for τ =30 s).

Experimentally, it was possible to determine the composition of a number of NPs somewhat below the calculated detectability limit. This indicates that the simulated values of $C_{Ag,0}^{\mathrm{MMF}}$ are slightly conservative. As noted above, the *MMF* simulations are dependent on a (Eq. 5.8) which is related to the ratio of the peak over the background. Experimentally, a varied from particle to particle depending on the probe size with respect to the NP diameter, the thickness and composition of the substrate supporting the NP and the intensity profile of the probe (given a convergence angle).

These variations can be held responsible for the overestimation of $C_{Ag,0}^{\mathrm{MMF}}$ with respect to the experimental data. If necessary, one can evaluate $C_{Ag,0}^{\mathrm{MMF}}$ for any set of given conditions by using DTSA to predict the value of a. Given the experimental difficulty when dealing with the EDXS characterization of beam-sensitive NPs and the large uncertainties associated with small-scale analysis, the simulation nevertheless describes to a reasonable level of accuracy the expected detection levels of EDXS of the Au-Ag NPs.

5.6.4 Detection Limits and Nanophase Diagram A popular method to evaluate experimentally the melting point variation with NP of different size and composition is to perform hotstage *in-situ* experiments (Buffat and Borel 1976). If the composition of the NPs lies below the *MMF* or falls below it during the analysis, then some portions of the nanophase diagram will not be available to the experimentalist.

This concept is demonstrated with the Au-Ag system where both the variation of *MMF* and the melting point can be related. We start by expressing the melting point depression of a Au-Ag alloy as a function of the NP size (Eq. 2.4) (Wautelet 1991; Wautelet et al. 2000). Here, $\alpha_{Au} = 1.5\,\mathrm{nm}^{-1}$ and $\alpha_{Ag} = 2.2\,\mathrm{nm}^{-1}$ (Wautelet 1991) and the juxtaposition of the phases is not considered, for simplicity. Fig. 5.10 shows the melting point depression of pure Au (top curve) and pure Ag (bottom curve). Since the liquidus and solidus of the fully miscible Au-Ag phase diagram almost overlap, we use the approximation $\mathrm{T}_{liquidus} \approx \mathrm{T}_{solidus} \approx \mathrm{T}_{melting}$. Consequently, the melting point of a Au-Ag NP of any composition of a given radius can be computed from a vertical tie-line connecting the pure Ag and pure Au curves. The dotted line represents the melting point corresponding to an alloy having a composition equal to $C_{Ag,0}^{\mathrm{MMF}}$, as determined previously (Eq. 5.10). Above the dotted curve, it would not be possible to determine the composition of the alloyed NP while below it, at least 5 EDX spectra could be recorded and the composition deduced using the method described in this section. For example, a 7.7 nm diameter NP would need to have an Ag content <50 % at. in order to experimentally measure its expected melting temperature of ~970 K.

As expected from Fig. 5.10, the regions of the nanophase diagram accessible to the experimentalist will be more restricted for smaller NPs. Alternatively, the composition range over which experiments could be carried increases asymptotically with the NP size.

This method demonstrates the concept of relating the detectability limit to the nanophase diagram. However, difficulties would arise in the context of experimentally demonstrating these limits in the case of the Au-Ag nanosystem. For large particles, where a limited range of Ag composition can be measured with confidence (say for $R > 4$ nm), hotstage experiments would have to be carried above 800 K. At these temperatures, sublimation becomes non-negligible in the case of nanoparticles. It

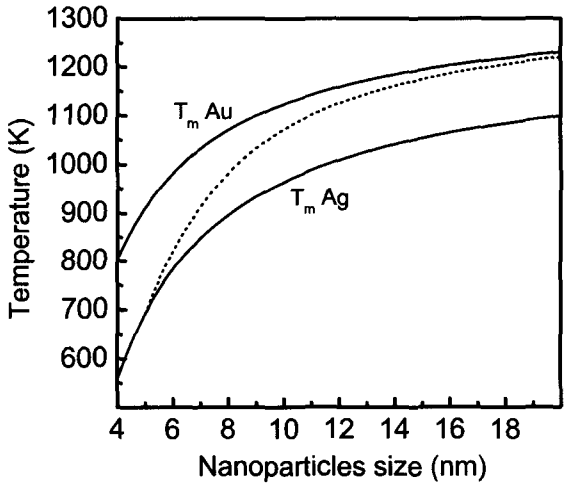

FIG. 5.10: Melting point depression of Au (top solid curve) and Ag (bottom solid curve) as a function of NP diameter. The region below the dotted curve indicates the portion of the nanophase diagram where experimental data could be collected. The regions above the dotted line will not provide sufficient counts for analysis. Parameters used to compute $C^{\mathrm{MMF}}_{Ag,0}$ are identical to those used to calculate Fig. 5.9, with τ= 30 s.

would be possible to measure the melting point of the NPs only if the total loss of Ag *via* sublimation could be accounted for during heating and the experiment itself.

5.7 Conclusion

An EDXS microanalysis method for determining the composition of alloyed NPs containing electron beam-sensitive elements is described. The method is demonstrated for alloyed NPs of varying Ag-Au composition. Practical limitations to precise EDXS measurements are evaluated by estimating the minimal detectability fraction (*MMF*) of Ag in Au-rich NPs of various sizes. Since the EDXS spectra and TEM images show that Ag is removed from a NP during electron beam irradiation at 200 kV, the required acquisition time to ensure a high level of precision and detectability translates into sufficient electron dose to decrease the Ag:Au ratio. The Ag atoms are removed from the surface via a sputtering mechanism since Ag is not lost when working at a lower acceleration voltage (100 kV). It is, however, suggested that direct displacement or knock-on damage is the rate-limiting process, since it would assist the transport of Ag atoms to the surface of the NP. This hypothesis could eventually be confirmed in a hotstage experiment at high temperature, where diffusion of the atomic species to the surface of a NP can no longer be a limiting process. Therefore, it is suggested as a future work to evaluate the trend of the displacement cross-section of Ag as a function of temperature: according to the present model, it would increase with temperature to reach a maximum given by the theoretical cross-section.

We studied the evolution of Ag content as a function of electron beam exposure normalized to a constant Au counting rate to determine the initial content of the NPs using a weighted linear regression method. From these measurements and the determination of the damage cross-section, we estimated that for each Ag X-ray detected, one Ag atom was lost due to electron beam damage. By combining the estimated *MMF* with the experimentally determined damage and the ionization cross-sections, we determined the minimal detection limit required for the proposed procedure to be carried out with statistical confidence.

It is also important to note that this technique could be easily extended to the analysis of beam-sensitive alloyed NPs of light elements and transition metals using electron energy-loss spectroscopy given the advantages of the technique in the detection of these elements (Leapman and Hunt 1991).

Analytical TEM is a powerful method to detect nanoscale phenomena but suffers intrinsic limitations related to the *observer principle* (conceptually related to, but not to be confused with Heisenberg's uncertainty principle). Indeed, the intense electron beam will necessarily alter the state of a material, especially if the probed subregions are nanostructured. Moreover, when probing close to a phase transition point, electron beam heating can locally stabilize or induce phase change. The outcome of such an experiment could be misleading when investigating the phase stability of nanostructured materials unless the extent of the phenomenon is properly known.

From a theoretical perspective, there exists a definite need to understand the physics of electron beam damage and heating in nanoscale materials. Finally, it is suggested to develop standard tools and methods based on valid and precise models to qualitatively evaluate the electron beam damage or heating when it cannot be prevented.

Chapter 6

Stability of Au–Pt Nanoparticles

6.1 Introduction

In Chapter 3, we explored the consequence of size on the stability of a liquid core/solid shell Au–Pt nanoparticle (NP) (Fig. 3.9(a)). We also computed the miscibility gap for Au–Pt NPs of various sizes (Fig. 3.13). The main purpose of this Chapter is to provide experimental evidence of the size effect on the phase stability of Au–Pt NPs using the characterization techniques developed in Chapter 4.

Two classes of questions arise concerning the thermodynamic stability of NPs:

- *(i) Shape and phase juxtaposition*: What would be the most stable configuration of a segregated NP? To cite a few possibilities, the system could adopt a core-shell geometry (if so, which phase would be at the core?); a segregated structure on either side of a flat interface; or even chess-board like structure (Le Bouar et al. 1998; Guiton and Davies 2007). Several possibilities also arise for the nature of the interface: it could be crystallographically flat or diffuse, and, depending on the relative mismatch, coherent, semi-coherent, or incoherent. In the case of a coherent interface, would a stress field distributed within the NP accommodate the presence of a mismatch, and in return, affect the NP equilibrium? And finally, would the equilibrium shape of a NP composed of two solid phases still be a simple sphere with the possibility of faceting or would a more complex shape be taken?

- *(ii) Composition and kinetics*: If two phases coexist within a NP, such as the α and α' of the Au–Pt phase diagram, what would be their respective composition and how would they differ from the bulk phase diagram? Would spinodal decomposition occur in a nanosystem and if so, how would the kinetics of the decomposition be affected by the presence of surfaces and interfaces?

We have certainly tried to address some of the questions raised above by taking some of the size-dependent terms into consideration in the calculations performed in Chapter 3. However, other theoretical aspects could not be addressed by the calculation because of a number of assumptions and approximations that were used pertaining to the interface and surface energies. In this Chapter, we provide *a posteriori* answers to some of the questions raised above by the study of the internal structure of

Au(core)-Pt(shell) (Au@Pt) NPs annealed at various times and temperatures. The other questions will remain open but we will describe possible experiments that could address them.

This Chapter is divided in five sections. Following a descriptions of the experimental procedure and the challenges encountered in such experiments, in Section 6.3 we compare the radial composition profile of a NP annealed at low temperature to the numerical simulations of the diffusion within a composite sphere. Section 6.4 shows the various stages of transformation of a Au-Pt NP annealed at higher temperatures. The comparison of the composition of the segregated phases with the bulk phase diagram is discussed in terms of size effects in Section 6.5. Finally, Section 6.6 is devoted to discussions and speculations on the interface separating segregated phases.

6.2 Annealing Au@Pt nanoparticles

Au@Pt NPs were first loaded onto a silicium-supported silicon nitride membrane as discussed in Section 4.4. Two methods are used to anneal NPs at a given temperature:

- *(i) Ex-situ annealing*: A $1/4''$ diameter quartz tube was first sealed at one end using an oxygen/natural gas torch and connected to a vacuum system. The quartz tube was then heated to high temperatures using the torch while being pumped to promote desorption of impurities. After cooling, the NP-loaded TEM grid was introduced in the tube and connected again to the pumping station. A residual pressure of $\sim 10^{-5}$–10^{-6} Torr, was ensured using a cold trap before high purity helium or argon was backfilled into the tube. The ampule was then sealed off with the torch;

  The pressure in the tube depended on the annealing temperature and was chosen to avoid overpressure. Typically, for annealing temperatures of 300°, 600° and 800 °C, the ampule was sealed at ~50, 30 and 20 kPa, respectively. The ampule was then inserted into a furnace for a specified temperature and time and subsequently quenched in water. The role of the gas was to ensure a high quenching rate by promoting the heat transfer from the quartz tube wall to the NPs.

- *(ii) In-situ annealing*: Thin specimens can be heated *in-situ* inside a transmission electron microscope (TEM) using a hotstage. The heating and cooling time for a 600 °C experiment is typically about 5 min and occurs in high vacuum (10^{-6}–10^{-7} Torr). It was not possible to probe the chemistry of the NPs by EDXS during the *in-situ* anneal since spurious X-rays generated by the modified holder would have flooded the detection system.

Although the nominal composition of Au@Pt NPs (i.e. the size of the Au core and the thickness of the Pt shell) was quite uniform from one particle to another,

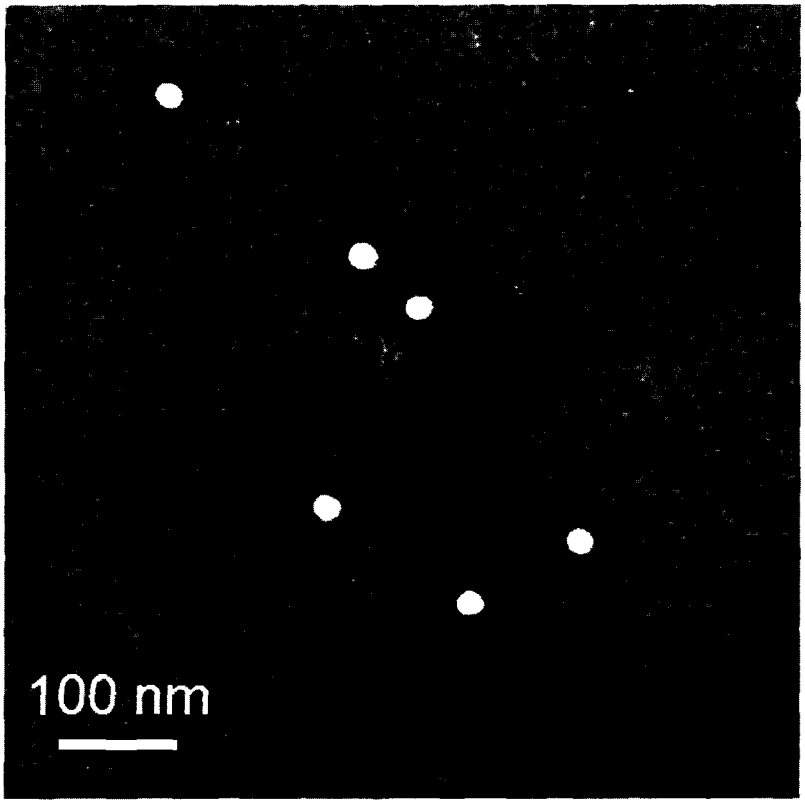

FIG. 6.1: STEM micrograph of Au@Pt annealed 1 day at 300 °C showing zones free of Pt clusters surrounding the NPs.

some variation occurred upon annealing. Let us recall that the final colloidal solution contained fine Pt clusters, some of which constituted the shell of the Au@Pt NPs. Upon annealing, the Pt clusters lying in the proximity of NPs diffused and slightly increased the Pt content of the NPs. The annular dark-field (ADF) scanning TEM (STEM) micrograph in Fig. 6.1 shows evidence of a Pt clusters-depleted ring surrounding individual Au-Pt NPs.

Surprisingly, the most challenging aspect of annealing NPs was to avoid contamination. As a consequence of high reactivity intrinsic to NPs, the metallic species present in the vapor would invariably diffuse within the NPs upon annealing. Despite extreme care in the preparation of the specimen, when Ti, Ni or Mo mesh grids were used, the NPs could be contaminated up to 30% at. with Cu, Fe, Zn, Ag* or other low-vapor pressure transition metals. The relative amount of contaminants with re-

*Cu and Ag preferentially segregated in the Au-rich part of the NP while Fe and Zn would typically be found on the Pt-rich phase. Sn, Ag and In were sometimes detected within the NPs, likely originating from cross-contamination with specimen prepared by other users in the laboratory, at the time of preparation.

spect to Au and Pt increased with annealing time. For heavily contaminated NPs, the contaminant was observed to precipitate on one side of the NP, and, in some cases, oxidize. The contaminants would only be detected within the NPs and not on the surrounding substrate. The detection of such contaminants was not due to instrumental contribution by the microscope since they were not detected in the NPs prior to annealing.

Identifying and avoiding the source of the contaminants was a painfully long process. First, the water to prepare the Au@Pt NPs was changed to distilled and deionized-type water (provided by Milli-Q^{TM}-type systems) and care was taken to avoid the contact with metals. Dedicated glassware was used for the chemical synthesis. Various substrates were used to coat the Ti, Ni and Mo grids: commercial (SPI Supplies) and home-made (Section 4.4) amorphous carbon films and plasma coated amorphous silicon nitride films. The deposition method (plasma evaporation, arc discharge and ion sputtering) and the equipment used for depositing carbon on the grids was changed several times together with the type (graphite rods, HOPG) and supplier of carbon. The quartz tubes were precleaned and pre-annealed. Prior to the gas backfill, the quartz tube was pumped for longer times and the pumping station and vacuum lines were individually replaced, and finally the lab space, where the specimen preparation took place, was moved to a cleaner location. To trap the contaminants, the TEM grids were annealed in the presence of Au NPs coating the quartz ampule. None of the precautions mentioned above significantly reduced the contaminant level within the NPs.

The test which identified the origin of the contaminants as the metallic TEM grid was the following: a silicon-supported silicon nitride membrane and a commercial amorphous carbon-coated Mo grid, both from SPI Supplies, were each loaded with Au@Pt NPs and, one after the other, annealed at 600 °C for 3 h in the JEOL TEM using a hotstage. The grids where then transferred to an analytical holder for analysis. While the Cu level within the NPs on the Mo grid reached 25% at., the NPs from the Si-nitride membrane were found to be free from such contaminants. The Si-nitride membranes were thus preferred over the metallic-mesh TEM grids to perform the experiments.

Whether the AuPt NPs-loaded Si membrane were annealed in a TEM or in a quartz ampule in a regular furnace, a low level of contamination ($\lesssim$3–5% at. Zn, preferentially segregated in the Pt) could be detected within individual NPs. The advantage of using the quartz ampule setup for annealing the NPs over the TEM hotstage is the higher quenching rate. Therefore, the experiments discussed in this Chapter were obtained with Si-nitride membranes annealed in a quartz ampule and we can quote a level $\lesssim$3–5% at. Zn, in all the NPs studied.

6.3 Spherical Diffusion Profile

6.3.1 Experimental Diffusion Profile Following a 24 h annealing at 300 °C, it appears clear from the EDX maps of Au@Pt NPs in Fig. 6.2 that the core-shell configuration is preserved. From the HREM image, the fine Pt clusters forming the Pt shell have sintered into several crystalline domains (Fig. 6.2(a)). Although the EDX map somewhat resemble that of a Au@Pt NP (see for instance Fig. 4.5), when their (projected) radial diffusion profiles (Fig. 6.2(c)) are compared, one realizes that interdiffusion has taken place. Indeed the shell is enriched with up to ~25% Au and some Pt has diffused to the core, as compared with a pristine Au@Pt NP. The Bracewell's and Beniaminy's reconstructed concentration profiles are shown in Fig 6.2(d) (Section 4.6.3). From the reconstruction, the composition of the Au-rich section is roughly constant throughout the core and is estimated to ~82%. Given the nominal composition of the NP of Fig. 6.2 (~ 64% at. Au) and its size (~21 nm diameter), one can easily confirm that the interface must be located at a radius of ~9.2 nm.

6.3.2 Simulated Diffusion Profile The parameters (size and composition of the core and the shell) extracted from the NP in Fig. 6.2 can now be used as input for the simulation of interdiffusion in a composite sphere. The purpose of this simulation is to estimate the total time for a Au@Pt NP to saturate its respective components at a given temperature. We simulated the interdiffusion in a spherical symmetry with initial conditions given by the Au@Pt configuration with boundary conditions defined by the solubility limits of Au in Pt and Pt in Au. To satisfy the constraint of mass balance, we needed to consider a moving boundary, a complication that prevented us from using directly the tools available in subroutine libraries for solving sets of second-order parabolic partial differential equations.

The simulations presented in this Section were coded with Matlab™. We have implemented the numerical solution to the moving boundary diffusion problem to calculate the profile of a binary alloy having a spherical symmetry. The code (listed in Appendix F) uses a Murray-Landis variable grid spacing according to the algorithm developed by Tanzilli and Heckel (1968). We have modified the algorithm to incorporate a composition-dependent diffusion coefficient (Darken 1948), following the suggestions made by Sekerka and Wang (1999). The code solves a set of two differential equations based on Fick's second law of diffusion by finite-difference techniques under the constraint of mass balance flux through the interface. Table 6.1 lists all the important parameters used in the simulation.

The diffusion coefficient is the parameter having the greater impact on the total homogenization time and is unfortunately the most imprecise. It was preferable to

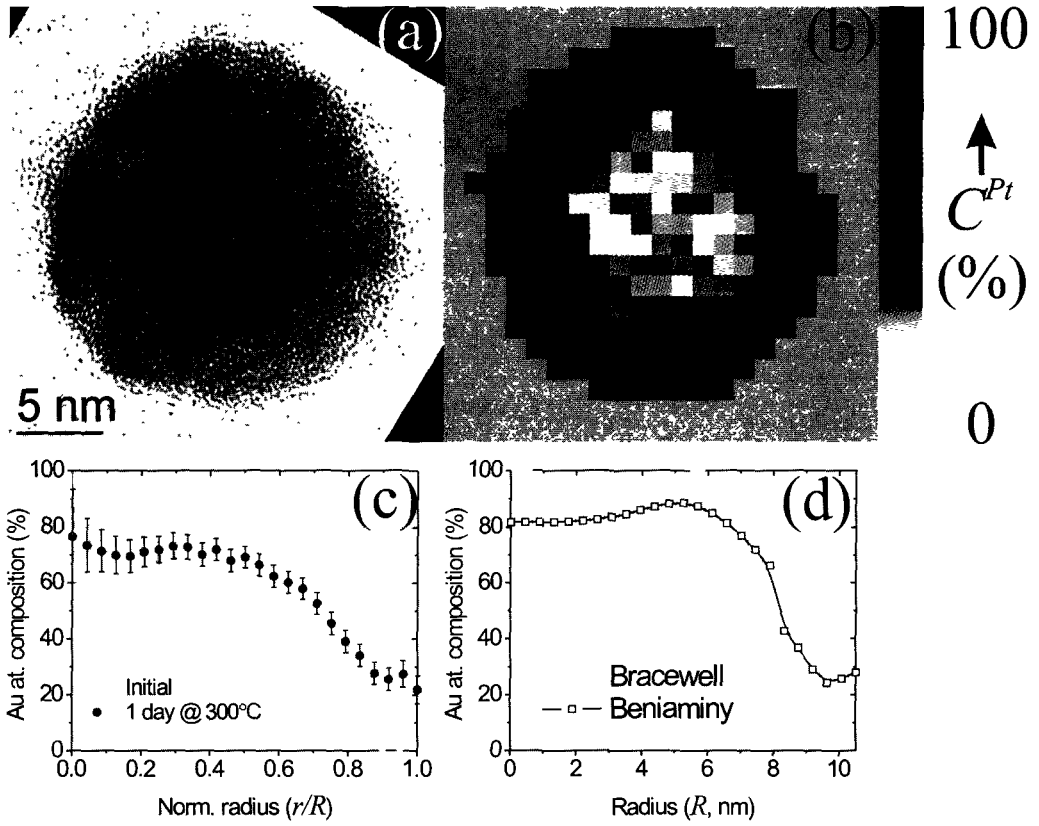

FIG. 6.2: HREM (a) and EDX map (b) of an initially pure Au@Pt NP annealed at 300 °C for a day. (c) Angular projection of the EDX map shown in (b) (black circles) compared with that of an as-synthesized NP (grey squares). The abscissa scale is normalized by the radius of the particle to facilitate comparison. (d) Radial reconstruction of the angular profile of (b) using Bracewell's (grey line) and Beniaminy's (open squares) algorithms discussed in Section 4.6.3.

choose diffusion parameters from thin films experiments rather than bulk ones (e.g. Bolk (1961)) for two reasons. Firstly, data points from bulk experiments have been obtained at high temperatures and would need to be extrapolated over a large temperature range, hence introducing unacceptable uncertainties. Secondly, the diffusion mechanism within NPs is expected to share some similarities with that of a thin film. The activation energies of the diffusion coefficients in thin films are usually typical of grain boundary-controlled mechanism.

It is not obvious which diffusion mechanism would apply to our NPs. Fig. 6.2(a) shows that the NP is composed of several grains suggesting that a grain boundary diffusion model should be adopted. However, an argument could be made that surface diffusion should dominate, given the intrinsic high surface-to-volume ratio of NPs. According to empirical relationships, the lattice (D_L), grain-boundary (D_{GB}) and

TABLE 6.1: Parameters used for the numerical simulation of interdiffusion within a Au@Pt NP. The terminal compositions are taken from the example in Fig. 6.2(d). The parameters of the diffusion coefficients of Au in Pt are taken from McGuire et al. (1978) and those of Pt in Au, from Sinha et al. (1974).

	Core	**Shell**
Starting composition (at.% Au)	100	0
Terminal composition (at.% Au)	82	25
Starting geometry (radius, nm)	9.0	10.5
Terminal geometry (radius, nm)	9.2	10.5
D_0 (cm^2/s)	1.8×10^{-2} [a]	6.6×10^{-8}
Q (eV)	1.65	0.95
Number of nodes	75	25

[a]There is an inconsistency in reference McGuire et al. 1978 concerning the preexponential factor: the abstract, the body of the text and conclusion cite a value of 0.18 cm^2/s while the data displayed in the Arrhenius plot (Fig. 4 of the paper) is annotated with an equation having a preexponential factor equal to 0.018 cm^2/s. The fit was redone with the available data points to confirm the value of 0.018 cm^2/s to be correct.

surface (D_S) diffusion coefficients can be evaluated using (Ohring 2002, p644-6, citing Balluffi and Blakely 1975 and Gjostein 1973):

$$D_L = 0.5 \exp(-\frac{17.0\,T_M}{T})\ \mathrm{cm}^2/\mathrm{s} \tag{6.1a}$$

$$\delta D_{GB} = 1.5 \times 10^{-8} \exp(-\frac{8.9\,T_M}{T})\ \mathrm{cm}^2/\mathrm{s} \tag{6.1b}$$

$$D_S = 0.014 \exp(-\frac{6.54\,T_M}{T})\ \mathrm{cm}^2/\mathrm{s}, \tag{6.1c}$$

where T_M is the melting point and T the temperature. The width of the grain boundary, δ, is usually taken as 5 Å. For Au, at 300 °C, $D_L \approx 3.0 \times 10^{-18}$ cm^2/s, $D_{GB} \approx 2.9 \times 10^{-10}$ cm^2/s and $D_S \approx 3.3 \times 10^{-9}$ cm^2/s. Furthermore, D_{GB} should be significantly larger in the presence of small sized crystallites. According to the master curves of Ohring (2002, p650, citing Gupta 1988), for a grain size of 10 nm, $D_{GB} \approx 1.6 \times 10^{-4}$ cm^2/s. These figures are several orders of magnitude larger than the diffusion coefficients of Pt in Au proposed by Sinha et al. (1974) ($\sim 2.9 \times 10^{-16}$ cm^2/s), at 300 °C. Nevertheless, in the following discussion, we will use the diffusion coefficient taken from experimental data, rather than empirical relations such as Eqs. 6.1.

Note that the values of the preexponential factor and activation energy obtained by Sinha et al. (1974) are deduced from experiments conducted on 550 nm-thick films between 325 and 600 °C while the experiments of McGuire et al. (1978) were performed on 550 nm-thick films between 477 and 627 °C. We chose to extrapolate the diffusion coefficients over a rather large temperature range, from 100 to 1000 °C.

These will be rather crude assumptions, but are necessary for the discussion. One could recompute the results of the simulation with any chosen model by slightly changing the code supplied in Appendix F.

In the simulation, the diffusion coefficients of one component in the other are computed for the desired temperature using an Arrhenius relation (with the relevant parameters listed in Table 6.1). The composition-dependent diffusion coefficient, $\widetilde{D}(C)$, is locally evaluated using Darken's relation (Darken 1948):

$$\widetilde{D}(C) = D_{\mathrm{Au}} C^{Pt} + D_{\mathrm{Pt}} C^{Au}. \tag{6.2}$$

An increased number of nodes was chosen to reproduce the core since the Pt shell quickly homogenized. The time step was typically $\lesssim 10^{-2}(r/N_r)^2/D$, to ensure numerical stability (Tanzilli and Heckel 1968), where r, N_r and D are the core radius, number of nodes for the core and the diffusion coefficient, respectively. The simulation is stopped after a time referred hereafter as the equilibration time, t_{Tot}, and is defined as the time required for the system to satisfy the following equilibrium conditions: *(i)* the compositions of both phases have reached 99.9% of their terminal composition and *(ii)* the interface has attained at 99.9% of its final position. We define a total homogenization time, t_{Hom}, as the time required for the core and the shell to satisfy the homogenization criteria. Similarly, the time required for the interface to stop can be defined as t_{Int}.

Snapshots at various times of the radial composition profiles of an evolving Au@Pt NP at 300 °C are shown in Fig. 6.3(a). After only a minute or so (dashed curve), the Pt shell is already saturated with Au and exhibits a homogenous profile while the core is developing the typical diffusion profile near the interface. After ~20 min (dash-dot curve), the simulation is terminated, since the composition is considered homogeneous in both phases and the interface is stalled. Notice the unconventional movement of the interface: following an early and large displacement towards the center, the interface slowly returns to its equilibrium position in the opposite direction. This can be explained as follows: at first, Au diffuses into the Pt shell and saturates it almost instantaneously , making the interface recede into the Au core. The rest of the process is limited by the diffusion of Pt within the core, making the interface move back slowly in the opposite direction towards the equilibrium position. We can expect this kind of interface motion whenever the diffusion coefficient of the core and the shell differ substantially.

The simulations are performed at various temperatures and the equilibration time is plotted as a function of temperature in Fig. 6.3(b) (full line). As expected, t_{Tot} decays more or less exponentially with temperature. From these simulations, we can expect that an annealing time of a day is more than sufficient to homogenize the NPs at 300 °C while a few seconds are required for any temperature above 500 °C. The dashed curve in Fig. 6.3(b) represents the fraction, t_{Int}/t_{Tot}, of the equilibration time required for the interface to reach its final position. Below ~400 °C, the system

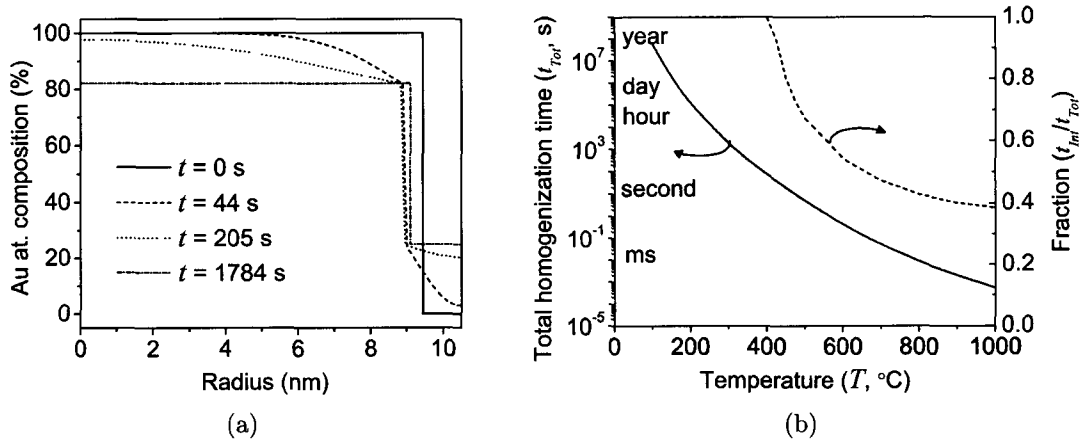

FIG. 6.3: (a) Simulated radial diffusion profile of an initially core-shell NP (full line) after 58 (dashed line), 219 (dotted) and 1346 s (dash-dotted) at 300 °C. (b) Trend of the total equilibration time of a Au@Pt NP for the temperature range 100–1000 °C (left scale, full line). The fraction of the equilibration time required to stabilize the position of the interface is also shown (right scale, dashed curve). Data are simulated with parameters listed in Table 6.1.

satisfies the homogenization criteria well before the interface stabilizes ($t_{Hom} \ll t_{Int}$). Above this threshold temperature, the interface stabilization time becomes a significant fraction of the total simulation time. We can relate this ratio to the ability of the system to undergo structural changes. At low temperatures, the homogenization process is favored while structural changes, such as interface movement, are enhanced at higher temperatures. This could explain the retention of the spherical diffusion profile at a low temperature such as in the case reported in Fig. 6.2(b).

In the simulations presented, only the radial movement of the interface is considered. The expansion or contraction of the spherical interface boundary is a result of the species redistribution between the shell and the core. If the interface no longer retains a spherical symmetry, then the diffusion behavior should rather be modeled using a different geometry.

At this point, it is necessary to compare the diffusion processes occurring within the NPs with the calculated quenching time. If the quenching time is slower or comparable to the total equilibration time (as calculated above) or the characteristic diffusion times, then one can expect the diffusion to occur during quenching, which would considerably affect the interpretability of the results. Here we invoke concepts of heat transfer to estimate the time required for NPs to cool to a low temperature, say 200 °C, where diffusion is –for all practical purposes– halted, even for NPs, according to the graph in Fig. 6.3(a).

The NPs-loaded TEM grid sits at the bottom of a 6 mm diameter ampule (1.15 mm wall thickness) filled with He or Ar. To estimate a conservative value of the quenching

TABLE 6.2: Comparison of the equilibration time for a core-shell NP, the quenching time and the characteristic time for diffusion at temperatures of interest. See text for details.

Temperature	**Total equilibration time**	**Quenching time**	**Characteristic time**
T, °C	t_{Hom}, s	t_{Quen}, s	t_{Cha}, s
300	1.78×10^{3}	8.0×10^{-4}	3.57×10^{3}
600	4.37×10^{-1}	1.1×10^{-3}	4.74
800	8.69×10^{-3}	1.6×10^{-3}	4.48×10^{-1}

time, we will neglect the heat propagation through the ends of the tube and the heat flow through the point of contact of the TEM specimen with the quartz wall. A reasonable assumption is to consider instantaneous heat transfer from the NPs to the gas and from the water to the quartz tube wall: the heat flow is considered to be solely controlled by the ambient gas within the ampule. The problem simplifies considerably: we are left with a 3.7 mm diameter cavity filled with He at a given temperature. From the extensive literature existing on water quenching (Poirier and Geiger 1994, p265), we can estimate the heat transfer coefficient in the order of $\sim 10^4$ $\mathrm{W\,m^{-2}K^{-1}}$. The thermal conductivity and thermal diffusivity of He at 500 °C are 7.78×10^{-2} $\mathrm{W\,m^{-1}K^{-1}}$ and 7.68×10^{-4} $\mathrm{m^2 s^{-1}}$, respectively (Poirier and Geiger 1994, p619). The time required for the center of the cylinder of gas to reach 200 °C upon a quench in water (at 15 °C) can be deduced by solving the heat conduction equation in cylindrical coordinates with the appropriate boundary conditions. The characteristic diffusion time of Au (the fastest diffusing species of the Au-Pt system) can be estimated from the well-known relation: $t_{Cha} = L^2/D(T)$, where L is the characteristic length (taken here as 10 nm, the radius of the NP) and $D(T)$, the diffusion coefficient of Pt in Au at a given temperature T (values are taken from Table 6.1).

Table 6.2 compares the total equilibration time, characteristic time for diffusion and quench time at the temperatures of interest. It can be appreciated that the quench time is orders of magnitude shorter than the characteristic diffusion time across a 20 nm diameter NP at the temperatures of interest (300-800 °C) but comparable to the total equilibration time at high temperatures. It should be safe to assume that the conclusions drawn for the experiments at 300 °C are independent of the quench rate of NPs. Alternatively, if homogenization profiles were analyzed from NPs annealed at high temperatures ($\gtrsim$800 °C), then the true annealing temperature would be considered lower than the ambient temperature of the furnace. Much shorter characteristic times are expected if we use the diffusion coefficients computed with Eqs. 6.1 rather than those obtained by Sinha et al. (1974). In these circumstances, the same conclusions are inapplicable and considerably faster quench rates would be required to capture the nanostructure at high temperatures.

There is need to adapt the concept of diffusion coefficient to nanosystems as the following demonstration will show. Let us assume that the equilibrium vacancy concentration, X_v^e, can be written as (Porter and Easterling 1992):

$$X_v^e = \exp\frac{\Delta S_v}{R}\exp\frac{-\Delta H_v}{RT}, \tag{6.3}$$

where T is the temperature, R is the gas constant, ΔS_v and ΔH_v are respectively, the change in the entropy and enthalpy, upon adding one mole of vacancy. Taking the first term of Eq. 6.3 to be equal to $\sim$3 and $\Delta H_v \simeq$1 eV per metal atom (both values are suggested by Porter and Easterling 1992, p44), one can expect $\sim 5 \times 10^{-6}$ vacancies per metallic atom at 600 °C. However, in a 10 nm diameter Au NP, one can count about 3.2×10^4 atoms, which is less than a single vacancy per NP at this temperature. Given that the vacancies are required for all active diffusion processes, these estimates imply that diffusion would be forbidden in small systems. A realistic approach is to consider an "effective" diffusion coefficient, which takes into account the residence time of a vacancy within a NP of a given size. Accordingly, as the size of the NP increases, the residence time also increases in such a way that the effective diffusion coefficient approaches its bulk equivalent. The additional requirements to the traditional approach of random jumps should include the presence of a spherical boundary and a point of entry on a given surface. A size-dependent diffusion coefficient would definitely be useful to better understand and ultimately predict high-temperature behavior of NPs. We refer the reader to a paper by Shibata et al. (2002) for a thorough discussion of this topic from a molecular dynamics perspective.

The simulations presented here assume that the composite sphere geometry is preserved indefinitely. Even for low temperatures, it is a matter of time before an instability in the shell leads to a breakdown of the spherical symmetry. An example of an early collapse of the spherical symmetry is shown in Fig. 6.4 by the EDX map of the NP annealed at 300 °C for a day. The eccentricity of the core is obvious and we can assume that it precedes the evolution of the structure towards a more stable configuration.

6.4 Morphogenesis of Au@Pt NPs

After only 10 min at 600 °C, the initial core-shell symmetry (Figs 6.5(a,b)) is completely lost, as seen in Figs. 6.5(c,d). It appears, in the particular case of Fig. 6.5(d), that the Au core is diffusing to the surface as the Pt shell recedes. Again, the Pt clusters have sintered into 4–6 nm domains.

This transformation cannot be considered as spinodal decomposition, nor is the morphology typical to this type of phase transformation since the starting phase is not a solid solution. We can speculate that the morphogenesis is triggered by compositional or structural fluctuation or instability in the shell. The analysis of

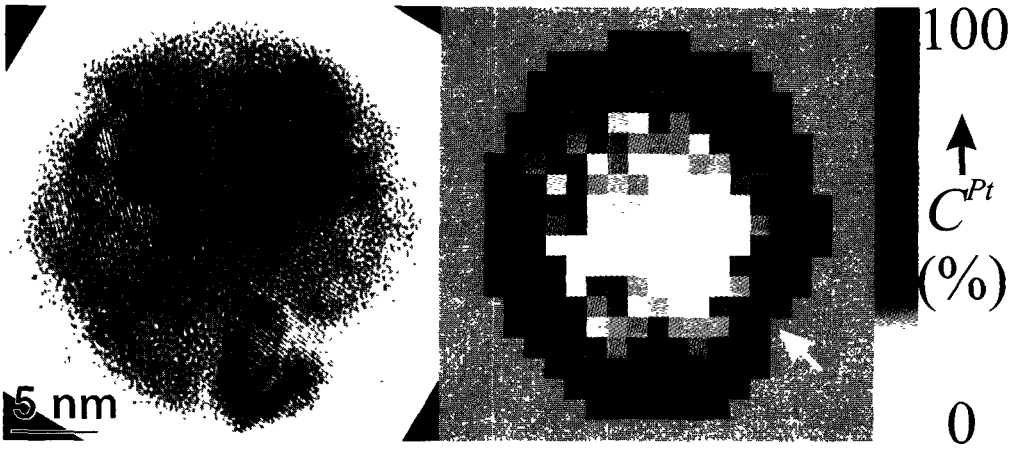

FIG. 6.4: HREM (a) and EDX map (b) of a Au@Pt NP annealed 1 day at 300 °C with a Au-rich core exhibiting slight eccentricity.

the stability of an isotropic core-shell NP against a compositional or structural local variation (or periodic variation, i.e. characterized by a wavelength) would provide the grounds for such a speculation, but was not attempted here.

Following a 3 h annealing at 600 °C, the NP becomes completely phase segregated as depicted in Figs. 6.5(e,f), with a flat interface separating a Au-rich and a Pt-rich subregions. The NPs were not always found in this orientation, most of the particles had their interface tilted with respect to the electron beam (e.g., looking ahead in Fig. 6.6(d,e)), therefore giving the wrong impression that a large concentration gradient existed. In the following discussions, we will focus on the specific cases where the interface was the sharpest.

Figs. 6.6(a,b) and (d,e) show two examples of Au-Pt NPs after 8 h annealing with the same type of internal structure as after a 3 h anneal. Since no change in morphology is observed between 3 and 8 h, we can assume that this configuration – composed of a Au-rich and a Pt-rich halves– is found experimentally to be more stable than the core-shell configuration. This result also demonstrates that the structures such as those found after 10 min at 600 °C (Figs. 6.5(c,d)) are intermediate or transient configurations. Finally, at 800 °C, only 2 h were sufficient to induce the segregated morphology (Figs. 6.7(a,b,d,e)).

We can presume that the system is minimizing the area of the interface by adopting a configuration with a flat interface. We can speculate that the driving force for the transformation is provided by the minimization of the interfacial area. The observations are contrary to the common expectation of having the element of the lowest surface energy at the surface of a core-shell structure.

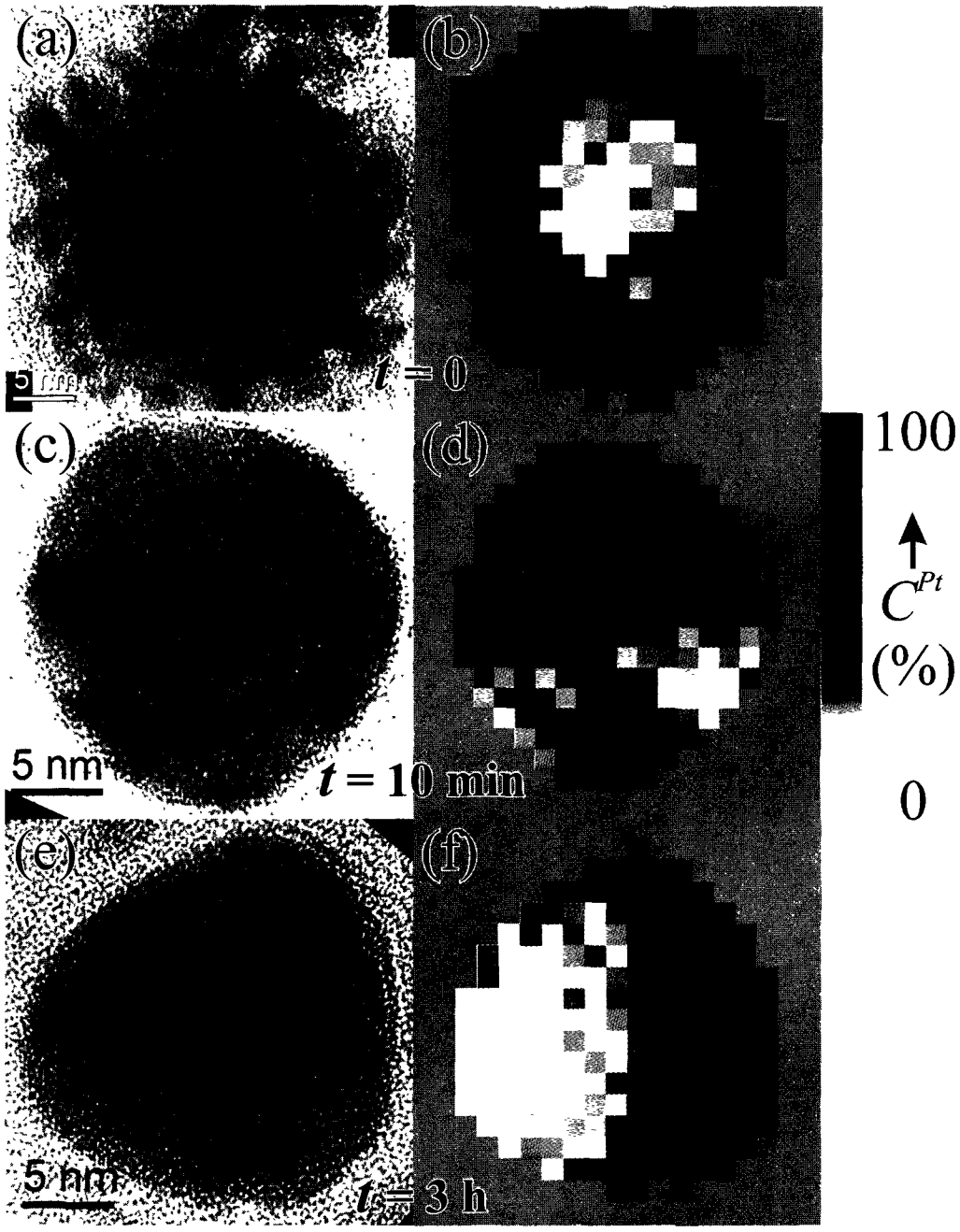

FIG. 6.5: HREM (left panels) and corresponding EDX map (right panels) showing the morphogenesis of an initially Au@Pt NP (a,b) after 10 min (c,d) and 3 h (e,f) at 600 °C.

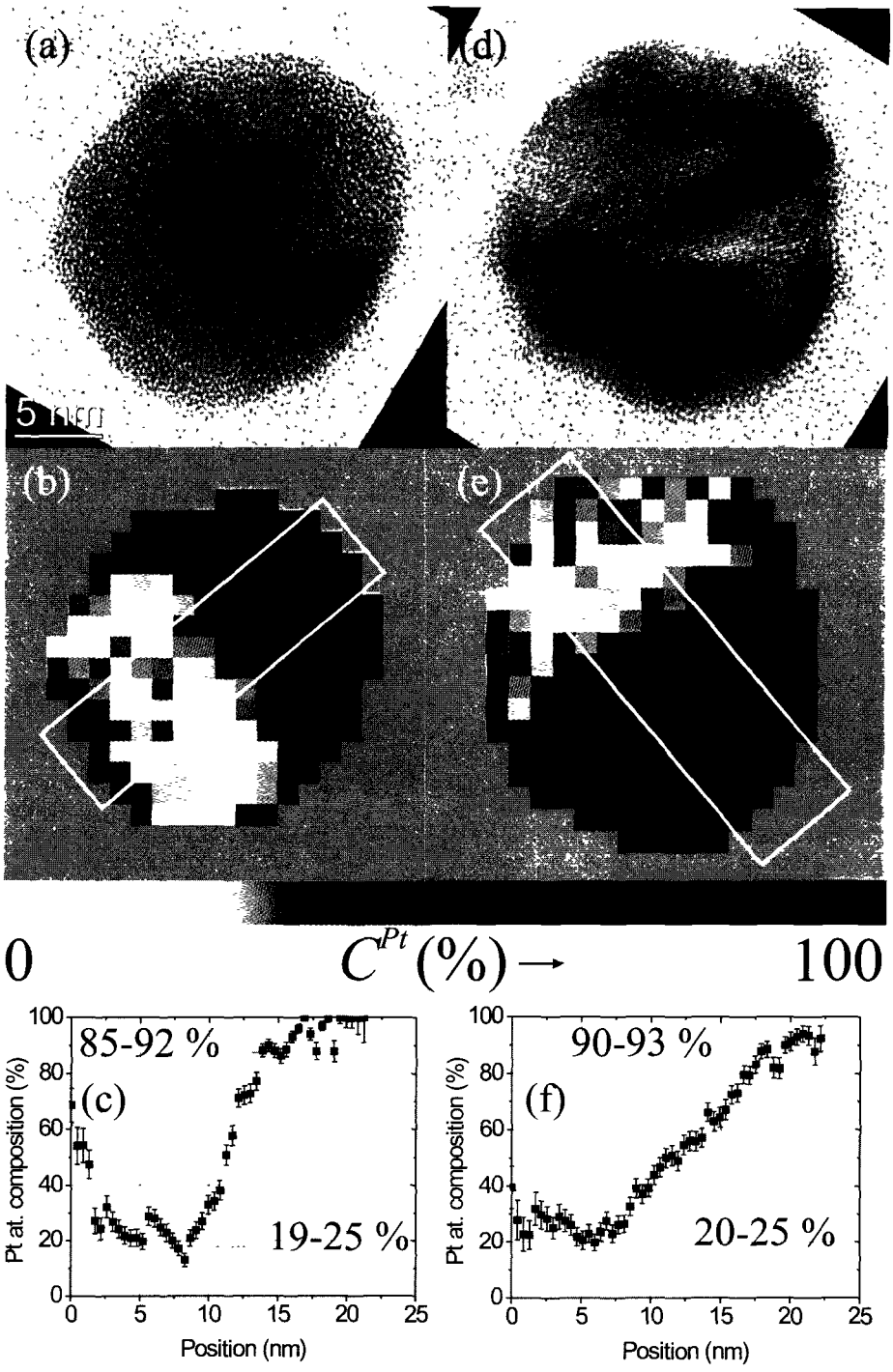

FIG. 6.6: Two examples ((a–c) and (d–f)) of phase segregated Au-Pt NPs after annealing at 600 °C with corresponding HREM micrographs (top panels), EDX maps (center panels) and integrated profiles across the interface (bottom panels). The profiles are generated by projecting the data points from the region selected in the white boxes drawn on the EDX maps along the interface. The origin of the profiles is on the left-side of the box. The estimated compositions of each side of the NP are indicated on the profiles.

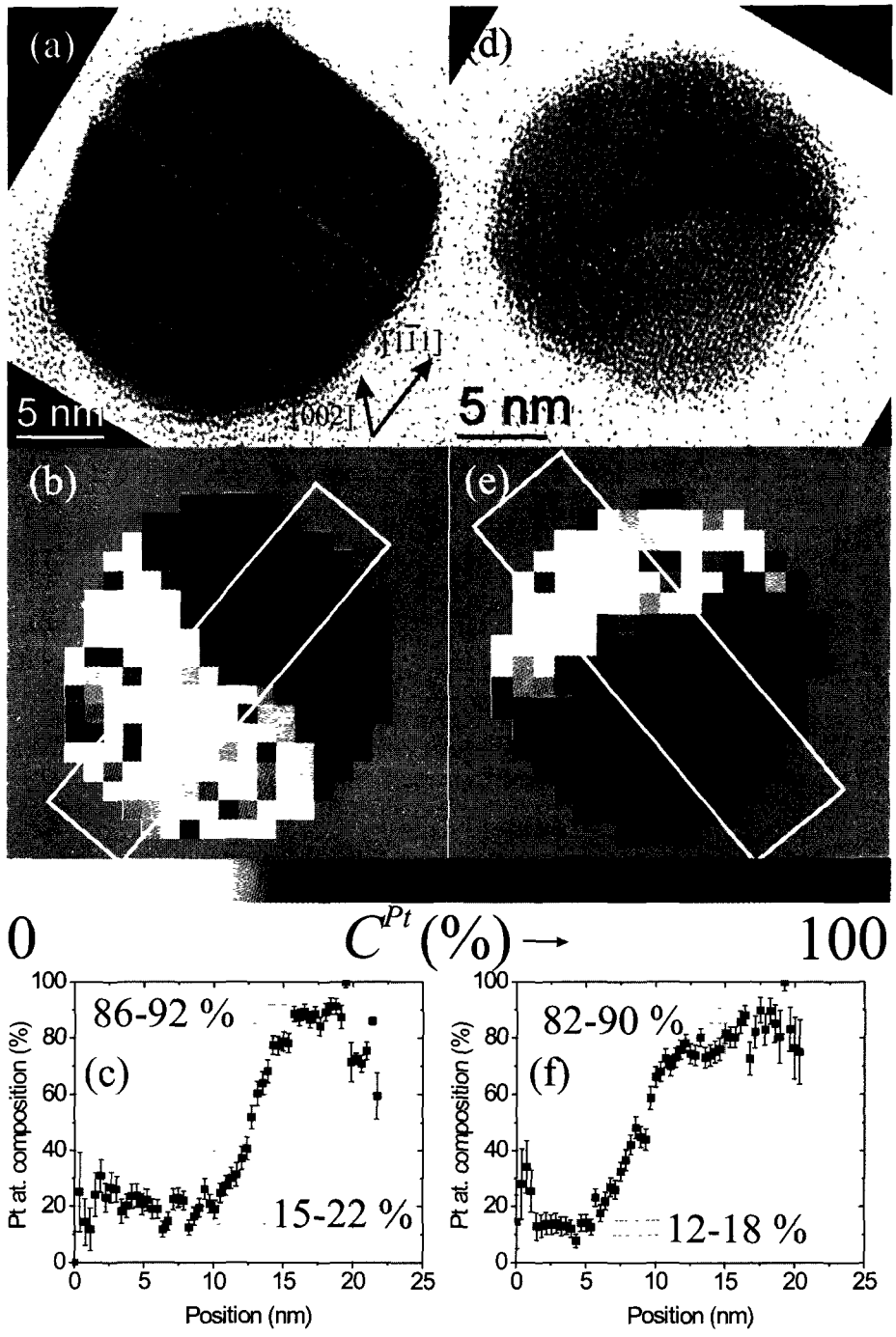

FIG. 6.7: Two examples ((a–c) and (d–f)) of phase segregated Au-Pt NPs after annealing at 800 °C with corresponding HREM micrographs (top panels), EDX maps (center panels) and integrated profiles across the interface (bottom panels). The profiles are generated by projecting the data points from the region selected in the white boxes drawn on the EDX maps along the interface. The origin of the profiles is on the left-side of the box. The estimated compositions of each side of the NP are indicated on the profiles.

We suggested that the core-shell structure retained at 300 °C is unstable and given more time, it would evolve irreversibly towards the configuration observed at higher temperatures. In Section 6.3, we demonstrated that the diffusion coefficients within NPs computed by empirical relations such as Eqs. 6.1 are several orders of magnitude higher than those used for the simulation. If the diffusion coefficients were indeed 5 or 6 orders of magnitude larger, the final configuration of the NPs would be achieved in less than a second at 300 °C, (according to the characteristic times of Table 6.2). However, after an annealing of 24 h at 300 °C, the NPs still exhibited a core-shell symmetry. This suggests that the diffusion coefficients used in the simulations were actually slightly *too high* by at least an order of magnitude (at 300 °C). The same conclusions can be drawn by inspection of Fig. 6.5(d): 600 s were not sufficient to allow the NPs to reach their equilibrium structure. When compared to the characteristic time of 5 s, one realizes that the diffusion coefficients need to be at least 2 orders of magnitude larger at this temperature.

The peculiar contrast observed at the interface in the HREM micrograph (Fig. 6.7(a)) suggests the existence of a small tilt with respect to the [110] zone axis. In this particular case, the interface is straight and a clear orientational relationship exists between the Au-rich and the Pt-rich phases. In comparison, Fig. 6.5(f) shows a phase segregated Au-Pt NP (3 h at 600 °C) with a slightly *curved* interface. We will discuss the nature of the interface in more details in Section 6.6.

The profiles in Figs. 6.6(c,f) and Figs. 6.7(c,f) were obtained from the projection of the pixels contained in the tilted white box drawn in the EDX map. The dataset was projected parallel to the interface and the profile displays the composition along the length of the white box from the Au-rich to the Pt-rich side of the NP. The width and the tilt of the interface can be deduced from the profiles, if certain assumptions are satisfied. For example, in Fig. 6.6(c), the interface spans from the ~10 to 13 nm relative position while in Fig. 6.6(f), it is noticeably wider and extends from ~6 to 20 nm. From simple trigonometry arguments, the angle of the normal of the interface with respect to the electron beam path is equal to $\arcsin(w/D)$, where w is the width of the interface and D, the NP diameter. The interface tilts in Figs. 6.6(c) and (f) are thus estimated to 7° and 36°, respectively. This estimate does not take into account the electron beam broadening, the uncertainty in estimating the angle of the integration box or the presence of a curved interface, all of which can broaden the image of a straight interface and, consequently lead to an overestimation in the tilt angle.

6.5 Surface Effects on the Au–Pt Phase Diagram

Phase-segregation can also be mapped using quantitative HREM (q-HREM) if a sharp set of lattice fringes is apparent throughout the region of interest(Hÿtch 1997; Snoeck et al. 1998; Hÿtch et al. 1998). The Au-Pt system is ideal in this regard since it follows closely Vegard's law (Fig. 6.8). In other words, since the lattice parameter is

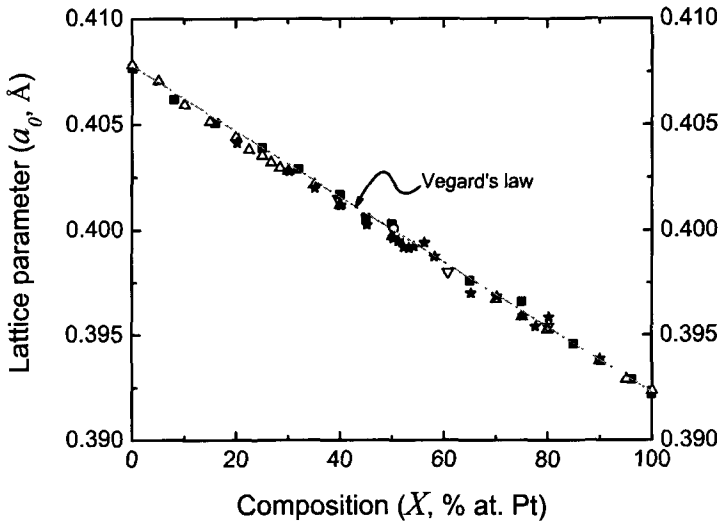

FIG. 6.8: Trend of the lattice parameter of a Au-Pt alloy with Pt content. The data was compiled by Okamoto and Massalski (1985). Vegard's law (grey line) is shown for comparison. ■ Johansson and Linde 1930, ○ Raub and Worwag 1955, △ Grube et al. 1951, ▽ Carpenter 1967, ★ Darling et al. 1953.

TABLE 6.3: Expected strain of the Pt-rich side of the AuPt NP in Fig. 6.7(a,b) relative to the Au-rich side. The strain is calculated from Vegard's law, using the lattice parameters of Au and Pt, taken as 4.0782 and 3.9242 Å, respectively.

Particle side	**Composition** at. Pt, %	**Lattice parameter** a_0, Å	**Relative strain** ϵ, %
Pt-rich	86–92	3.937–3.946	~2.4–2.9
Au-rich	15–22	4.044–4.055	

proportional to the composition, it can therefore be mapped from the relative strain. We take for example the NP annealed at 800 °C shown earlier (Fig. 6.7(a,b)). The Pt profile across the interface (Fig. 6.7(c)) reveals that the composition of the Au- and Pt-rich sides of the NP varies between 15–22% and 86–92% at. Au, respectively. Using Vegard's law, the relative strain of the Pt-rich side with respect to the Au-rich side translates to a 2.5–2.9% strain (Table 6.8). This analysis excludes the surroundings of the interface since the stress may not be entirely compositional in nature in this region.

Using the lattice spacing of the HREM micrograph (Fig. 6.7 (a)), it is possible to generate a strain map. Random variations in the fringe spacing and orientation in real space blur the corresponding spot in Fourier space. The spatial distribution of the

variation of the lattice can be mapped from the analysis of a given feature in Fourier space. Hÿtch et al. (1998) developed an algorithm that can map in real space the deviation from a reference lattice based on the analysis of the corresponding reflection in Fourier space. The technique allows one to generate an image whose intensity is related to the local lattice variation with respect to a reference point.

The {002} reflections were used to generate the strain map in Fig. 6.9(b)[†] with respect to the local lattice parameter marked by a white circle in the Au-rich part of the NP. The strain map is consistent with the EDX map (Fig. 6.9(a)): the NP is separated by a straight interface and the relative strain difference between both halves is roughly equal to the relative strain calculated from Vegard's law (Table 6.3). EDX and strain maps are two independent signals, each having their respective artifacts. However, taken together, they can be used in a complementary fashion to check the validity of small fluctuations observed in each individual map. For example, the edge of the AuPt NP marked by an arrow in Fig. 6.9(a) shows a local increase in the Pt content with respect to the surrounding areas. This fluctuation can be readily confirmed by a corresponding strain decrease. However, the sharp fluctuation observed at the bottom of the strain map (pointed arrow in Fig. 6.9(b)) is not accounted for in the EDX map as it arises from delocalization of the lattice fringe overshadowing the atomic planes present on the edge of the NP. In the center of the NP, a region of high strain appears to be concentrated along lines running parallel to the interface. This feature can be assigned to the absence of a coherent set of lattice fringes in the corresponding region of the HREM image, as noted above.

The boundaries of the miscibility gap of a NP at a given temperature can be drawn from the profiles in Figs. 6.6(c,f) and Figs. 6.7(c,f). The average composition of each phase of the NP can be interpreted as the solubility limit of the system and can be compared with that of the bulk. The average composition can be estimated by the level of the plateau on either side of the interface. The measured ranges are compared with the bulk solubilities and those computed for a 10 nm radius NP using Butler equations (Eqs. 3.23) in Table 6.4. For the Au-rich branch of the miscibility gap, the experimental range at 600 °C coincides with the bulk solubility. However, at 800 °C, the measured solubility appears to be much lower than that of either the bulk or a 10 nm radius NP. Alternatively, for the Pt-rich branch of the miscibility gap, the measured solubilities are significantly higher (i.e., more Au is allowed in Pt-rich solid solution) than the expected bulk phase diagram. The higher Au solubilities observed in the Pt-rich part of the NP is in agreement at both temperatures with the predicted solubility of a 10 nm radius NP, as computed using Butler equations.

One can argue that the estimation of the composition range suffers from subjectivity and cannot be compared to the bulk solubility in all fairness. To confirm the tendencies discussed, the data in the profiles of Figs. 6.6 and 6.7 can be represented

[†]The strain map was generated using a script written by M. Hÿtch (CMES-CNRS, Toulouse) using a software "Geometrical Phase Analysis" (commercialized by HREM Research Inc.). A similar map was also obtained using a similar script written by J.-L. Rouvière (CEA, Grenoble).

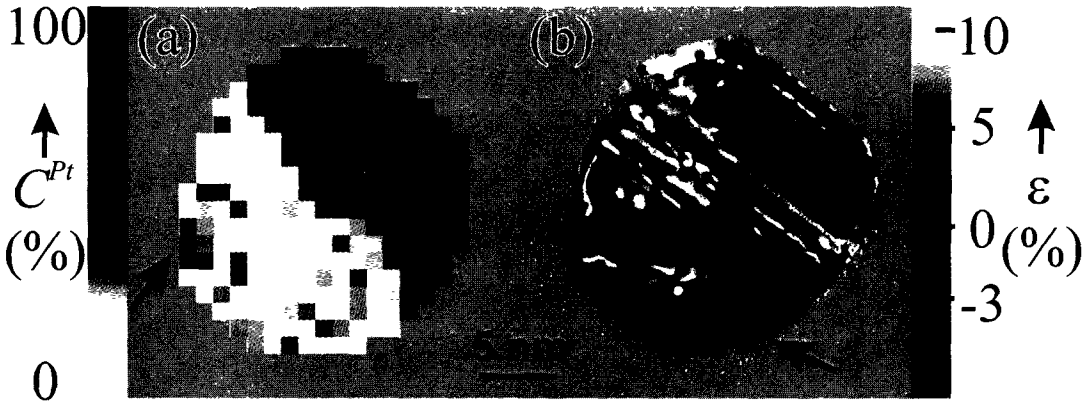

FIG. 6.9: (a) EDXS and corresponding strain map (b) of the AuPt NP in Fig. 6.7(a) (annealed at 800 °C) with their respective legend. The relative strain is calculated with respect to the local lattice parameter marked by the white dot. The background of the EDX and the strain maps were set to a grey level by correspondence with the NP contrast of the STEM (a) and the HREM (b) images, respectively (see Section 4.6.2).

TABLE 6.4: Composition range observed in the segregated phases of AuPt NPs taken from profiles in Figs. 6.6(c,f) and 6.7(c,f) at 600° and 800 °C, respectively. Values are compared with the bulk miscibility gap (Okamoto and Massalski 1985) and those calculated for a 10 nm radius NP using the surface energies computed with Butler equations (Eqs. 3.23).

	600 °C		**800 °C**	
	Au-rich	**Pt-rich**	**Au-rich**	**Pt-rich**
	at. Pt, %		at. Pt, %	
Profile in (c)	15–25	85–92	15–22	86–92
Profile in (f)	20–25	90–95	12–18	82–90
Bulk	19	98	25	95
10 nm NP	18	96	24	92

by a histogram graphs (the top panel of Figs. 6.10(a) and 6.10(b), respectively). The data of the profiles of both NPs at each temperature are combined in the histogram, using a bin size that was set to a value (4%) slightly below the average uncertainty of the measurements. This allows the objective and convenient comparison of the experimental NP solubilities with those of the bulk (black dashed line) and those calculated for a 10 nm radius NP (grey dashed line).

The histograms in Figs. 6.10(a,b) do not report on the individual uncertainty of the EDXS measurements. This poses a problem, since the data points far from the interface, which bears the signal of interest, are probed over the thin portion of the

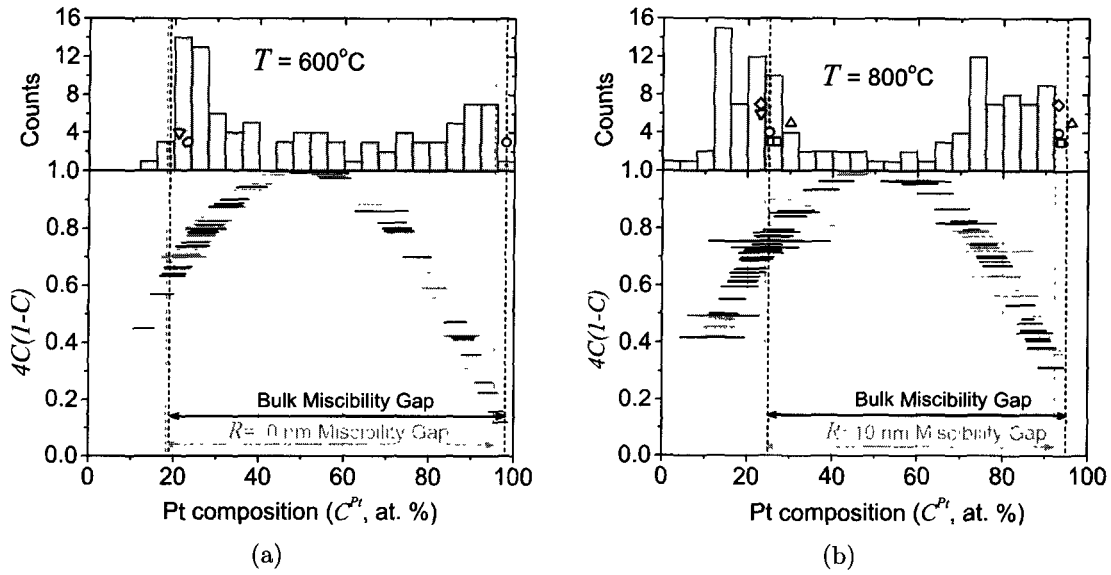

FIG. 6.10: Top panels: Composition histograms (top panels) constructed from profiles of the annealed NPs at 600° (a) and 800 °C (b) (data taken from the profiles in Fig. 6.6(c,f) and 6.7(c,f), respectively). Black dashed lines mark the bulk miscibility compositions. Grey dashed lines mark the miscibility computed for a 10 nm radius AuPt NP using the methodology discussed in Section 3.3. Histogram bar width = 4%. Scatter points in the histograms refer to experimental data from which the bulk phase diagram was assessed (compiled by Okamoto and Massalski (1985)): □ Johansson and Linde 1930, ○ Wictorin 1938, △ Tiedema et al. 1957, ▽ Raub and Falkenburg 1964, ◇ Wictorin 1947. Bottom panels: Different representation of the composition distribution of the same profiles. The individual error bars are reported as the stick length. The ordinates are artificially set to spread the data according to an arch. Grey and black sticks refer to the data in the profiles in (c) and (f) of Figs. 6.6 or 6.7, respectively.

NP, making them uncertain. This argument can be overruled by plotting the same data with individual error bars, such as in the bottom panel of Figs. 6.10(a,b). The data points are now represented by a horizontal bars having their width equal to the 2σ error (Eq. 4.6). The Pt compositions, C are represented on the abscissa and the ordinates are artificially set to $4C(1-C)$, an arbitrary function that conveniently spreads the data points. Black and grey bars refer to each of the two NPs analyzed in Figs. 6.6 and 6.7, respectively. From these plots, it is possible to confirm that the difference between the solubility of Au in Pt within the NP and that of the bulk phase diagram is larger than the measurement uncertainty.

A last argument can be made from the consideration of the uncertainty associated with the miscibility gap of the bulk phase diagram. The miscibility gap is based on a model whose parameters were optimized by Okamoto and Massalski (1985) with results obtained from prior studies of Au-Pt system alloys. The scatter points added on the histograms of Figs. 6.10 refer to the experimental data compiled by Okamoto

and Massalski (1985) at the corresponding temperatures. These values are part of the database used to assess and optimize the Au-Pt phase diagram. It is possible to compute the uncertainty of the miscibility gap boundaries (Malakhov 1997) although it requires one to collect all previous data acquired on the Au-Pt system with their respective measurement uncertainty. Given the extensive dataset available for the Au-Pt system and the relative consistency of the experiments, we do not expect the uncertainty of the miscibility gap in the 600°–800 °C range to overlap the our data points. In any case, it can be argued that the shift observed is larger than the uncertainty of both the experimental measurements and the assessed phase diagram.

The same conclusions can be reached from all three representations of the results (profiles, histograms and the $4C(1-C)$ plots) namely that experimental miscibility points appear to be shifted towards Au-rich values, except for the Au-rich branch of the 600 °C plot. This tendency is surprising compared to the traditional trend of size-induced solubility shift. Indeed, it was discussed in Section 2.3 that a size decrease leads to an increased phase solubility. The statement is true when considering the solubility of a matrix phase with respect to a precipitate. However, we stress the fact that the situation in the case of a dividing Au–Pt NP is different since only *one* phase is concerned. Although these experiments do not confirm or invalidate the model developed in Section 3.3 to predict the dependence of the miscibility gap with size, they share the same trends, namely that the shifts observed are small but significant for the Pt-rich branch.

We finish this Section by presenting results from the annealing behavior of AuPt NPs with a composition close to the miscibility gap. The nominal composition, as discussed in Section 4.4, could be varied by controlling the thickness of the Pt shell. We show in Fig. 6.11 the HREM and EDXS analysis of two NPs with nominal compositions of 25% (a,b) and 32% (c,d) annealed at 600 °C. The former NP has a slightly higher Pt content which likely arises from the presence of a larger number of Pt clusters that have diffused in the NP during annealing, as discussed in Section 6.2. Since the composition is close to the Au-rich branch of the miscibility gap, the NP appears almost single-phased except for a small subregion. It is interesting to note that the small Pt-containing region is completely contained near the surface with an interface that is no longer straight, but sharply curved within the NP. This type of geometry was consistent with the HREM and EDX maps of three other NPs (not shown). Furthermore, the observed NPs appeared spherical and did not exhibit protuberance at the surface.

The average composition of the Au-rich part of both NPs in Figs. 6.11 (b,d) is ~22%, thus slightly higher than the predicted bulk solubility of Pt in Au (~19%). Should the temperature have been slightly higher, complete solubility could have been expected. Unfortunately, it was not possible to deduce the composition of the Pt-rich phase due to the unknown inner structure of the NPs shown in Fig. 6.11. This information could have been of interest for this study since the Pt radius of the small insert has a much smaller curvature than the rest of the NP.

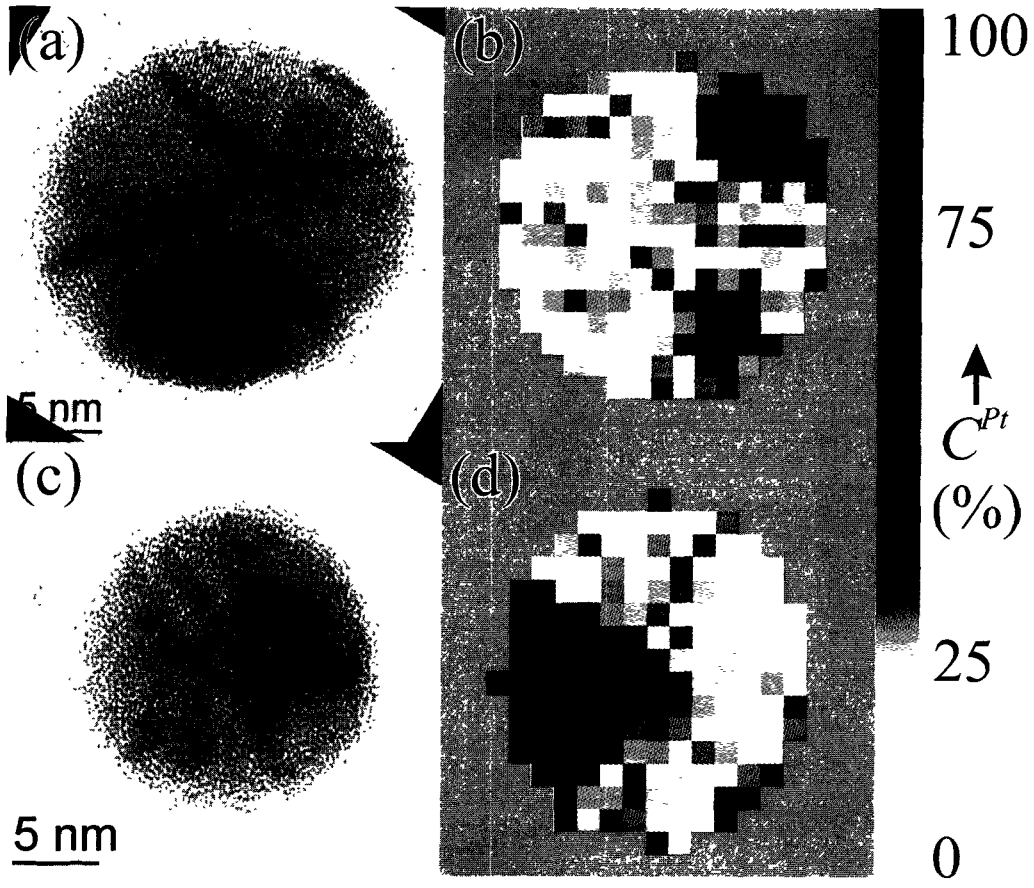

FIG. 6.11: HREM (left panels) and corresponding EDX maps (right panels) of two Au@Pt NPs having a 3:1 Au to Pt initial ratio annealed at 600 °C for 3 h. The nominal compositions of the top (a,b) and bottom (c,d) NP are 25 and 32% at. Pt, respectively.

6.6 Discussion on the Nature of the Interface

The following discussion relates to the HREM, EDX (Fig. 6.7(a-c)) and strain map (Fig. 6.9) of the Au-Pt NP annealed at 800 °C. This NP is of particular interest since it can be considered as a bicrystal separated by an interface. We devote the entire Section to a discussion of the nature of this particular interface based on the information collected by TEM-related techniques.

According to the strain map in Fig. 6.9(b), the average relative strain in the NP is estimated between 2.4% and 2.9% (Table 6.3). Such a large relative strain can either be accommodated by an array of dislocations at the interface (van der Merwe-type geometrically necessary dislocations (van der Merwe 1963a, 1963b)) or by stress distributed (non-uniformly) within the NP. If the dislocations were not present, then the strain would need to be accommodated by long-range stresses. In

such a situation, since Pt is stiffer than Au, the Au-rich hemisphere of the NP would contract to match the lattice parameter of the Pt-rich side. The typical signature of a strain associated with such a single-sided contraction of the NP would be composed of a zero-strain invariant central plane with a local strain increasing towards the edge of the NP and being maximal near the interface. Since this signature is not observed in Fig. 6.9(b) and the strain appears rather mostly uniform in either part of the NP, we conclude that the strain is likely accommodated at the interface by a set of misfit dislocations. In the particular case of the NP in Figs. 6.7(a) and 6.9(b), the HREM and phase signature of dislocations at the interface could be overshadowed by the peculiar contrast visible near the interface.

By indexing the HREM micrograph in Fig. 6.7, one can deduce that the interface is parallel to the $[\bar{1}13]$ direction and the $(1\bar{1}1)$ plane. Given the lattice spacing of the $\{111\}$ planes, the relative mismatch (Table 6.3) and the size of the interface ($\sim$20 nm), we can expect that only 2-3 dislocations are necessary to accommodate the strain in one dimension. It is possible to estimate the two-dimensional configuration of a set of misfit dislocations at the interface of a thin film using the concepts pioneered by van der Merwe (1963a, 1963b). Let us approximate the particular NP in Fig. 6.6(a) as a finite Pt substrate with a thin Au overlayer. Given the thickness of the Au "film", it is reasonable to question whether the compression of the film on the substrate can be completely accommodated by an homogeneous plane strain. There exists a critical misfit, η_c, for a given thickness, h_c, below which adding a threading dislocation does not lower the total energy of the interface. Using the semi-empirical relation $h_c/a_0 = 0.114\eta_c^{-1.22}$ (van der Merwe and Jesser 1988), where a_0 is the lattice constant of the interfacial plane (interatomic distance along the <111> direction) and $\eta \sim 2.4-2.9\%$, we estimate the critical thickness to fall in the range $\sim$2.4–3.0 nm. Since the thickness of the Au-rich overgrowth is about 6 times this value, we expect that only a small fraction of the strain will be indeed relieved by threading dislocations. On the other hand, one can argue that the theory on which the semi-empirical relationship is based upon approximates the lattices sites on either side of an interface by a truncated Fourier series. However, Fourier series cannot appropriately model the finite size of the interface of a divided NP. Furthermore, the proximity of the free surface would lead to stress relaxation. In any case, this small network of dislocations was challenging to observe by HREM and could not be achieved in the framework of these particular experiments[‡].

Let us suppose a diffuse character to the interface shown in Fig. 6.6(c). We wish to explore the hypothesis according to which the 5 nm-thickness of the interface associated with the composition profile can be assigned to the natural width of a diffuse interface. Following Cahn and Hilliard (1958), we can estimate the interface width using

[‡]We have successfully imaged dislocations at the interface of divided NPs by HREM and have generated the corresponding strain maps, but these particular NPs were heavily contaminated. One example is shown in Fig. B-5.

TABLE 6.5: Physical properties of Au, Pt (Lide 2005) and the Au–Pt binary system (Okamoto and Massalski 1985).

Property	Symbol	Units	Au	Pt
Density	ρ	kg/m^3	19.30	21.09
Lattice constant	a_0	Å	4.0782	3.9242
Atomic number	A	kg/mol	0.197	0.195
Shear modulus	λ	GPa	27	61
Poisson ratio	σ	–	0.44	0.38
Gradient energy coefficient	κ	J/m	7×10^{-11}	
Critical temperature	T_c	K	1533	
Critical composition	X_c	% at. Pt	61	

$$l = 2(X_\alpha - X_c)\left(\frac{\kappa}{\Delta f_{Max}}\frac{A}{\rho}\right)^{1/2} \tag{6.4}$$

where κ is the gradient energy coefficient (in J/m), Δf_{Max} is the maximum free energy per moles referred to a standard state of an equilibrium two-phase mixture, ρ is the density (kg/m^3), A is the atomic mass (kg/mol) and X_α and X_c are the equilibrium and critical compositions, respectively. The values of the physical properties of Au, Pt and Au-Pt system are listed in Table 6.5. The gradient energy coefficient, κ, can be expressed as $1/3\, r_0^2 T_c \rho / A$[§], where r_0 is the average lattice constant, T_c is the critical temperature and R the gas constant. When the depression of κ is substituted into Eq. 6.4, it reduces to:

$$l = 2(X_c - X_\alpha)\left(\frac{1}{3}\frac{r_0^2 R T_c}{\Delta f_{Max}}\right)^{1/2}. \tag{6.5}$$

If we assume that the interface retains its high temperature properties following the quenching from 800 °C, $l \approx 8$ Å, according to Table 6.6, which is much thinner than the measured profile width. Some values of the interface width for other temperatures are reported in Table 6.6. We conclude that, if the interface had a diffuse character, its intrinsic width could not entirely account for the width of 5 nm of the interface of the profile shown in Fig. 6.6(c), unless a tilt is present.

We can roughly estimate the interface energy per area of the NP in Fig. 6.7(a), γ_{Int}, by summing the various contributions of a semi-coherent interface:

$$\gamma_{Int} = \gamma_{Che} + \gamma_{Hom} + \gamma_{Dis}, \tag{6.6}$$

[§]Although this relation is valid for regular solutions, we use it for the Au-Pt system to obtain an estimate. Methods for determining the gradient energy coefficient for a non-regular system can become quite involved (Asta and Hoyt 2000; Lass et al. 2006, for instance).

TABLE 6.6: Calculated width of the interface, l (Eq. 6.5) and interfacial energy of a Au-Pt interface at various temperatures. The total interfacial energy (γ_{Tot}) is the sum of the chemical coherent energy (γ_{Che}, Eq. 6.7), the mean energy of misfit per unit area (γ_{Dis}, Eq. 6.8a) and the homogeneous strain energy (γ_{Hom}, Eq. 6.8b).

T °C	l Å	γ_{Che}	γ_{Hom}	γ_{Dis}	γ_{Tot}
			mJ/m^2		
25	5.0	197	70	95	362
300	5.5	151	68	85	313
600	6.5	97	64	94	255
800	7.9	61	59	91	211

where γ_{Che}, γ_{Hom} and γ_{Dis} are the contribution from the chemical coherent energy and the surface energies associated to a plane strain and to a network of dislocations, respectively.

The chemical coherent surface energy component of a diffuse coherent interface, γ_{Che} in J/m^2, can be estimated at a given temperature using the Cahn-Hilliard equation (Cahn and Hilliard 1958):

$$\gamma_{Che} = 2\int_{X_\alpha}^{X_\beta} [\kappa \Delta f(X)\rho/A]^{1/2}\,\mathrm{d}X, \tag{6.7}$$

where $\Delta f(X)$ (J/mol) is the molar free energy referred to a standard state of an equilibrium two-phase mixture.

The surface energies associated with a plane strain and with a network of dislocations, γ_{Hom} and γ_{Dis}, respectively, can be computed using Eqs. 29 and 31 in the paper by van der Merwe (1963a):

$$\gamma_{Dis} = \frac{\mu_{Int} c}{4\pi^2}\{1+\zeta-(1+\zeta^2)^{1/2}\} \tag{6.8a}$$

$$\gamma_{Hom} = -\frac{\mu_{Int} c \zeta}{4\pi^2}\ln\{2\zeta(1+\zeta^2)^{1/2}-2\zeta^2\}, \tag{6.8b}$$

where ζ is expressed by

$$\zeta = \frac{2\pi\lambda c}{\mu p}. \tag{6.9}$$

λ is a function of the mechanical constants while c and p are related to the lattice constants of Au-rich (a_α) and Pt-rich (a_β) phase:

$$\lambda = \left(\frac{1-\sigma_\beta}{\mu_\beta}+\frac{1-\sigma_\alpha}{\mu_\alpha}\right)^{-1} \tag{6.10a}$$

$$c = \frac{2a_\beta a_\alpha}{a_\beta + a_\alpha}. \tag{6.10b}$$

$$p = \frac{a_\beta a_\alpha}{a_\alpha - a_\beta}, \tag{6.10c}$$

where μ and σ are the shear modulus and Poisson ratio, respectively with the subscripts α, β and Int referring to the Au-rich phase, Pt-rich phase and interface, respectively. The lattice constant follows Vegard's law, the Poisson ratio was approximated to vary linearly with composition and the compositional-dependent shear modulus was fitted to a cubic polynomial calculated using the relations suggested by Friedel (1955)[¶]. Once again, we stress the fact that Eqs. 6.8–6.10 are derived by considering an infinite plane, a necessary conditions to describe the periodicity of the atomic lattice and the threading dislocations. Therefore, the values of γ_{Hom} and γ_{Dis} computed in Table 6.6 are likely upper estimates since we expect surface relaxation to accommodate a certain fraction of the misfit strain.

All three contributions to the interface energy increase with decreasing temperature. This can be understood easily: at lower temperature, the composition difference between the α and β phases is larger, leading to a larger chemical surface energy. At low temperature, γ_{Hom} and γ_{Dis} will also be larger owing to the larger misfit.

If we suppose the NP of Fig. 6.7(a) to have adopted an equilibrium shape, we can deduce the interfacial energy based on the knowledge of the surface energy of the faces. This can be done by applying the concepts of vector thermodynamics developed by Hoffman and Cahn (1972) (see also Cahn and Hoffman 1974). This theory successfully predicts the equilibrium shape of two crystals sharing an interface through thermodynamic considerations. The approach considers the surface tension as a force normal to the surface while surface anisotropy, acting as a torque, contributes to the local force balance as a tangential force applied to the surface. The theory of vector thermodynamics is considered as an extension of the Wulff or the so-called "γ" plots.

Assuming the NP of Fig. 6.7(a) is a bicrystal composed of a Au-rich and Pt-rich phase separated by a flat interface, we can find the origin of the Wulff shape on each side of the interface. This is done by intersecting perpendiculars erected at the center of the crystal faces, as sketched in Fig. 6.12. The distance from the center to one of the faces is proportional to the specific surface energy of that plane. It can be shown that the distance between the origins of the crystal is proportional to the interface energy.

The surface energies of the {100} and {111} planes of Au and Pt, listed in Table 6.7, were calculated from molecular dynamics simulations (Zhang et al. 2004).

[¶]The four coefficients of the cubic polynomial, $\mu(X)$, describing the composition variation of the shear modulus with the composition are solved using the values of the shear modulus of the pure Au and Pt components and the knowledge of $\partial\mu(X)/\partial X$ as $X \to 0$ or 1 which are functions of Poisson ratios and the shear moduli of the pure components (Friedel 1955). Note that $\mu(X)$ exhibits only a slight deviation from the linear approximation.

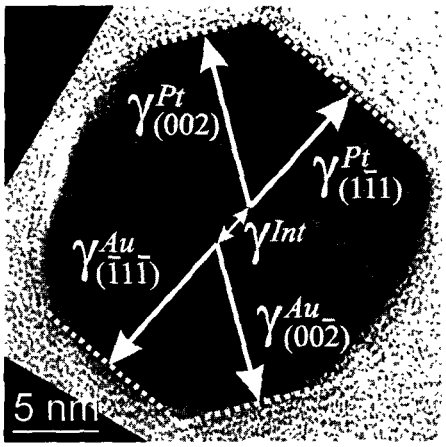

FIG. 6.12: NP of Fig. 6.7(a) with an overlaid Wulff construction. γ refers to the surface energy represented by a vector whose magnitude is proportional to the surface energy and direction is collinear with the crystallographic plane normal (Miller indices indicated as subscripts). The vectors intersect at the origin of each crystal, on either side of the interface. The distance separating the origins is directly proportional to the interface energy, γ_{Int}.

TABLE 6.7: Theoretical and measured surface and interface energy of the NP in Fig. 6.12. Theoretical values for Au and Pt for different crystallographic orientations are taken from Zhang et al. (2004). The interface energy is deduced from the proportionality arising between the distance and the surface energy of the Au-rich half of the NP.

	Surface energy mJ/m^2		**Distance** nm	
Planes	{100}	{111}	{100}	{111}
Au	1083	886	9.1	8.9
Pt	2168	1656	9.8	8.5
Ratio(Pt/Au)	2.0	1.9	1.1	1.0
Interface	**420 – 470**		3.9	

From the diagram, it apears that the surface energies of the Au-rich half are similar to their Pt-rich counterparts, which is in apparent contradiction with the relative values of the surface energy of the pure components. However, let us recall that the phases are not pure, according to the profile in 6.7(c). In fact, this observation is in agreement with the surface energy, as computed using Butler equations (Fig. 3.12(d)) at 800 °C: the surface energy of a 90% at. Pt-rich alloy is expected to be slightly lower than that of Au.

To calculate the interface energy, the proportionality constant relating the surface energy with the distance measured on the TEM image is needed. Assuming that the surface energy is described correctly by Butler equations, the surface energy of Au-rich alloys is expected to be more or less constant with composition. Depending whether we use the {100} or {111} Au planes to scale the TEM micrograph to the surface energy, the interfacial energy can be estimated to lie between 420 and 470 mJ/m^2. This estimate is rather closer to the interfacial energy of a grain boundary (Murr 1975, p131-132) than to the energy of a semi-coherent interface. The estimate is more than twice as large as the calculated surface energy of 211 mJ/m^2 (Table 6.6), hence mitigating the hypothesis of a coherent interface.

6.7 Conclusion and Outlook

Two questions were posed at the beginning of this Chapter. The first one was related to the phase-separating behavior of a binary NP and the second was concerned with the validity of the bulk phase diagram when applied to NPs. The attempt was to provide an empirical answer to these questions by annealing 20 nm diameter Au-Pt NPs initially in a core-shell configuration.

The core-shell geometry was found to be unstable: the NPs invariably evolved towards a shape composed of two hemispheres separated by a relatively flat interface. We speculated on the existence of a driving force to minimize the area of the interface. The morphogenesis was found to be a two-step process: interdiffusion, which saturates the phases occurred first, while structural changes related to the movement of the interface, were much slower. At low temperatures (300 °C), the core-shell geometry could be retained in the absence of a critical instability. At higher temperatures (>600 °C), the spherical symmetry evolved towards the stable configuration in a matter of minutes, consistent with the trends obtained by numerical simulations.

As mentioned in Section 2.4.2, according to Xiao et al. (2006), it was concluded from molecular dynamics simulations that the core-shell configuration stabilizes a Au-Pt NP. Without contradicting the conclusions of Xiao's study, we provide an experimental demonstration that a segregation along a relatively flat interface leads to a more stable configuration than a core-shell one. We can further note that this type of configuration is in complete agreement with the observations of Howe et al. (2003), which noted that Ag-Cu NPs α and β phases segregated in the same way, although the NPs in this case were somewhat larger (40–100 nm).

The composition of the Au- and Pt-rich lobes of the NP were found to differ from the bulk phase diagram. At 600° and 800 °C, the Au solubility in the Pt-rich phase was found to be higher than the bulk by 4–5% at., a difference that is significant with respect to the experimental uncertainty of both the EDXS measurements and the solubilities of the assessed bulk phase diagram. In comparison, there was a marked

tendency at 800 °C for the Au-rich side of the NPs to have a lower Pt solubility than the bulk, although this tendency was not reproduced at 600 °C.

We used the model based on a surface energy computed with Butler equations developed in Section 3.3 to explain the difference between the composition measured within the NPs and the solubilities predicted by the bulk phase diagram. The tendencies of the model and the experimental observations are in qualitative agreement (i.e., increased solubility on the Pt-rich side of the NP). However, much more experimental data acquired with a broader range of NP composition, size and annealing temperatures would be necessary to verify the extent of the applicability of the model to such nanosystems.

We briefly explored the effect of nominal composition by annealing a Au-Pt NP with a thinner Pt shell. It was found that at 600 °C, a 25% Pt NP was almost single phased. It would be of interest to experimentally study spinodal decomposition occurring within a NP. The experiment could be performed with the following procedure: 1) anneal the NPs in the single-phase region of the phase diagram (e.g., a 25% at. Pt NP at a temperature of 800 °C); 2) quench at a lower temperature (e.g. 300 °C); 3) hold for various times to induce various stages of spinodal decomposition and 4) quench to room temperature.

By performing a Wulff analysis on the HREM image of a segregated Au-Pt NP having a flat interface, the interface energy could be deduced to about $\sim$445(25) mJ/m^2. This value is about twice as large as the one computed for a semi-coherent interface. In addition, according to the same Wulff construction, the magnitude of the surface energy of the Au-rich and the Pt-rich phases are similar, in agreement with the estimations provided by Butler equations. The exact nature of the interface could not be confirmed and further HREM work is required to confirm the presumed network of misfit dislocations at the NPs interface.

The Gibbsian approach can be viewed as a "top-down" method to determine the phase stability of nanosystems. The mathematical treatment of such a numerical calculations becomes tedious as the number of approximations are replaced by constraints to the minimization. "Bottom-up" approaches, such as those provided by molecular dynamics, could arguably, be proven more adapted to handle the complexities of such nanosystems and also provide valuable insight on the kinetics of transformation.

We chose the Au–Pt system to study the stability of nanophase systems but many others potentially could be studied. Binary NPs of noble metals (e.g. any combination of the following elements: Au, Pt, Pd, and Ag) provide two notorious advantages for this type of study. Firstly, numerous recipes to control the size, shape and composition of such noble metal bimetallic NPs are becoming available with progress in inorganic synthetic chemistry (Habas et al. 2007, for instance). Secondly, oxidation is absent in such noble metals system and greatly facilitates their analysis.

Chapter 7

Conclusion and Outlook

7.1 General Conclusions

Following a review on the topic of the size-dependency of binary phase diagrams, we concluded that many (sometimes conflicting) theoretical models on the phase stability of nanoparticles (NPs) were not directly validated. Alternatively, empirical models to explain observed phase stability of NPs could hardly be transported to other binary systems. In an attempt to reconcile theory and experiment, we investigated the effect of size on the phase stability of Au-Pt NPs.

The theoretical aspect of this thesis was modeling the size-dependent Au-Pt phase diagram. We developed a graphical method (the "Gibbs-Thomson curves") to illustrate the concept of size-induced phase transformation under the constraint of mass balance. We demonstrated the existence of a composition range where coexistence of the liquid and the solid phases is forbidden thermodynamically. Within this range, discontinuous melting occurs, in agreement with other studies (e.g. Jesser et al. 2004). The miscibility gap was plotted for several particle sizes using a different approach. It was shown that the shift of the miscibility branches with size was solely dependent on the nonlinear terms related to temperature and composition. This led to a counter-intuitive conclusion: the miscibility gap branches shift towards the Au-rich side of the phase diagram with decreasing NP sizes.

To study the phase stability of NPs, it was essential to assess the spatial and analytical precision of transmission electron microscopy (TEM)-related techniques and adapt them to the analysis of NPs. We developed an array of TEM-related tools adapted specifically for an in-depth analysis of Au-Pt NPs. In particular, we developed a procedure to generate quantitative EDX maps in which the borders of the features could be defined by correlating the micrographs acquired in different modes. We also implemented and tested with energy-dispersive X-ray spectroscopy (EDXS) and electron energy-loss spectroscopy (EELS) an algorithm to retrieve the inner profile from an object with spherical symmetry. The precision and the limits of the method were assessed experimentally with Au@Pt and Co@CoO NPs having known internal structure.

Size-related phenomena are often probed using TEM, since the size, internal structure, phase and composition can be determined from individual NPs. We have demonstrated the feasibility of performing accurate quantification of electron beam-sensitive

NPs. We developed a method to determine the composition of a binary Au-Ag NP while accounting for the depletion of its component (Ag) during EDXS analysis. The trend of the EDXS detection limit with size and composition was evaluated by performing a series of spectra simulation and by fitting the experimental data to a model. These trends defined an experimental window in the size-dependent Au-Ag phase diagram in which data points could be potentially collected for the study of the phase stability of binary NPs.

We have experimentally demonstrated for the first time that the core-shell configuration of two-phase solid NPs is unstable. Indeed, by annealing ~20 nm diameter Au-Pt NPs initially in a core-shell configuration above 600 °C, the particle phase almost instantaneously segregates into a Au-rich and Pt-rich components separated by a relatively flat interface. This geometry was observed in other metallic systems (Yasuda and Mori 2002; Howe et al. 2003), however, the novelty of this study is two-fold: first, the core-shell geometry was forced on the system, since it was the starting geometry prior to annealing and second, a detailed chemical and structural analysis of the segregating NP is provided by precise TEM techniques before, during and after the annealing, thus giving a unique insight to the different stages of the morphogenesis.

For a 20 nm diameter phase-separated Au-Pt NP, we could provide detailed chemical information with a spatial resolution of ~1.2 nm and correlate it to a strain map, generated by the HREM signal. The composition of each separating phase was precisely measured and was found to significantly differ from the bulk phase diagram. At high temperature, it was confirmed that the solubility of Au in Pt was higher within the Pt-rich portion of the NPs with respect to the bulk phase diagram. However, the solubility of Pt in the Au-rich phase was reduced for these NPs. Both trends were in qualitative agreement with those of the size-dependent miscibility gap, as computed in Chapter 3.

7.2 Future Work

In this study, we chose to focus on selected theoretical aspects of the thermodynamics of NPs and on development of the experimental techniques to perform an in-depth characterization of individual Au-Pt NPs in specific conditions. An avenue for further work includes experimentally mapping the size-composition-temperature axes over a broader range than what was explored here. This might reveal the existence of critical sizes or compositions where segregation is repressed or a core-shell configuration stabilized, as hypothesized by some of the models reviewed in Chapter 2.

Although we were able to estimate the interface energy to ~420–470 mJ/m^2, using a graphical approach, some doubts remain on its semi-coherent nature. Further study includes determining the precise nature of the interface and confirming its associated surface energy. The results can be compared with those of different systems and in-

cluded in a thermodynamic model. Eventually, one could develop a general approach or strategy to predict the configuration, phase and distribution of the constituents within a NP of a given size, nominal content and temperature.

The curvature and the stability of a dividing interface could potentially have a definite impact on the properties of bimetallic NPs. Apart from fulfilling a scientific interest of the topic of phase stability, the proposed study could help devise an approach to predict the properties of a NP. In this regard, the synthesis and the preparation methods could be adjusted to optimize a desired property for a given technological application. The prospect of extending these studies to NPs of other bimetallic systems while probing their properties seems promising, especially in view of their catalytic, magnetic and optical potential.

Appendix A

Laser-Synthesized NiTi Reactive Nanostructures

A-1 Introduction

Bulk Ni-Ti exhibit a martensitic transformation and are known shape memory alloys. NiTi thin films are appealing to microactuators (Miyazaki and Ishida 1999) because of their much faster response than their bulk counterpart due to their much faster cooling rate. A natural extension implies using NiTi NPs or nanostructures thereof, hence the necessity of investigating the effect of size on the phase stability and phase transformation behavior.

The Ni-Ti system (the phase diagram is shown in Fig. A-1) was initially selected in order to study size-induced effects on the composition range of the non-stoichiometric phases. This system was chosen since its intermetallic phases exhibit nearly vertical phase boundaries. These vertical phase boundaries allow the experimental distinction between a supersaturation effect and a true compositional shift of the phase boundaries due to the size effect, following the quench of a nanoparticle (NP) from a high temperature single-phase field of the phase diagram to a two-phase field. Furthermore, electron energy-loss spectroscopy (EELS) and energy dispersive X-ray spectroscopy (EDXS) signals of these compounds are both strong and readily interpretable.

The laser ablation was carried out by R. Hughes (Brockhouse Institute for Materials Research). Excimer (λ = 248 nm) pulsed laser ablation (PLD) was used to synthesize the intermetallic nanoparticles (NPs). The composition of the NPs could be controlled by the target stoichiometry. The as-produced NPs are usually metastable as a consequence of the high cooling rates. A thermodynamically stable state could have been achieved either by using a TEM hotstage or the laser-oven technique, described in Appendix B.

These experiments did not allow one to study the nanosize effects because of the systematic formation of an oxide layer forming on each NP, despite extensive precautions taken during the synthesis to avoid oxidation. The formation of this shell complicated significantly the study of the size effect since it *(i)* created a radial Ti diffusion gradient at the surface of the NP, *(ii)* modified the surface energy, and *(iii)* introduced an additional interface. This high affinity for oxygen could have been

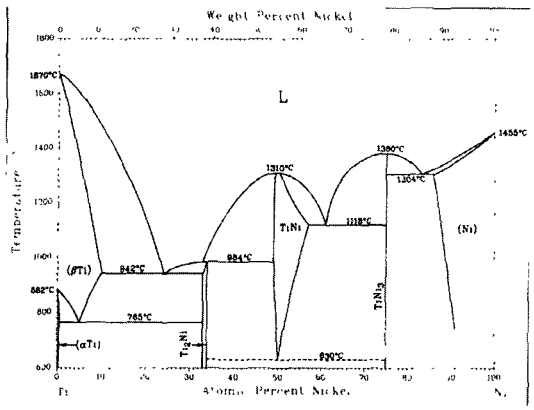

FIG. A-1: Ni-Ti bulk phase diagram from Massalski (1990).

anticipated, given the strong bonds of intermetallics and enhanced surface reactivity typical of small particles.

In spite of the limited success in studying size-related phenomena, we will nevertheless devote this Appendix to the synthesis and TEM investigation of the various nanostructures obtained. Following a literature review on laser synthesis of NPs in a buffer gas, we describe the effect of pressure on the morphology of the resulting nanostructures. The nature and the formation of the oxide will then be investigated followed by a description of the different methods undertaken to prevent oxidation and understand its origin. We conclude with a TEM investigation performed on the various types of nanostructures obtained.

A-2 Literature Review

Under very low gas pressure (<1 Torr), laser ablation creates a long plume, perpendicular to the ablation surface which contains species traveling at very high velocities. A continuous and relatively flat film can thus be grown on a substrate set to intercept the plume. In the presence of a higher gas pressure, the ablated species lose some of their kinetic energy as a consequence of the interaction with the gas molecules, and are considerably slowed down and cooled (Dietz et al. 1981). Once sufficiently slow, the species nucleate into clusters and grow as NPs (Wood et al. 1998). The following Section describes two NPs synthesis techniques based on this method: the Laser Ablation of Microspheres (LAM) and the Laser Vaporization with Controlled Condensation (LVCC).

A-2.1 Laser-ablation of microspheres (LAM). A low yield of agglomerated NPs having a broad size distribution can easily be achieved by the laser ablation of flat targets in a buffer gas. It was later demonstrated that by using a target made of dispersed micron-sized particles instead of a flat surface, a much higher yield of non-agglomerated NPs could be produced (Becker et al. 1996). It is speculated that the absence of aggregation is due to the photoionization of the particle to a high charged state by the laser, causing the NPs to repel each other. A scale-up of this technique was designed in which the feedstock powder is supplied through a nozzle which fills the laser focal volume between pulses (Fig. A-2(a)). By adding an *ex-situ* size selector, a very high yield of narrow-sized distribution of NPs can be achieved (< 20 nm). Defect-free NPs of Si, Ag, W and Au could be produced using this technique. Semiconductor nanocrystals such as CdSe, GaN and ZnO and ceramics such as WC, SiC and $YBa_2Cu_3O_7$ have also been synthesized using this apparatus while preserving the stoichiometry of the feedstock particles.

The gas type and pressure and the laser fluence are the process parameters having the largest influence on the mean size of the produced NPs. If the feedstock particles are dispersed on a surface, then the NP mean size generally decreases with the laser fluence. An increase in pressure causes the NPs size distribution to shift towards larger values.

A-2.2 Laser vaporization with controlled condensation (LVCC). The LVCC technique (Pithawalla et al. 2002) uses a slightly different setup for the NPs synthesis, as shown in Fig. A-2(b). The NPs are produced in an environment where a temperature and an electrical gradient are applied to the system to assist their growth. The temperature gradient is created by heating the lower plate and cooling the top plate while an electrical potential applied to these plates generated an electrical field. The temperature gradient induces a convective current to force the condensation of the particles onto the cold plate and suppresses further growth. During the experiment, the chamber is filled with either a high purity buffer gas such as He or Ar. Both plates are separated by a glass ring which acts as a window for a Nd:YAG laser ($\lambda = 532$ nm) to ablate a bulk target of interest positioned on the bottom plate.

An interconnected filamentous network of magnetic intermetallic 5–10 nm diameter FeAl NPs is produced with this method. From EDXS and X-ray photoelectron spectroscopy (XPS) measurements, the NPs were found to be partially oxidized. Furthermore, partial segregation of aluminum and oxygen was found on the NPs surface. It is believed that the filament network morphology is a result of the applied electric field during the process.

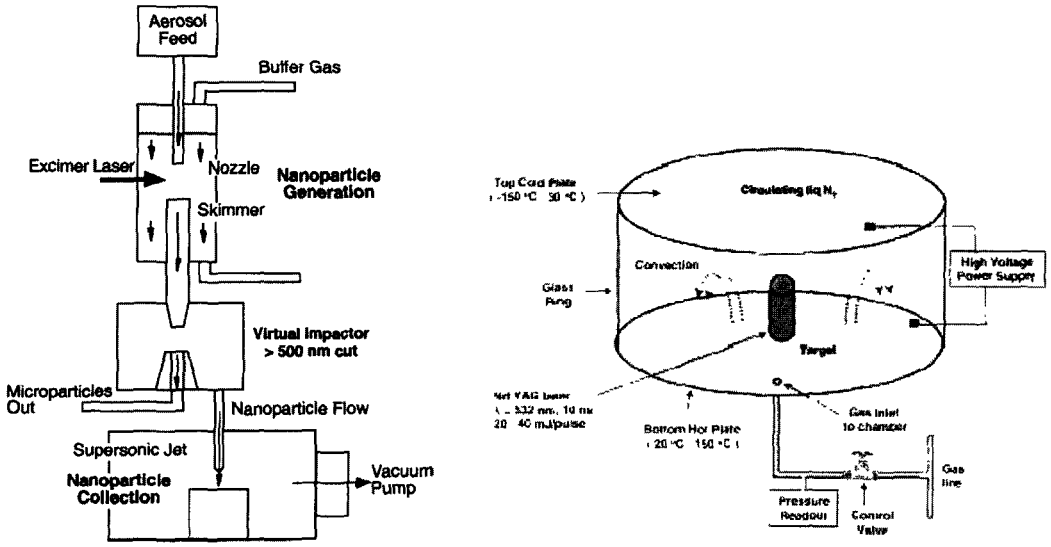

FIG. A-2: (a) Scale-up of the LAM apparatus used to manufacture NPs in a flowing aerosol (Cai et al. 1998). (b) Experimental setup of the LVCC process (Pithawalla et al. 2002).

A-3 Materials and Method: Ni-Ti Nanostructures

The Ni-Ti NPs synthesis method was based on a simplified version of the LVCC setup (we have omitted the electric field or temperature gradient). Nanostructures were produced using excimer laser pulses (20 ns duration, $\lambda = 248$ nm, 10 Hz repetition rate, 250 mJ/pulse) incident on an arc-melted NiTi (1:1 at.) target. The target was located in a deposition chamber (Fig. A-3) under vacuum. The diffusion pump used in conjunction with a liquid-nitrogen trap yielded a dynamic vacuum of $\sim 10^{-7}$ Torr. The NPs were also generated with various static background pressures of Ar (0.32, 1.5, 5, 100 and 380 Torr). Care was taken to trap the residual oxygen in the Ar gas using a Ti-getter furnace prior to introduction in the chamber. The ablated species were collected on a holey C-coated Cu mesh TEM grid placed $\sim$4 cm from the target and secured on a pivoting arm. Prior to collection, the substrate was tilted away from the line of sight of the plume while the target surface was cleaned with 200 laser shots. A low coverage (sufficient for TEM investigation) of nanostructures could then be obtained within 5 min collection time.

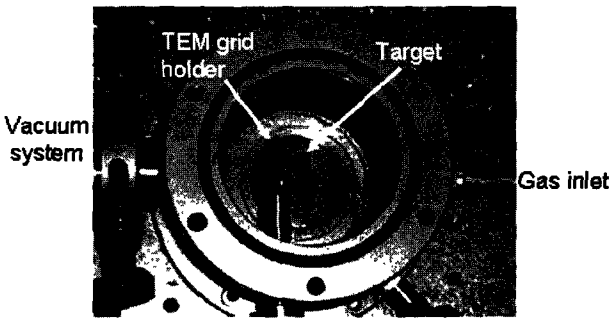

FIG. A-3: Picture of the laser ablation chamber showing the target and the TEM grid holder (facing the target).

A-4 Results and Discussion

A-4.1 Pressure-Dependent Morphology Three distinct nanostructure morphologies were produced in different proportions, depending on the Ar background pressure (Fig. A-4). Fine clusters (1–3 nm diameter, Fig. A-4(a)) were produced at low pressures and disappeared as the background pressure was increased from vacuum to 380 Torr. Chains (fractal-like aggregates with a 5–10 nm diameter arms) and NPs (20±8 nm diameter) appear at pressures larger than 320 mTorr. At low pressures (1.5–5 Torr, Fig. A-4(b)), very few NPs were present compared to chains, while at higher pressures (100–380 Torr) the volume fractions of chains and NPs became similar. A low gas pressure minimizes the collision frequency: the formed clusters reach the substrate without further interaction. High gas pressure not only causes deceleration of the ablated species traveling to the substrate, but also broadens their velocity distribution (Irissou 2005). Only chains and NPs (Fig. A-4(c)) could thus form at higher gas pressures from the aggregation of clusters that have a higher collision probability. The histogram in Fig. A-4(d) shows the relative occurrence of clusters, chains and NPs for specimen prepared at various pressures of the Ar buffer gas. The values in Fig. A-4(d) were compiled by inspection of TEM micrographs taken from different specimen and can be considered as semi-quantitative estimates of the relative volume fractions of the nanostructures.

Once formed at high background pressure, the condensed species (NPs and chains) travel from the target to the TEM grid, using the momentum acquired upon laser ablation. During drift, the fastest (smallest) particles will collide and aggregate with slower (larger) structures and construct fractal-like networks of particles, as observed in Fig. A-4(c). Similar types of structures are produced from various physical (top-down) approaches (e.g. gas evaporation processes) (Kurumada et al. 2004). There exists no models in the literature to explain quantitatively the change of nanostructure

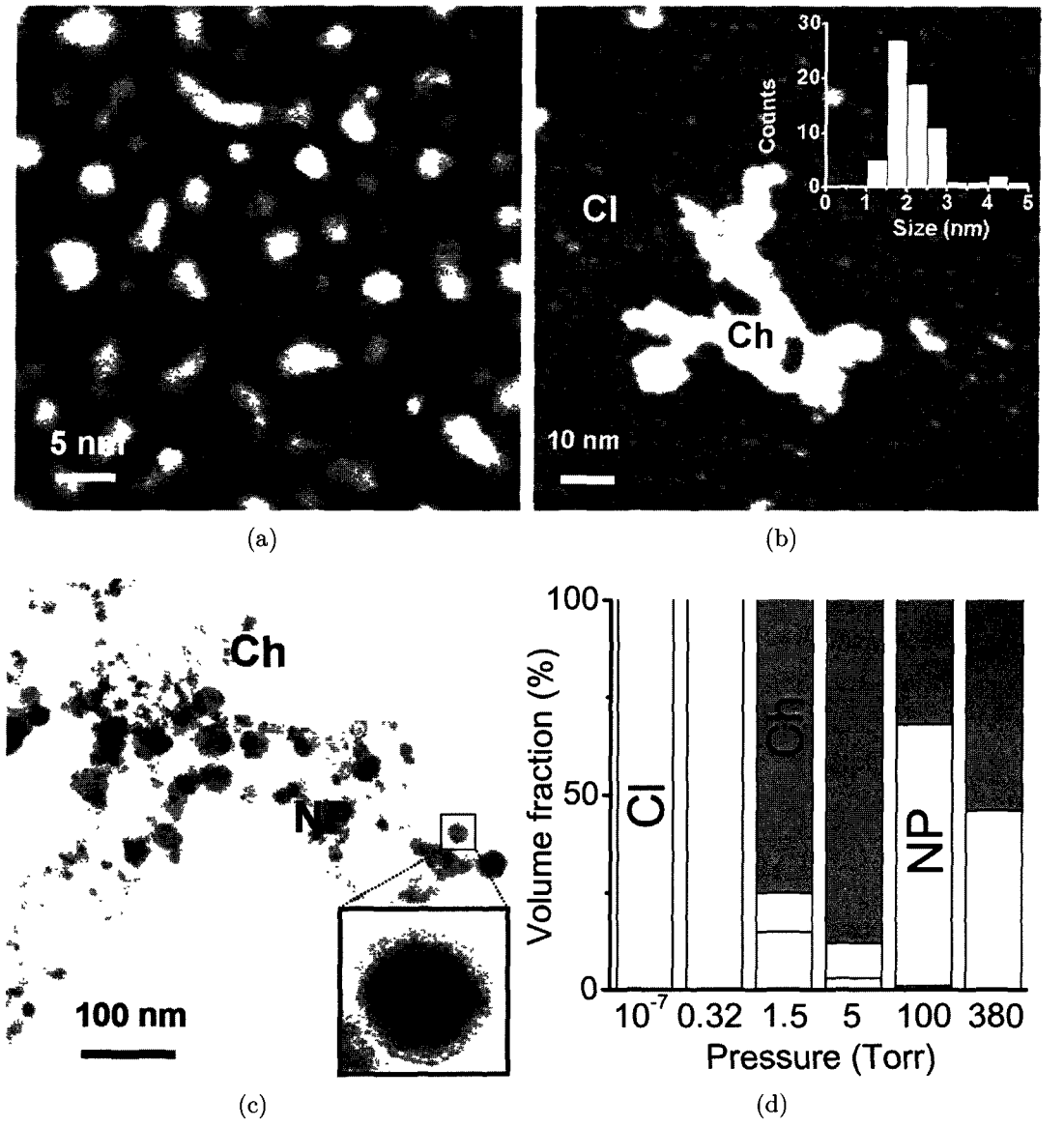

FIG. A-4: Laser-produced Ni-Ti nanostructures with increasing Ar background pressure. (a) ADF-STEM image of clusters produced at 320 mTorr. (b) STEM image of clusters (marked Cl) and chains (marked Ch) produced at 1.5 Torr with corresponding cluster size histogram in inset. (c) TEM BF micrograph of chains with details of a core-shell structure shown in inset. (d) Semi-quantitative volume fraction of Clusters (Cl), Chains (Ch) and NPs for a specimen prepared with a background pressure from vacuum (10^{-7}) to half of an atmosphere (380 Torr).

morphology within this pressure range (10^{-7}–380 Torr). The existent models for laser processes are limited to pressures below ~10 Torr.

A-4.2 Oxide Shell Formation The Ni-Ti nanostructures were found to be consistently covered by a Ti oxide, as deduced from EELS point analysis.

The following procedure was followed in order to understand the origin of the oxidation and eventually try to avoid it. Three targets were introduced in the chamber filled with 380 Torr of Ar: Mg, NiTi and Cr. Mg was first ablated to getter as much O as possible from the gas present in the chamber (with the substrate facing away from the target). Deposition of the Ni-Ti nanostructures was then carried out within the "purified" gas followed by laser ablation of Cr under vacuum, exposing both sides of the TEM grid to the plume. The deposition of a Cr layer was done to protect the NPs from further oxidation and to help determine the source of oxygen. If oxidation was *ex situ*, then Cr would act as a sacrificial layer to protect the NP and only a Cr oxide (Cr_2O_3) would be detected on the surface of the NPs. If oxidation occurs *in situ* (despite the precautions taken), we would rather expect a Ti-depleted NiTi core, surrounded by two concentric oxide shells: an inner Ti oxide shell and an outer Cr_2O_3.

Fig. A-5(a) shows an ADF-STEM image of a NP (bright central region) embedded in a large shell (lighter surrounding phase) to which several other smaller NPs are attached to. Fig. A-5(b) shows the result of an EELS profile performed along the dotted line of Fig. A-5(a). The reference spectrum of the O K edge of Cr_2O_3 (Fig. A-5(b), top left corner) was recorded directly from the shell. A separate TiO_2 sample was used to collect the O K edge reference spectrum displayed in the top-right corner of Fig. A-5(b). The difference of the O K edge fine structure of Cr_2O_3 and TiO_2 (top panel inset, Fig. A-5(b)) was used to evaluate the contribution of both oxides to the O K edge of the line profile using multiple linear least square fit. The $O(TiO_2)$ profile is consistent with the presence of an oxide of a shell, probed in projection. The $O(Cr_2O_3)$ profile suggests that Cr_2O_3 constitutes the outer layer (not necessarily having a spherical symmetry). The description of the particle is completed by the inspection of the atomic fraction of Ti, Cr and Ni traces in the lower panel of Fig. A-5(b). The profiles are all consistent with a heavily Ti-depleted NiTi core embedded in a chromium oxide shell. In light of these results, we conclude that:

1. Oxidation occurs *in situ* and was unavoidable, given our equipment;

2. An ultra-high vacuum ($<10^{-9}$) and sub-ppb O levels in the chamber gas are necessary to synthesize oxide-free NiTi NPs.

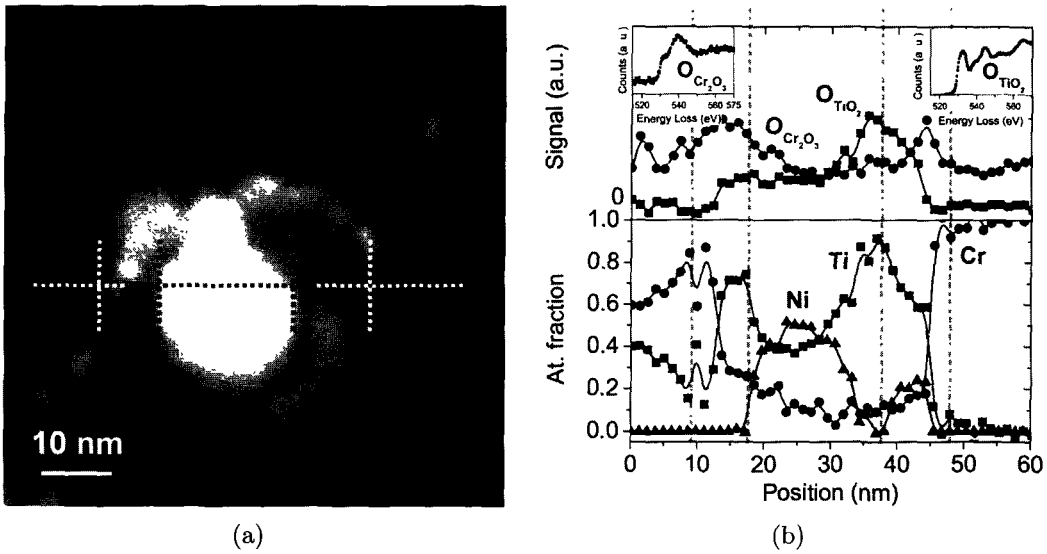

(a) (b)

FIG. A-5: (a) STEM image of a 20 nm diameter NiTi NP surrounded by a shell with other smaller NPs attached to it. (b) EELS analysis was performed along the dotted line in (a) from which various signals were extracted. Top panel: Multiple linear least-square fit of the extracted O K edge showing the contribution of Cr_2O_3 (red circles) and TiO_2 (blue squares) (both references are displayed in the insets). Bottom panel: Relative composition of Ti (blue squares), Cr (red circles) and Ni (black triangles). A B-spline line connects the datasets as a guide to the eye. The position of the heavy dashed vertical lines in the STEM image are reproduced on the profile and mark the position of the interfaces.

A-4.3 Characterization of NiTi NPs Since we had limited success in preventing oxidation, we will nevertheless discuss the characterization of the as-produced NiTi nanostructures (synthesized using no precautions to avoid oxidation except for using the getter furnace). Different oxide characteristics are observed for each type of nanostructures provided. Clusters network (see darker phase in the STEM micrograph of Fig. A-4(a)) and chains appear embedded in an oxide sheath while the oxide layer around the NP appears brighter in bright field TEM (inset, Fig. A-4(c)). The O K edge fine structure of the clustered network is consistent with that of the TiO_2 reference. Further information on these nanostructures are deduced from the EELS analysis shown in Fig. A-6. When the probe is on a white particle (as observed in STEM, Fig. A-6(a)), Ti, O and Ni are detected while only Ti and O constitute the regions between the particles. An EELS map was acquired over four Ni-rich clusters to confirm the observations obtained by spot analysis. At each pixel of this map, an EELS spectrum was recorded and the intensity of the Ti L_{23}, O K and Ni L_{23} edges are extracted. The Ti:Ni and Ti:O ratios are then generated using theoretical cross sections and displayed with an associated temperature scale (Fig. A-6(b)). The depletion of Ti in the vicinity of the Ni-rich particle is evident from this map. Furthermore, between the Ni clusters, the Ti:O ratio is found to lie in the 0.6–0.9 range, consistent

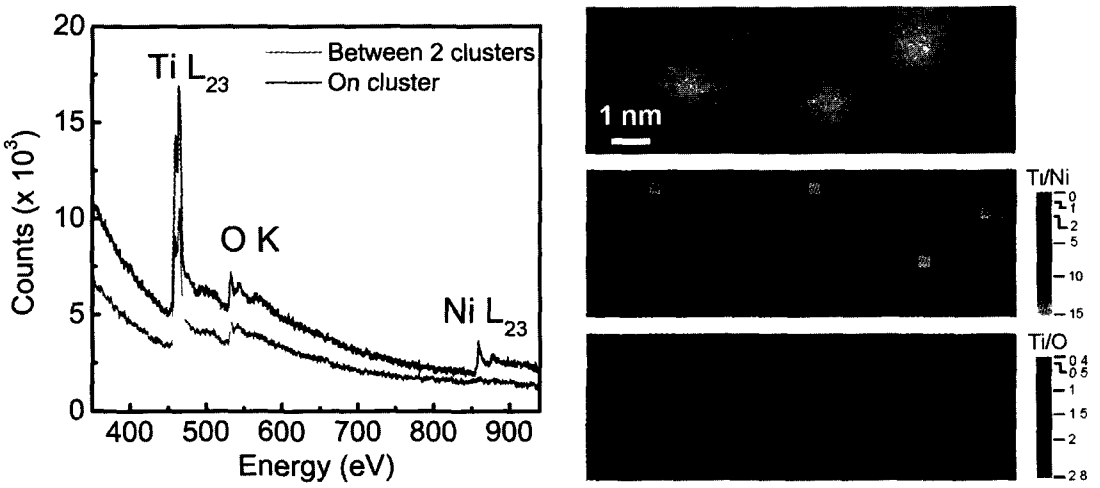

(a) (b)

FIG. A-6: (a) EELS point analysis performed on Ni-Ti substructures produced by laser ablation of a NiTi target with a background pressure of 320 mTorr of Ar. When the probe is positioned directly above a cluster, Ti, O and Ni are detected, while only Ti and O are detected between clusters. (b) Ti:Ni and Ti:O ratios temperature maps generated with signals of Ti L_{23}, Ni L_{23} and O K edges. The EELS fine structure details and the Ti:O ratio are both consistent with the presence of TiO_2.

with the presence of TiO_2. From these observations, it appears that a fine network of NiTi clusters first populated the a-C substrate and selective oxidation have then drawn the Ti out of the clusters to form a layer of TiO_2.

We confirmed qualitatively the results by analyzing the nanostructures by EFTEM (Fig. A-7). The lattice fringes are barely visible in the zero-loss filtered image of the 1–2 nm Ni-rich clusters (Fig. A-7(a)). The corresponding EFTEM color map (Fig. A-7(b)), recorded using the three windows method, shows Ni (blue channel) and Ti (orange channel) distribution. A line profile (Fig. A-7(c)) was taken across 3 clusters intercepted by the dotted line in Fig. A-7(b) and showed that the Ni and Ti signals are anticorrelated and that the drift correction and alignment procedures were successful.

As discussed above, NiTi NPs form at higher pressure and develop an oxide shell, as shown in Fig. A-8. The shell often appears incomplete, as it the case from the bottom-left NP in Fig. A-8(a) (the shell of the three other NPs could also be incomplete but could be in a different orientation). The formation of these incomplete shells could be related to preferential oxidation of a particular set of lattice planes, available on the surface of the NP.

An EELS profile was performed following the dotted line in Fig. A-8(a). The top panel of Fig. A-8(b) compares the O K edge from the shell and from the surface of the shells with a TiO_2 reference spectrum recorded using similar experimental conditions.

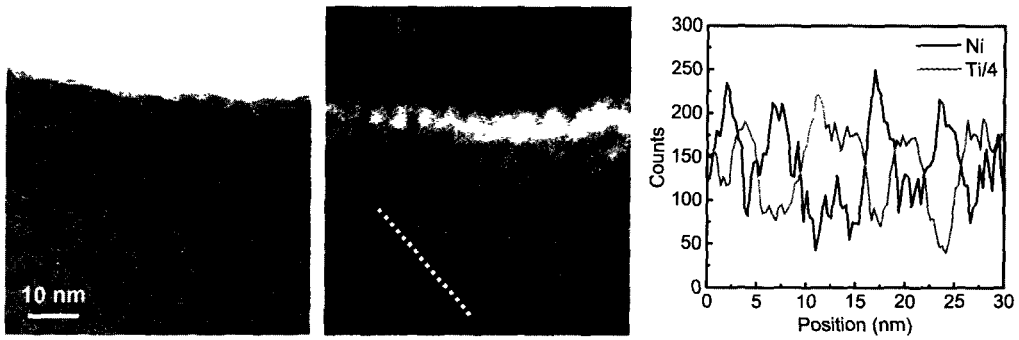

FIG. A-7: (a) Zero-loss energy-filtered plane-view image of NiTi clusters network prepared by laser ablation of a NiTi target using a background pressure of 320 mTorr Ar. The species are collected on a holey a-C TEM grid (the edge of a hole is seen at the top). (b) Composite image constructed with the Ti L_{23} (orange channel) and Ni L_{23} (blue channel) edges showing Ni-rich clusters embedded in a TiO_x network. (c) Intensity profile along the dotted line in the map (b) confirming the segregation of Ni and Ti.

The O K edge fine structure of the surface is clearly different from the shell and could be possibly assigned to either one of the various titanium oxides or hydroxides that could have formed at the surface of the oxide shell. The O K edge of the shell is consistent with TiO_2 across the whole energy range except for a subtle discrepancy in the fine structure at ~538 eV (arrow, Fig. A-8(b), top panel). This shoulder is assigned to the main feature of the spectrum recorded from the surface. Indeed, if the spectrum at the surface is different than from the rest of the NP, we can expect a contribution of the signal of the surface, even when probing the center of the NP.

The composition of the TiO_2 shell is confirmed by EELS quantification (bottom panel, Fig. A-8(b)). Ti surface depletion is apparent from the Ti concentration profile as Ti likely diffused from the particle outwards, forming a surface layer of TiO_2. It should be noticed that no trace of Kirkendall porosity was found within the NPs, as the proximity of the surface likely assisted the diffusion of the vacancies to the surface.

A-5 Conclusion and Outlook

The main disadvantage of fabricating intermetallic NPs using the laser method is the propensity of these NPs for oxidation or contamination. The high temperatures reached during laser processes favors the reaction of the ablated species and its environment. Moreover, the surface of the NPs is intrinsically more reactive to oxidation or adsorption. In order to study size-induced thermodynamic effects occurring in

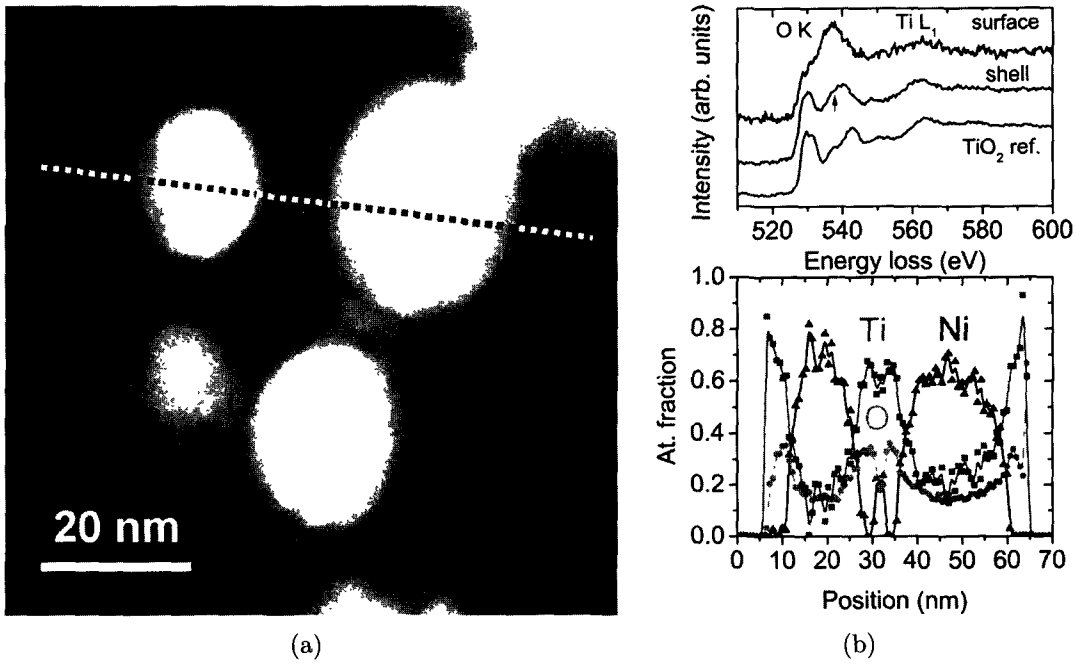

(a) (b)

FIG. A-8: (a) ADF-STEM image of four Ni-Ti NPs surrounded by a 3–4 nm-thick TiO_2 shell. (b) Top panel: EELS O K edges extracted from the line profile taken along the dotted line in (a) from the very surface of the shell and the "bulk" of the shell exhibiting different fine structures. Arrow points to a feature discussed in the text. The TiO_2 O K edge is also shown for comparison purposes. Bottom panel: Ti (dark grey squares), Ni (black triangles) and O (light grey circles) atomic fraction profile evidencing the TiO_2 shell and the depletion of Ti at the surface. The Ni profile exhibits a small peak between both NPs and arises from the presence of a small Ni cluster caught in between both NPs (visible with increased contrast). A B-spline curve connecting the data serves as a guide to the eye.

intermetallic NPs, the laser process would therefore need to be carried out in an ultra pure environment.

We have nevertheless demonstrated the influence of pressure on the formation of Ni-Ti nanostructures deposited by laser ablation. Nanostructures with features at the 2–3 nm scale were formed at low pressure ($\lesssim$1.5 Torr) while interconnected NPs could form at pressures, above $\sim$5 Torr. The formation of these structures could eventually be modeled in terms of fractal mathematics and geometry. A similar approach was used to model the growth of nanostructures using molecular beam epitaxy (Brabási and Stanley 1995) or gas-flame particle synthesis (Schmid 2004; Morgan et al. 2006). The scaling laws could then be studied as a function of growth parameters associated to the laser (wavelength, intensity, repetition rate) and the buffer gas (pressure, molecular mass, temperature). The formation mechanism of the various structures during growth in the gas phase could be studied by intercepting the species at various distances from the target.

The Ni-Ti nanostructures were found to be covered with TiO_2, which resulted in surface depletion of Ti below the oxide scale. The presence of an oxide shell prevented the size-dependent features expected for NPs from being measured and studied. Not only is an ultra-high vacuum setup necessary to avoid contact with oxygen, but the NPs requires an inhibition layer such as a-C to protect them from oxidation, once out of the chamber. Such a layer may also affect the surface of the NP and consequently, alter its thermodynamic property.

The laser-solid method provides a mean to synthesize intermetallic NPs with a radial gradient controlled by the thickness of the oxide shell. If these NPs could be proven useful, one could optimize the parameters of an oxidizing atmosphere to control surface depletion. The NPs could then undergo a reducing chemical treatment to remove the oxide layer and prevent further oxidation or aggregation by using a capping agent or by the deposition of an inhibition layer. It is interesting to note that if oxidation completely consumes the metal, one could even obtain an empty oxide shell following the formation of a Kirkendall porosity at the center of the NP (Yin et al. 2004).

Appendix B

Nanostructures Synthesized *via* Laser Ablation of a Solid at High Temperature

B-1 Introduction

We describe in this Appendix our attempts to fabricate thermodynamically stable Au-Pt nanoparticles (NPs) with controllable composition and size using the laser-oven method. We have adapted the laser-oven setup typically used for the fabrication of carbon nanotubes. The process is based on the laser ablation of a graphite-metal catalysts pellet at a high temperature and pressure. The purpose was to obtain Au–Pt NPs embedded in a layer of amorphous carbon (a-C) to prevent aggregation during *in-situ* annealing. According to the Au-C and Pt-C *bulk* phase diagram (Massalski 1990), there is no solubility of C in either Au or Pt, making the formation of Au–Pt NPs embedded in an inert matrix of a-C possible.

The purpose of these experiments was to initially study the size-dependent thermodynamic phenomena involved in *binary* nanosystems. Unfortunately, Fe was detected in nearly all the Au-Pt NPs produced with the laser-oven method. These experiments could therefore not validate theoretical models such as those proposed in Section 3.3. Precautions were taken to avoid Fe contamination: e.g. pre-sputtering the target surface before deposition, avoiding direct contact between the piston and the pellet during pressing. None of these methods have changed the amount of Fe in the specimen and the source of Fe remains an open question.

We first briefly discuss the carbon nanotube laser synthesis method and its applicability to the synthesis of bimetallic NPs. The experimental setup and operating conditions are then described. We then discuss the effect of annealing temperature and target composition on the size, size distribution and average composition of the Au-Pt(Fe) NPs. In spite of the Fe contaminant, we will present examples in which several transmission electron microscopy (TEM)-related techniques are applied simultaneously to infer on the structure and the formation of these laser-produced NPs.

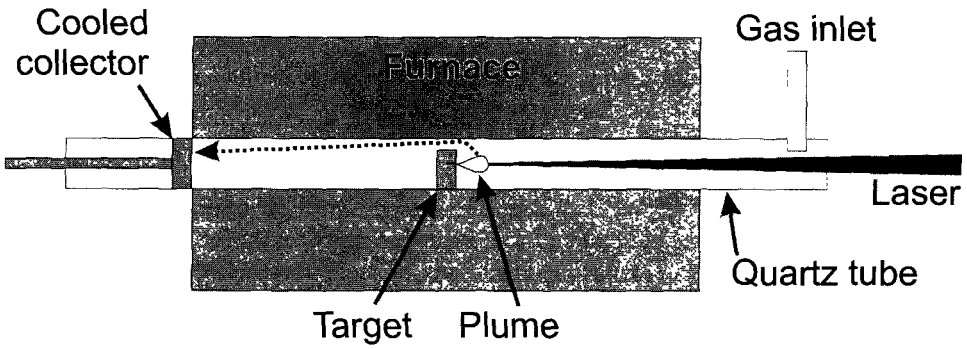

FIG. B-1: Experimental setup of the laser-oven method for the synthesis of NPs.

B-2 Literature Review

The laser-oven method was initially designed for the preparation of single-wall carbon nanotubes (Guo et al. 1995, Fig. B-1). For the carbon nanotubes production, a laser ablates a target made of carbon to which a minute amount of catalysts (Co and Ni powders) is added. The target is set inside a quartz tube heated by an oven at high temperature (1200 °C). A gas (usually argon, 500 Torr) flows in a laminar fashion in the direction of the laser and carries the ablated species to a cooled collector, placed at the exit-end of the furnace. Upon laser ablation, the species are ejected from the target and the metal NPs solidifies within an a-C matrix from which carbon nanotubes are catalyzed. The metal NPs remain dispersed and drift in the oven towards the cold collector on which the species are quenched. This process leads to the formation of C-Co-Ni alloyed NPs at high temperature from which carbon nanotubes are nucleated. The growth of the carbon nanotubes is known to occur at high temperatures, during drift within the tube, between the target and the collector. While this method has not been directly used for the synthesis of binary NPs, it shares the same parameters as the LLVC (Section A-2.2) and the LAM (Section A-2.1) methods. The main advantage of this technique is the possibility of annealing *in situ* the NPs. Furthermore, the annealing parameters can be easily controlled: the temperature is set by the furnace (the heat transfer transfer is ensured by the gas) and the annealing time can be varied with the gas flow and the position of the target with respect to the cooled collector.

B-3 Materials and Method: Synthesis of Au-Pt NPs

The following experiments were performed at the Steacie Institute for Molecular Science (National Research Council of Canada). The laser target is composed of pressed graphite pellet with the top portion containing the metal-graphite mixture (Fig. B-2(a)). To achieve this composite pellet, 1.5 g of graphite powder is inserted in

a 1/4"-diameter mold and slightly compacted using a piston. The piston is removed and a mixture composed of 0.5 g of graphite powder and 170 mg of Au (Alpha Aesar 0.8–1.5 μm) and Pt powders (Alpha Aesar 0.15–0.45 μm) is then added. The pellet is then repressed to $\sim$0.5 tons and placed on a quartz boat, slid into a 2" quartz tube and positioned at the center of a furnace. Molybdenum slugs placed behind the target prevented the pellet from moving during the ablation (this movement is the consequence of the laser recoil). A laser (λ = 1064 nm, pulse width = 7–9 ns, repetition rate = 10 Hz) entering the front end of the furnace (Fig. B-2(b)) through a quartz window was slightly collimated on the Au-Pt-rich side of the pellet (with a spot size 2–3 mm, yielding a laser intensity of $\sim 5 \times 10^{-8}$ W/cm^2 and a fluence of $\sim$4 J/cm^2). Species were ablated under Ar (250 Torr) and then carried to the exit end of the furnace (Fig. B-2(c)) with a flow rate of 150 SCCM. The species dwelled downstream in the hot region of the furnace over a distance of $\sim$40 cm, which ensured an annealing time between 1 and 2 min, depending on the temperature of the furnace, before being quenched on a cooled collector covered with an aluminum foil. Following an ablation time of 3 min (or 1800 shots), the aluminum foil was covered with soot. The furnace was cooled to room temperature between each run under a flow of Ar. The soot was then collected in methanol from which a drop of the suspension was left to dry on a holey carbon TEM Cu grid.

Table B-1 shows the average composition (as measured by EDXS) of the Au-Pt NPs from samples produced with different starting Au to Pt powder ratios and at various temperatures. The difference between the composition of the target and the sample is a clear indication of the incongruency of the ablation. This is not typical of nanosecond laser ablation, but could be possible with visible or infrared radiation (Bauerle 2000, p262, 464). Given the boiling point and the enthalpy of vaporization of Au (3031 K and 340 kJ/mol, respectively) are much lower than those of Pt (4100 K and 510 kJ/mol, respectively), we can expect, a *higher* ablation rate for Au. Indeed, for a given heat quantity, the volume being brought to the boiling point would be larger for Au than for Pt. However, it is clear from Table B-1, that the ablation rate of Pt is higher. The higher ablation rate of Pt can be mainly be attributed to its absorbtivity (A) at a wavelength of 1064 nm being 15 times larger than that of Au ($A_{\mathrm{Au}} = 0.02$ and $A_{\mathrm{Pt}} = 0.27$ (Bauerle 2000)). The very low absorptivity of Au for the laser would counterbalance the influence of its higher boiling point and enthalpy of vaporization. Many equations were developed (Bauerle 2000, p232) to estimate the ablation rate of materials in various conditions. These require the value of many parameters at temperatures near the boiling point, such as the gas capacity and the thermal diffusivity, which are neither available nor precise. Furthermore, these equations were developed for laser ablation or vaporization operating under low background pressure ($\lesssim$ 10 Torr) and low substrate temperatures. At higher background pressures and higher substrate temperatures, the interaction of the laser with the plume complicates significantly the understanding of the phenomenon and makes any attempt to estimate the ablation rate meaningless.

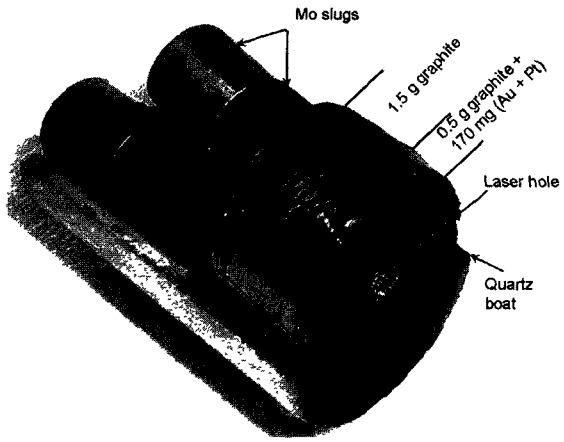

(a)

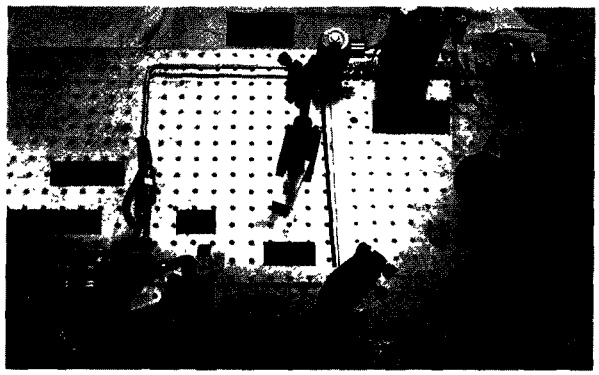

(b)

(c)

FIG. B-2: Pictures of experimental setup used to fabricate Au–Pt NPs based on the carbon nanotube synthesis apparatus. (a) view of the different sections of a graphite pellet. (b) Front-end view of the setup showing the trace of the laser and the gas inlet. (c) Rear-end view of the setup showing the cooled collector, and the gas exhaust.

TABLE B-1: Laser-oven experimental parameters (temperature, annealing time and powder ratios) and corresponding average NP composition and maximum NP diameter found in the specimen. The metal to graphite weight ratio was ~1:3.

Sample	Annealing time °C	Temperature s	Target (% at. Au)	Specimen (% at. Au)	Max NP size (nm)
A	600	109	50	33	
B	600	109	67	58	1–3
C	600	109	80	80	
D	600	109	95	95	
E	800	89	67	58[a]	
F	800	89	80	80[a]	4–5
G	1000	75	67	58[a]	
H	1000	75	80	80[a]	10–15
I	1200	65	67	58[a]	
J	1200	65	80	80[a]	13–20

[a]The average composition is assumed equivalent to the corresponding composition at 600 °C.

The reflectivity would have been lower for both metals at shorter laser wavelength. However, the NP synthesis would not have taken advantage of the large penetration depth of the laser, typical for longer wavelengths.

Fig. B-3 shows the bulk Au-Pt phase diagram with the experimental data points reproduced from Table B-1. The coordinates of the data points mark the average sample composition and furnace temperature. The temperatures and compositions of the specimen were chosen to span the Au-rich branch of the bulk miscibility gap of the phase diagram.

B-4 Results and Discussion

B-4.1 Temperature-Dependent Morphology Figures B-4 show bright-field micrographs of Au-Pt NPs synthesized at various furnace temperatures taken using the same magnification at: (a) 600°, (b) 800°, (c) 1000° and (d) 1200 °C. From the simple inspection of the images in Figs. B-4, there is an obvious tendency for the size and the width of the size distribution of the NPs to increase with temperature. The maximum size of the NPs are also reported in Table B-1. At 600 °C, the particles are clusters in the 1–3 nm diameter range, while at 1200 °C, NPs were found with diameters in the 13–20 nm range. Interestingly, clusters 1–3 nm in size are present even in samples synthesized at higher temperatures (e.g. Fig. 7.4(d)). The growth

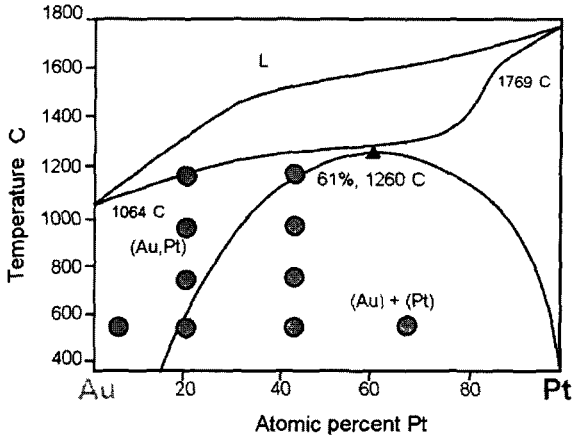

FIG. B-3: Au-Pt phase diagram (adapted from Massalski (1990)). The temperature and composition of the discs correspond to the annealing temperature and average composition of the NPs synthesized using the laser-oven technique.

of the clusters to larger NPs have likely occurred before the formation of a-C around the metallic species, so presumably early after nucleation, while still in front of the target. Growth during drifting of the particle from the target to the collector could have been difficult but possible, since a-C provided a steric barrier to the diffusion of species. However, NPs could have sintered and/or annealed during this period. At high temperature, the surface of the a-C particles appears smoother than at lower temperatures as a result of enhanced mobility of the species and their tendency to minimize their surface-to-volume ratio.

B-4.2 Elemental distribution of Au-Pt NPs EDXS measurements and mapping revealed that Fe preferentially segregates with Pt up to an Fe:Pt atomic ratio of ~1:3. This composition suggests the formation of the stoichiometric phase $FePt_3$, one of the various stoichiometric phases reported in the Fe-Pt phase diagram (Massalski 1990). It should also be noted that some oxygen was detected by EDXS but could not be spatially correlated to Fe, suggesting that Fe remained in a metallic (or intermetallic) state.

Several TEM-related analyses of a typical NP, from sample I are shown in Fig. B-5. Fig. B-5(a) shows the HREM micrograph of a 10 nm diameter NP embedded in a small a-C particle. The HREM fringes correspond to the d_{200} spacing of Au. The lattice spacing of the bottom-half of the NP was found to be 3–4% smaller than those of the top-half. The darker region at the center of the NP arises from the presence of a misfit dislocation, easily identified from Fig. B-5(b), generated from Fourier filtering the (200) and $(\bar{2}00)$ reflections.

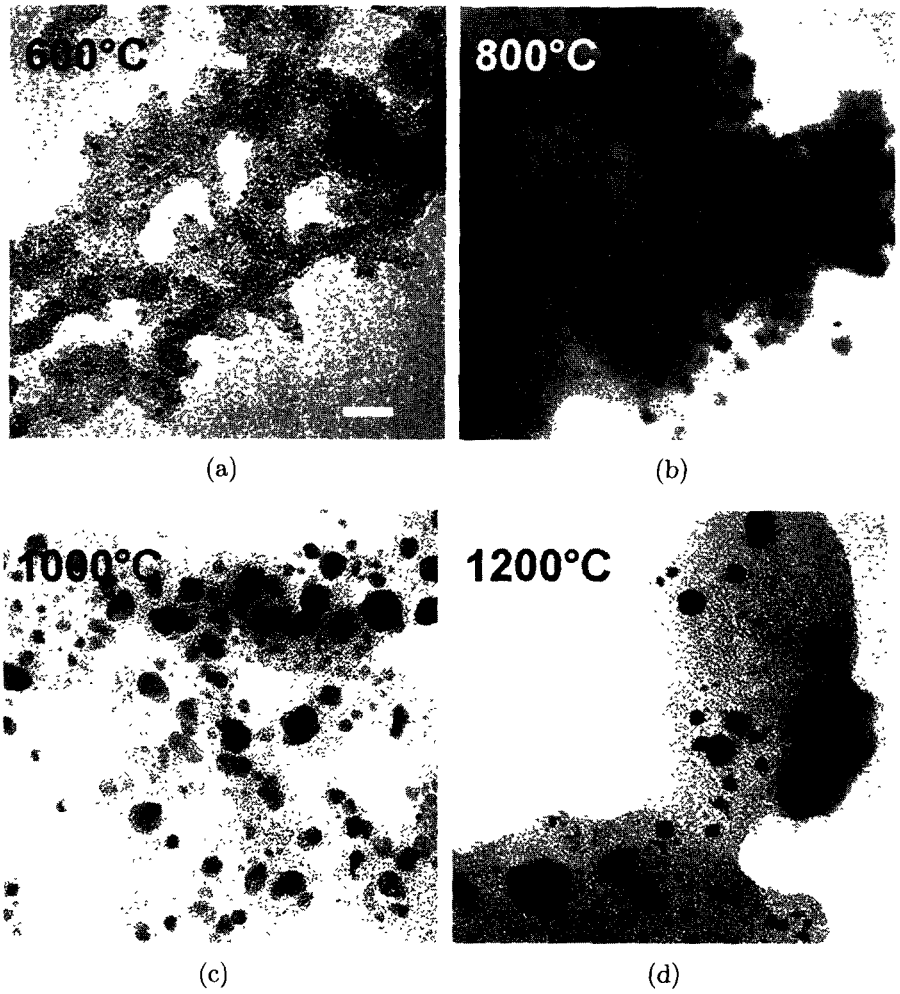

FIG. B-4: TEM micrographs of Au-Pt NPs embedded in amorphous carbon prepared by laser ablation of a target having a nominal composition of Au:Pt 3:1 (samples C, F, H and J, see Table B-1) at (a) 600 °C, (b) 800 °C, (c) 1000 °C and (d) 1200 °C. (scalebar = 15 nm)

Figure B-5(c) shows the EDX map of the same NP and was generated by assigning the red, blue and green channels to the intensity of the Au $L_{\alpha 1}$, Pt $L_{\alpha 1}$ and Fe K_{α} peaks, respectively. It is clear that Au and Pt have segregated on either side of an interface, while the smaller particle on the bottom right-hand side of the main particle is Pt-rich. The position of the interface is close to the location of the dislocation, confirming that it accommodates the compositional strain. Note also that a small misorientation can be measured between the direction of the lattice fringes of the top half and the bottom half of the NP.

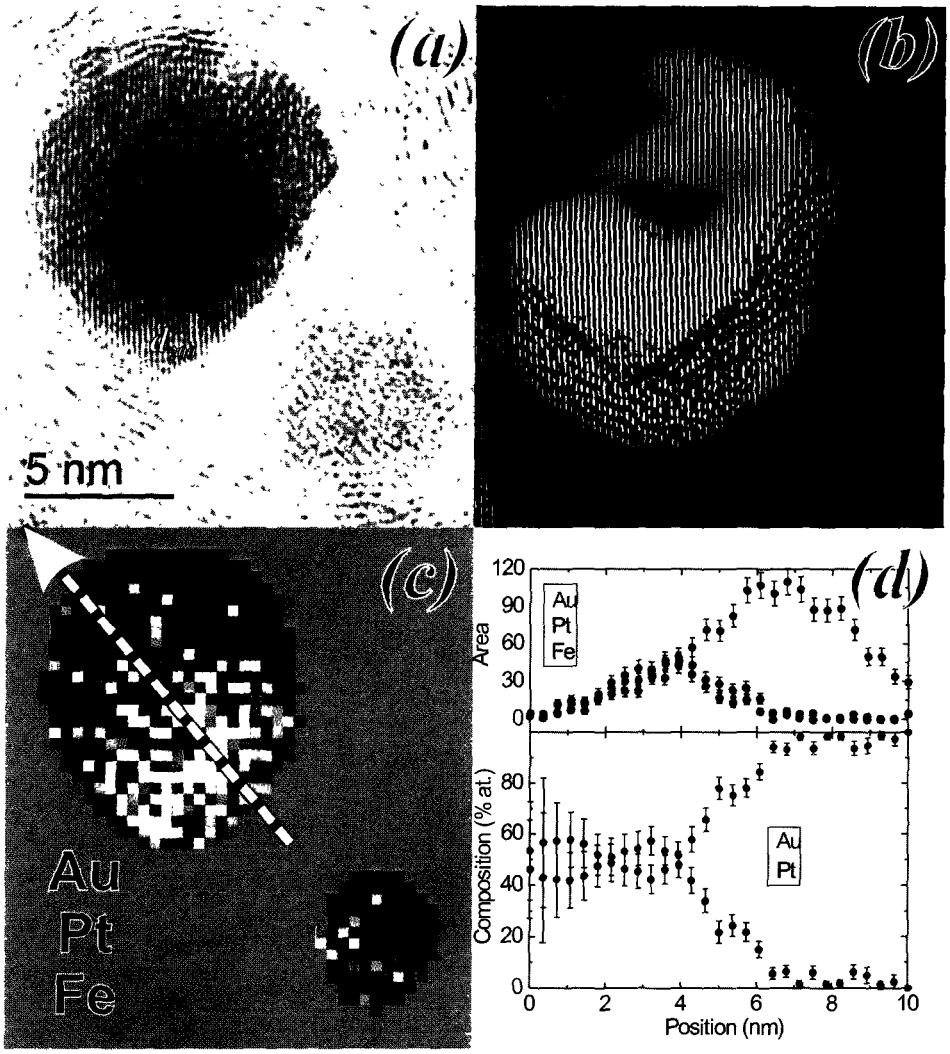

FIG. B-5: (a) HREM micrograph of a 10 nm diameter Au-Pt NP fabricated with the laser-oven technique (sample I) showing the (200) a lattice fringe of Au. (b) Fourier analysis of the same particle showing an edge dislocation highlighted by the dotted circle. The purple dotted line is a free hand drawn contour of the HREM image in (a). The background of the particle was processed to reflect the background of the HREM image. (c) EDX map showing Au (red) and Pt (blue) and Fe (green) segregation within the same NP. Dotted arrow indicates the trace and direction of the EDX profile in (d). The profile was derived from the map in (c) by projecting the spectrum image to a plane perpendicular to the interface. The area is deduced by fitting a Gaussian to the Au (red circles) and Pt (blue circles) L_α and Fe K_α (black circles) peaks (top panel). Error bars are simply the square root of the area. The bottom panel shows the atomic concentration profile of Au (red circles) and Pt (blue circles) (Fe is not considered). The error bars are computed according to the methodology described in Section 4.6.1.

Figure B-5(d) shows an EDX line profile taken perpendicular to the interface. The line profile was derived from collapsing the EDX map on the white dotted arrow drawn in Fig. B-5(c). The segregation of Au and Pt is evident in this NP as Au appears predominantly on the top-left half of the NP while Pt, Au and Fe are all present in the bottom-right half of the NP. The bottom panel of Fig. B-5(d) shows the relative concentration of Au and Pt (Fe was omitted from the calculation) across the NP interface. The error bar was calculated according to the methodology described in Section 4.6.1. The top-left half of the NP is found to be composed of nearly pure Au while the bottom-right half of the NP is found to be composed of about 52% at. Au. The atomic fraction of Fe, Au and Pt in the bottom-right half are evaluated to 26%, 34%, and 39%, respectively using the standardless quantification option in INCA (the Au L_α, Pt L_α and Fe K_α peaks were selected for quantification).

Similar features were observed in EDX maps acquired from particles taken from samples H and I: namely that NPs segregated in two phases, one being nearly pure Au and the other containing different levels of Au, Pt and Fe. The effect of the presence of Fe is evident, if we compare these results to the case where Fe is absent, such as those presented in Section 6.5. Recall that when only Au and Pt are present, the NP phase separated into Pt-rich and Au-rich NPs in which Pt was detected to a level of 20–25% at. in the Au-rich phase. The evaluation of the phase stability of a 3 component system, however, is outside the scope of this thesis.

Annealing twins could be observed in several NPs. Considering the size of the system, other types of grain boundaries would have been unstable at such a high temperature anneal. It is known (Fullman and Fisher 1951) that annealing twins can decrease the overall interfacial free energy of a grain boundary. In NPs, the situation can be different: It was demonstrated (Marks 1984) that defects such as twins and staking faults could *stabilize* FCC-derived structures typical to clusters (dodecahedra or icosahedra). Upon growth of the clusters beyond a critical size, the defects would become unstable. However, a complete atomic rearrangement (without nucleation) is required to change phase, which is kinetically improbable.

B-5 Conclusion and Outlook

The purpose of the experiments presented in this Appendix was two-fold: first, to demonstrate that phase separation was independent of the synthesis technique or thermal history of the specimen and second, to explore the phase separation of smaller-sized NPs over a larger temperature range.

We were successful in preparing Au-Pt of various sizes, compositions and annealing conditions. Whether NPs were annealed at 1000 °C or 1200 °C, internal separation of a nearly pure Au and an unknown phase composed of Au, Pt and Fe was observed. The presence of Fe contaminant unfortunately prevented any conclusions pertaining to Au-Pt nanophase diagram to be drawn from these observations. The NPs fabricated

at lower temperatures were too small to generate enough signal to determine if phase separation occurred. It would have been instructive to determine at least if both Au and Pt were present in individual clusters, although the presence of Fe would have discouraged any discussions on the phase stability of binary NPs.

Although contamination was an issue, the technique is nevertheless very promising in the framework of the study of phase stability of nanoparticles. It provides a versatile method to fabricate binary NPs that can be annealed at a broad range of temperatures and times and be quenched with high cooling rates. This method is especially advantageous on the microscopy side, since the NPs are embedded in a very thin network of amorphous carbon that can often be found to bridge over a hole of a holey carbon film and hence minimize the contribution of the substrate to the analytical signal. The technique could also be easily extended to other systems provided that a non-reactive embedding medium can be found such as a-C for Au and Pt.

Appendix C

Codes to Generate Concentration Maps

C-1 Digital Micrograph Script to Generate a Concentration Map

The concentration maps and corresponding error maps such as in Fig. 4.5 were generated following a number of steps, that we shall detail. Some of our scripts will be listed here. It should be noted that there exists a number of other useful Digital Micrograph™ (DM) scripts which can be downloaded from a web site hosted by the Graz University of Technology* (Mitchell and Schaffer 2005).

1. First, export an energy-dispersive X-ray (EDX) spectrum image (SI) from INCA. The .raw file is accompanied by a .rpl file (readable with NotePad) giving the input parameters for other programs or filters to decode the data (e.g. data type, byte order, size, etc). From DM, select File → Import Data and follow the instructions to import the EDX SI into a readable data cube. The data needs to be converted to EELS (Spectrum → Convert Data to...) and the "Data type" needs to be changed to "Real" (Edit → Change Data type...). Crop the spectrum by selecting the region from which the X-rays map was collected (Select the region of interest and chose Volume → Extract from Selected Region). One can chose to sum neighboring pixels (Volume → re-bin...) if the signal-to-noise level per pixel is low.

2. With the SpectrumPicker tool, generate the sum spectrum of a large area. Returning to the sum profile, select a large, flat region of the background next to the EDX peaks of interest. From the EELS → Assign ROI as → submenu, select "Signal" followed by "Extract Signal Integral" from the "Extract" submenu to generate an image of the background intensity by choosing the "Parent spectrum-image".

3. To generate background-subtracted elemental maps, the following steps need to be taken. Generate a background-subtracted SI by first fitting the background below the peaks of interest. Click and drag over a background area preceding the EDX peak with the Ctrl key depressed and fit the background.

*Available at www.felmi-zfe.tugraz.-at/dm_scripts/

The background model may need to be changed to linear or constant (EELS → Background Model...). Select EELS → Extract → Signal to generate a background-subtracted SI.

4. With the SpectrumPicker tool, generate another sum spectrum map (on the background-subtracted SI), and draw a box around an EDX peak on the profile. Make sure the nonlinear least-square (NLLS) preferences for fitting multiple NLLS is set to "simultaneously" (Spectrum → NLLS Fitting → Preferences...) and chose "fit a Gaussian to ROI" from the same sub-menu. Repeat this step for another Gaussian on the EDX spectrum. If overlap occurs, make sure the residuals are minimal by optimizing the position of the Gaussians, simply by sliding the selection box around the peak maxima back and forth. From the NLLS Fitting sub-menu select "Constrain Model Parameters" and fix Center and full-width at half maximum (FWHM) for both Gaussians. Once satisfied with the fit, select "Output Fit Values to Result Window", and save the values of the FWHM for future reference. Finally from the NLLS sub-menu, select "Apply Model to Parent Spectrum Image" to generate two images, each corresponding to the local amplitude of the fitted Gaussians.

5. Export to a .tif image the STEM image acquired in parallel and open it in DM. The image dimension (in pixels), and relative position of the features with respect to the border of the image must coincide with those of the EDX SI. One may scale the image size with Edit → Scale. Find the average intensity of the background and save for further reference. The background of the final concentration map will be defined by pixels having an intensity below the identified threshold.

6. Run the following script to generate a color-coded concentration and corresponding uncertainty maps with the background pixels set to a grey shade. The script implements Eqs. 4.3b-4.11 and the concepts discussed in Section 4.6.1 and 4.6.2 to define the background of the features. The user is prompted to select the elemental images together with the background map. The concentration will be expressed in terms of "Element A". Several calculations parameters are required (Fig. C-1): the k_{AB}-factor, number of channels over which the background was integrated, the confidence interval ($\pm 1\sigma$, $\pm 2\sigma$, etc.) and the FWHM of each Gaussian. An extra parameter, "Background threshold" is prompted and works as a filter to exclude low-counts (a high number increases artificially the selectivity of the filter). If the background is to be defined by the STEM image, then set the background threshold to 0 and enter the average intensity of the background of the STEM image.

```
/*Script to compute concentration map and corresponding
uncertainties given a confidence level. User is first prompted to
select two elemental maps and a background map and then must provide
```

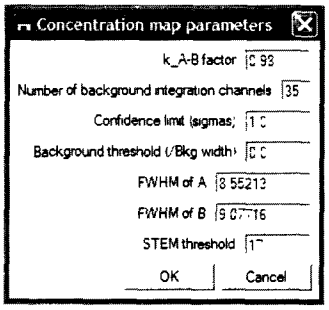

FIG. C-1: Screen shot of the dialog prompting the user to input computation parameters for the calculation of the concentration map.

```
details on the calculations parameters. A color-coded concentration
map is generated with corresponding upper and lower confidence of
the concentration. Background is set to a grey shade by
correspondence with the STEM image acquired in parallel.

Elemental maps must be previously generated by fitting Gaussians on
EDXS gaussian peaks on each pixel of the spectrum image, using the
nonlinear least-square fit routines available in DM.

Variable names reference : Au --> A and Pt-->B
*/
Image Au, Pt, Bkg, STEM

Number w    // Background window width
Number k    // k-factor Au-Pt C_Au/C_Pt = k * I_Au/I_Pt
Number Cl   // Confidence level, 1 = 1sigma, 2 = 2sigma, etc.
Number Ib   // to treat the case where no counts are included in background
Number Th   // Threshold on the STEM image used to crop

//Obtained from Gaussian fit:
//ensure width and position were constrained
Number FWHM_A, FWHM_B

//&&&&&&&&&&&&&&&&&&&&&&&&&&&&&&&&&&&&&&&&&&&&&&&&&&&&&&&&&&&&&&&&
//BEGIN DIALOG
if(!GetThreeLabeledImagesWithPrompt("Select elmental maps.", \
        "Concentration expressed in terms of element A ",    \
        "Elemental Image A", Au, "Elemental Image B", Pt, \
        "Background", Bkg))\
   exit(0)
```

```
if(!GetOneLabeledImageWithPrompt("Select STEM Image", \
        "Select STEM Image", "STEM Image", STEM))exit(0)

//Declarations for dialog
TagGroup Conc_Map_Dialog, Conc_Map_Dialog_Items
Object Conc_Map_Dialog_Window
TagGroup k_item, k_slot
TagGroup w_item, w_slot
TagGroup Cl_item, Cl_slot
TagGroup Ib_item, Ib_slot
TagGroup FWHM_A_Item, FWHM_A_Slot
TagGroup FWHM_B_Item, FWHM_B_Slot
TagGroup STEM_item, STEM_Slot

//Create a dialog
Conc_Map_Dialog = DLGCreateDialog("Concentration map parameters",\
                                  Conc_Map_Dialog_Items)
Conc_Map_Dialog_Window = alloc(UIframe).Init(Conc_Map_Dialog)

//Create items
k_item = DLGCreateRealField("k_A-B factor", k_slot, 0.98, 10, 3)
w_item = DLGCreateIntegerField("Number of background integration channels"\
                               ,w_slot, 35, 4)
Cl_item = DLGCreateRealField("Confidence limit (sigmas)", Cl_slot,\
                             1, 10, 3)
Ib_item = DLGCreateRealField("Background threshold (/Bkg width)",\
                             Ib_slot, 0, 10, 3)
FWHM_A_item = DLGCreateRealField("FWHM of A", FWHM_A_Slot, 8.62441 , 15, 6)
FWHM_B_item = DLGCreateRealField("FWHM of B", FWHM_B_Slot, 9.06631 , 15, 6)
STEM_item = DLGCreateIntegerField("STEM threshold",\
                             STEM_slot, 6500, 10)

//Add items to dialog
Conc_Map_Dialog.DLGAddElement(k_item).DLGAnchor("East")
Conc_Map_Dialog.DLGAddElement(w_item).DLGAnchor("East")
Conc_Map_Dialog.DLGAddElement(Cl_item).DLGAnchor("East")
Conc_Map_Dialog.DLGAddElement(Ib_item).DLGAnchor("East")
Conc_Map_Dialog.DLGAddElement(FWHM_A_item).DLGAnchor("East")
Conc_Map_Dialog.DLGAddElement(FWHM_B_item).DLGAnchor("East")
Conc_Map_Dialog.DLGAddElement(STEM_item).DLGAnchor("East")

//Layout
Conc_Map_Dialog.DLGTableLayout(1,7,1)

//Show the dialog
If(!Conc_Map_Dialog_Window.pose())exit(0)//
```

```
//Read from dialog and assign values
k = k_slot.DLGGetValue()
w = w_slot.DLGGetValue()
Cl = Cl_slot.DLGGetValue()
Ib = Ib_slot.DLGGetValue()
FWHM_A = FWHM_A_slot.DLGGetValue()
FWHM_B = FWHM_B_slot.DLGGetValue()
Th = STEM_slot.DLGGetValue()

//END DIALOG
//&&&&&&&&&&&&&&&&&&&&&&&&&&&&&&&&&&&&&&&&&&&&&&&&&&&&&&&&&&&&&&&&
//BEGIN MAPS COMPUTATION

//Get rid of negative values and
//Compute a background-subtracted Gaussian fit
Au  = tert(Au<0, 0, Au)
Pt  = tert(Pt<0, 0, Pt)
Bkg = tert(Bkg<0, 0, Bkg)

//Get image, window size and zoom display
Number X_Size, Y_size, X_Win, Y_Win
GetSize(Au, X_size, Y_Size)
Number Zoom = GetZoom(Au)
GetWindowSize(Au, X_Win, Y_Win)

Image C_Au = RealImage("At. Concentration of A", 4, X_Size, Y_Size)
Image Cmin = RealImage("Max At. Concentration of A", 4, X_Size, Y_Size)
Image Cmax = RealImage("Min At. Concentration of A", 4, X_Size, Y_Size)

// Modified ratio for the case where pure Au or Pt is encountered
Image R_prime = RealImage("R prime", 4, X_Size, Y_Size)

Number Pi = Pi()
//Integregted Area = F1* FWHM * height
Number F1 = sqrt(Pi/(4*log(2)))
// 1.189*FWHM maximizes the peak over background for low peak
Number F2 = 1.189
//Factor to calculate detectability limit
Number F3 = erf(F2*sqrt(log(2)))

Number FWHM_Pt = FWHM_B
Number FWHM_Au = FWHM_A
Number Ib_min = Ib/w

Image I_Pt = Pt * FWHM_Pt * F1
```

```
Image I_Au = Au * FWHM_Au * F1

C_Au = k*I_Au/(k*I_Au+I_Pt)
Cmax = C_Au*(1+ Cl*sqrt(I_Pt/I_Au*(I_Pt + I_Au)/(I_Pt + k*I_Au)**2))
Cmin = C_Au*(1- Cl*sqrt(I_Pt/I_Au*(I_Pt + I_Au)/(I_Pt + k*I_Au)**2))

// Estimated background under peak with 1.2*FWHM
Image Ib_Pt = Cl*sqrt(2*Bkg/w*FWHM_Pt*F2) + Ib_min
Image Ib_Au = Cl*sqrt(2*Bkg/w*FWHM_Au*F2) + Ib_min
//Area of peak when window = 1.2*FWHM
Image J_Au = I_Au*F3
Image J_Pt = I_Pt*F3

// If both peaks are above the detection limits
// C_min is negative because of low counts or CMin>CMax
// set pixel value to a negative
Cmax    = tert(J_Au <= Ib_Au && J_Pt > Ib_Pt &&\
           (Cmin <= 0 || Cmin > Cmax), 0.01, Cmax)
Cmin    = tert(J_Au < Ib_Au && J_Pt > Ib_Pt &&\
           (Cmin < 0 || Cmin > Cmax), -1, Cmin)

//Case where Au peak is undected but Pt peak detected:
//C = N/A and confidence interval is calculated with detectability limit
C_Au    = tert(J_Au < Ib_Au && J_Pt >= Ib_Pt, 0, C_Au)
R_Prime = tert(J_Au < Ib_Au && J_Pt >= Ib_Pt, Ib_Au/J_Pt*k, R_Prime)
Cmin    = tert(J_Au < Ib_Au && J_Pt >= Ib_Pt, 0, Cmin)
Cmax    = tert(J_Au < Ib_Au && J_Pt >= Ib_Pt, R_prime/(1+R_prime), Cmax)

//Case where Pt peak is undected but Au peak detected:
//C = N/A and confidence interval is calculated with detectability limit
C_Au    = tert(J_Au >= Ib_Au && J_Pt < Ib_Pt, 1, C_Au)
R_Prime = tert(J_Au >= Ib_Au && J_Pt < Ib_Pt, J_Au/Ib_Pt*k, R_Prime)
Cmin    = tert(J_Au >= Ib_Au && J_Pt < Ib_Pt, R_prime/(1+R_prime), Cmin)
Cmax    = tert(J_Au >= Ib_Au && J_Pt < Ib_Pt, 1, Cmax)

// No peaks are detected
C_Au    = tert(J_Au < Ib_Au && J_Pt < Ib_Pt, 0, C_Au)
Cmin    = tert(J_Au < Ib_Au && J_Pt < Ib_Pt, -1, Cmin)
Cmax    = tert(J_Au < Ib_Au && J_Pt < Ib_Pt, -1, Cmax)

//END MAPS COMPUTATION
//&&&&&&&&&&&&&&&&&&&&&&&&&&&&&&&&&&&&&&&&&&&&&&&&&&&&&&&&&&&&&&&&
//BEGIN CROPPING AND DISPLAY
Image C_Temp //Dummy image for display
Number ll //counter
```

```
//Display concentration maps
for (ll=1;ll<=3;ll++)
{
    if (ll==1)
        C_Temp := C_Au
        SetName(C_Temp, "Concentration map of A")
    if (ll==2)
        C_Temp := CMin
        SetName(C_Temp, "Lower bound of the "+ Cl +\
                " sigma confidence interval")
    if (ll==3)
        C_Temp := CMax
        SetName(C_Temp, "Upper bound of the "+ Cl +\
                " sigma confidence interval")
    //Comment out these two lines if no cropping is required
    //Negative values are set to 0.01, a value which is assigned
    //the grey shade.
    C_Temp  = tert(C_Temp <= 0, 0.01, C_Temp)
    C_Temp *= tert(STEM <= Th, 0, 1)

    //Color mode 4 = Temperature color table
    C_Temp.setcolormode(4)
    ImageDisplay imageDisp = C_Temp.ImageGetImageDisplay(0)

    //First pixel of the ''Temperature'' Color Look-up input Table (CLUT)
    //set to grey level R,B,G = 128,128,128 and includes 0.01
    Image Ref:=ImageDisplayGetInputColorTable(imagedisp)
    Ref[0,0,1,1]=RGB(128,128,128)
    imageDisp.ImageDisplaySetInputColorTable(Ref)

    imageDisp.ImageDisplaySetContrastLimits(0, 1)
    showimage(C_Temp)

    SetWindowSize(C_Temp, X_Win, Y_Win)
    SetImagePositionWithinWindow(C_Temp, 0, 0)
    SetWindowPosition(C_Temp, 100+ll*100, 100+ll*100)
    SetZoom(C_Temp, Zoom)
    UpdateImage(C_Temp)
    imageDisp.ImageDisplaySetContrastLimits(0, 1)
}
//END CROPPING AND DISPLAY
//&&&&&&&&&&&&&&&&&&&&&&&&&&&&&&&&&&&&&&&&&&&&&&&&&&&&&&&&&&&&&&&&
```

C-2 Utility Scripts

SI with the x or y dimension are unity are referred to as linescans. Usually, the x axis is assigned to energy, and the y axis, to a spatial dimension. Linescans cannot be processed by the script above unless the linescan is "rotated" in such a way that the z axis (depth) is assigned to energy. This can be done by running the following script:

```
//Simple script to convert a linescan to a single row SI
//Run this script with the linescan in front image
//Hit OK to convert to EELS.

Image src:=GetFrontImage()
Number xsize, ysize
GetSize(src, xsize, ysize)

Image rot = RealImage("", 4, ysize, 1, xsize)
rot[irow, iplane, icol] = src

showimage(rot)
//Converting to EELS for access using the SpectrumPicker tool
ChooseMenuItem("Spectrum","Convert Data To","EELS")
```

Alternatively, a profile in a graph display can be converted to a single row of pixels by choosing the "Raster" display in the Display → Display Type submenu. Should the user need to convert the SI back to a linescan, just run the following script:

```
//Simple script to convert a single row SI to a linescan
//Run this script with the SI in front image
//Hit OK to convert to EELS.

Image src := GetFrontImage()
Number xsize, ysize, zsize
Get3DSize(src, xsize, ysize, zsize)

Image rot=RealImage("", 4, zsize, xsize)
rot = src[irow, iplane, icol]

showimage(rot)
//Converting to EELS for access using the SpectrumPicker tool
ChooseMenuItem("Spectrum","Convert Data To","EELS")
```

Finally, we have addressed the question of rotational integration or projection in Section 4.6.3. Rotational averaging is an operation that is commonly performed on micrographs, especially diffraction patterns. The code for performing a rotational

average of a single image can be found on a public domain Gatan script. However, the following performs a rotational average of a SI:

```
/*Performs a rotational integration on a SI between energy channels
LowerBound and UpperBound and displays the result as a single row
SI. Hit OK to convert to EELS./*

Image front:=GetFrontImage()
Number xsize, ysize, zsize, samples=512
get3dsize(front, xsize, ysize, zsize)
Number k=2*PI()/samples, UpperBound, LowerBound

//Input here the lower and upper channels where integration should
//be performed. Restrict the range to avoid long computation times.
LowerBound = 370
UpperBound = 800
Image warped:=RealImage("warped", 4, xsize/2, samples, zsize)
Image Integrated := RealImage("Integrated",4, xsize/2, 1, zsize)

Number i

For (i=LowerBound;i<UpperBound;i++)
{
//This bit does all the job. Some of it is adapted from a code available on
//the Gatan public domain.
warped[0,0,i,xsize/2, samples, i+1] = \
            warp(slice2(front,0, 0, i, 0, xsize, 1, 1, ysize, 1),\
            icol * sin(irow * k) + xsize/2,\
            icol * cos(irow * k) + ysize/2 )
}

Integrated[icol, 0, iplane] += warped

//Comment out the next line to obtain a rotational average
//0.5 is added to icol to avoid having null values at the center.
Integrated *= 4*Pi()*(icol+0.5)/samples

showimage(integrated)
//Uncomment the following to diagnostic problems
//showimage(warped)
//Converting to EELS for access using the SpectrumPicker tool
ChooseMenuItem("Spectrum","Convert Data To","EELS")
```

Appendix D

Codes for Numerical Abel and Inverse Abel Transforms

We have referred to an Abel transform in Chapter 4.6.3 when discussing the projection of a radial function onto an axis. We list in this Appendix the codes used to perform a numerical Abel transform and inverse Abel transform, that allows one to find the radial profile given its projection. All codes are written in Digital Micrograph™ (DM) version 3.11.1, GMS 1.6.1.

The code is based on the algorithm proposed by (Bracewell 1986, p262-6), which reduces the Abel transform to a convolution following a variable transform. We will follow the same notation as Bracewell's in his book (1986). Noting r, the radial position and $f(r)$, a radial profile, we can define $f_A(x)$ as the Abel transform of f, on the projected axis, x. A variable transform is first performed, letting $\xi = x^2$ and $\rho = r^2$, and putting $f_a(x) = F_A(x^2)$ and $f(r) = F(r^2)$. It can be demonstrated (Bracewell 1986, p262-6) that the numerical Abel transform reduces to the convolution of the transformed profile with a set of precalculated coefficients.

D-1 Numerical Abel Transform

The following script demonstrates how this can be done.

```
//N     :   number of data points on the profile
//one   :   dummy variable = 1
//k     :   counter
Number N, one, k
//Assign f_r to profile
Image f_r:= GetFrontImage()
//Assign number of data points to N
GetSize(F_r, N, one)
//Function warp() fails for image which one or more dimension >2^13
//sqrt(2^13)^91, so 91 is the maximum size of a profile.
if(N>90)
    {
    beep()
    okdialog("Dimension must be < 91 pixels !")
    exit(0)
```

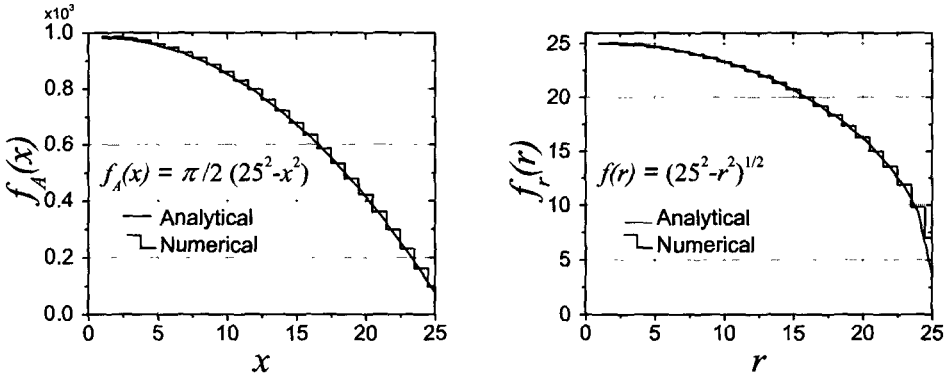

FIG. D-1: Numerical Abel transform (a) and inverse Abel transforms (b) of a model function (step-line) compared with the analytical solution (continuous line).

```
    }
//Variable transform : r-->rho^2 and f_r --> F_rho
//Map profile onto F_rho
Image F_rho:=RealImage("", 4, N**2, 1)
//icol and irow are intrinsic variables
F_rho = warp(f_r, sqrt(icol), irow)
//K_ are the set of coefficients needed to perform the transform
Image K_ := RealImage("K", 4, N**2, 1)
K_=2*sqrt(icol+1)-2*sqrt(icol)
Image Fa_ksi := RealImage("", 4, N**2, 1)
//Convolution sum between image and coefficients
For (k=0; k<=N**2-1; k++)
    {
    Fa_ksi[0,k, 1, k+1] = Sum(K_[0,0, 1, N**2-k]*F_rho[0, k, 1, N**2])
    }
//Transforms back: sqrt(ksi)-->x and Fa_ksi-->Fa_x
Image Fa_x := RealImage("Fa_x", 4, N, 1)
Fa_x = warp(Fa_ksi,icol**2, irow)
//Display final result
Showimage(Fa_x)
```

We can test the script with a model function, $f(r) = \sqrt{(a^2 - r^2)}$ for which the Abel transform is known analytically $f_A(x) = \frac{1}{2}\pi(a^2 - x^2)$. Fig. D-1(b) shows that the numerical transform and its analytical transform are indistinguishable. Variables have the same meaning as for the Abel transform.

D-2 Numerical Inverse Abel Transform

The numerical inverse Abel transform can be performed using a similar script:

```
Number N, one, k
Image Fa_x:=GetFrontImage() GetSize(Fa_x, N, one)
//Function warp() fails for image which one or more dimension >2^13
//sqrt(2^13)~91, so 90 is the maximum size of a profile.
if(N>90)
    {
    beep()
    okdialog("Dimension must be < 91 pixels !")
    exit(0)
    }
//Variable transform : x-->ksi^2 and f_x --> F_x
//Map profile onto Fa_ksi
Image Fa_ksi:=RealImage("Fa_ksi", 4, N**2, 1)
Fa_ksi = warp(Fa_x, sqrt(icol), irow)
if(N>90)
    {
    beep()
    okdialog("Dimension must be < 91 pixels !")
    exit(0)
    }
//K_ are the set of coefficients needed to perform the transform
Image K_:= RealImage("K", 4, N**2, 1) K_=2*sqrt(icol+1)-2*sqrt(icol)
Image F_rho := RealImage("F_r", 4, N**2, 1)
//Convolution sum between image and coefficients
For (k = N**2; k>=1; k--)
    {
    F_rho[0, k-1, 1, k]=(Fa_ksi[0, k-1, 1, k]-\
                        sum(K_[0, 0, 1, N**2-k+1]*\
                        F_rho[0, k-1, 1, N**2]))/2
    }
//Transforms back: sqrt(rho)-->r and Fa_rho-->Fa_r
Image F_r := RealImage("F_r", 4, N, 1) F_r = \
                                warp(F_rho, icol**2, irow)
//Display final result
Showimage(F_r)
```

We can also test this script with the same model function. The analytical inverse Abel transform of the function $f_A(x) = \frac{1}{2}\pi(a^2 - x^2)$ is $f(r) = \sqrt{(a^2 - r^2)}$. Fig. D-1(b) shows again that the numerical and analytical transforms overlap.

Appendix E

Models for Elemental Depletion in an Alloyed Nanoparticle

E-1 Volume-Limited Model

Let a and b be the constituents of a nanoparticle (NP). If a is the beam-sensitive constituent, then the mass loss rate at any time is proportional to the number of remaining a atoms in the NP, the damage cross-section in this model, σ_v and dose, κ:

$$\frac{dn_a}{dt} = -n_a \sigma_v \kappa. \tag{E-1}$$

The number of i atoms (a or b, in our case) in a NP can be written as

$$n_i = C_i Z V N_A, \tag{E-2}$$

where C_i is the atomic fraction of i in the NP, V is the volume of the particle, $C_b = 1 - C_a$, N_A, is Avogadro's number and Z, the atomic volume, defined in our system as

$$Z = \frac{(\rho_a C_a A_a + \rho_b C_b A_b)}{(C_a A_a + C_b A_b)^2}, \tag{E-3}$$

where ρ_i and A_i are the density and atomic number of species i.

We wish to express the concentration ratio, C_a/C_b, of a NP with initial composition $(C_a/C_b)_0$, after an acquisition time τ, given a damage cross-section σ, and dose d.

Let $x = C_a/C_b = n_a/n_b$, then we can rewrite Eq. E-1 as

$$\frac{dx}{dt} = -x \sigma_v \kappa. \tag{E-4}$$

Separating the variables and integrating yields:

$$\int_{x=x_0}^{x} \frac{dx}{x} = \int_{t=0}^{t=\tau} -\sigma_v \kappa \, dt, \tag{E-5}$$

Solving for x demonstrates that the concentration ratio follows an exponential decay:

$$x = x_0 \exp(-\sigma_v \kappa \tau). \tag{E-6}$$

Note that expression E-6 is independent of the volume or the shape of the NP, provided that the dose remains constant during the electron irradiation.

E-2 Surface-Limited Model

We express the loss rate now being proportional to the number of sensitive atoms on the surface of a NP, n_a^s, and a damage cross-section, σ_s

$$\frac{dn_a}{dt} = -n_a^s \sigma_s \kappa. \tag{E-7}$$

We then write Eq. E-7 in terms of concentration raito, x, giving:

$$\frac{dx}{dt} = -\frac{n_a^s}{n_b} \sigma_s \kappa. \tag{E-8}$$

We can approximate the number of i atoms contained in a monolayer of a surface S as

$$n_i^S = C_i S Z \delta, \tag{E-9}$$

where δ is the thickness of a monolayer, that can be approximated to $Z^{-1/3}$. We can now express n_a^S in terms of total number of a atoms by combining Eqs. E-2 and E-8:

$$n_a^S = n_a \frac{1}{Z^{1/3}} \frac{S}{V}. \tag{E-10}$$

For a spherical NP, we can rewrite Eq. E-9 only in terms of the number of atoms a:

$$n_a^S = (36\pi C_a n_a^2)^{1/3}. \tag{E-11}$$

Writing Eq. E-10 in terms of concentration ratio defined above, x, and the constant number of b atoms:

$$n_a^S = (36\pi)^{1/3} n_b^{2/3} \frac{x}{(x+1)^{1/3}}. \tag{E-12}$$

Substituting Eq. E-12 in Eq. E-8, separating the variables and writing the integral yields:

$$\int_{x=x_0}^{x} \frac{(x+1)^{1/3}}{x}\, dx = \int_{t=0}^{t=\tau} -\left(\frac{36\pi}{n_b}\right)^{1/3} \sigma_s \kappa \, dt. \tag{E-13}$$

Solving the integral by parts gives the transcendental equation relating implicitly the concentration ratio after an exposure τ to electron irradiation:

$$g(x') = g(x'_0) - \left(\frac{36\pi}{n_b}\right)^{1/3} \sigma_s \kappa \tau, \tag{E-14}$$

where

$$x' = (x+1)^{1/3} \text{ and } x'_0 = (x_0+1)^{1/3}, \tag{E-15}$$

and $g(x)$ is a function defined by

$$g(x) = 3x + \ln\left[\frac{(x-1)}{x^2(x+1)^2}\right] - \sqrt{3}\arctan\left[\frac{1}{\sqrt{3}}(2x+1)\right]. \tag{E-16}$$

Fig. E-1 compares the volumetric model to the surface model, letting

$$\sigma_v \kappa = \left(\frac{36\pi}{n_b}\right)^{1/3} \sigma_s \kappa = 2 \tag{E-17}$$

and $x_0 = 1$.

Given the similarity of the curves, it is experimentally difficult to determine which model the electron beam-induced Ag loss in NPs follows, especially with the noise in the experimental data points. If we let $\sigma_v = \left(\frac{36\pi}{n_b}\right)^{1/3} \sigma_s$, then the only possible method to discern between the models on a mathematically basis is to perform the experiment with particles having a wider range of sizes and compositions, in order to vary n_b. In the size range explored (6-22 nm), there was no obvious dependency of σ_d to either NP size or composition (Fig. 5.8(b)), strengthening the hypothesis of the volumetric model. Another suggestion to validate the model is to retry these experiments with a hot stage, say at 600° –800 °C. Since it is suggested that diffusion, limited at low temperatures, is induced by electron beam knock-on damage, then, at high temperatures, diffusion would no longer be the rate-limiting mechanism and the effective sputtering cross-section should therefore approach the theoretical one. This

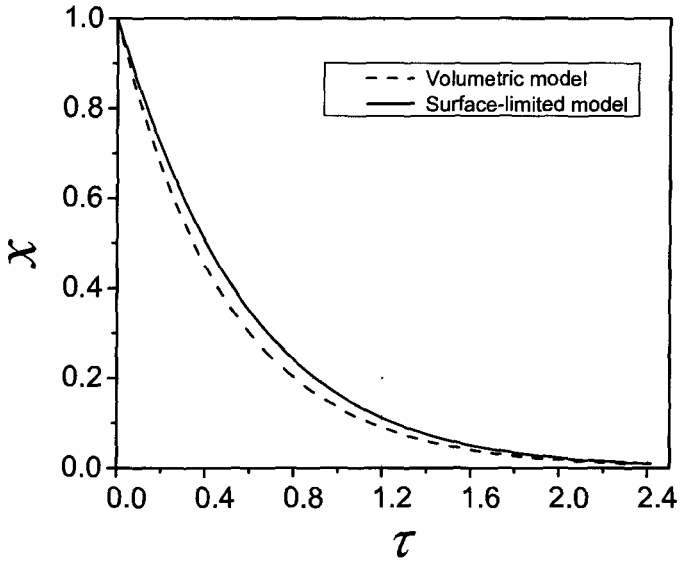

FIG. E-1: Depletion (expressed as a concentration ratio, x) of an initially equimolar NP after an exposure τ to the electron beam according to a volume-(dashed line) and surface-(solid line) limited models (see text for value of parameters).

experiment might be complicated with other possible depletion mechanisms such as sublimation (since the vapor pressure of Ag is 4 order of magnitude larger than that of Au) expected to be enhanced by the capillarity effect.

Appendix F

Matlab code for moving boundary problem in spherical symmetry

Figs 6.3 and the results of the simulations performed in Section 6.3.2 were generated by running a computer program written in Matlab™ that simulates interdiffusion in a composite sphere. This Appendix supplies additional information on this program and provides its complete listing.

The code was specifically designed to simulate the diffusion within a core-shell composite sphere and is mainly inspired from the algorithm proposed by Tanzilli and Heckel (1968). Fick's diffusion equation in each phase is expressed in terms of finite difference. A variable transform allows contraction or expansion of the radius axis to track the moving boundary. The algorithm was modified to include composition-dependent diffusion coefficients in each phase. This was done by rewriting Fick's equations in terms of finite difference equations with a diffusion coefficient determined by Darken's relation, as proposed by Sekerka and Wang (1999, p.258-9).

During computation, the program displays two curves that are updated after a given number of time steps. The curve in the top panel of Fig. F-1(a) is a screen shot of the instantaneous radial diffusion profile. The bottom panel of Fig. F-1(a) shows the real-time position of the interface relative the initial core radius. The program stops when the core becomes homogeneous to a level of 99.9% and the interface have reached 99.9% of its equilibrium position. Once the program is terminated, the program calls a function to create a final window (Fig. F-1(b)) which includes the final profile, interface position with time and displays all the computation parameters.

The code nevertheless contains many limitations as it was written solely for the purpose of generating Figs. 6.3:

- The code assumes that the shell homogenizes well before the core. For the parameters we have explored, this was always the case;

- In a $A-B$ binary system, the mean composition of A, $\overline{C}$, must be such that the two phases are present at equilibrium. In other words, noting α and β, the phases present in the shell and the core, respectively, and $C^{\alpha\beta}$ and $C^{\beta\alpha}$, the solubilities of A in phases α and β, respectively, this condition requires that $C^{\alpha\beta} < \overline{C} < C^{\beta\alpha}$;

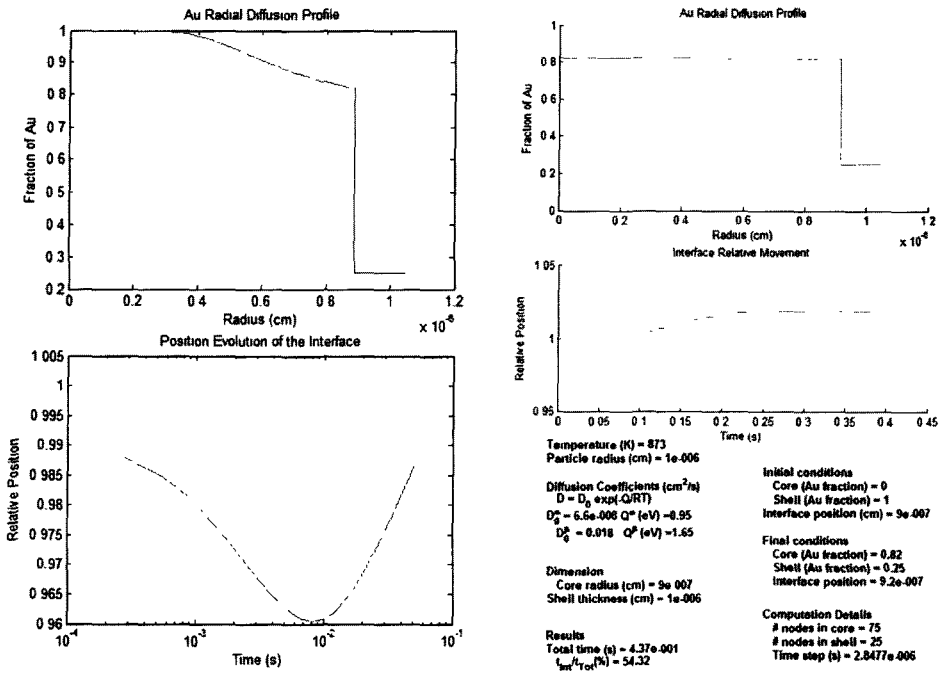

(a) (b)

FIG. F-1: (a) Instantaneous screen shot of the window which includes the composition profile and the interface movement generated by the Matlab program (after 55 ms) and (b) window containing the final display showing all the computation parameters. The interface movement (normalized with respect to the initial interface position) in (a) is seen moving towards the center at early times and after $\sim 0.5 \times 10^{-5}$ s, stalls and reverses direction, as explained in Section 6.3.2. In (b) the interface movement curve flattens at around 240 ms. This corresponds to the time at which the interface have reached its equilibrium position. This time also corresponds to t_{Int}/t_{Tot} multiplied by the "Total time" (displayed under the "Results" heading).

- Although a composition-dependent diffusion coefficient was included in the finite difference, the "thermodynamic factor" (Darken 1948) was not;
- The code is not fully optimized and could make better use of user-defined functions to avoid redundancy in the code. It would be worth checking if some parts of the code can be carried by library-defined functions.

```
% Calculates the diffusion profile in a core-shell composite sphere.
% All concentrations are in terms of the component rich in the core,
% hereafter denoted as beta, the shell being alpha.
% The code is tested for the case where the shell homogenizes before the
% core. The code is based on the algorithm by Tanzilli and Heckel (1968),
% modified to include a composition-dependent diffusion coefficient
% determined by Darken's relation. This add-on was implemented following
```

```
% the methodology of Sekerka & Wang (1999, p258-259).
% Variable names follow Tanzilli and Heckel (1968).

% Limitation: exit is forced if the mean composition is not within the
% two-phase region. Could be easily corrected by modifying code. Also, the
% shell is assumed to homogenize well before the core (yet another
% avenue for improvement).
clear;
%-----------------------------------------------------------
% ***Diffusion properties in cm^2/s***
% Diffusion coefficient = D0*exp[-Q/(RT)]
T = 800+273; %Temperature
R = 8.615e-5;  %Boltzmann cst eV/K
D_0_alpha = 6.6e-8;
Q_alpha = 0.95; %eV
D_alpha = D_0_alpha*exp(-Q_alpha/R/T);
D_0_beta = 0.018;
Q_beta = 1.65; %eV
D_beta = D_0_beta*exp(-Q_beta/R/T);
%-----------------------------------------------------------
% Initial profile in the core
C_beta_0 = 1;
% Solubility limit at the core side of the interface
C_beta_alpha = 0.82;
% Initial profile in the shell
C_alpha_0 = 0;
% Solubility limit at the shell side of the interface
C_alpha_beta = 0.25;
% Diffusion coefficient, as computed by Darken's relation
D_alpha_beta = D_alpha*C_alpha_beta + D_beta*(1-C_alpha_beta);
D_beta_alpha = D_alpha*C_beta_alpha + D_beta*(1-C_beta_alpha);
%-----------------------------------------------------------
% Dimensionless parameter
Delta = C_beta_alpha-C_alpha_beta;
%-----------------------------------------------------------
% Geometry and initial conditions
% Initial length of interface (l) and total length (L) in cm
l = 2*9e-7; L = 2*10.5e-7;
% Mean composition. Should be constant throughout the computation.
C_bar = (l/L)^3;
% Number of nodes in the beta (r) phase and total number of nodes (N)
r = 75; N = 100;
% Initial position of the interface
Xi_ov_2 = l/2;

% Initial concentration profile
```

```
C_ini(1:r-1) = C_beta_0; C_ini(r+1:N) = C_alpha_0;

% Fictious nodes at extremities to force zero flux at boundary
% (derivative = 0)
C_0 = C_ini(1); D_0 = D_beta; C_ini(N+1) = C_ini(N-1);
% C is a spatial vector containing the composition profile
C = C_ini;
% D is a spatial vector containing the diffusion coefficients
D = D_alpha*C_ini + D_beta*(1-C_ini);

% Minimal time step to ensure numerical stability.
% Decrease Time_Factor if numerical oscillations at the interface amplify
Time_Factor=1e-1; Delta_t = Time_Factor*(Xi_ov_2/(r-2))^2/(D_beta);
% Initialize Variables
Total_time = 0; t_beta_0 = 0;
%-------------------------------------------------------------
% Initialization
% Break to display diffusion profile and interface movement at every
% Step_Rec step. Low numbers may lead to computing and memory overload.
Step_Rec = 1000;

% Program terminated if mean composition lies outside of the two-phase
% region. Code could be modified to take into account all situations
if C_bar > C_beta_alpha | C_bar < C_alpha_beta
    error('Average composition must be in the 2-phase');
    return
end
% Expected interface position position
Final_int_pos = (((1/2)^3*(C_beta_0-C_alpha_0)-...
                  (L/2)^3*(C_alpha_beta-C_alpha_0))/Delta)^(1/3);
% Initialize flag. Becomes true when core is homogenized
Flag_Is_Homo = false;
% Loop exit criteria. Convergence criteria.
Criteria = 0.001;
%-----------------------------------------------------------------------
% Counter reset
jj = 0;
% Main loop
% While the interface is still moving and the core is not homogeneous
while Xi_ov_2 < Final_int_pos & ~Flag_Is_Homo
    % Compute Interface Position
    jj = jj + 1;
    Diff_term_1 = D_alpha_beta*(N-r)*...
                  (-C(r+2) + 4*C(r+1) - 3*C_alpha_beta)/...
                  (2*(L/2-Xi_ov_2));
    Diff_term_2 = D_beta_alpha*r*...
```

```
                (C(r-2) -4*C(r-1) + 3*C_beta_alpha)/(2*Xi_ov_2);
    d_Xi_2_dt = 1/(C_beta_alpha-C_alpha_beta)*(Diff_term_1 - Diff_term_2);
    Xi_ov_2 = Xi_ov_2 + Delta_t*d_Xi_2_dt;

    % Compute concentration profile in the alpha phase
    C(r) = C_alpha_beta;
    D(r) = D_alpha_beta;
    n=r+1:N;
    D(n) = D_alpha*C(n) + D_beta*(1-C(n));
    dC_alpha_dt(n) = (N-n)/(L/2-Xi_ov_2).*(C(n+1) - C(n-1))/...
                     2*d_Xi_2_dt + D(n)*(N-r)^2.*...
                     (C(n-1)-2*C(n)+C(n+1))/(L/2-Xi_ov_2)^2 + ...
                     D(n)./(Xi_ov_2+(n-r)*(L/2-Xi_ov_2)/(N-r))*...
                     (N-r).*(C(n+1)-C(n-1))/(L/2-Xi_ov_2) +...
                     ((N-r)/(L/2-Xi_ov_2))^2*((D(n+1) - D(n-1))/2).*...
                     ((C(n+1) - C(n-1))/2);

    C(n) = C(n) + Delta_t*dC_alpha_dt(n);

    % Handling exception at n=1 before computing beta phase. Updated just
    % after beta computation
    dC_beta_dt_1 = 1/Xi_ov_2*(C(2)-C_0)/2*d_Xi_2_dt + ...
                   D(1)*r^2*(C_0-2*C(1)+C(2))/Xi_ov_2^2 + ...
                   D(1)*r^2*(C(2)-C_0)/Xi_ov_2^2 + ...
                   (r/Xi_ov_2)^2*((D(2) - D_0)/2)*((C(2) - C_0)/2);

    % Compute concentration profile in the beta phase
    C(r) = C_beta_alpha;
    D(r) = D_beta_alpha;
    n=2:r-1;
    D(n) = D_alpha*C(n) + D_beta*(1-C(n));
    dC_beta_dt(n) = n/Xi_ov_2.*(C(n+1)-C(n-1))/2*d_Xi_2_dt + ...
                    D(n)*r^2.*(C(n-1)-2*C(n)+C(n+1))/Xi_ov_2^2 + ...
                    D(n).*r^2.*(C(n+1)-C(n-1))./(n*Xi_ov_2^2) + ...
                    (r/Xi_ov_2)^2*((D(n+1) - D(n-1))/2).*...
                    ((C(n+1) - C(n-1))/2);
    C(n) = C(n) + Delta_t*dC_beta_dt(n);
    % Update concentration at C(1)
    C(1) = C(1) + Delta_t*dC_beta_dt_1;
    % Update Diffusion coefficient at C(1)
    D(1) = D_alpha*C(1) + D_beta*(1-C(1));
    % Update concentration at center
    d_C_0 = 6*D(1)*r^2*(C(1)-C_0)/Xi_ov_2^2;
    C_0 = Delta_t*d_C_0 + C_0;
    D_0= D_alpha*C_0 + D_beta*(1-C_0);
    % Update fictious node for concentration at alpha boundary
```

```
    C(N+1) = C(N-1);
    D(N+1) = D_alpha*C(N+1) + D_beta*(1-C(N+1));

    % Capture composition profile and relative interface movement
    % at every Step_Rec steps.
    if rem(jj,Step_Rec) == 0
        Interface_movement(jj/Step_Rec) = Xi_ov_2;
        Delta_X_alpha = (L/2-Xi_ov_2)/(N-r);
        Delta_X_beta = Xi_ov_2/r;
        X_scale_transformed = cat(2, 0:Delta_X_beta:Xi_ov_2,...
                                    Xi_ov_2:Delta_X_alpha:L/2) ;
        Time_Scale = 0:Delta_t*Step_Rec:Delta_t*(jj)-Delta_t*Step_Rec;
        Profile_Scale = cat(2,C_0, C(1:r-1), ...
                            C_beta_alpha, C_alpha_beta,...
                            C(r+1:N));
        % Display plots
        subplot(6,2,[1:6]); ...
                plot(X_scale_transformed, Profile_Scale);...
                title('Au Radial Diffusion Profile');...
                xlabel('Radius (cm)');...
                ylabel('Fraction of Au');
        subplot(6,2,[7,12]);...
                semilogx(Time_Scale,...
                         2*Interface_movement/l ); ...
                title('Position Evolution of the Interface');...
                xlabel('Time (s)');...
                ylabel('Relative Position');
        % This variable holds all the plotted graphs and
        % could be used to generate a movie
        M(jj/Step_Rec) = getframe;
    end
    % Check to see if core is homogeneous. If it is, raise flag and exit
    % loop at the beginning of next iteration.
    if abs((C(1)-C(r))/(C(1)+C(r))) < Criteria & ~Flag_Is_Homo
        Homo_Marker_Time = jj*Delta_t;
        Flag_Is_Homo = true;
    end
end

% Loop to homogenize single phase at the core without moving interface
% shell is assumed homogeneous
if ~Flag_Is_Homo
    Dissolution_Marker = jj;
    % Mark the time at which the interface has stopped moving
    Time_to_dissolution = jj*Delta_t;
    C(r) = C_beta_alpha;
```

```
while abs((C(1)-C(r))/(C(1)+C(r))) > Criteria
     jj = jj + 1;
     dC_beta_dt_1 = 1/Xi_ov_2*(C(2)-C_0)/2*d_Xi_2_dt + ...
           D(1)*r^2*(C_0-2*C(1)+C(2))/Xi_ov_2^2 + ...
           D(1)*r^2*(C(2)-C_0)/Xi_ov_2^2 + ...
           (r/Xi_ov_2)^2*((D(2) - D_0)/2)*((C(2) - C_0)/2);
     n=2:r-1;
     D(n) = D_alpha*C(n) + D_beta*(1-C(n));
     dC_beta_dt(n) = n/Xi_ov_2.*(C(n+1)-C(n-1))/2*d_Xi_2_dt + ...
                D(n)*r^2.*(C(n-1)-2*C(n)+C(n+1))/Xi_ov_2^2 + ...
                D(n).*r^2.*(C(n+1)-C(n-1))./(n*Xi_ov_2^2) + ...
                (r/Xi_ov_2)^2*((D(n+1) - ...
                                D(n-1))/2).*((C(n+1) - C(n-1))/2);
     C(n) = C(n) + Delta_t*dC_beta_dt(n);
     % Update concentration at C(1)
     C(1) = C(1) + Delta_t*dC_beta_dt_1;
     D(1) = D_alpha*C(1) + D_beta*(1-C(1));
     % Update concentration at center
     d_C_0 = 6*D(1)*r^2*(C(1)-C_0)/Xi_ov_2^2;
     C_0 = Delta_t*d_C_0 + C_0;
     D_0= D_alpha*C_0 + D_beta*(1-C_0);
    if rem(jj,Step_Rec)== 0
        Interface_movement(jj/Step_Rec) = Xi_ov_2;
        Delta_X_alpha = (L/2-Xi_ov_2)/(N-r);
        Delta_X_beta = Xi_ov_2/r;
        X_scale_transformed = [0:Delta_X_beta:Xi_ov_2,...
                               Xi_ov_2:Delta_X_alpha:L/2];
        Time_Scale = 0:Delta_t*Step_Rec:Delta_t*(jj)-...
                                        Delta_t*Step_Rec;
        Profile_Scale = cat(2,C_0, C(1:r-1), ...
                            C_beta_alpha, C_alpha_beta,...
                            C(r+1:N));
        subplot(6,2,[1:6]); ...
                plot(X_scale_transformed, Profile_Scale);...
                title('Au Radial Diffusion Profile');...
                xlabel('Radius (cm)');...
                ylabel('Fraction of Au');
        subplot(6,2,[7,12]);...
                semilogx(Time_Scale,...
                         2*Interface_movement/l ); ...
                title('Position Evolution of the Interface');...
                xlabel('Time (s)');...
                ylabel('Relative Position');
        M(jj/Step_Rec) = getframe;
    end
end
```

```
end

%-----------------------------------------------
% Output final results
% Final interval in the alpha and beta phase
Delta_X_alpha = (L/2-Xi_ov_2)/(N-r); Delta_X_beta = Xi_ov_2/r;

% Reconstruct time scale for future use in plotting.
% Calculation of the total time and the fraction taken for the
% the core to homogenize. At low temperatures, the total time
% is limited by the interface movement.
if Flag_Is_Homo
    Total_time = Homo_Marker_Time;
    t_beta_0 = 1
else
    Total_time = Time_to_dissolution + ....
                 (jj-Dissolution_Marker)*Delta_t;
    t_beta_0 = Time_to_dissolution/Total_time;
end

% Generate axes for plotting
X_scale_transformed = [0:Delta_X_beta:Xi_ov_2,...
                       Xi_ov_2:Delta_X_alpha:L/2];
Profile_Scale = cat(2,C_0, C(1:r-1),...
                    C_beta_alpha, ...
                    C_alpha_beta, C(r+1:N));
Time_Scale = Delta_t*Step_Rec:Delta_t*Step_Rec:Delta_t*(jj);

% Calls the function for final display.
createfigure(X_scale_transformed, Profile_Scale,...
             Time_Scale, 2*Interface_movement/l, ...
             T, D_0_alpha, D_0_beta,...
             Q_alpha, Q_beta,C_alpha_0,  C_beta_0,...
             C_alpha_beta, C_beta_alpha, l, L, Final_int_pos,...
             r, N, Delta_t, Total_time, t_beta_0)
```

The programs calls the function "createfigure" to display the final profile and the interface tracking:

```
% Function to display the final profile and plots the interface
% movement. All the computation parameters are printed at the bottom
% of the graphs.

function createfigure(x1, y1, x2, y2,T, D_0_alpha, D_0_beta,...
                      Q_alpha, Q_beta, C_alpha_0,  C_beta_0,...
                      C_alpha_beta, C_beta_alpha, l, L, Final_int_pos,...
```

```
                    r, N, Delta_t, Total_time, t_beta_0)
%% Create figure
figure1 = figure;

%% Create axes
axes1 = axes('OuterPosition',[0 0.6543 1 0.3457],'Parent',figure1);
    ylim(axes1,[0 1]);
    title(axes1,'Au Radial Diffusion Profile');
    xlabel(axes1,'Radius (cm)');
    ylabel(axes1,'Fraction of Au');
    hold(axes1,'all');

%% Create plot
plot1 = plot(x1,y1,'Parent',axes1);

%% Create axes
axes2 = axes('OuterPosition',[0 0.3693 1 0.285],'Parent',figure1);
    title(axes2,'Interface Relative Movement');
    xlabel(axes2,'Time (s)');
    ylabel(axes2,'Relative Position');
    hold(axes2,'all');

%% Create semilogx
semilogx1 = semilogx(x2,y2,'Parent',axes2);

%% Create textbox
annotation1 = annotation(...
  figure1,'textbox',...
  'Position',[0.0964 0.214 0.2956 0.1169],...
  'EdgeColor','none',...
  'FitHeightToText','on',...
  'FontWeight','bold',...
  'String',{['Diffusion Coefficients (cm^2/s)'],...
            ['   D = D_0 exp(-Q/RT) '],...
            ['   D_0^{\alpha} = ',num2str(D_0_alpha, '%10.2g'),...
             '   Q^{\alpha} (eV) =', num2str(Q_alpha)],...
            ['   D_0^{\beta}  = ', num2str(D_0_beta , '%10.2g'),...
             '   Q^{\beta} (eV) =', num2str(Q_beta) ]});

%% Create textbox
annotation2 = annotation(...
  figure1,'textbox',...
  'Position',[0.5514 0.1554 0.3406 0.1912],...
  'EdgeColor','none',...
  'FitHeightToText','on',...
  'FontWeight','bold',...
```

```
  'String',{['Initial conditions'], ...
            ['   Core (Au fraction) = ', num2str(C_alpha_0)], ...
            ['   Shell (Au fraction) = ', num2str(C_beta_0)], ...
            ['   Interface position (cm) = ', num2str(1/2, '%10.2g')], ...
            [],['Final conditions'],...
            ['   Core (Au fraction) = ', num2str(C_beta_alpha)], ...
            ['   Shell (Au fraction) = ', num2str(C_alpha_beta)], ...
            ['   Interface position = ', num2str(Final_int_pos, ...
                                                 '%10.2g')]});

%% Create textbox
annotation3 = annotation(...
  figure1,'textbox',...
  'Position',[0.09769 0.1212 0.2455 0.0817],...
  'EdgeColor','none',...
  'FitHeightToText','on',...
  'FontWeight','bold',...
  'String',{['Dimension'],...
            ['   Core radius (cm) = ', num2str(1/2, '%10.2g')], ...
            ['   Shell thickness (cm) = ', num2str(L/2, '%10.2g')]});

%% Create textbox
annotation4 = annotation(...
  figure1,'textbox',...
  'Position',[0.5501 0.01513 0.3586 0.1271],...
  'EdgeColor','none',...
  'FitHeightToText','on',...
  'FontWeight','bold',...
  'String',{['Computation Details'],...
            ['   # nodes in core = ', num2str(r)], ...
            ['   # nodes in shell = ', num2str(N-r)], ...
            ['   Time step (s) = ', num2str(Delta_t)]});

%% Create textbox
annotation5 = annotation(...
  figure1,'textbox',...
  'Position',[0.09769 0.011 0.2892 0.1004],...
  'EdgeColor','none',...
  'FitHeightToText','on',...
  'FontWeight','bold',...
  'String',{['Results'],...
            ['   Total time (s)  = ', num2str(Total_time, '%10.2e')], ...
            ['   t_{Int}/t_{Tot}(%) = ', num2str(t_beta_0*100, '%4.2f')]});

%% Create textbox
annotation6 = annotation(...
```

```
figure1,'textbox',...
'Position',[0.09769 0.342 0.2982 0.0431],...
'EdgeColor','none',...
'FontWeight','bold',...
'String',{['Temperature (K) = ', num2str(T)],...
          ['Particle radius (cm) = ', num2str(L/2, '%10.2g')]},...
'FitHeightToText','on');
```

Bibliography

Ah, C. S., Han, H. S., Kim, K., & Jang, D. J. 2000. *Photofragmentation dynamics of n-dodecanethiol-derivatized silver nanoparticles in cyclohexane.* Journal of Physical Chemistry B **104**(34) 8153–8159.

Allen, B. C. 1972. *Liquid Metals: Chemistry and physcis.* New York: Marcel Dekker.

Allen, G. L. & Jesser, W. A. 1984. *The Structure and Melting Character of Sub-Micron In-Sn and Bi-Sn Particles.* Journal of Crystal Growth **70**(1-2) 546–551.

Anikin, K. V., Melnik, N. N., Simakin, A. V., Shafeev, G. A., Voronov, V. V., & Vitukhnovsky, A. G. 2002. *Formation of ZnSe and US quantum dots via laser ablation in liquids.* Chemical Physics Letters **366**(3-4) 357–360.

Ardell, A. J. & Maheshwari, A. 1995. *Coherent Equilibrium in Alloys Containing Spherical Precipitates.* Acta Metallurgica et Materialia **43**(5) 1825–1835.

Arepalli, S. 2004. *Laser ablation process for single-walled carbon nanotube production.* Journal of Nanoscience and Nanotechnology **4**(4) 317–325.

Asta, M. & Hoyt, J. J. 2000. *Thermodynamic properties of coherent interfaces in f.c.c.-based Ag-Al alloys: A first-principles study.* Acta Materialia **48**(5) 1089–1096.

Bae, C. H., Nam, S. H., & Park, S. M. 2002. *Formation of silver nanoparticles by laser ablation of a silver target in NaCl solution.* Applied Surface Science **197** 628–634.

Balluffi, R. W. & Blakely, J. M. 1975. *Special Aspects of Diffusion in Thin Films.* Thin Solid Films **25**(2) 363–392.

Bauerle, D. 2000. *Laser Processing and Chemistry* (3rd ed.). Berlin: Springer.

Becker, M. F., Brock, J. R., & Keto, J. W. 1996. *Process for the Production of Nanoparticles.*

Beniaminy, I. & Deutsch, M. 1980. *A Spline-Based Method for Experimental-Data Deconvolution.* Computer Physics Communications **21**(2) 271–277.

Berman, R. 1975. *An electron microscope study of solid-liquid phase transitions in In-Pb alloys and pure In, Pb, and Sn.* Ph. D. thesis, Simon Fraser University.

Bolk, A. 1961. *Kirkendall Effect and Diffusion in the Gold-Platinum System-II.* Acta Metallurgica **9** 543–652.

Brabási, A.-L. & Stanley, H. E. 1995. *Fractal concepts in surface growth.* Cambridge: Cambridge University Press.

Bracewell, R. N. 1956. *Strip Integration in Radio Astronomy.* Australian Journal of Physics **9**(6) 198–217.

Bracewell, R. N. 1986. *The Fourier Transform and Its Applications* (2nd ed.). New York: McGraw-Hill Book Company.

Braidy, N., Behal, S., Adronov, A., & Botton, G. A. 2007. *Investigation of the Oxide Shell Forming on ϵ-Co Nanocrystals.* Micron In press.

Braidy, N., Jakubek, Z., Simard, B., & Botton, G. A. 2007. *Quantitative Energy Dispersive X-ray Microanalysis on Electron Beam-Sensitive Alloyed Nanoparticles.* Microscopy & Microanalysis In press.

Buffat, P. & Borel, J. P. 1976. *Size Effect on Melting Temperature of Gold Particles.* Physical Review A **13**(6) 2287–2298.

Butler, J. A. V. 1932. *The Thermodynamics of the Surface of Solutions.* Proceedings of the Royal Society of London A **135**(827) 348–375.

Cahn, J. W. 1980. *Surface Stress and the Chemical-Equilibrium of Small Crystals .1. The Case of the Isotropic Surface.* Acta Metallurgica **28**(10) 1333–1338.

Cahn, J. W. & Hilliard, J. E. 1958. *Free Energy of a Nonuniform System. I. Interfacial Free Energy.* The Journal of Chemical Physics **28**(2) 258–167.

Cahn, J. W. & Hoffman, D. W. 1974. *A Vector Thermodynamics for Anisotropic Surfaces II. Curved and Faceted Surfaces.* Acta Metallurgica **22** 315–324.

Cahn, J. W. & Larché, F. 1982. *Surface Stress and the Chemical-Equilibrium of Small Crystals .2. Solid Particles Embedded in a Solid Matrix.* Acta Metallurgica **30**(1) 51–56.

Cahn, J. W. & Larché, F. 1984. *A Simple-Model for Coherent Equilibrium.* Acta Metallurgica **32**(11) 1915–1923.

Cai, H., Chaudhary, N., Lee, J., Becker, M. F., Brock, J. R., & Keto, J. W. 1998. *Generation of metal nanoparticles by laser ablation of microspheres.* Journal of Aerosol Science **29**(5-6) 627–636.

Carpenter, R. W. 1967. *Growth of Modulated Structure in Gold-Platinum Alloys.* Acta Metallurgica **15** 1567–1572.

Chadderton, L. T. 1965. *Radiation Damage in Crystals.* London and New York: Methuen, Wiley, J.

Chatterjee, K., Howe, J. M., Johnson, W. C., & Murayama, M. 2004. *Static and in situ TEM investigation of phase relationships, phase dissolution, and interface motion in Ag-Au-Cu alloy nanoparticles.* Acta Materialia **52**(10) 2923–2935.

Chen, Y. H., Tseng, Y. H., & Yeh, C. C. 2002. *Laser-induced alloying Au-Pd and Ag-Pd colloidal mixtures: the formation of dispersed Au/Pd and Ag/Pd nanoparticles.* Journal of Materials Chemistry **12**(5) 1419–1422.

Chen, Y. H. & Yeh, C. S. 2001. *A new approach for the formation of alloy nanoparticles: laser synthesis of gold-silver alloy from gold-silver colloidal mixtures.* Chemical Communications (4) 371–372.

Cheng, G. J., Romero, D., Fraser, G. T., & Walker, A. R. H. 2005. *Magnetic-field-induced assemblies of cobalt nanoparticles.* Langmuir **21**(26) 12055–12059.

Christensen, A., Ruban, A. V., Stoltze, P., Jacobsen, K. W., Skriver, H. L., Nørskov, J. K., & Besenbacher, F. 1997. *Phase diagrams for surface alloys.* Physical Review B **56**(10) 5822–5834.

Christensen, A., Stoltze, P., & Nørskov, J. K. 1995. *Size Dependence of Phase-Separation in Small Bimetallic Clusters.* Journal of Physics-Condensed Matter **7**(6) 1047–1057.

Cliff, G. & Lorimer, G. W. 1975. *The quantitative analysis of thin specimens.* Journal of Microscopy **103** 203–207.

Coene, W. M. J., Thust, A., Op de Beeck, M., & Van Dyck, D. 1996. *Maximum-likelihood method for focus-variation image reconstruction in high resolution transmission electron microscopy.* Ultramicroscopy **64**(1-4) 109–135.

Compagnini, G., Scalisi, A. A., & Puglisi, O. 2003. *Production of gold nanoparticles by laser ablation in liquid alkanes.* Journal of Applied Physics **94**(12) 7874–7877.

Couchman, P. R. & Jesser, W. A. 1977. *Thermodynamic Theory of Size Dependence of Melting Temperature in Metals.* Nature **269** 481–483.

Craig, I. J. D. 1979. *Inversion of Abel's Integral-Equation in Astrophysical Problems.* Astronomy and Astrophysics **79**(1-2) 121–127.

Darken, L. S. 1948. *Diffusion, Mobility and Their Interraction through Free Energy in Binary Metallic Systems.* Transactions of the American Institute of Minerals and Metallurgical Engineering **175** 184–201.

Darling, A. S., Mintern, R. A., & Chaston, J. C. 1952-1953. *The Gold-Platinum System.* Journal of the Institute of Metals **81** 125–132.

Daw, M. S. & Baskes, M. I. 1984. *Embedded-Atom Method - Derivation and Application to Impurities, Surfaces, and Other Defects in Metals.* Physical Review B **29**(12) 6443–6453.

Deutsch, M. & Beniaminy, I. 1982. *High-Accuracy Deconvolution Method Using Spline Functions.* Review of Scientific Instruments **53**(1) 90–95.

Deutsch, M., Notea, A., & Pal, D. 1989. *Abel Reconstruction of Piecewise Constant Radial Density Profiles from X-Ray Radiographs.* Applied Optics **28**(15) 3183–3186.

Dietz, T. G., Duncan, M. A., Powers, D. E., & Smalley, R. E. 1981. *Laser Production of Supersonic Metal Cluster Beams.* Journal of Chemical Physics **74**(11) 6511–6512.

Dvoryadkina, G. K., Ivanov, A. S., & Borisov, S. A. 1980. *On Redistribution of Impurities in Small Particles by Rising Diffusion.* Fizika Metallov I Metallovedenie **50**(3) 633–634.

Egerton, R. F. 1996. *Electron Energy Loss Spectroscopy in the Electron Microscope, second edition.* New York and London: Plenum Press.

Egerton, R. F. 1999. *Spatial resolution of nanostructural analysis by electron energy-loss spectroscopy and energy-filtered imaging.* Journal of Electron Microscopy **48**(6) 711–716.

Egerton, R. F. & Crozier, P. A. 1997. *The effect of lens aberrations on the spatial resolution of an energy-filtered TEM image.* Micron **28**(2) 117–124.

Egerton, R. F., Li, P., & Malac, M. 2004. *Radiation damage in the TEM and SEM.* Micron **35**(6) 399–409.

Egerton, R. F. & Rauf, I. 1999. *Dose-rate dependence of electron-induced mass loss from organic specimens.* Ultramicroscopy **80**(4) 247–254.

Egerton, R. F. & Rossouw, C. J. 1976. *Direct Measurement of Contamination and Etching Rates in an Electron-Beam.* Journal of Physics D **9**(4) 659–663.

Elghanian, R., Storhoff, J. J., Mucic, R. C., Letsinger, R. L., & Mirkin, C. A. 1997. *Selective Colorimetric Detection of Polynucleotides Based on the Distance-Dependent Optical Properties of Gold Nanoparticles.* Science **277** 1078–1081.

Feldheim, D. L. & Foss, C. A. (Eds.) 2001. *Metal Nanoparticles: Synthesis Characterization & Applications.* New York: Marcel Dekker.

Fiori, C. E., Swyt-Thomas, C., & Myklebust, B. 2003, National Institute of Standards and Technology, USA. www.cstl.nist.gov/div837/Division/outputs/DTSA/DTSA.htm. *Desktop Spectrum Analyzer (DTSA).*

Fjelstad, P. & Ginchev, I. 2003. *Volume, Surface Area, and the Harmonic Mean.* Mathematics Magazine **76**(2) 126–129.

Foiles, S. M. 1985. *Calculation of the Surface Segregation of Ni-Cu Alloys with the Use of the Embedded-Atom Method.* Physical Review B **32**(12) 7685–7693.

Fojtik, A. & Henglein, A. 1993. *Laser Ablation of Films and Suspended Particles in a Solvent - Formation of Cluster and Colloid Solutions.* Berichte Der Bunsen-Gesellschaft-Physical Chemistry Chemical Physics **97**(2) 252–254.

Frank, J. 1992. *Electron Tomography: Three-dimensional Imaging with the Electron Microscope.* New York and London: Plenum Press.

Frens, G. 1973. *Controlled Nucleation for the Regulation of the Particle Size in Monodispersed Gold Suspensions.* Nature Physical Science **241** 20–22.

Friedel, J. 1955. *Deviation from Vegard's Law.* Philosophical Magazine **46** 514–516.

Fullman, R. L. & Fisher, J. C. 1951. *Formation of Annealing Twins During Grain Growth.* Journal of Applied Physics **22**(11) 1350–1355.

García, E. & Puimedín, J. 2004. *Optimal integration window for peak area estimation.* Journal of Analytical Atomic Spectrometry **19**(10) 1391–1393.

Gibbs, J. 1875-1878. *On the Equilibrium of Heterogeneous Substances.* Transactions of the Connecticut Academy **III** 343–524.

Gile, W. W. 1982. *Characterization and melting behavior of co-vapor deposited Pb-Bi microcrystals.* Ph. D. thesis, University of Virginia.

Gjostein, N. A. 1973. *Diffusion.* Metals Park, Ohio: American Society of Metals.

Goldstein, J. I., Costley, J. L., Lorimer, G. W., & Reed, S. J. B. 1977. *Quantitative X-ray Analysis in the Electron Microscope.* Chicago: IITRI.

Goldstein, J. I., Williams, D. B., & Cliff, G. 1986. *Quantitative X-Ray analysis.* In D. C. Joy, A. D. J. Romig, and J. I. Goldstein (Eds.), *Principles of Analytical Electron Microscopy*, pp. 156–217. New York and London: Plenum Press.

Grube, G., Schneider, A., & Esch, U. 1951. *Gold-Platinum System.* Festschrift aus Anlass des 100-jahrigen Jubilaums, Heraus, W. C. G.m.b.H. 20–42.

Guiton, B. S. & Davies, P. K. 2007. *Nano-Chessboard Superlattices Formed by Spontaneous Phase Separation in Oxides.* Nature Materials **6** 586–591.

Guo, T., Nikolaev, P., Thess, A., Colbert, D. T., & Smalley, R. E. 1995. *Catalytic Growth of Single-Walled Nanotubes by Laser Vaporization.* Chemical Physics Letters **243**(1-2) 49–54.

Gupta, D. 1988. *Diffusion Phenomena in Thin Films and Microelectronic Materials.* Park Ridge, New Jersey.

Ha, J. H., Nam, Y. U., Cheon, M. S., & Hwang, Y. S. 2004. *An improved Abel inversion method modified for tangential interferometry in tokamak.* Review of Scientific Instruments **75**(10) 3408–3410.

Habas, S. E., Lee, H., Radmilovic, V., Somorjai, G. A., & Yang, P. 2007. *Shaping binary metal nanocrystals through epitaxial seeded growth.* Nature Materials **6** 692–697.

Hajcsar, E. E., Underhill, P. R., Smeltzer, W. W., & Dawson, P. T. 1987. *A Determination of the Temperature-Dependence of Segregation for a 56 a/o Ni-Co Alloy on (111) and (210) Faces Using AES.* Surface Science **191**(1-2) 249–258.

Hajj, G. A. & Romans, L. J. 1998. *Ionospheric electron density profiles obtained with the global positioning system: Results from the GPS/MET experiment.* Radio Science **33**(1) 175–190.

Hanzen, K. J. 1960. *Theoretische Untersuchungen über den Schmelzpunkt kleiner Kügelchen.* Zeitschrift für Physik A **157**(5) 523–553.

Heddersen, J., Chumanov, G., & Cotton, T. M. 1993. *Laser-Ablation of Metals - a New Method for Preparing SERS Active Colloids.* Applied Spectroscopy **47**(12) 1959–1964.

Henglein, A. 1993. *Physicochemical Properties of Small Metal Particles in Solution - Microelectrode Reactions, Chemisorption, Composite Metal Particles, and the Atom-to-Metal Transition.* Journal of Physical Chemistry **97**(21) 5457–5471.

Herring, C. 1950. *Effect of Change of Scale on Sintering Phenomena.* Journal of Applied Physics **21** 301–303.

Herring, C. 1951. *Some Theorems on the Free Energies of Crystal Surfaces.* Physical Review **82**(1) 87–93.

Hillert, M. 1998. *Phase Equilibria, Phase Diagrams and Phase Transformations: Their Thermodynamic Basis.* Cambridge: Cambridge University Press.

Hirotsu, Y. & Sato, K. 2005. *Growth and atomic ordering of hard magnetic L1(0)-FePt, FePd and CoPt alloy nanoparticles studied by transmission electron microscopy: alloy system and particle size dependence.* Journal of Ceramic Processing Research **6**(3) 236–244.

Hodak, J. H., Henglein, A., Giersig, M., & Hartland, G. V. 2000. *Laser-induced inter-diffusion in AuAg core-shell nanoparticles.* Journal of Physical Chemistry B **104**(49) 11708–11718.

Hoffman, D. W. & Cahn, J. W. 1972. *A Vector Thermodynamics for Anisotropic Surfaces I. Fundamentals and Application to Plane Surface Junctions.* Surface Science **31** 368–388.

Horita, Z., Sano, T., & Nemoto, M. 1987. *Simplification of X-Ray Absorption Correction in Thin-Sample Quantitative Microanalysis.* Ultramicroscopy **21**(3) 271–276.

Howe, J. M., Mebed, A. M., Chatterjee, K., Li, P., Murayama, M., & Johnson, W. C. 2003. *Effect of phase fraction on the tri-junction in two-phase nanoparticle systems.* Acta Materialia **51**(5) 1359–1372.

Howe, J. M. & Saka, H. 2004. *In situ transmission electron microscopy studies of the solid-liquid interface.* MRS Bulletin **29**(12) 951–957.

Howitt, D. G. 1986. *Radiation effects encountered by inorganic materials in analytical electron microscopy.* In D. C. Joy, A. D. J. Romig, and J. I. Goldstein (Eds.), *Principles of Analytical Electron Microscopy*, pp. 375–392. New York and London: Plenum Press.

Hren, J. J. 1986. *Barriers to AEM: Contamination and Etching.* In D. C. Joy, A. D. J. Romig, and J. I. Goldstein (Eds.), *Principles of Analytical Electron Microscopy*, pp. 353–376. New York and London: Plenum Press.

Huh, J. Y., Lee, H., & Johnson, W. C. 2005. *Particle size effects on the coherent phase equilibria of binary nanoparticles.* Metals and Materials International **11**(5) 357–363.

Hÿtch, M. J. 1997. *Analysis of variations in structure from high resolution electron microscope images by combining real space and Fourier space information.* Microscopy Microanalysis Microstructures **8**(1) 41–57.

Hÿtch, M. J., Snoeck, E., & Kilaas, R. 1998. *Quantitative measurement of displacement and strain fields from HREM micrographs.* Ultramicroscopy **74**(3) 131–146.

Iida, T. & Guthrie, R. I. L. 1988. *The Physical Properties of Liquid Metals.* Oxford: Oxford Science Publications Clarendon Press.

Illy, S., Tillement, O., Machiz, F., Dubois, J. M., Massicot, F., Fort, Y., & Ghanbaja, J. 1999. *First direct evidence of size-dependent structural transition in nanosized nickel particles.* Philosphical Magazine A **79**(5) 1021–1031.

Inasawa, S., Sugiyama, M., & Koda, S. 2003. *Size controlled formation of gold nanoparticles using photochemical growth and photothermal size reduction by 308 nm laser pulses.* Japanese Journal of Applied Physics Part 1 **42**(10) 6705–6712.

Irissou, E. 2005. *Nouveaux alliages métastables nanostructurés par déposition par ablation laser à flux croisés (Cross-beam laser ablation deposition of novel nanostructured metastable alloys).* Ph. D. thesis, Institut National de la Recherche Scientifique.

Ivanov, A. S. & Borisov, S. A. 1988. *Effect of Particle-Size on Surface Segregation.* Soviet Powder Metallurgy and Metal Ceramics **27**(10) 770–772.

Ivanov, A. S., Dvoryadkina, G. K., & Borisov, S. A. 1983. *Surface Segregation of Atoms in Solid-Solution Small Particles.* Zhurnal Fizicheskoi Khimii **57**(2) 444–447.

Jacobsen, K. W., Nørskov, J. K., & Puska, M. J. 1987. *Interatomic Interactions in the Effective-Medium Theory.* Physical Review B **35**(14) 7423–7442.

Jesser, W. A., Shiflet, G. J., Allen, G. L., & Crawford, J. L. 1999. *Equilibrium phase diagrams of isolated nano-phases.* Materials Research Innovations **2**(4) 211–216.

Jesser, W. A., Shneck, R. Z., & Gile, W. W. 2004. *Solid-liquid equilibria in nanoparticles of Pb-Bi alloys.* Physical Review B **69**(14) 144121.

Jiang, Z. Y., Huang, R. B., Xie, S. Y., Xie, Z. X., & Zheng, L. S. 2001. *Synthesis of silver selenide bicomponent nanoparticles by a novel technique: Laser-solid-liquid ablation.* Journal of Solid State Chemistry **160**(2) 430–434.

Jin, R., Cao, Y., Mirkin, C. A., Kelly, K. L., Schatz, G. C., & Zheng, J. G. 2001. *Photoinduced Conversion of Silver Nanospheres to Nanoprisms.* Science **294** 1901–1903.

Johansson, C. H. & Linde, J. O. 1930. *Crystal Structures, Electrical Resistance, Thermal Forces, Heat Conductivity, Magnetic Susceptibility, Hardness, and Tempering Phenomena in the System Gold-Platinum in Relation to the Phase Diagram.* Annals of Physics **5**(6) 762–792.

Johnson, W. C. 2001. *Spinodal decomposition in a small radially stressed sphere.* Acta Materialia **49**(17) 3463–3474.

Jones, H. 1971. *Surface Energy of Solid Metals.* Metal Science Journal **5** 15–18.

Kabashin, A. V., Meunier, M., Kingston, C., & Luong, J. H. T. 2003. *Fabrication and characterization of gold nanoparticles by femtosecond laser ablation in an aqueous solution of cyclodextrins.* Journal of Physical Chemistry B **107**(19) 4527–4531.

Kalal, M. & Nugent, K. A. 1988. *Abel Inversion Using Fast Fourier-Transforms.* Applied Optics **27**(10) 1956–1959.

Kaptay, G. 2005. *A method to calculate equilibrium surface phase transition lines in monotectic systems.* Calphad-Computer Coupling of Phase Diagrams and Thermochemistry **29**(1) 56–67.

Kaptay, G., Báder, E., & Bolyán, L. 2000. *Interfacial forces and energies relevant to production of metal matrix composites.* In *Solidification and Gravity 2000*, Volume 329-3 of *Materials Science Forum*, pp. 151–156.

Kasama, A., Iida, T., & Morita, Z.-i. 1976. *Temperature Dependence of Surface Tension of Liquid Pure Metals.* Journal of the Japan Institute of Metals **40**(10) 1030–1038.

Kaufman, L. & Bernstein, H. 1970. *Computer Calculation of Phase Diagrams with Special Reference to Reractory Metals.* New York: Academic Press.

Kelly, T. F. 1987. *An Experimental X-Ray-Detector Efficiency Function Determined Using Pure Submicron Spheres - an Approach to Quantification.* Ultramicroscopy **22**(1-4) 175–189.

Kim, Y., Johnson, R. C., & Hupp, J. T. 2001. *Gold Nanoparticle-Based Sensing of Spectroscopically Silent Heavy Metal Ions.* Nano Letters **1**(4) 165–167.

Kingston, C. T. & Simard, B. 2003. *Fabrication of carbon nanotubes.* Analytical Letters **36**(15) 3119–3145.

Knotek, M. L. & Feibelman, P. J. 1978. *Ion Desorption by Core-Hole Auger Decay.* Physical Review Letters **40**(14) 964–967.

Kobayashi, T. R., Ikeda, K. S., Shimizu, Y., & Sawada, S. 2002. *Isothermal dynamics simulations of spontaneous alloying in a microcluster.* Physical Review B **66**(24) 245412.

Koenig, F. 1950. *On the Thermodynamic Relation Between Surface Tension and Curvature.* Journal of Chemical Physics **18**(4) 449–459.

Kubel, C., Voigt, A., Schoenmakers, R., Otten, M., Su, D., Lee, T. C., Carlsson, A., & Bradley, J. 2005. *Recent advances in electron tomography: TEM and HAADF-STEM tomography for materials science and semiconductor applications.* Microscopy and Microanalysis **11**(5) 378–400.

Kumikov, V. K. & Khokonov, K. B. 1983. *On the Measurement of Surface Free-Energy and Surface-Tension of Solid Metals.* Journal of Applied Physics **54**(3) 1346–1350.

Kurumada, M., Kimura, Y., Suzuki, H., Kido, O., Saito, Y., & Kaito, C. 2004. *TEM study of early Ni_4Ti_3 precipitation and R-phase in Ni-rich NiTi nanoparticles.* Scripta Materialia **50**(11) 1413–1416.

Lakis, R. E., Lyman, C. E., & Stenger, H. G. 1995. *Alumina-Supported Pt-Rh Catalysts .1. Microstructural Characterization.* Journal of Catalysis **154**(2) 261–275.

Laplace, P. S. 1829. *Traité de Mécanique Céleste*, Volume Supplement to the tenth book. Paris: L'Imprimerie de Crapelet.

Larché, F. C. 1990. *Coherent Phase-Transformations.* Annual Review of Materials Science **20** 83–99.

Lass, E. A., Johnson, W. C., & Shiflet, G. J. 2006. *Correlation between CALPHAD data and the Cahn-Hilliard gradient energy coefficient kappa and exploration into its composition dependence.* Calphad-Computer Coupling of Phase Diagrams and Thermochemistry **30**(1) 42–52.

Le Bouar, Y., Loiseau, A., & Khachaturyan, A. G. 1998. *Origin of chessboard-like structures in decomposing alloys. Theoretical model and computer simulation.* Acta Materialia **46**(8) 2777–2788.

Leapman, R. D. & Hunt, J. A. 1991. *Comparison of Detection Limits for EELS and EDXS.* Microscopy, Microanalysis, Microstructures **2**(2-3) 231–244.

Lee, I., Han, S. W., & Kim, K. 2001. *Production of Au-Ag alloy nanoparticles by laser ablation of bulk alloys.* Chemical Communications (18) 1782–1783.

Lide, D. R. (Ed.) 2004-2005. *CRC Handbook of Chemistry and Physics 85th edition.* CRC Press.

Liebhafsky, A. H., Pfeiffer, G. H., & Zemany, D. P. 1960, In A. Engstrm, V. Cosslett, and H. Pattee (Eds.), *X-Ray Microscopy and X-Ray Microanalysis*, Stockholm, pp. 321–330. Elsevier Publishing Company.

Liu, H. B., Pal, U., Perez, R., & Ascencio, J. A. 2006. *Structural transformation of Au-Pd bimetallic nanoclusters on thermal heating and cooling: A dynamic analysis.* Journal of Physical Chemistry B **110**(11) 5191–5195.

Lozano-Perez, S. & Titchmarsh, J. M. 2007. *EFTEM assistant: A tool to understand the limitations of EFTEM.* Ultramicroscopy **107**(4-5) 313–321.

Lu, H. M. & Jiang, Q. 2004. *Size-dependent surface energies of nanocrystals.* Journal of Physical Chemistry B **108**(18) 5617–5619.

Lu, L. H., Sun, G. Y., Zhang, H. J., Wang, H. S., Xi, S. Q., Hu, J. Q., Tian, Z. Q., & Chen, R. 2004. *Fabrication of core-shell Au-Pt nanoparticle film and*

its potential application as catalysis and SERS substrate. Journal of Materials Chemistry **14**(6) 1005–1009.

Luo, J., Maye, M. M., Petkov, V., Kariuki, N. N., Wang, L. Y., Njoki, P., Mott, D., Lln, Y., & Zhong, C. J. 2005. *Phase properties of carbon-supported gold-platinum nanoparticles with different bimetallic compositions.* Chemistry of Materials **17**(12) 3086–3091.

Lyman, C. E., Hepburn, J. S., & Stenger, H. G. 1990. *Quantitative Pt and Rh Distributions in Pollution-Control Catalysts.* Ultramicroscopy **34**(1-2) 73–80.

Lyman, C. E., Lakis, R. E., & Stenger, H. G. 1995. *X-Ray-Emission Spectrometry of Phase-Separation in Pt-Rh Nanoparticles for Nitric-Oxide Reduction.* Ultramicroscopy **58**(1) 25–34.

Mafune, F., Kohno, J., Takeda, Y., & Kondow, T. 2001. *Dissociation and aggregation of gold nanoparticles under laser irradiation.* Journal of Physical Chemistry B **105**(38) 9050–9056.

Mafune, F., Kohno, J., Takeda, Y., & Kondow, T. 2003a. *Formation of gold nanonetworks and small gold nanoparticles by irradiation of intense pulsed laser onto gold nanoparticles.* Journal of Physical Chemistry B **107**(46) 12589–12596.

Mafune, F., Kohno, J., Takeda, Y., Kondow, T., & Sawabe, H. 2000a. *Formation and size control of sliver nanoparticles by laser ablation in aqueous solution.* Journal of Physical Chemistry B **104**(39) 9111–9117.

Mafune, F., Kohno, J., Takeda, Y., Kondow, T., & Sawabe, H. 2000b. *Structure and stability of silver nanoparticles in aqueous solution produced by laser ablation.* Journal of Physical Chemistry B **104**(35) 8333–8337.

Mafune, F., Kohno, J. Y., Takeda, Y., & Kondow, T. 2002a. *Growth of gold clusters into nanoparticles in a solution following laser-induced fragmentation.* Journal of Physical Chemistry B **106**(34) 8555–8561.

Mafune, F., Kohno, J. Y., Takeda, Y., & Kondow, T. 2002b. *Full physical preparation of size-selected gold nanoparticles in solution: Laser ablation and laser-induced size control.* Journal of Physical Chemistry B **106**(31) 7575–7577.

Mafune, F., Kohno, J. Y., Takeda, Y., & Kondow, T. 2003b. *Formation of stable platinum nanoparticles by laser ablation in water.* Journal of Physical Chemistry B **107**(18) 4218–4223.

Mafune, F. & Kondow, T. 2003c. *Formation of small gold clusters in solution by laser excitation of interband transition.* Chemical Physics Letters **372**(1-2) 199–204.

Mafune, F. & Kondow, T. 2004. *Selective laser fabrication of small nanoparticles and nano-networks in solution by irradiation of UV pulsed laser onto platinum nanoparticles.* Chemical Physics Letters **383**(3-4) 343–347.

Malakhov, D. V. 1997. *Confidence intervals of calculated phase boundaries.* Calphad-Computer Coupling of Phase Diagrams and Thermochemistry **21**(3) 391–400.

Marks, L. D. 1984. *Surface-Structure and Energetics of Multiply Twinned Particles.* Philosophical Magazine A **49**(1) 81–93.

Massalski, T. B. 1990. *Binary alloy phase diagrams* (2 ed.), Volume 3. Materials Park, Ohio.

McCartney, M. R., Crozier, P. A., Weiss, J. K., & Smith, D. J. 1991. *Electron-Beam-Induced Reactions at Transition-Metal Oxide Surfaces.* Vacuum **42**(4) 301–308.

McGuire, G. E., Wisseman, W. R., & Holloway, P. H. 1978. *Diffusion Studies of Au through Electroplated Pt Films by Auger-Electron Spectroscopy.* Journal of Vacuum Science & Technology **15**(5) 1701–1705.

Mejía-Rosales, S. J., Fernández-Navarro, C., Pérez-Tijerina, E., Montejano-Carrizales, J. M., & José-Yacáman, M. 2006. *Two-stage melting of Au-Pd nanoparticles.* Journal of Physical Chemistry B **110**(26) 12884–12889.

Michael, J. R. & Williams, D. B. 1987. *A Consistent Definition of Probe Size and Spatial-Resolution in the Analytical Electron-Microscope.* Journal of Microscopy-Oxford **147** 289–303.

Mitchell, D. R. G. & Schaffer, B. 2005. *Scripting-customised microscopy tools for Digital Micrograph(TM).* Ultramicroscopy **103**(4) 319–332.

Miyazaki, S. & Ishida, A. 1999. *Martensitic transformation and shape memory behavior in sputter-deposited TiNi-base thin films.* Materials Science and Engineering A **275** 106–133.

Molenbroek, A. M., Haukka, S., & Clausen, B. S. 1998. *Alloying in Cu/Pd nanoparticle catalysts.* Journal of Physical Chemistry B **102**(52) 10680–10689.

Montarou, C. C., Gaylord, T. K., & Dachevski, A. I. 2006. *Residual stress profiles in optical fibers determined by the two-waveplate-compensator method.* Optics Communications **265**(1) 29–32.

Morgan, N. M., Wells, C. G., Goodson, M. J., Kraft, M., & Wagner, W. 2006. *A new numerical approach for the simulation of the growth of inorganic nanoparticles.* Journal of Computational Physics **211**(2) 638–658.

Mori, H., Komatsu, M., Takeda, K., & Fujita, H. 1991. *Spontaneous Alloying of Copper into Gold Atom Clusters.* Philosophical Magazine Letters **63**(3) 173–178.

Mori, H. & Yasuda, H. 1996. *Effect of cluster size on phase stability in nm-sized Au-Sb alloy clusters.* Materials Science and Engineering A **217** 244–248.

Morita, Z.-i. 1976. *No Title.* Bulletin of Japan Institute of Metals **125** 743–.

Murr, L. E. 1975. *Interfacial Phenomena in Metals and Alloys.* Reading, Mass. : Addison-Wesley Pub. Co., Advanced Book Program.

Oen, O. S. 1973. *Cross-Section for Atomic Displacements in Solids by Fast Electrons.* Technical report, Oak Ridge National Lab.

Ohring, M. 2002. *Materials Science of Thin Films Deposition and Structure* (2nd ed.). San Diego San Francisco New York Boston London Syndey Tokyo: Acedemic Press.

Okamoto, H. & Massalski, T. B. 1985. *The Au-Pt (Gold-Platinum) System.* Bulletin of Alloy Phase Diagrams **6**(1) 46–56.

Palatnik, L. S. & Boiko, B. T. 1961. *Equilibrium Diagram of Al-Cu Alloys in Thin Films.* The Physics of metals and metallography. **11**(1) 119–123.

Park, H. K. 1989. *A New Asymmetric Abel-Inversion Method for Plasma Interferometry in Tokamaks.* Plasma Physics and Controlled Fusion **31**(13) 2035–2046.

Park, S.-J., Taton, T. A., & Mirkin, C. A. 2002. *Array-Based Electrical Detection of DNA with Nanoparticle Probes.* Science **2002** 1503–1506.

Pawlow, P. 1909. *ber die Abhngigkeit des Schmelzpunktes von der Oberflchenenergie eines Festen Krpers.* Zeitschrift für Physikalische Chemie **65** 1–35.

Pellicer, J., Manzanares, J. A., & Mafe, S. 1995. *The Physical Description of Elementary Surface Phenomena - Thermodynamics Versus Mechanics.* American Journal of Physics **63**(6) 542–547.

Pithawalla, Y. B., Deevi, S. C., & El-Shall, M. S. 2002. *Preparation of ultrafine and nanocrystalline FeAl powders.* Materials Science and Engineering A **329** 92–98.

Poirier, D. R. & Geiger, G. H. 1994. *Transport Phenomena in Materials Processing.* Warrendale: TMS.

Porter, D. A. & Easterling, K. E. 1992. *Phase Transformations in Metals and Alloys.* London: Chapman & Hall.

Powell, M. 1967, Harwell Subroutine Library - Science and Technology Facilities Council UK- Computational Science and Engineering Department. *VC03-Smooth weighted least squares fit to given data by cubic spline.*

Puntes, V. F., Krishnan, K. M., & Alivisatos, A. P. 2001. *Colloidal nanocrystal shape and size control: The case of cobalt.* Science **291** 2115–2117.

Purdy, G. R. 1971. *Widmanstätten Precipitation from Non-Ideal Solid Solution: α in β-CuZn.* Metal Science Journal **5** 81–85.

Qi, W. H. & Wang, M. P. 2002. *Size effect on the cohesive energy of nanoparticle.* Journal of Materials Science Letters **21**(22) 1743–1745.

Ram, S. 2001. *Allotropic phase transformations in HCP, FCC, and BCC metastable structures in Co-nanoparticles.* Materials Science and Engineering A **304-306** 923–927.

Ramos de Debiaggi, S. 1999. *Phase stability of Ni-Al nanoparticles.* Journal of Materials Research **14**(7) 2849–1999.

Raub, E. & Falkenburg, G. 1964. *The System Gold-Platinum-Rhodium and the Binary System of Its Components.* Zeitschrift für Metallkunde **55** 392–397.

Raub, E. & Worwag, G. 1955. *The Gold-Platinum-Palladium Alloys.* Zeitschrift für Metallkunde **46**(7) 513–515.

Rodríguez-López, J. L., Montejano-Carrizales, J. M., Pal, U., Sánchez-Ramirez, J. F., Troiani, H. E., García, D., Miki-Yoshida, M., & José-Yacamàn, M. 2004. *Surface reconstruction and decahedral structure of bimetallic nanoparticles.* Physical Review Letters **92**(19).

Romig, A. D. J. & Goldstein, J. I. 1979, In D. E. Newbury (Ed.), *Microbeam analysis 1979*, San Francisco, pp. 124–128. San Francisco Press.

Schamp, C. T. & Jesser, W. A. 2006. *Two-phase equilibrium in individual nanoparticles of Bi-Sn.* Metallurgical and Materials Transactions A **37A**(6) 1825–1829.

Schmid, G. 2004. *Nanoparticles: From Theory to Application.* Weinheim: Wiley-VCH Verlag GmbH & Co. KGaA.

Schmid, G., Lehnert, A., Malm, J. O., & Bovin, J. O. 1991. *Ligand-Stabilized Bimetallic Colloids Identified by HRTEM and EDX.* Angewandte Chemie-International Edition in English **30**(7) 874–876.

Sekerka, R. F. & Wang, S. L. 1999. *Moving Phase Boundary Problems.* In I. H. Aaronson (Ed.), *Lectures on the Theory of Phase Transformations* (2nd ed.). Warrendale: TMS.

Sharma, A. K. & Gupta, B. D. 2006. *Fibre-optic sensor based on surface plasmon resonance with Ag-Au alloy nanoparticle films.* Nanotechnology **17**(1) 124–131.

Shibata, T., Bunker, B. A., Zhang, Z., Meisel, D., Vardeman, C. F., & Gezelter, J. D. 2002. *Size-Dependent Spontaneous Alloying of Au-Ag Nanoparticles.* Journal of American Chemical Society **124** 11989–11996.

Shimizu, Y., Ikeda, K. S., & Sawada, S. 2001. *Spontaneous alloying in binary metal microclusters: A molecular dynamics study.* Physical Review B **64**(7).

Shirinyan, A., Wautelet, M., & Belogorodsky, Y. 2006b. *Solubility diagram of the Cu-Ni nanosystem.* Journal of Physics-Condensed Matter **18**(8) 2537–2551.

Shirinyan, A. S. & Gusak, A. M. 2004a. *Phase diagrams of decomposing nanoalloys.* Philosophical Magazine **84**(6) 579–593.

Shirinyan, A. S., Gusak, A. M., & Wautelet, M. 2005. *Phase diagram versus diagram of solubility: What is the difference for nanosystems?* Acta Materialia **53**(19) 5025–5032.

Shirinyan, A. S. & Wautelet, M. 2004b. *Phase separation in nanoparticles.* Nanotechnology **15**(12) 1720–1731.

Shuman, H., Somlyo, A. V., & Somlyo, A. P. 1976. *Quantitative Electron-Probe Microanalysis of Biological Thin-Sections - Methods and Validity.* Ultramicroscopy **1**(4) 317–339.

Sibbald, M. S., Chumanov, G., & Cotton, T. M. 1996. *Reduction of cytochrome c by halide-modified, laser-ablated silver colloids.* Journal of Physical Chemistry **100**(11) 4672–4678.

Sinha, A. K., Smith, T. E., & Sheng, T. T. 1974. *Thin Film Diffusion of Platinum in Gold.* Thin Solid Films **22** 1–10.

Snoeck, E., Warot, B., Ardhuin, H., Rocher, A., Casanove, M. J., Kilaas, R., & Hÿtch, M. J. 1998. *Quantitative analysis of strain field in thin films from HRTEM micrographs.* Thin Solid Films **319**(1-2) 157–162.

Statham, P. J. 1977. *Deconvolution and Background Subtraction by Least-Squares Fitting with Pre-Filtering of Spectra.* Analytical Chemistry **49**(14) 2149–2154.

Storhoff, J. J., Elghanian, R., Mucic, R. C., Mirkin, C. A., & Letsinger, R. L. 1998. *One-Pot Colorimetric Differentiation of Polynucleotides with Single Base Imperfections Using Gold Nanoparticle Probes.* Journal of the American Chemical Society **120**(9) 1959–1964.

Storhoff, J. J., Lazarides, A. A., Mirkin, C. A., Letsinger, R. L., Mucic, R. C., & Schatz, G. C. 2000. *What Controls the Optical Properties of DNA-Linked Gold Nanoparticle Assemblies?* Journal of the American Chemical Society **122**(19) 4640–4650.

Sugimoto, T. 2001. *Monodispersed Particles.* Amsterdam: Elsevier.

Sun, Y. & Purdy, G. R. 2006. *Unstable solid solution formation by repeated cold rolling of Au-Pt multilayers.* Canadian Metallurgical Quarterly **45**(1) 131–134.

Sundman, B., Jansson, B., & Andersson, J. O. 1985. *The Thermo-Calc Databank System.* CALPHAD-Computer Coupling of Phase Diagrams and Thermochemistry **9**(2) 153–190.

Suresh, A., Mayo, M. J., & Porter, W. D. 2003. *Thermodynamics of the tetragonal-to-monoclinic phase transformation in fine and nanocrystalline yttria-stabilized zirconia powders.* Journal of Materials Research **18**(12) 2912–2921.

Sutton, A. P. & Chen, J. 1990. *Long-Range Finnis Sinclair Potentials.* Philosophical Magazine Letters **61**(3) 139–146.

Tanaka, T., Hack, K., & Hara, S. 2000. *Calculation of surface tension of liquid Bi-Sn alloy using thermochemical application library ChemApp.* Calphad-Computer Coupling of Phase Diagrams and Thermochemistry **24**(4) 465–474.

Tanaka, T. & Hara, S. 2001a. *Thermodynamic evaluation of nano-particle binary alloy phase diagrams.* Zeitschrift für Metallkunde **92**(11) 1236–1241.

Tanaka, T. & Hara, S. 2001b. *Thermodynamic evaluation of binary phase diagrams of small particle systems.* Zeitschrift für Metallkunde **92**(5) 467–472.

Tanzilli, R. A. & Heckel, R. W. 1968. *Numerical Solutions to the Finite, Diffusion-Controlled Two-Phase, Moving-Interface Problem (with Planar, Cylindrical, and Spherical Interfaces).* Transactions of the Metallurgical Society of AIME **242** 2313–2321.

Taton, T. A., Mirkin, C. A., & Letsinger, R. L. 2000. *Scanometric DNA Array Detection with Nanoparticle Probes.* Science **289** 1757–1760.

Thomson, J. 1849. *Theoretical Considerations on the Effect of Pressure in Lowering the Freezing Point of Water.* Transactions of the Royal Society of Edinburgh **16** 575–580.

Thomson, J. 1862. *On the Crystallization and Liquefaction, as Influenced by Stresses Tending to Change Form in the Crystals.* Proceedings of the Royal Society of London **11** 473–481.

Thomson, J. J. 1888. *Application of Dynamics to Physics and Chemistry.* London: MacMillan & Co.

Thomson, W. 1871. *On the Equilibrium of Vapour at a Curved Surface of Liquid.* The Philosphy Magazine **42**(282) 452–488.

Tiedema, T. J., Bouman, J., & Burgers, W. G. 1957. *Precipitation in Gold-Platinum Alloys.* Acta Metallurgica **5** 310–321.

Tolman, R. C. 1949. *The Effect of Droplet Size on Surface Tension.* Journal of Chemical Physics **17**(3) 333–337.

Trivedi, R. K. 1975. *Theory of capillarity.* In H. I. Aaronson (Ed.), *Lectures on the Theory of Phase Transformations* (2 ed.)., pp. 135–164. Warrendale, Pennsylvania: The minerals, Metals & Materials Society.

Tsuji, T., Iryo, K., Nishimura, Y., & Tsuji, M. 2001. *Preparation of metal colloids by a laser ablation technique in solution: influence of laser wavelength on the ablation efficiency (II).* Journal of Photochemistry and Photobiology A **145**(3) 201–207.

Tsuji, T., Iryo, K., Ohta, H., & Nishimura, Y. 2000. *Preparation of metal colloids by a laser ablation technique in solution: Influence of laser wavelength on the efficiencies of colloid formation.* Japanese Journal of Applied Physics Part 2 **39**(10A) L981–L983.

Tsunekawa, S., Ito, S., Kawazoe, Y., & Wang, J. T. 2003. *Critical size of the phase transition from cubic to tetragonal in pure zirconia nanoparticles.* Nano Letters **3**(7) 871–875.

Vallée, R., Wautelet, M., Dauchot, J. P., & Hecq, M. 2001. *Size and segregation effects on the phase diagrams of nanoparticles of binary systems.* Nanotechnology **12**(1) 68–74.

van der Merwe, J. H. 1963a. *Crystal Interfaces. Part I. Semi-Infinite Crystals.* Journal of Applied Physics **34**(1) 117–122.

van der Merwe, J. H. 1963b. *Crystal Interfaces. Part II. Finite Overgrowth.* Journal of Applied Physics **34**(1) 123–127.

van der Merwe, J. H. & Jesser, W. A. 1988. *An Exactly Solvable Model for Calculating Critical Misfit and Thickness in Epitaxial Superlattices - Layers of Equal Elastic-Constants and Thicknesses.* Journal of Applied Physics **63**(5) 1509–1517.

Wautelet, M. 1990. *Size Effect on the Melting (or Disordering) Temperature of Small Particles.* Solid State Communications **74**(11) 1237–1239.

Wautelet, M. 1991. *Estimation of the Variation of the Melting Temperature with the Size of Small Particles, on the Basis of a Surface-Phonon Instability Model.* Journal of Physics D **24**(3) 343–346.

Wautelet, M., Dauchot, J. P., & Hecq, A. 2003a. *Size effects on the phase diagrams of nanoparticles of various shapes.* Materials Science & Engineering C **23**(1-2) 187–190.

Wautelet, M., Dauchot, J. P., & Hecq, M. 2000. *Phase diagrams of small particles of binary systems: a theoretical approach.* Nanotechnology **11**(1) 6–9.

Wautelet, M., Dauchot, J. P., & Hecq, M. 2003b. *On the phase diagram of non-spherical nanoparticles.* Journal of Physics-Condensed Matter **15**(21) 3651–3655.

Weissmüller, J., Bunzel, P., & Wilde, G. 2004. *Two-phase equilibrium in small alloy particles.* Scripta Materialia **51**(8) 813–818.

Weisstein, E. W. Last modified: 2003. *Harmonic Parameter.* MathWorld - A Wolfram Web Resource **http://mathworld.wolfram.com /HarmonicParameter.html**.

Wictorin, C. G. 1938. *The Separation of Gold-Platinum Alloys.* Annals of Physics **33** 509–516.

Wictorin, C. G. 1947. *Studies in Gold Platinum Alloys.* Stockholm.

Wilbraham, H. 1848. *On a Certain Periodic Function.* Cambridge and Dublin Mathematical Journal **3** 198–201.

Wilde, G., Bunzel, P., Rosner, H., & Weissmüller, J. 2007. *Phase equilibria and phase diagrams of nanosealed systems.* Journal of Alloys and Compounds **434** 286–289.

Williams, D. B. & Carter, C. C. 1996. *Spectrometry IV.* In *Transmission Electron Microscopy*, pp. 632–633. New York: Plenum Press.

Williams, D. B., Papworth, A. J., & Watanabe, M. 2002. *High resolution X-ray mapping in the STEM.* Journal of Electron Microscopy **51** S113–S126.

Williams, F. L. & Nason, D. 1974. *Binary alloy surface compositions from bulk alloy thermodynamic data.* Surface Science **45** 377–408.

Wittenberg, L. 1972. *Volume contraction during melting: emphasis on lanthanide and actinide metals.* Journal of Chemical Physics **56**(9) 4526–4533.

Wonnacott, H. T. & Wonnacott, J. R. 1981. *Time Series.* In *Regression: A Second Course in Statistics*, pp. 208–277. New York, Chichester, Brisbane, Toronto: John Wiley & Sons.

Wood, R. F., Leboeuf, J. N., Chen, K. R., Geohegan, D. B., & Puretzky, A. A. 1998. *Dynamics of plume propagation, splitting, and nanoparticle formation during pulsed-laser ablation.* Applied Surface Science **129** 151–158.

Wulff, G. 1901. *Zur Frage der Geschwindigkeit des Wachsthums und der Auflosung der Krystallflachen.* Zeitschrift für Kristallographie, Mineralogie und Petrographie, Leipzig **34** 449–531.

Xiao, S., Hu, W., Luo, W., Wu, Y., Li, X., & Deng, H. 2006. *Size effect on alloying ability and phase stability of immiscible bimetallic nanoparticles.* European Physical Journal B **54**(4) 479–484.

Yang, G. W., Wang, J. B., & Liu, Q. X. 1998. *Preparation of nano-crystalline diamonds using pulsed laser induced reactive quenching.* Journal of Physics-Condensed Matter **10**(35) 7923–7927.

Yasuda, H. & Mori, H. 1992. *Spontaneous Alloying of Zinc Atoms into Gold Clusters and Formation of Compound Clusters.* Physical Review Letters **69**(26) 3747–3750.

Yasuda, H. & Mori, H. 2002. *Phase diagrams in nanometer-sized alloy systems.* Journal of Crystal Growth **237** 234–238.

Yasuda, H., Mori, H., & Furuya, K. 2000. *Spontaneous atom mixing and unmixing in metallic nanoparticles.* Philosophical Magazine Letters **80**(3) 181–186.

Yasuda, H., Mori, H., Komatsu, M., & Takeda, K. 1993. *Spontaneous Alloying of Copper Atoms into Gold Clusters at Reduced Temperatures.* Journal of Applied Physics **73**(3) 1100–1103.

Yeh, M. S., Yang, Y. S., Lee, Y. P., Lee, H. F., Yeh, Y. H., & Yeh, C. S. 1999. *Formation and characteristics of Cu colloids from CuO powder by laser irradiation in 2-propanol.* Journal of Physical Chemistry B **103**(33) 6851–6857.

Yin, Y. D., Rioux, R. M., Erdonmez, C. K., Hughes, S., Somorjai, G. A., & Alivisatos, A. P. 2004. *Formation of hollow nanocrystals through the nanoscale Kirkendall Effect.* Science **304**(5671) 711–714.

Young, T. 1805. *An Essay on the Cohesion of Fluids.* Philosophical Transactions of the Royal Society of London **95** 65–87.

Yudasaka, M., Kasuya, Y., Kokai, F., Takahashi, K., Takizawa, M., Bandow, S., & Iijima, S. 2002. *Causes of different catalytic activities of metals in formation of single-wall carbon nanotubes.* Applied Physics A **74**(3) 377–385.

Zhang, J., Worley, J., Dénommée, S., Kingston, C., Jakubek, Z. J., Deslandes, Y., Post, M., Simard, B., Braidy, N., & Botton, G. A. 2003. *Synthesis of metal alloy nanoparticles in solution by laser irradiation of a metal powder suspension.* Journal of Physical Chemistry B **107**(29) 6920–6923.

Zhang, J. M., Ma, F., & Xu, K. W. 2004. *Calculation of the surface energy of FCC metals with modified embedded-atom method.* Applied Surface Science **229**(1-4) 34–42.

Ziebold, T. O. 1967. *Precision and Sensitivity in Electron Microprobe Analysis.* Analytical Chemistry **39**(8) 858–861.

Zreiba, N. A. & Kelly, T. F. 1990. *X-Ray Depth Distribution Function, $\phi(\rho z)$, for Thin Spheres.* X-Ray Spectrometry **19**(6) 275–283.